2-28-2017 12:00 AM

Electrochemical and Modelling Studies on Simulated Spent Nuclear Fuel Corrosion under Permanent Waste Disposal Conditions

Nazhen Liu, *The University of Western Ontario*

Supervisor: Dr. David Shoesmith, *The University of Western Ontario*
Joint Supervisor: Dr. James Noël, *The University of Western Ontario*
A thesis submitted in partial fulfillment of the requirements for the Doctor of Philosophy degree in Chemistry

Recommended Citation
Liu, Nazhen, "Electrochemical and Modelling Studies on Simulated Spent Nuclear Fuel Corrosion under Permanent Waste Disposal Conditions" (2017). *Electronic Thesis and Dissertation Repository*. 4412.
https://ir.lib.uwo.ca/etd/4412

Abstract

The safety assessment models for the deep geological disposal of spent nuclear fuel require a fundamental understanding of the corrosion of spent fuel in a failed waste container. The overall research goal of this project is to investigate the corrosion of simulated spent fuel under permanent disposal conditions, using both model simulations and experimental investigations. A model for fuel corrosion has been expanded to determine the relative importance of radiolytic hydrogen and hydrogen from corrosion of the steel vessel in suppressing fuel corrosion. It was shown that, for CANDU (CANada Deuterium Uranium) fuel with moderate in-reactor burnup, only micromolar concentrations of hydrogen from steel corrosion are required to completely suppress fuel corrosion. In a partially closed system (i.e., within cracks in the fuel) radiolytic hydrogen alone can suppress corrosion to a negligible level. The model was validated by comparing the calculated corrosion rates with published measurements. Agreement between calculated and measured rates indicated that corrosion is controlled by the rate of radiolytic production of oxidants, in particular hydrogen peroxide, irrespective of the reactivity of the fuel.

Experimentally, the influence of rare earth doping on the reactivity of UO_2 was investigated. For RE^{III}-doped UO_2, the onset of matrix dissolution was accompanied by the enhanced oxidation of the matrix to $U^{IV}_{1-2x}U^{V}_{2x}O_{2+x}$. This can be attributed to the onset of tetragonal lattice distortions as oxidation proceeds which leads to the clustering of defects, enhanced diffusion of O_I (interstitial oxygen) to deeper locations and destabilization of the fluorite lattice. A further investigation of the doping effect was performed on a series of $(U_{1-y}Gd_y)O_2$ materials ($y = 0$, 0.01, 0.03, 0.05, 0.07 and 0.10). Overall the increase in doping up to 10% does not exert a major influence on reactivity possibly due to the competition between an increase in the number of (O_v)s (oxygen vacancy) and a contraction in the lattice constant.

Keywords

Uranium dioxide, Corrosion, Nuclear waste disposal, Modelling, COMSOL, Electrochemistry, Rare earth doping, Defects.

Co-Authorship Statement

Chapter 5 contains the contribution of Dr. Heming He, who performed the AFM and CS-AFM analyses on $UO_{2.002}$ specimen.

Chapter 6 contains the contribution of Dr. Jandee Kim and Dr. Jeongmook Lee from Korean Atomic Energy Research Institute (KAERI). We synthesized the materials and collected the raw data of XRD and Raman together. Dr. Young-Sang Youn assisted with the calculation of lattice parameters from the XRD data.

Acknowledgments

First and foremost, I would like to thank my supervisors Prof. David Shoesmith and Prof. James Noël. I would like to thank Dave for giving me an opportunity to work for him. Dave is the most knowledgable and modest person that I ever met. I really appreciate his genuine concern to students, his attitude towards work and expertise in science. The experience of working with him is a precious asset in my life. I would also like to thank Prof. James Noël for answering millions of questions when I got confused, for pulling me together when I was falling apart. He is not only a great supervisor, but also a trustworthy friend.

My special thanks go to Dr. Zack Qin for providing valuable guidance and feedback to my modelling work. I would also like to thank Dr. Dmitrij Zagidulin, Dr. Jian Chen and Dr.Vahid Dehnavi, for their knowledge and always being there to help.

I would like to thank Surface Science Western, especially Dr. Mark Biesinger and Ms. Mary Jane Walzak for their assistance with XPS and Raman analyses.

I would also like to thank Dr. Jandee Kim, Dr. Jeongmook Lee, Dr.Young-Sang Youn, Dr. Jong-Goo Kim, Dr. Yeong-Keong Ha and Dr. Jong-Yun Kim from Korean Atomic Energy Research Institute (KAERI), for their assistance and hospitality during our collaboration. It was definitely a memorable experience for me.

Many thanks go to my talented colleagues in the Shoesmith and Wren groups, my amazing friends in Chemistry department, for being supportive over the past 4 years. I will always cherish our friendship.

My deepest gratitude goes to my parents for their endless love and support, especially my mother who always being there for me, loves me with all her passion, and believes in me unconditionally. And to my grandparents, you were taken away from me way too early, how I wish you were here to spend this moment with me. You are truly missed.

Lastly, I would like to thank my husband, Yong Tian, for being such a wonderful friend and partner. I couldn’t have done this without you. I am grateful to have shared my life with you.

This thesis is dedicated to my grandparents

Yumin Li
李玉民
(1920 – 1988)

Yunying Ma
马云英
(1920 – 1995)

Table of Contents

List of Tables

List of Figures

List of Symbols and Acronyms

at%	Atomic percent
AFM	Atomic force microscopy
CANDU	Canada deuterium uranium
CSV	Cathodic stripping voltammetry
CS-AFM	Current-sensing atomic force microscopy
CV	Cyclic voltammogram
D_R	Radiation dose rate
E	Potential
e^-	Electron
E_{CORR}	Corrosion potential
EIS	Electrochemical impedance spectroscopy
$[Fe^{2+}]_{bulk}$	Bulk concentration of Fe^{2+}
g_i	g-value for species i
$[H_2]_{bulk}$	Bulk concentration of H_2
$[H_2]_{crit}$	Critical $[H_2]$ that can completely suppress fuel corrosion
k	Reaction rate constant
K_{sp}	Solubility constant
MPM	Mixed Potential Model

NWMO	Nuclear Waste Management Organization
O_I	Interstitial oxygen
O_v	Oxygen vacancy
Q	Electric charge
Q_A	Anodic charge
Q_C	Cathodic charge
Q_D	Dissolution charge
R	Reaction rate
RE	Rare earth
SCE	Saturated calomel electrode
SEM	Scanning electron microscopy
SHE	Standard hydrogen electrode
SIMFUEL	Simulated nuclear fuel
s_ε	Noble metal particle coverage
wt%	Weight percent
XPS	X-ray photoelectron spectroscopy
XRD	X-ray diffraction
ε-particles	Noble metal fission product
ρ	Density

Chapter 1

1 Introduction

1.1 Project Background

Nuclear power is one of the leading low-carbon power generation methods of producing electricity. The median “total life-cycle greenhouse gas emissions per unit of energy generated” for nuclear fission-electric power is 12 g CO_2 eq/kWh, compared to 820 and 490 g CO_2 eq/kWh for coal and fossil gas [1]. The use of nuclear energy rather than these other energy sources preserves air quality and the Earth’s climate. Of the major energy sources, nuclear energy has perhaps the lowest impact on the environment. While nuclear power generates clean energy, it comes with the responsibility of managing the radioactive fuel waste [2]. The predominant forms of high level nuclear waste requiring disposal are the spent fuel bundles discharged from CANDU (CANada Deuterium Uranium) reactors and the large fuel assemblies discharged from LWR (Light Water Reactor) and PWR (Pressurized Water Reactor) reactors [3, 4].

The recommended approach for the long term management of used nuclear fuel in Canada is adaptive phased management [5]. This concept is based on multiple barriers: the used fuel bundles, durable metal containers, a clay buffer around the container, and a deep stable geologic environment, as illustrated in Fig. 1.1. The repository would be located 500 meters underground in a stable crystalline [6] or sedimentary [7] rock formation. Spent nuclear fuel bundles discharged from CANDU reactors would be sealed in Cu-coated carbon steel containers. The containers would then be placed in excavated tunnels or boreholes and surrounded by compacted bentonite clay.

While the prospects for the development of long-lived nuclear waste containers is very promising [8, 9], it is judicious to examine the consequences of container failure. The failure of the container would result in wet and potentially oxidizing conditions on the fuel surface leading to its corrosion [10]. Since, the majority of the radionuclides in used fuel (UO_2) are located within the oxide grains, their release rate to the environment would be determined by the fuel corrosion/dissolution rate. Therefore, it is important to investigate the surface reactivity of the

UO_2 in order to understand fuel corrosion/dissolution mechanisms and to determine the fuel's ability to retain individual radionuclides.

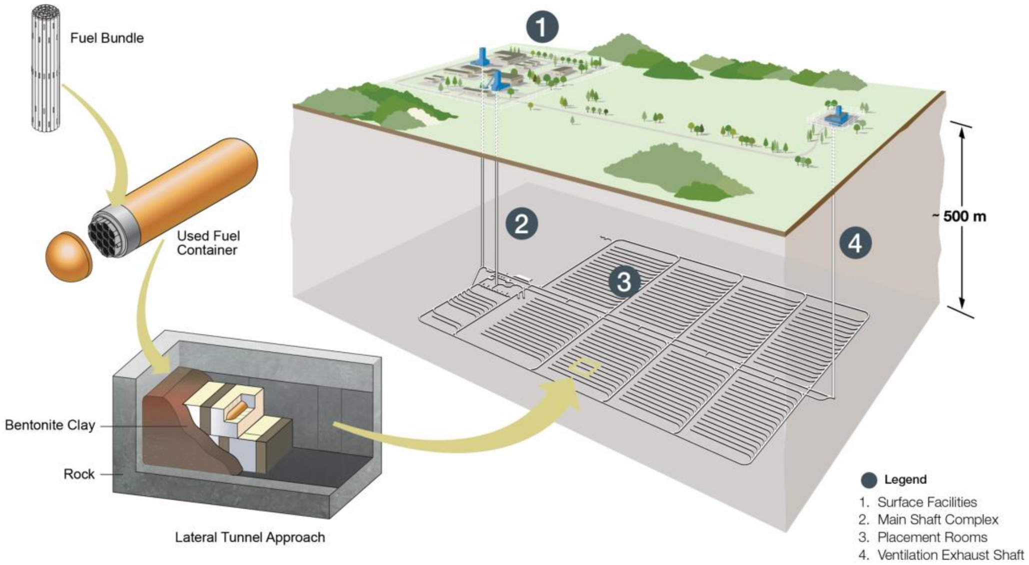

Figure 1.1: Illustration of the deep geological repository concept showing the container, placement rooms, and the tunnel layout [5].

The solubility of UO_2 is extremely limited under reducing conditions, but increases substantially under oxidizing conditions, as shown in Fig. 1.2. Consequently, the stability of UO_2 will be determined by the redox conditions to which it is exposed.

The concentration of dissolved oxidants in the repository is expected to be extremely low, since environmental oxidants (e.g., O_2 dissolved in groundwater) will be consumed rapidly by container corrosion and mineral/biological oxidation processes in the clay surrounding the container. The only source of oxidants inside a failed container would, therefore, be the radiolysis of water [12]. The β/γ radiation fields associated with the fission products in spent fuel will decay very fast over the first 500 years. However, α-radiation will remain high up to $\sim 10^5$ years making α-radiolysis of water a dominant source of oxidants [13]. The interaction of water and radiation produces a number of reactive species, among which the molecular species (H_2O_2, H_2 and O_2) are the predominant products [14, 15]. The molecular oxidant, H_2O_2, has been shown to be the primary oxidant available to drive fuel corrosion [10, 16].

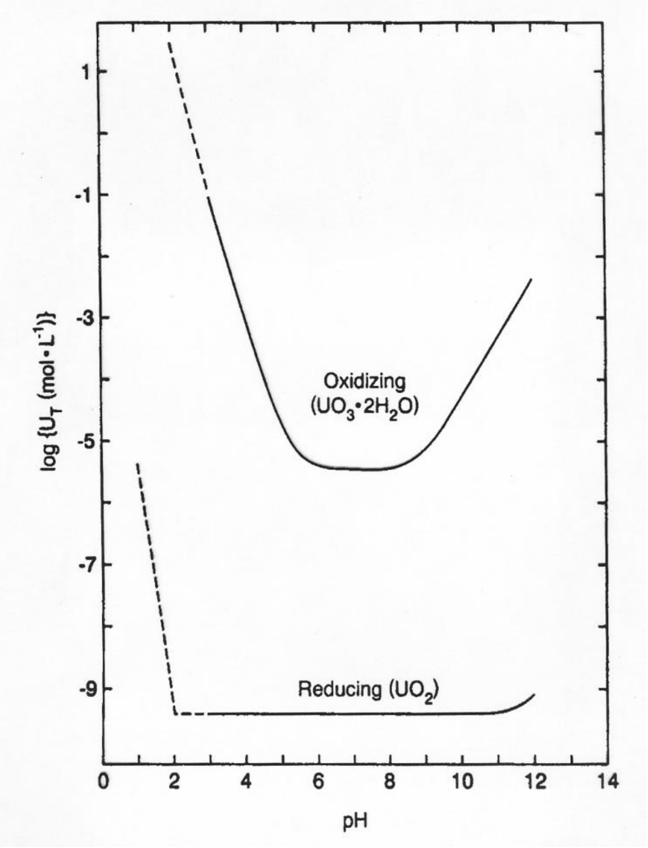

Figure 1.2: Solubility of uranium dioxide (UO_2) and schoepite ($UO_3 \cdot 2H_2O$) as a function of pH at 25°C [11], U_T on the y axis indicates total uranium.

The corrosion of the fuel will be influenced by other features which affect the redox conditions developed at the fuel surface. In an anaerobic environment, the steel vessel will corrode to produce Fe^{2+} and H_2 on contact with groundwater. Therefore, two corrosion fronts exist within a failed waste container, one at the spent fuel surface and the other at the steel surface. The safety assessment of deep geological disposal of spent nuclear fuel requires a fundamental understanding of the processes controlling fuel corrosion, the initial reaction leading to the release of most radionuclides to the groundwater [10].

1.2 Basic Properties of UO_2

1.2.1 Structural Properties

Crystalline UO_2 can be described as a simple cubic O^{2-} sublattice within a face centered cubic (fcc) sublattice of U^{4+} ions which forms a fluorite structure (Fig. 1.3), one of the most flexible structures capable of generating many derivative structures. The unit cell parameter is a = 5.470 Å, with ionic radii of $r_{U^{4+}}$ = 0.97 Å and $r_{O^{2-}}$ = 1.40 Å [17, 18]. The U is coordinated by eight equivalent oxygen atoms at the corners of a cube, each of which is in turn surrounded by a tetrahedron of four equivalent U atoms. Also interstitial sites are present in the lattice, which can accommodate additional O^{2-} ions without causing a major distortion of the fluorite lattice. Oxidation involves the injection of these extra O^{2-} ions and requires an appropriate number of U^{IV} to be oxidized to U^{V}/U^{VI} in order to maintain charge neutrality [19].

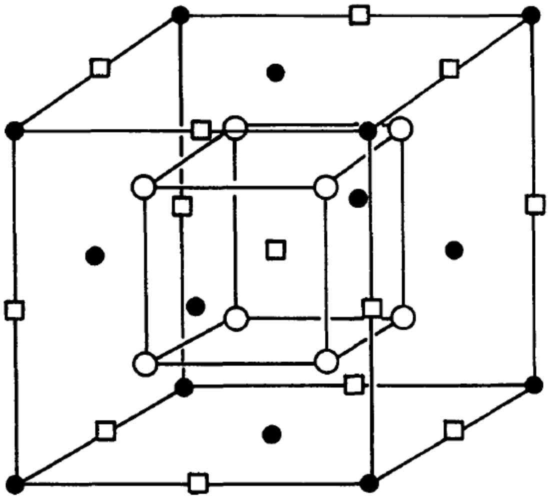

Figure 1.3: Fluorite crystal structure of stoichiometric UO_2. (●) U atoms; (○) O atoms; (□) empty interstitial lattice sites.

When UO_2 is oxidized, no extra lines are observed in X-ray powder photographs until the composition $UO_{2.25}$ is reached [20]. Up to that point, UO_{2+x} consists of a solid solution of excess oxygen atoms in the fluorite matrix of UO_2. Neutron diffraction and X-ray photoelectron spectroscopic studies have shown that, for compositions from $UO_{2.13}$ to $UO_{2.25}$ (U_4O_9), the incorporation of additional O atoms leads to a structural rearrangement. O atoms are observed to occupy newly identified interstitial positions, displaced from the original cubically coordinated sites by ~1 Å in the [110] and [111] directions, without disturbing the U sublattice [19, 21-24]. This defect structure is named the Willis cluster which contains two O' atoms, two oxygen vacancies and two O'' atoms, and is shown illustratively in Fig. 1.4. A more recent study investigated the point defects and their clustering behavior in nonstoichiometric UO_{2+x} based on density functional theory [25]. The calculations showed that point defects formed when $x < 0.03$ and defect clustering became unavoidable when $x > 0.03$. As x approached 0.25, the dominant defect structure changed from the Willis cluster to a cuboctahedral cluster.

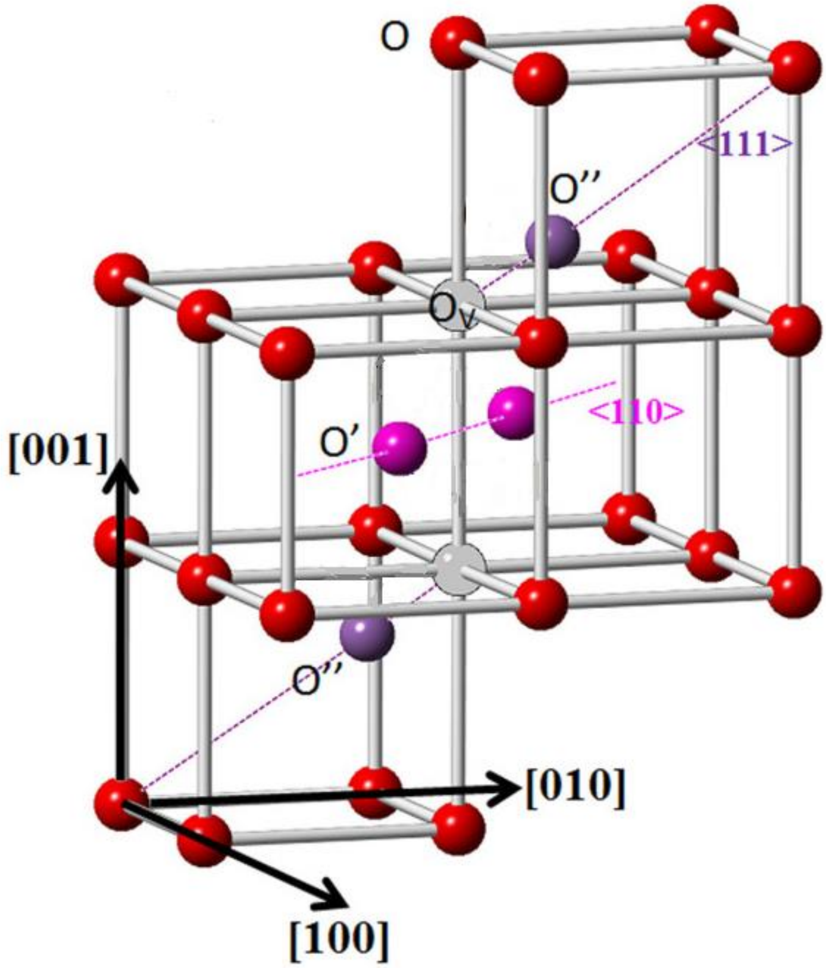

Figure 1.4: Illustration showing the 2:2:2 cluster in UO_{2+x} [26].

When $x = 0.25$, the disordered UO_{2+x} phase changes to an ordered phase U_4O_9. Weak additional lines appear on X-ray powder photographs [20], indicating the development of long-range ordering with a superlattice, in which the large unit cell contains $4\times4\times4$ fluorite cells. As UO_2 is further oxidized to $UO_{2.33}$ (U_3O_7), the fluorite lattice becomes significantly distorted due to the formation of tetragonal pseudocubic structures derived from the fluorite structure with the c/a ratio varying from 0.986 to 1.032 [27, 28]. Beyond $UO_{2.33}$, further oxidation in air requires a major structural rearrangement, to a more open, layer-like phase with lower density [29]. The structure of U_3O_8 is shown in Fig. 1.5. The solid is a layered structure where the layers are bridged by oxygen atoms, each layer contains uranium atoms which are coordinated with oxygen atoms.

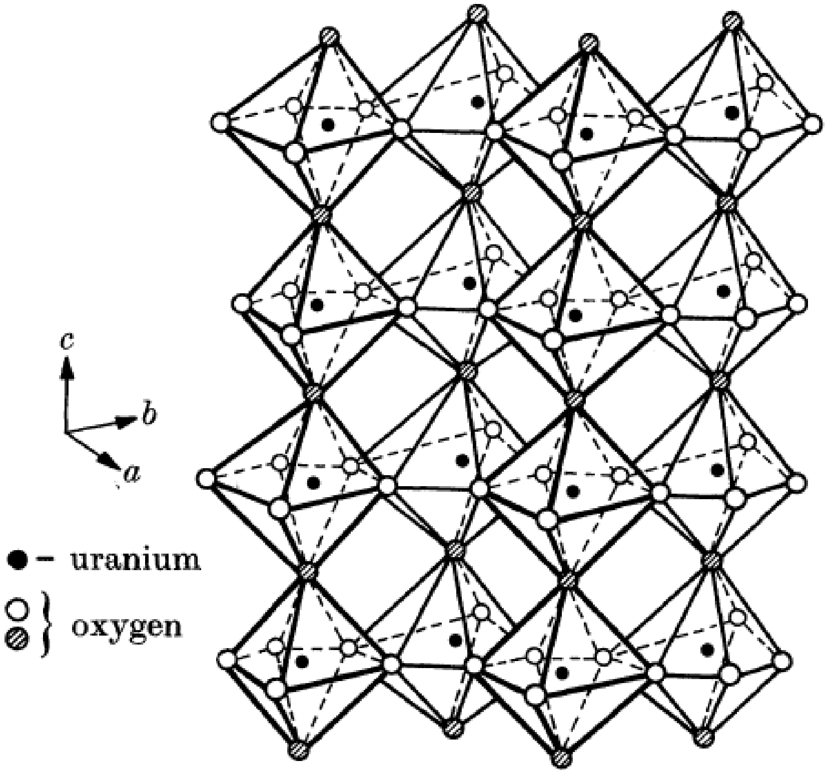

Figure 1.5: Chains of pentagonal bipyramids sharing vertices in U_3O_8 [27].

In its stoichiometric form, UO_2 can be considered as a Mott-Hubbard insulator [30-32], characterized by a partially filled cationic shell which has a sufficiently narrow bandwidth of the 5f level that the mobility of electrons is restricted by Coulomb interaction [33]. Electronic conductivity is supported by the activated process of small polaron hopping [34-36] in which the normally localized electrons can be transferred from one cation to the next by a series of thermally assisted jumps.

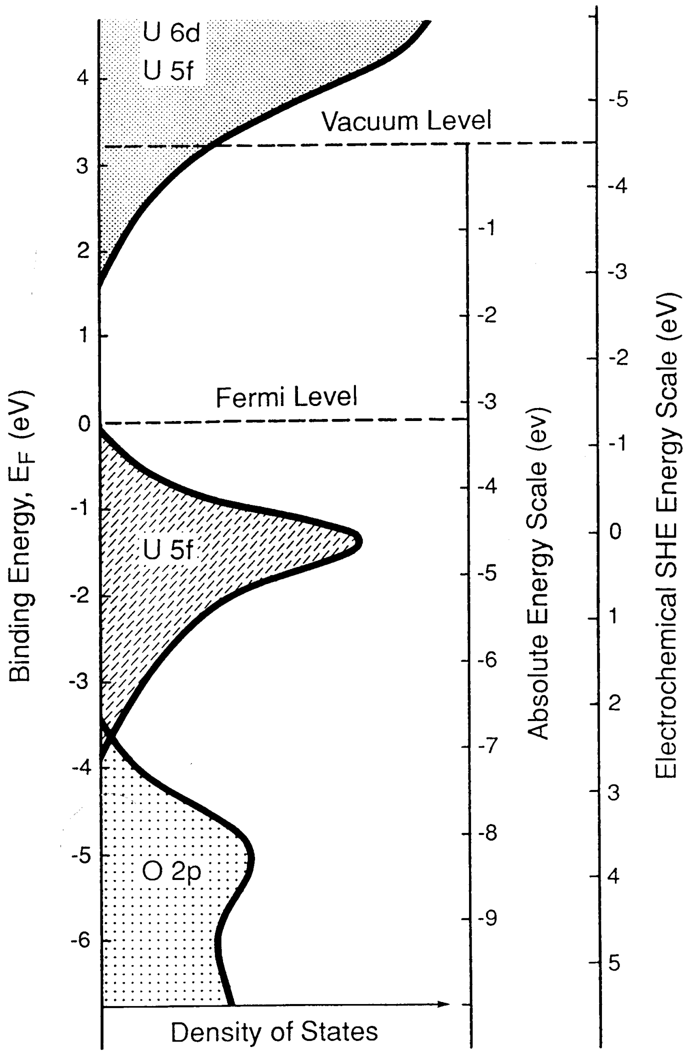

Figure 1.6: Schematic illustration of the band structure diagram for UO_2, and its relationship to important energy scales (from electrochemical and spectroscopic data) [11].

A schematic energy level diagram for UO_2 is given in Fig. 1.6 [11]. The narrow U 5f band falls in the gap between the filled valence band and the empty conduction band. The valence band consists of mainly O 2p characteristics (with some contribution from U 6d and 5f orbitals), while the conduction band is a mixture of overlapping orbitals of U 7s, 6d and 5f. The occupied and unoccupied U 5f levels are known as the lower and upper Hubbard bands, respectively. For stoichiometric UO_2, electronic conductivity requires promotion of electrons from the occupied U 5f level to the conduction band, which has a high activation energy (1.1 eV) and, hence, a low probability at room temperature [35]. However, fabricated UO_2 pellets possess a slight excess of

O present as interstitial O^{2-} ions. To maintain charge balance, a fraction of U^{IV} will be oxidized to U^{V}/U^{VI}, a process which creates holes in the occupied U 5f Hubbard band, which can migrate by the polaron hopping mechanism, with a low activation energy (~0.2 eV) [37-39]. Thus, hyperstoichiometric UO_{2+x} can be treated as a p-type semiconductor which is able to conduct an electric current for electrochemical reactions occurring at its surface.

Substitution of U^{IV} by lower valence cations (e.g., Gd^{III}) in the UO_2 lattice would also require an oxidation of U^{IV} to a higher state (U^{V}) creating mobile holes and, hence, increasing conductivity [40, 41]. Thus, although the composition of simulated fuel pellets used in the project is expected to be very close to stoichiometric, the conductivity is enhanced by the rare earth dopants.

1.2.2 Thermodynamic Properties

A wide range of U phases and soluble U species are thermodynamically possible in groundwater systems, as shown in Fig. 1.7. Over the pH region 6-9, UO_2 in its reduced form (U^{IV}) would be highly insoluble. At the U concentration used to construct this diagram (10^{-9} mol L^{-1}, close to the solubility of UO_2 in neutral solutions), U_4O_9 would be thermodynamically stable on the surface of UO_2. However, the solubility increases by many orders of magnitude under oxidizing conditions, Fig. 1.2, and UO_2 dissolves by oxidation to uranyl (UO_2^{2+}) ions.

Both UO_2^{2+} and U^{4+} ions are extensively hydrolyzed in aqueous solutions to form species such as $U_x(OH)_y^{(4x-y)+}$ for U^{4+} at pH > 1, and $(UO_2)_x(OH)_y^{(2x-y)+}$ for UO_2^{2+} at pH > 4 [42]. The dissolution rate of oxidized U^{VI} from a fuel surface will be strongly influenced by complexing species, such as peroxide, carbonate, or nitrate, which greatly enhance solubility, or phosphate, silica, or vanadate, which reduce the solubility [29, 43].

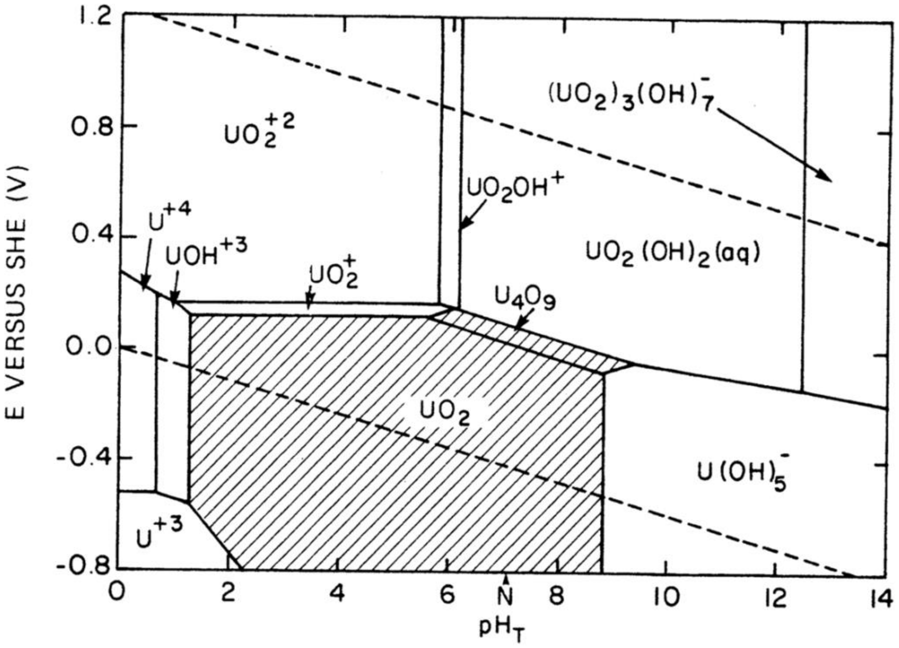

Figure 1.7: Potential-pH diagram for the uranium/water system at T 25°C. Uranium concentration is 10^{-9} mol L^{-1} [44].

1.2.3 Electrochemical Properties

Cyclic voltammetry is a convenient and rapid tool for obtaining information about electron transfer processes and measuring the changes on the UO_2 surface due to oxidation/reduction reactions [45, 46]. A cyclic voltammogram (CV) obtained on UO_2 is shown in Fig. 1.8. The various stages of oxidation and reduction are numbered on the plot. On the forward scan, a shoulder (I) is observed in the potential range –0.8 to –0.4 V (vs. SCE), where the bulk stoichiometric UO_2 is thermodynamically stable. It has been proposed that the oxidation in region I can be attributed to the presence of non-stoichiometry in the UO_2 surface, possibly within grain boundaries [46]. Surface oxidation in this region appears reversible, as all anodic charge consumed on the forward scan can be recovered on the reverse scan. Peak II is attributed to the oxidation of the UO_2 matrix involving the incorporation of O^{2-} ions at interstitial sites in the fluorite lattice. While the exact composition of this thin layer is difficult to determine, a limiting stoichiometry of $UO_{2.33}$ appears to be obtained around –0.1 V. Further oxidation at higher potentials results in dissolution as UO_2^{2+}, which contributes to the rising current in region (III). On the reverse scan, a peak (IV) is sometimes observed at ~–0.2 V. The small amount of charge associated with this peak suggests that it is due to the reduction of an adsorbed species formed at anodic potentials, which is less stable than the oxidized U in the UO_{2+x} layer [46]. Peak V is attributed to the reduction of oxidized layers, $UO_{2.33}$ and/or $UO_3 \cdot yH_2O$, formed on the anodic scan. The large current increase in region VII is due to the reduction of H_2O to H_2.

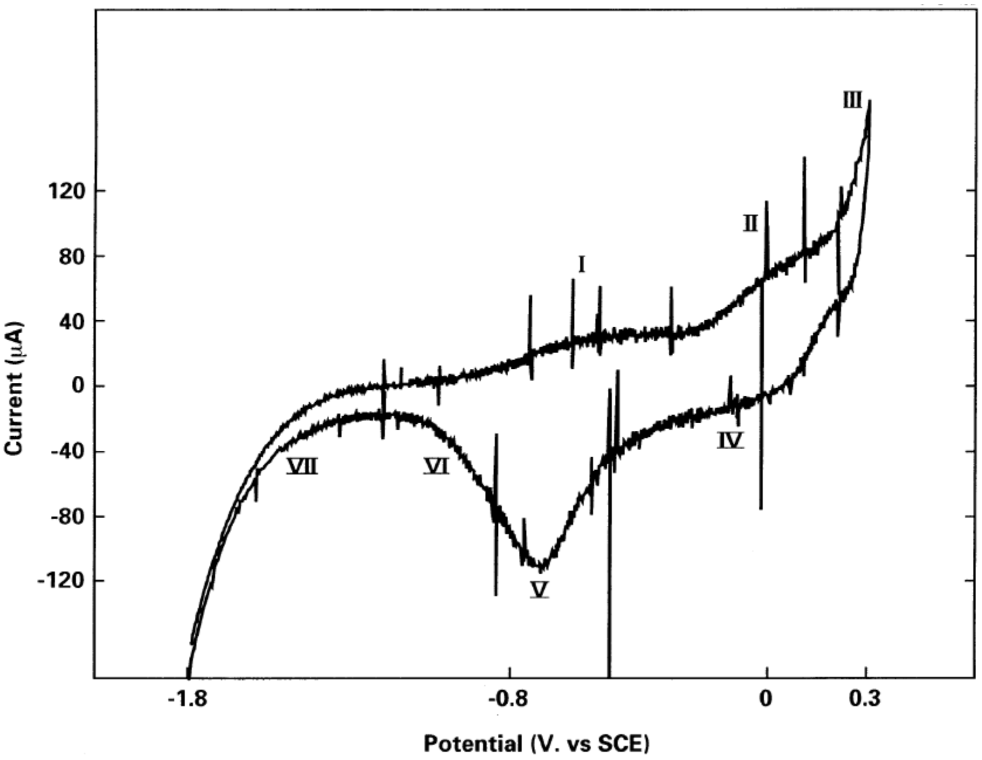

Figure 1.8: Cyclic voltammogram recorded on a rotating UO_2 electrode at 10 mV s^{-1} and a rotation rate of 16.7 Hz using IR compensation in a 0.1 mol L^{-1} $NaClO_4$ at pH 9.5. The Roman numbers indicate the various stages of oxidation or reduction described in the text [10].

Fig. 1.9 shows a summary of the composition of a UO_2 surface as a function of surface redox condition (indicated as the corrosion potential, E_{CORR}) in an aqueous environment. The potential ranges for some important electrochemical processes on UO_2, including surface oxidation and dissolution, are also shown. The correlation between the surface composition and potential in Fig. 1.9 was determined by a combination of electrochemical and surface analytical experiments [10, 47]. The range of corrosion potential in a failed waste container predicted by a Mixed Potential Model is indicated by an arrow A [48]. The vertical dashed line at –0.4 V (vs. SCE), represents the thermodynamic threshold for surface oxidation. For potentials greater than –0.4 V, fuel corrosion is expected to occur. Below –0.4 V, the stability of UO_2 will be determined by the chemical dissolution of UO_2 (as U^{IV}). Since the solubility of U^{IV} is extremely low (Fig. 1.2), this chemical dissolution rate will be very low.

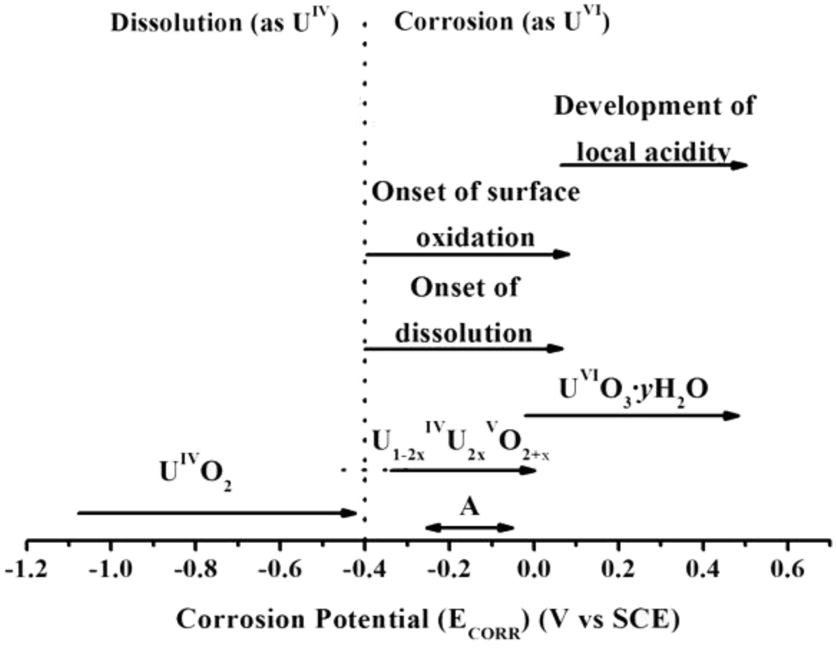

Figure 1.9: Composition and corrosion behavior of UO_2 as a function of the UO_2 corrosion potential [10, 49]. A indicates the range of corrosion potential in a failed waste container predicted by a Mixed Potential Model [48].

CANDU fuel is a solid ceramic oxide (UO_2) fabricated into pellets with a diameter of about 12 mm [50]. These pellets are sealed inside tubes (~0.5 m long) made of Zircaloy-4 (chemical composition by weight: Cr: 0.12 ± 0.0003%, Fe: 0.23 ± 0.002%, Sn: 1.33 ± 0.02%, O: 0.116 ± 0.003%, Zr balance) [51], and arranged in a circular array in fuel bundles (Fig. 1.10). This fuel assembly weighs 24.8 kg, of which 22.8 kg is UO_2 and 2.0 kg is Zircaloy [52]. As of June 2015, a total of approximately 2.60 million used CANDU fuel bundles were in storage at reactor sites.

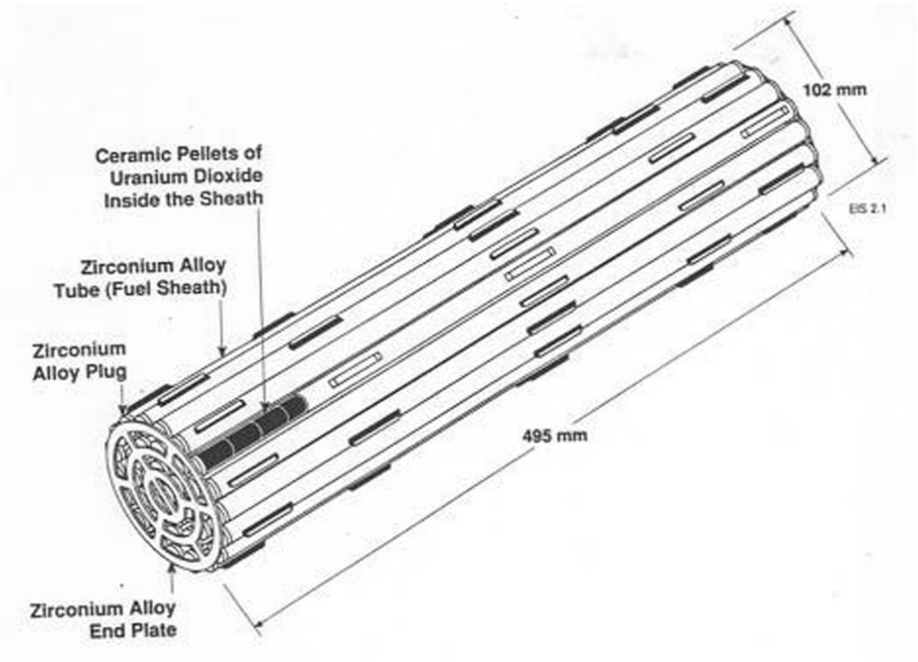

Figure 1.10: Typical CANDU fuel bundle [47].

1.2.4 Spent Nuclear Fuel

Spent fuel is mainly UO_2 (> 95%) with the remainder being the radioactive fission products and actinides produced during the in-reactor process. The inventory of radionuclides within the fuel depends on in-reactor burn-up (the energy extracted from a primary nuclear fuel source, measured as the actual energy released per mass of initial fuel) and the linear power rating (the power produced per unit length) of the fuel [53]. Fig. 1.11 shows three categories of radionuclides for which eventual release mechanisms under disposal conditions would be expected to be different.

(1) The gap inventory (e.g., He, I, C, Cs), comprising radionuclides which are volatile at reactor operating temperatures, and migrate to the fuel/sheath gap during reactor operation, which would be expected to be soluble, and released on contact with groundwater;

(2) The grain boundary inventory composed of those radionuclides which have segregated to grain boundaries within the fuel. They can diffuse at high in-reactor temperatures and congregate in alloy precipitates, referred to as ε-particles (e.g., Mo, Ru, Rh, Pd). It also includes radionuclides which are stable as oxides but incompatible with the UO_2 matrix (Rb, Cs, Ba, Zn, Nb, Mo, Te, Sr), which can separate into secondary precipitates. These phases tend to have the general composition

ABO_3 and to adopt a cubic perovskite-type structure. Their release will depend on their chemical nature and the physical and chemical properties of the grain boundaries and could require a protracted period of exposure to groundwater;

(3) The matrix inventory (most radionuclides fall into this category), consisting of species retained within the fuel grains and whose release will be controlled by the dissolution properties of the fuel. This inventory includes radionuclides which remain as substitutional ions within the fuel matrix including actinides (Np, Pu, Am, Cm) and the rare earths (La, Ce, Pr, Nd, Pm, Sm, Eu, Gd, Y).

Among these radionuclides, the ones of greatest environmental concern in a geologic repository will be those that have a combination of high radiotoxicity, geochemical mobility, and a long half-life. Examples are ^{99}Tc, ^{129}I, ^{79}Se, ^{135}Cs, ^{239}Pu, ^{237}Np, and ^{235}U [54].

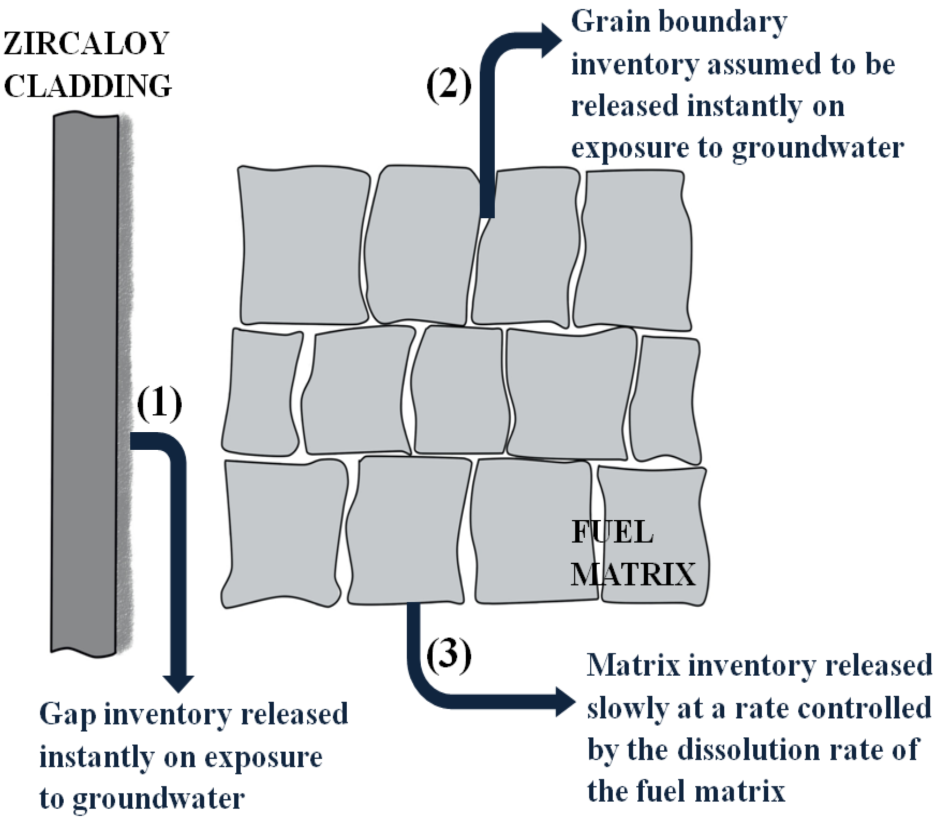

Figure 1.11: Schematic showing the three general categories of radionuclides [50].

When irradiated, the fuel undergoes a number of microstructural and compositional changes involving the formation of rare earth (RE^{III}) elements and noble metal (ε) particles, and the development of non-stoichiometry [55], which are expected to have the most significant influences on fuel corrosion. Fig. 1.12 shows an SEM image of an irradiated fuel surface with the features due to in-reactor irradiation noted. The RE^{III} elements cause an increase in the electrical conductivity of the fuel matrix, and the noble metal (ε) particles can act as either cathodes or anodes (depending on the prevailing redox conditions in the exposure environment) galvanically coupled to the UO_2 matrix. Studies using atomic force microscopy (AFM), current sensing-AFM and scanning electrochemical microscopy clearly demonstrated that the fuel reactivity increased substantially with highly non-stoichiometric clusters being $\geq 10^3$ more reactive than close-to-stoichiometric UO_2 [55]. While the exact anodic oxidation mechanism remains to be resolved, the higher O_I (interstitial oxygen) mobility at higher degrees of non-stoichiometry may enhance a deeper and more extensive surface oxidation.

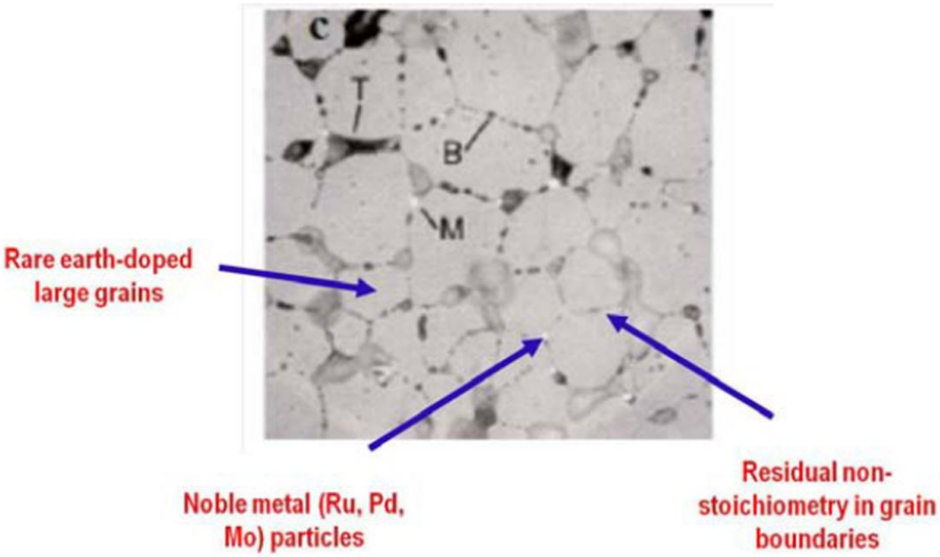

Figure 1.12: Scanning electron micrograph of irradiated fuel (burn-up 770 MWh/kgU) [53].

On discharge from reactor, the fuel is highly radioactive, but its activity decreases quickly. As shown in Fig. 1.13, for CANDU fuel, the β/γ irradiation would decay rapidly within the first few hundred years. Beyond this period, the decay process would be dominated by the long-lived actinides most of which decay by the emission of α-particles ($^{4}_{2}\mathrm{He}^{2+}$). It seems reasonable to expect that waste containment preventing contact of the fuel with groundwater can be achieved over the time period when β/γ radiation fields are significant, making α-radiation which persists for considerably longer time periods, the most likely source of oxidants in a failed, groundwater-flooded waste container.

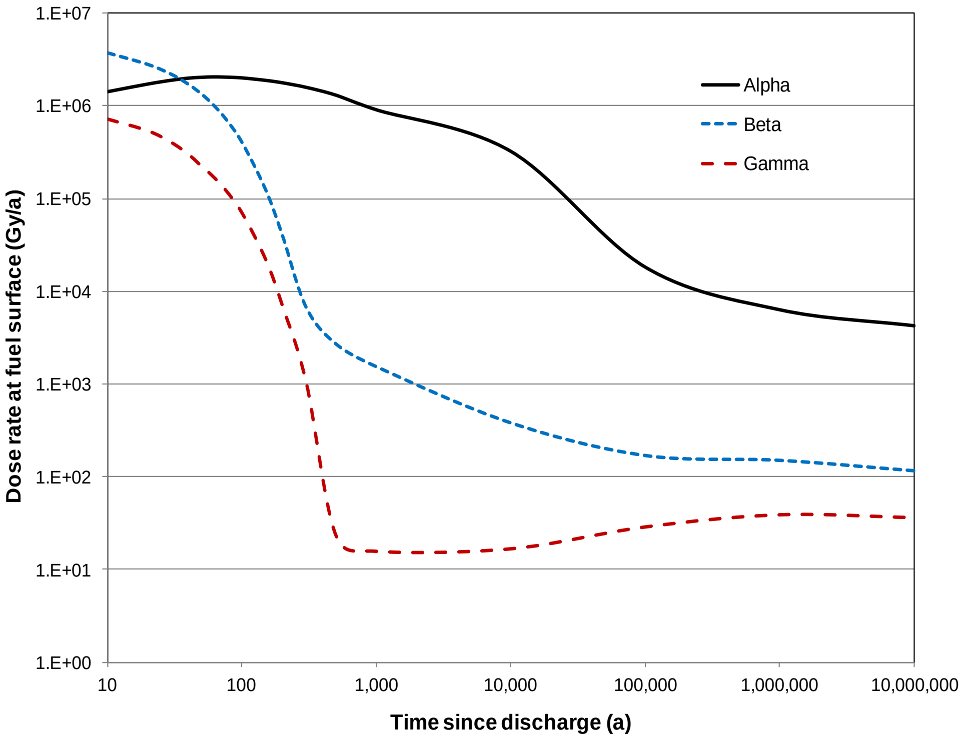

Figure 1.13: α, β, and γ radiation dose rates with respect to time for water in contact with a CANDU fuel bundle with a burn up of 220 MWh/kgU [13].

1.3 Reactions in a Failed Waste Container

In a failed waste container, two corrosion fronts will be established, one on the fuel surface driven by the radiolytic oxidants, and a second one on the carbon steel surface sustained by water reduction and producing the potential redox scavengers, Fe^{2+} and H_2. Fig. 1.14 illustrates the redox coupling of the two corrosion fronts via the interactions of the radiolytic oxidant, H_2O_2, and its potential decomposition product, O_2, and the anoxic corrosion products, $Fe^{2+}$and H_2. A complex series of homogeneous solution reactions and heterogeneous surface reactions will have a very significant influence on the redox conditions within the failed container and, hence, on the fuel corrosion/radionuclide release process.

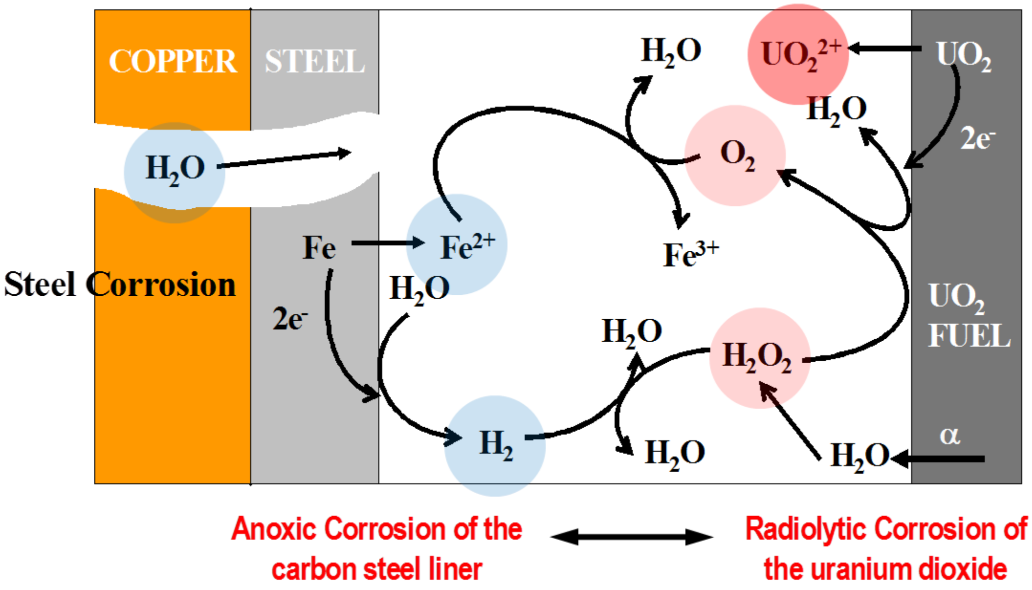

Figure 1.14: Illustration showing the corrosion scenario inside a failed nuclear waste container [47].

Figure 1.15 summarizes the main reactions controlling the redox conditions and, hence, the process of fuel corrosion. The reactions are: (1) the production of a series of decomposition products by water radiolysis; (2) the oxidative dissolution of UO_2 supported by H_2O_2 reduction; (3) the reduction of oxidized uranium (U^V/U^{VI}) by H_2 oxidation; (4) the scavenging of H_2O_2 in homogeneous solution by reaction with Fe^{2+}; (5) the reaction of H_2O_2 with H_2 catalyzed by noble metal particles; and (6) the decomposition of H_2O_2 to O_2 and H_2O.

1.3.1 Water Radiolysis

Since the α-radiolysis of water is the driving force for spent fuel oxidation/dissolution (corrosion), the influence of α-dose rate on the corrosion of UO_2 materials has been intensively studied [57-63]. A wide range of studies of the corrosion rate as a function of α-dose have been summarized by Poinssot et al. [63], and showed a clear increase in corrosion rate with increasing α-source strength. The interaction of α-radiation with water yields a series of decomposition products (H_2, H_2O_2, $H^•$, $OH^•$, $HO_2^•$, e_{aq}^-, H^+ and OH^-) [15, 64], among which the molecular species are dominant. The radical species have concentrations orders of magnitude lower than those of the stable molecular products as a consequence of their high reactivity and, consequently, short lifetimes.

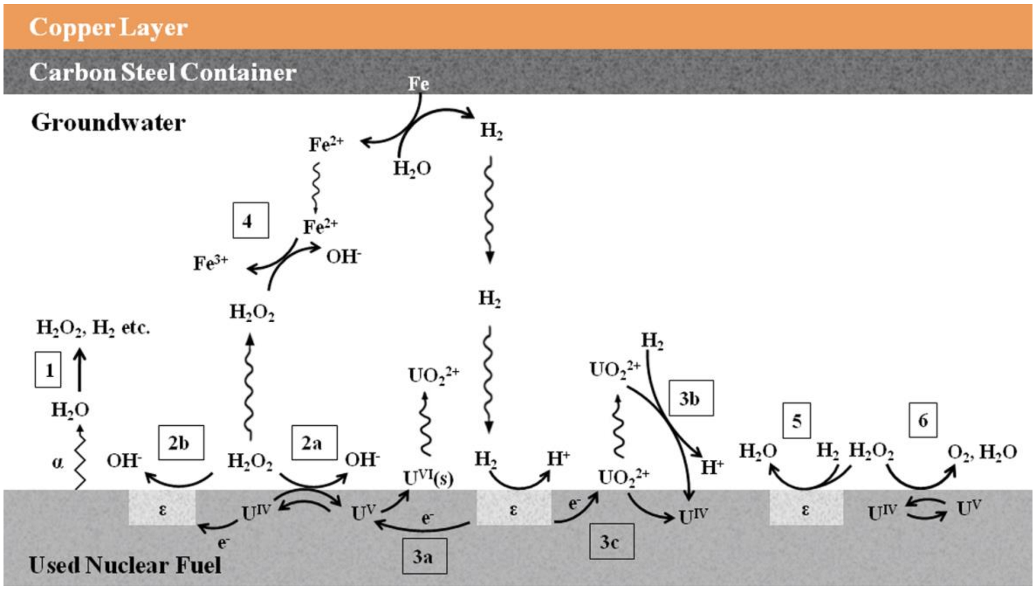

Figure 1.15: Schematic illustration of the main reactions inside a failed waste container [56].

A range of studies have calculated the dose rate profiles of α-radiation for different types of fuels using different approaches [13, 65, 66]. The α-dose rate in water in contact with a spent fuel bundle is determined by the source activity (which varies with different types of fuel, burnup and fuel age), the radiation energy and the distance from the source [14]. A typical energy of the α-particles from fuel decay is 5 MeV, corresponding to a path length of ~40 μm in water [65]. However, before reaching the fuel surface, the α-particles are attenuated by passage through the UO_2 matrix, and escape into the water with a reduced energy between 0 and 5 MeV. The geometrical distribution of the α-dose rate in a water layer ~40 μm thick has been found to follow an exponential decay with distance from the fuel surface [65].

The primary yields of radiolysis species are expressed by g values (the number of moles formed per joule of radiation energy absorbed), Table 1.1. The rate of radiolytic production for a species, *i*, is calculated using the expression

$$R_i = \mathrm{D_R} \times \mathrm{g}_i \times \rho_{\mathrm{H_2O}} \tag{1.1}$$

where $\mathrm{D_R}$ is the dose rate representing the rate of energy deposited per unit mass (of water in this case), g_i is the g-value of species *i*, and ρ_{H_2O} is the density of water.

Table 1.1: The primary yields (g-values) of α-radiolysis species [56].

Water decomposition species	g-value (μmol J^{-1})
H_2	0.1248
H_2O_2	0.104
e^-_{aq}	0.0156
$H^•$	0.0104
$OH^•$	0.0364
$HO_2^•$	0.0104
H^+	0.01872
OH^-	0.00312

1.3.2 UO_2 Oxidation by H_2O_2

The thermodynamic driving force for UO_2 corrosion is the potential difference between the redox potential of the groundwater ($E_{Red/Ox}$) and the equilibrium potential for UO_2 dissolution $(E_e)_{UO_2/UO_2^{2+}}$ [47].

Under such conditions the fuel will establish a corrosion potential (E_{CORR}) at which the anodic fuel dissolution rate ($UO_2 \rightarrow UO_2^{2+} + 2e^-$), termed the corrosion rate, will be equal to the rate of the oxidant reduction reaction ($Ox + 2e^- \rightarrow Red$). In a failed waste container, the reduction of H_2O_2 (the dominant oxidant) [67, 68] couples with the anodic dissolution of UO_2 which constitutes the overall fuel corrosion process (Fig. 1.16).

Both the UO_2 surface and the surface of ε-particles can support the cathodic reduction of H_2O_2 to drive the anodic dissolution of UO_2 (reactions 2a and 2b in Fig. 1.15),

$$UO_2 + H_2O_2 \longrightarrow UO_2^{2+} + 2OH^- \qquad (1.2)$$

The kinetics of these reactions has been studied, and rate equations for reactions 2a and 2b can be expressed as:

$$R_{2a} = k_{2a}\,[H_2O_2] \tag{1.3}$$

$$R_{2b} = k_{2b}\,s_\varepsilon\,[H_2O_2] \tag{1.4}$$

The rate constant $k_{2a} = 1.0 \times 10^{-8}$ m s^{-1}, was measured on a pure UO_2 pellet fabricated by Westinghouse [69]. The catalytic reaction 2b is also taken to be first-order with respect to H_2O_2 taking into account the surface fraction of ε-particles (s_ε). The experimental value for this catalytic rate constant k_{2b} is 6.92×10^{-6} m s^{-1} [70].

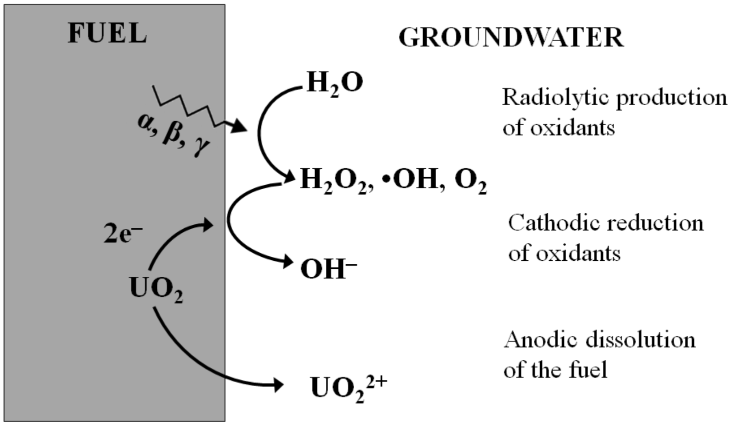

Figure 1.16: Illustration showing the coupling of cathodic oxidant processes to anodic fuel dissolution which constitutes the overall fuel corrosion process [47].

1.3.3 Reactions Involving H_2

Hydrogen has been shown to suppress UO_2 corrosion on a range of UO_2 materials ranging from spent fuel to α-emitter doped UO_2 and SIMFUELs [71-76]. The main source of H_2 within a failed container is the anaerobic corrosion of the steel vessel (as illustrated in Fig. 1.15), and dissolved H_2 concentrations as high as 0.038 mol L^{-1} are anticipated in sealed repositories [77]. Broczkowski et al. [76] used electrochemical methods to show that this suppression could be attributed to the formation of reductive radicals by H_2 oxidation catalyzed on the noble metal (ε) particles present in SIMFUEL pellets, which act as galvanically coupled anodes within the fuel matrix. This catalytic effect was confirmed by Jonsson et al. [70], who showed that during γ-irradiation, 1 bar H_2 was sufficient to inhibit UO_2 corrosion when 0.1 wt% Pd was present. In experiments conducted in an N_2 purged solution, 3 wt% Pd could prevent corrosion when only radiolytically produced H_2 was present. Because at room temperature, the dissolved molecular H_2 is known to be chemically inert, these experiments confirm that the activation of H_2 by noble metals is a key mechanism in suppressing fuel oxidation, as illustrated in Fig. 1.17.

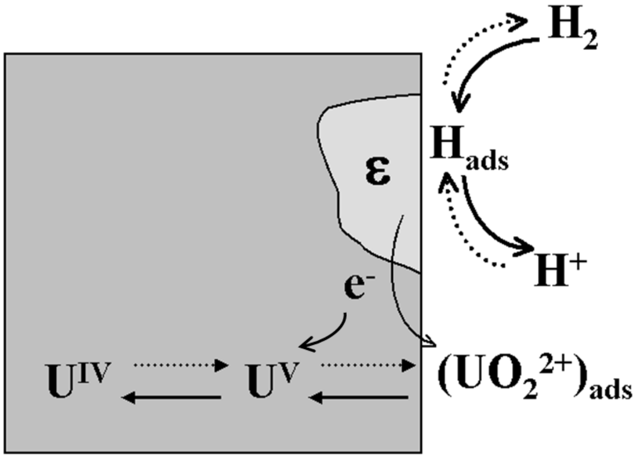

Figure 1.17: Illustration of a galvanic coupling between the UO_2 matrix and ε-particles [75].

There appear to be three possible pathways for reaction between U^V/U^{VI} and H_2 as indicated and numbered in Fig. 1.15. The reduction of oxidized surface species (U^V/U^{VI}) by H_2 oxidation on noble metal particles (reaction 3a) and of dissolved UO_2^{2+} either by reaction with H_2 in solution (reaction 3b) or with H_2 catalyzed on the fuel surface (reaction 3c). It is worth noting that reaction 3b and 3c are not expected to influence the release of radionuclides but only to lower the bulk concentration of UO_2^{2+}, assuming that the radionuclides (e.g. ^{99}Tc, ^{129}I, ^{79}Se, ^{135}Cs [54]) trapped within the fuel matrix are released irreversibly on UO_2 dissolution. The kinetics of these reactions has been studied in [78-80].

Other possible mechanisms by which H_2 can suppress the corrosion reaction include scavenging the radiolytic H_2O_2. Based on a comparison between electrochemical experiments on a UO_2 surface subjected to α-radiation and radiolysis model calculations, Wren et al. [64] suggested a two-step mechanism involving radiolytic H_2O_2 and H_2. In the first step, the OH radicals produced by the surface-catalyzed decomposition of H_2O_2 would react with H_2 produced by water radiolysis, resulting in the overall process, reaction (1.7), with the e^- produced and consumed in the surface catalytic cycle ($U^{IV} \leftrightarrow U^V$).

$$H_2O_2 + e^- \rightarrow OH^\bullet + OH^- \tag{1.5}$$

$$H_2 + OH^\bullet \rightarrow \left\{ H_2O + H^\bullet \right\} \rightarrow H_2O + H^+ + e^- \tag{1.6}$$

$$H_2O_2 + H_2 \rightarrow 2H_2O \tag{1.7}$$

Broczkowski [81] also showed evidence for this reaction on the surface of SIMFUEL with 3 at% simulated burn-up but containing no epsilon particles. The results strongly suggest that, while H_2 may not dissociatively absorb on UO_2, H_2O_2 does, and that the OH radical species formed can then be scavenged by H_2 leading to H_2O_2 consumption rather than fuel oxidation. However, Nilsson could find no evidence for this reaction in a system containing 2×10^{-4} mol L^{-1} H_2O_2 and up to 40 bar of H_2 ($\geq 2 \times 10^{-2}$ mol L^{-1} of dissolved H_2). Additionally, it has been observed that H_2 will reduce UO_2^{2+} when Pd is present [82]. The reason could be that for this scavenging process to occur, the concentration ratio $[H_2]/[H_2O_2]$ needs to be high. This may explain why a similar effect was not observed by Nilsson et al. since their concentration ratio was only $\sim 10^2$ [73]. It can be concluded that the scavenging of low concentrations of radiolytic oxidants would occur on the UO_2 surface in the presence of a sufficient H_2 concentration. However, the process appears to be kinetically slow when compared to the reaction rate on ε-particles or when H_2 is radiolytically activated [83, 84].

1.3.4 H_2O_2 Decomposition

Under corrosion conditions there are two competitive anodic reactions which can couple with the cathodic reduction of H_2O_2 (Fig. 1.18): the oxidative dissolution of UO_2 and the simultaneous oxidation of H_2O_2, the latter leading to H_2O_2 decomposition (reaction 6 in Fig. 1.15). Since only a fraction of H_2O_2 is consumed in oxidizing UO_2, this fraction is defined as the dissolution yield in some studies, which is the ratio between the concentrations of dissolved U and total consumed H_2O_2. According to Pehrman et al. [69], 86% of H_2O_2 consumption accounts for H_2O_2 decomposition on the surface of UO_2 pellets, and the fraction increases up to 99.8% for SIMFUEL (UO_2 specimens doped with non-radioactive fission products, including rare earths and noble-metal particles to mimic the effect of in-reactor irradiation [85]). Wu et al. used electrochemical methods to show that, at positive potentials, ~70% of the anodic current goes to

H_2O_2 oxidation and the remainder to UO_2 dissolution as UO_2^{2+} in solutions with relatively high [H_2O_2] (0.02 mol L^{-1}) [86].

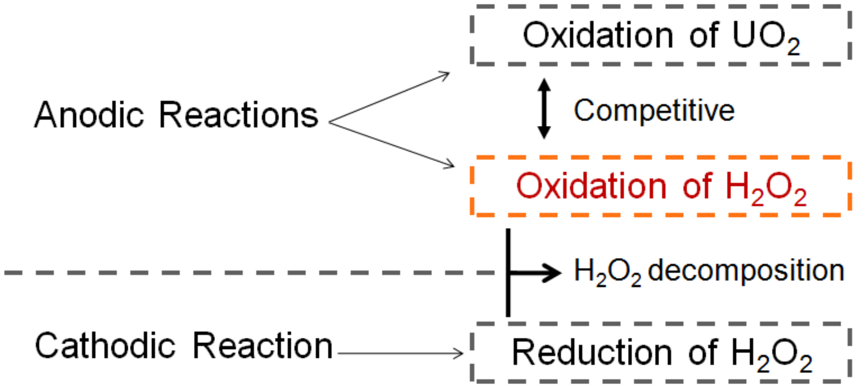

Figure 1.18: Schematic diagram showing the primary redox reactions involving H_2O_2 on a UO_2 surface [87].

Hiroki et al. studied the decomposition of H_2O_2 at water-ceramic oxide interfaces and found the oxide type had a strong effect on the decomposition rate, which increases in the order of $SiO_2 < Al_2O_3 < TiO_2 < CeO_2 < ZrO_2$ [88]. This study suggests selective reactive sites are responsible for H_2O_2 decomposition, and their number per unit of surface area varies with oxide type. Lousada et al. [89, 90] studied the mechanism of H_2O_2 decomposition on the surface of transition metal oxides (ZrO_2, TiO_2, and Y_2O_3), and proposed the existence of an adsorption step prior to decomposition, and the formation of $OH^\bullet$ as the primary product of the decomposition of H_2O_2. For decomposition on oxides on the surface of which redox transformations are possible (iron oxides being the prime example), decomposition has been shown to involve coupling with redox transformations (e.g. $Fe^{II} \leftrightarrow Fe^{III}$) within the oxide [91, 92]. Decomposition then proceeds via reactions involving these two oxidation states and radical species such as $OH^\bullet$ and $HO_2^\bullet$. This appears to be the case for H_2O_2 decomposition on UO_2 containing mixed oxidation states, as shown in Fig. 1.19.

Besides the UO_2 surface, the noble metal (ε) particles can also catalyze H_2O_2 decomposition. These particles are composed of fission products (Ru, Mo, Pd, and Rh) in the spent fuel [54]. Their ability to catalyze aqueous redox reactions on the fuel surface has been reported previously [78, 80, 82]. In recent dissolution studies [69, 93], a significant difference in the ratio between dissolved U and consumed H_2O_2 was found between pure UO_2 pellets and doped UO_2/SIMFUEL pellets. The much lower dissolution yield measured on SIMFUEL (containing ε-particles) than on pure UO_2 suggested a large fraction of the overall H_2O_2 consumption could be attributed to its decomposition on the particles.

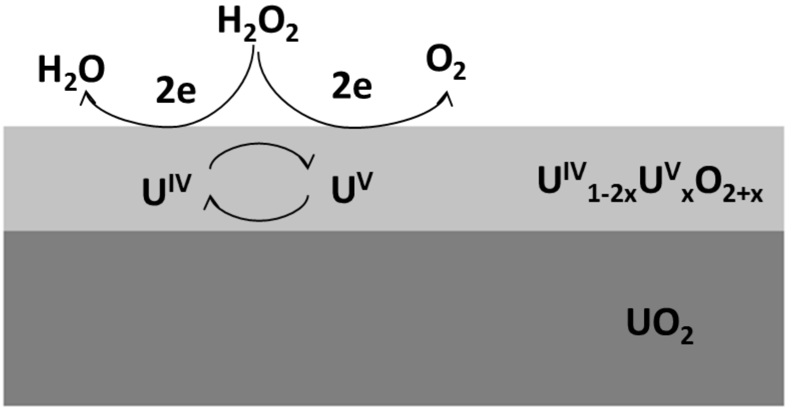

Figure 1.19: Schematic diagram showing catalysis of H_2O_2 decomposition by the mixed oxidation states present on the surface of UO_2 [10].

Studies also show that the decomposition rate of H_2O_2 depends on the alkalinity of the solution [94-96]. The carbonate-mediated decomposition of H_2O_2 has also been reported [97, 98].

1.4 Radiolytic Corrosion Model

The development of radiolytic models (in particular for α-radiolysis) for spent fuel corrosion has been reviewed [99]. A mixed potential model based on electrochemical parameters for fuel corrosion was developed [48]. This model consists of corrosion fronts on the fuel and steel vessel surfaces, interconnected by diffusion processes in the groundwater assumed to flood the container on failure. The model also included adsorption/desorption on solid surfaces within the container, precipitation/dissolution processes, and homogeneous redox reactions involving various species in the groundwater. While H_2O_2 decomposition to the less reactive O_2 and its scavenging by reaction with Fe^{2+} from steel corrosion were included in this model the key processes involving H_2 were not. Jonsson et al. [100] developed a comprehensive model which integrated the available kinetic data and tried to account for the geometrical distribution of the radiation dose rate at the surface of the fuel and the effects of the oxidant scavengers Fe^{2+} and H_2, fuel burn up, and ground water chemistry. It was concluded that a H_2 partial pressure of only 0.1 bar would effectively inhibit the dissolution of the spent fuel (aged ≥ 100 years). In the presence of 1 μmol L^{-1} Fe^{2+}, even 0.01 bar H_2 was calculated to be sufficient to stop fuel corrosion.

Using this database generated by Jonsson et al., Wu et al. [56, 101] developed a 1-dimensional model for fuel corrosion which includes the reactions involving H_2 and a full α-radiolytic reaction set. This model was subsequently expanded to account for the complex geometry of spent fuel, in particular the fracturing of the fuel pellets due to thermal stress during the in-reactor irradiation and the cooling process on discharge from reactor [102]. This 2-D model showed that the radiolytically-produced H_2 becomes more important in suppressing fuel corrosion if the fracture is deep and narrow.

1.5 Thesis Outline

One focus of this project is the development of a computational model to simulate fuel corrosion inside a failed container. The other focus is to investigate the influence of doping on the reactivity of UO_2 materials.

Chapter 2 briefly reviews the principles of the experimental techniques employed in this research.

In chapter 3, a 2-D model for the corrosion of spent nuclear fuel inside a failed nuclear waste container is presented. This model calculates the influences of various redox processes occurring within fractures in the fuel. It also calculates the relative importance of the two H_2 sources (H_2 produced by water radiolysis and H_2 produced by carbon steel corrosion) in controlling the fuel corrosion rate.

In chapter 4, a 1-D model is presented which simulates the corrosion process expected for α-emitter doped UO_2 not containing noble metal particles. The simulated steady-state corrosion rates are then compared with published experimental data. The model is also extended to calculate the corrosion rates for α-emitter doped UO_2 and spent fuel in a closed system, a possible scenario if the failure location on the container becomes sealed by the steel corrosion products.

In chapter 5, an electrochemical study of the reactivity of Dy-doped UO_2, Gd-doped UO_2, 1.5 at% SIMFUEL and $UO_{2.002}$ is presented. While all rare earth dopants are not expected to have an identical effect on UO_2, this comparison offers a first opportunity to determine their influence on the oxidative behavior of UO_2 in an aqueous environment.

In chapter 6, a series of $(U_{1-y}Gd_y)O_2$ materials were synthesized and characterized, and their electrochemical reactivity investigated. The influence of Gd^{III} doping on the characteristics of the $U^{IV}O_2$ fluorite lattice is determined by X-ray diffraction and Raman spectroscopy and related to its effect on reactivity using electrochemical techniques.

In chapter 7, an attempt is made to simulate the influence of radiolytic H_2 on UO_2 reactivity by producing H radicals electrochemically at cathodic potentials on heavily or non-doped UO_2. Their influence is investigated by measuring the effect of H radicals on the corrosion potential and by measuring the current due to re-oxidation of the UO_2 matrix reduced by H radicals.

1.6 References

[1] T. Bruckner, L. Fulton, E. Hertwich, A. McKinnon, D. Perczyk, J. Roy, R. Schaeffer, S. Schlömer, R. Sims, P. Smith, R. Wiser, Annex III: Technology-specific cost and performance parameters, in "Climate Change 2014: Mitigation of Climate Change", Cambridge University Press, 2014.

[2] NWMO, Choosing a Way Forward: The Future Management of Canada's Used Nuclear Fuel, Nuclear Waste Management Organization, Toronto, ON, 2005.

[3] R.C. Ewing, Long-term Storage of Spent Nuclear Fuel, Nature Mater. 14 (2015) 252-257.

[4] D.G. Bennett, R. Gens, Overview of European Concepts for High-level Waste and Spent Fuel Disposal with Special Reference Waste Container Corrosion, J. Nucl. Mater. 379 (2008) 1-8.

[5] NWMO, Implementing adaptive phased management 2016 to 2020, Nuclear Waste Management Organization, Toronto, ON, 2016.

[6] NWMO, Adaptive Phased Management - Used Fuel Repository Conceptual Design and Postclosure Safety Assessment in Crystalline Rock: Pre-Project Report, Report TR-2012-16, Nuclear Waste Management Organization, Toronto, ON, 2012.

[7] NWMO, Adaptive Phased Management - Postclosure Safety Assessment of a Used Fuel Repository in Sedimentary Rock: Pre-Project Report, Report TR-2013-07, Nuclear Waste Management Organization, Toronto, ON, 2013.

[8] D.W. Shoesmith, F. King, B.M. Ikeda, An Assessment of the Feasibility of Indefinite Containment of Canadian Nuclear Fuel Wastes, AECL-10972 COG-94-534, Whiteshell Laboratories, 1995.

[9] F. King, M. Kolar, The copper Container Corrosion Model Used in AECL's Second Case Study, Ontario Power Generation report: 06819-REP-01200-10041-R00, Toronto, ON, 2000.

[10] D.W. Shoesmith, Fuel Corrosion Processes under Waste Disposal Conditions, J. Nucl. Mater. 282 (2000) 1-31.

[11] D.W. Shoesmith, S. Sunder, W.H. Hocking, Electrochemistry of UO_2 Nuclear Fuel, in "Electrochemistry of Novel Materials", edited by J. Lipkowski, and P.N. Ross, VCH publishers, New York, 1994.

[12] L.H. Johnson, D.W. Shoesmith, Spent fuel, in "Radioactive Waste Forms for the Future", edited by W. Lutze, and R.C. Ewing, Elsevier, Amsterdam, 1988.

[13] S. Sunder, Alpha, Beta and Gamma Dose Rates in Water in Contact with Used CANDU UO_2 Fuel, AECL-11380 COG-95-340, Whiteshell Laboratories, 1995.

[14] J.W.T. Spinks, R.J. Woods, An Introduction to Radiation Chemistry, The Third Edition, John Wiley and Sons Inc., New York, 1990.

[15] G. Choppin, J.O. Liljenzin, J. Rydberg, Radiochemistry and nuclear chemistry, Butterworth-Heinemann, Oxford, 2001.

[16] E. Ekeroth, O. Roth, M. Jonsson, The Relative Impact of Radiolysis Products in Radiation Induced Oxidative Dissolution of UO_2, J. Nucl. Mater. 355 (2006) 38-46.

[17] T. Cardinaels, K. Govers, B. Vos, S. Van den Berghe, M. Verwerft, L. de Tollenaere, G. Maier, C. Delafoy, Chromia Doped UO_2 Fuel: Investigation of the Lattice Parameter, J. Nucl. Mater. 424 (2012) 252-260.

[18] F.Grønvold, High-Temperature X-ray Study of Uranium Oxides in the UO_2-U_3O_8 Region, J. Inorg. Nucl. Chem. 1 (1955) 357-370.

[19] B.T.M. Willis, Crystallographic Studies of Anion-excess Uranium Oxides, J. Chem. Soc., Farady Trans. 2 83 (1987) 1073-1081.

[20] P.B. Belbeoch, C. Piekarski, P. Perio, Structure de U_4O_9, Acta Cryst. 14 (1961) 837-843.

[21] B.T.M. Willis, Positions of the Oxygen Atoms in $UO_{2.13}$, Nature 197 (1963) 755-756.

[22] B.T.M. Willis, The Defect Structure of Hyper-stoichiometric Uranium Dioxide, Aeta Cryst. A34 (1978) 88-90.

[23] G.C. Allen, P.A. Tempest, J.W. Tyler, Coordination Model for the Defect Structure of Hyperstoichiometric UO_{2+x} and U_4O_9, Nature 295 (1982) 48-49.

[24] G.C. Allen, P. A. Tempest, The Accommodation of Oxygen Clusters in Hyperstoicheiometric Uranium Dioxide and Its Effects on Crystal Structure, J. Chem. Soc. Dalton Trans. (1983) 2673-2677.

[25] H.Y. Geng, Y. Chen, Y. Kaneta, M. Iwasawa, T. Ohnuma, M. Kinoshita, Point Defects and Clustering in Uranium Dioxide by LSDA+U Calculations, Phys. Rev. B 77 (2008) 104120.

[26] J. Wang, R.C. Ewing, U. Becker, Average Structure and Local Configuration of Excess Oxygen in UO_{2+x}, Sci. Rep. 4 (2014) 4216.

[27] G.C. Allen, P.A. Tempest, Ordered Defects in the Oxides of Uranium, Proc. R. Soc. Lond. A 406 (1986) 325-344.

[28] C.R.A. Catlow, Point Defect and Electronic Properties of Uranium Dioxide, Proc. R. Soc. Lond. A 353 (1977) 533-561.

[29] P.C. Burns, R. C. Ewing, A. Navrotsky, Nuclear Fuel in a Reactor Accident, SCIENCE 335 (2012) 1184-1188.

[30] P.W. Winter, The Electronic Transport Properties of UO_2, J. Nucl. Mater. 161 (1989) 38-43.

[31] S.M. Gilbertson, T. Durakiewicz, G.L. Dakovski, Y. Li, J.-X. Zhu, S.D. Conradson, S.A. Trugman, G. Rodriguez, Ultrafast Photoemission Spectroscopy of the Uranium Dioxide UO_2 Mott Insulator: Evidence for a Robust Energy Gap Structure, Phys. Rev. Lett. 112 (2014) 087402.

[32] L.E. Roy, T. Durakiewicz, R.L. Martin, J.E. Peralta, G.E. Scuseria, C.G. Olson, J.J. Joyce, E. Guziewicz, Dispersion in the MottInsulator UO_2: A Comparison of PhotoemissionSpectroscopy and Screened Hybrid Density Functional Theory, J. Comput. Chem. 29 (2008) 2288-2294.

[33] Y. Baer, J. Schoenes, Electronic Structure and Coulomb Correlation Energy in UO_2 Single Crystal, Solid State Commun. 33 (1980) 885-888.

[34] J.M. Casado, J. H. Harding, G.J. Hyland, Small-polaron Hopping in Mott-insulating UO_2, J. Phys.: Condens. Matter 6(1994) 4685-4698.

[35] P. Ruello, K.D. Becker, K. Ullrich, L. Desgranges, C. Petot, G. Petot-Ervas, Thermal Variation of the Optical Absorption of UO_2: Determination of the Small Polaron Self-energy, J. Nucl. Mater. 328 (2004) 46-54.

[36] A.J.E. Rettie, W.D. Chemelewski, D. Emin, C.B. Mullins, Unravelling Small-Polaron Transport in Metal Oxide Photoelectrodes, J. Phys. Chem. Lett. 7 (2016) 471-479.

[37] J.L. Bates, C.A. Hinman, T. Kawada, Electrical Conductivity of Uranium Dioxide, J. Am. Ceram. Soc. 50 (1967) 652-656.

[38] P. Nagels, J. Devreese, M. Denayer, Electronic Conduction in Single Crystals of Uranium Dioxide, J. Appl. Phys. 35 (1964) 1175-1180.

[39] J. Tateno, The Dielectric Properties at 9.1 GHz and Nature of Small Polarons in Nonstoichiometric Uranium Oxides, J. Chem. Phys. 81 (1984) 6130-6135.

[40] H. He, P.G. Keech, M.E. Broczkowski, J.J. Noël, D.W. Shoesmith, Characterization of the Influence of Fission Product Doping on the Anodic Reactivity of Uranium Dioxide, Can. J. Chem. 85 (2007) 702-713.

[41] M. Razdan, D.W. Shoesmith, Influence of Trivalent-Dopants on the Structural and Electrochemical Properties of Uranium Dioxide (UO_2), J. Electrochem. Soc. 161 (2014) H105-H113.

[42] I. Grenthe, J. Fuger, R.J. Konings, R.J. Lemire, A.B. Muller, C. Nguyen-Trung, H. Wanner, Chemical Thermodynamics of Uranium, North Holland, Amsterdam, 1992.

[43] D. Gorman-Lewis, P.C. Burns, J.B. Fein, Review of Uranyl Mineral Solubility Measurements, J. Chem. Thermodyn. 40 (2008) 335-352.

[44] J. Paquette, R.J. Lemire, A Description of the Chemistry of Aqueous Solutions of Uranium and Plutonium to 200ºC Using Potential pH Diagrams, Nucl. Sci. Eng. 79 (1981) 26-48.

[45] G.A. Mabboil, An Introduction to Cyclic Voltammetry, J. Chem. Educ. 60 (1983) 697-702.

[46] B.G. Santos, J.J. Noël, D.W. Shoesmith, The Effect of pH on the Anodic Dissolution of SIMFUEL (UO_2), J. Electroanal. Chem. 586 (2006) 1-11.

[47] D.W. Shoesmith, Used Fuel and Uranium Dioxide Dissolution Studies – A Review, report NWMO TR-2007-03, Nuclear Waste Management Organization, Toronto, ON, 2007.

[48] D.W. Shoesmith, M. Kolar, F. King, A Mixed-Potential Model to Predict Fuel (Uranium Dioxide) Corrosion within a Failed Nuclear Waste Container, CORROSION 59 (2003) 802-815.

[49] B.G. Santos, H.W. Nesbitt, J.J. Noël, D.W. Shoesmith, X-ray Photoelectron Spectroscopy Study of Anodically Oxidized SIMFUEL Surfaces, Electrochim. Acta 49 (2004) 1863-1873.

[50] J. McMurry, D.A. Dixon, J.D. Garroni, B.M. Ikeda, S. Stroes-Gascoyne, P. Baumgartner, T.W. Melnyk, Evolution of a Canadian Deep Geologic Repository: Base Scenario, Report 06819-REP-01200-10092-R00, Ontario Power Generation, Toronto, ON, 2003.

[51] A. Pshenichnikov, J. Stuckert, M. Walter, Microstructure and Mechanical Properties of Zircaloy-4 Cladding Hydrogenated at Temperatures Typical for Loss-of-coolant Accident (LOCA) Conditions, Nucl. Eng. Des. 283 (2015) 33-39.

[52] M. Garamszeghy, Nuclear Fuel Waste Projections in Canada-2015 Update, Report NWMO-TR-2015-19, Nuclear Waste Management Organization, Toronto, Canada, 2015.

[53] D.W. Shoesmith, The Chemistry/Electrochemistry of Spent Nuclear Fuel as a Wasteform, in "Uranium: Cradle to Grave", edited by P. Burns, and G. Sigmon, Mineralogical Society of Canada, Short Course Series Vol 43, 337-368 (2013).

[54] J. Bruno, R.C. Ewing, Spent Nuclear Fuel, ELEMENTS 2 (2006) 343-349.

[55] H. He, M. Broczkowski, K. O'Neil, D. Ofori, O. Semenikhin, D.W. Shoesmith, Corrosion of Nuclear Fuel (UO_2) Inside a Failed Nuclear Waste Container, Report NWMO TR-2012-09, Nuclear Waste Management Organization, Toronto, ON, 2012.

[56] L. Wu, Z. Qin, D.W. Shoesmith, An Improved Model for the Corrosion of Used Nuclear Fuel Inside a Failed Waste Container under Permanent Disposal Conditions, Corros. Sci. 84 (2014) 85-95.

[57] K. Ollila, E. Myllykylä, M. Tanhua-Tyrkkö, T. Lavonen, Dissolution Rate of Alpha-doped UO_2 in Natural Groundwater, J. Nucl. Mater. 442 (2013) 320-325.

[58] S. Stroes-Gascoyne, F. Garisto, J.S. Betteridge, The Effects of Alpha-radiolysis on UO_2 Dissolution Determined from Batch Experiments with ^{238}Pu-doped UO_2, J. Nucl. Mater. 346 (2005) 5-15.

[59] T. Mennecart, C. Cachoir, K. Lemmens, Influence of the Alpha Radiation on the UO_2 Dissolution in High pH Cementitious Waters, J. Radioanal. Nucl. Chem. 304 (2014) 61-66.

[60] T. Mennecart, B. Grambow, M. Fattahi, Z. Andriambololona, Effect of Alpha Radiolysis on Doped UO_2 Dissolution under Reducing Conditions, Radiochim. Acta 92 (2004) 611-615.

[61] V.V. Rondinella, H. Matzke, J. Cobos, T. Wiss, Leaching Behaviour of UO_2 Containing α-emitting actinides, Radiochim. Acta 88 (2000) 527-531.

[62] J. Cobos, L. Havela, V.V. Rondinella, J. De Pablo, T. Gouder, J. P. Glatz, P. Carbol, H. Matzke, Corrosion and Dissolution Studies of UO_2 Containing α-emitters, Radiochim. Acta 90 (2002) 597-602.

[63] C. Poinssot, C. Ferry, M. Kelm, B. Grambow, A. Martinez Esparza Valiente, L.H. Johnson, Z. Andriambololona, J. Bruno, C. Cachoir, J.-M. Cavedon, H. Christensen, C. Corbel, C. Jegou, K. Lemmens, A. Loida, P. Lovera, F. Miserque, J. de Pablo, A.

Poulesquen, J. Quinones, V. Rondinella, K. Spahiu, D.H. Wegen, Final Report of the European Project Spent Fuel Stability under Repository Conditions, Report CEA-R-6093, CEA, 2005.

[64] J.C. Wren, D.W. Shoesmith, S. Sunder, Corrosion Behavior of Uranium Dioxide in Alpha Radiolytically Decomposed Water, J. Electrochem. Soc. 152 (2005) B470.

[65] F. Nielsen, M. Jonsson, Geometrical α- and β-dose Distributions and Production Rates of Radiolysis Products in Water in Contact with Spent Nuclear Fuel, J. Nucl. Mater. 359 (2006) 1-7.

[66] F. Garisto, D.H. Barber, E. Chen, A. Inglot, C.A. Morrison, Alpha, Beta and Gamma Dose Rates in Water in Contact with Used CANDU Fuel, Report NWMO TR-2009-27, Nuclear Waste Management Organization, Toronto, ON, 2009.

[67] J.S. Goldik, J.J. Noël, D.W. Shoesmith, The Electrochemical Reduction of Hydrogen Peroxide on Uranium Dioxide Electrodes in Alkaline Solution, J. Electroanal. Chem. 582 (2005) 241-248.

[68] J.S. Goldik, J.J. Noël, D.W. Shoesmith, Surface Electrochemistry of UO_2 in Dilute Alkaline Hydrogen Peroxide Solutions, Electrochim. Acta 51 (2006) 3278-3286.

[69] R. Pehrman, M. Trummer, C.M. Lousada, M. Jonsson, On the Redox Reactivity of Doped UO_2 Pellets – Influence of Dopants on the H_2O_2 Decomposition Mechanism, J. Nucl. Mater. 430 (2012) 6-11.

[70] M. Trummer, O. Roth, M. Jonsson, H_2 Inhibition of Radiation Induced Dissolution of Spent Nuclear Fuel, J. Nucl. Mater. 383 (2009) 226-230.

[71] P. Carbol, J. Cobos-Sabate, J. Glatz, C. Ronchi, V. Rondinella, D.H. Wegen, T. Wiss, A. Loida, V. Metz, B. Kienzler, K. Spahiu, B. Grambow, J. Quinones, A. Martinez Esparza Valiente, The Effect of Dissolved Hydrogen on the Dissolution of ^{233}U Doped $UO_2(s)$, High Burn-up Spent Fuel and MOX Fuel, Report TR-05-09, Swedish Nuclear Fuel and Waste Management Co (SKB), Stockholm, 2005.

[72] S. Rollin, K. Spahiu, U.-B. Eklund, Determination of Dissolution Rates of Spent Fuel in Carbonate Solutions under Different Redox Conditions with a Flow-through Experiment, J. Nucl. Mater. 297 (2001) 231-243.

[73] D.W. Shoesmith, The Role of Dissolved Hydrogen on the Corrosion/dissolution of Spent Nuclear Fuel, Report NWMO TR-2008-19, Nuclear Waste Management Organization, Toronto, ON, 2008.

[74] M.E. Broczkowski, P.G. Keech, J.J. Noël, D.W. Shoesmith, Corrosion of Uranium Dioxide Containing Simulated Fission Products in Dilute Hydrogen Peroxide and Dissolved Hydrogen, J. Electrochem. Soc. 157 (2010) C275-C281.

[75] M.E. Broczkowski, J.J. Noël, D.W. Shoesmith, The Inhibiting Effects of Hydrogen on the Corrosion of Uranium Dioxide under Nuclear Waste Disposal Conditions, J. Nucl. Mater. 346 (2005) 16-23.

[76] M.E. Broczkowski, J.J. Noël, D.W. Shoesmith, The Influence of Dissolved Hydrogen on the Surface Composition of Doped Uranium Dioxide under Aqueous Corrosion Conditions, J. Electroanal. Chem. 602 (2007) 8-16.

[77] M.E. Broczkowski, D. Zagidulin, D.W. Shoesmith, The Role of Dissolved Hydrogen on the Corrosion/dissolution of Spent Nuclear Fuel, in: "Nuclear Energy and the Environment", American Chemical Society Symposium, 2010, Vol.1046, Chapter 26, pp. 349-380.

[78] M. Trummer, S. Nilsson, M. Jonsson, On the Effects of Fission Product Noble Metal Inclusions on the Kinetics of Radiation Induced Dissolution of Spent Nuclear Fuel, J. Nucl. Mater. 378 (2008) 55-59.

[79] E. Ekeroth, M. Jonsson, T.E. Eriksen, K. Ljungqvist, S. Kovács, I. Puigdomenech, Reduction of UO_2^{2+} by H_2, J. Nucl. Mater. 334 (2004) 35-39.

[80] S. Nilsson, M. Jonsson, On the Catalytic Effect of Pd(s) on the Reduction of $UO_2^{2+}$with H_2 in Aqueous Solution, J. Nucl. Mater. 374 (2008) 290-292.

[81] M.E. Broczkowski, The Effects of Hydrogen and Temperature on the Electrochemistry and Corrosion of Uranium Dioxide, PhD Thesis, Western University, London, ON, 2008.

[82] S. Nilsson, M. Jonsson, On the Catalytic Effects of UO_2(s) and Pd(s) on the Reaction between H_2O_2 and H_2 in Aqueous Solution, J. Nucl. Mater. 372 (2008) 160-163.

[83] F. King, M.J. Quinn, N.H. Miller, The Effect of Hydrogen and Gamma Radiation on the Oxidation of UO_2 in 0.1 M NaCl solution, Report TR-99-27, Swedish Nuclear Fuel and Waste Management Co (SKB), Stockholm, 1999.

[84] F. King, D.W. Shoesmith, Electrochemical Studies of the Effect of H_2 on UO_2 dissolution, Report TR-04-20, Swedish Nuclear Fuel and Waste Management Co (SKB), Stockholm, 2004.

[85] P.G. Lucuta, R.A.Verrall, H. Matzke, B.J. Palmer, Microstructural Features of SIMFUEL - Simulated High Burnup UO_2-based Nuclear Fuel, J. Nucl. Mater. 178 (1991) 48-60.

[86] L. Wu, D.W. Shoesmith, An Electrochemical Study of H_2O_2 Oxidation and Decomposition on Simulated Nuclear Fuel (SIMFUEL), Electrochim. Acta 137 (2014) 83-90.

[87] L. Wu, The Electrochemistry of Hydrogen Peroxide on Uranium Dioxide and the Modelling of Used Nuclear Fuel Corrosion under Permanent Disposal Conditions, PhD Thesis, Western University, London, ON, 2014.

[88] A. Hiroki, J.A. LaVerne, Decomposition of Hydrogen Peroxide at Water-Ceramic Oxide Interfaces, J. Phys. Chem. B 109 (2005) 3364-3370.

[89] C.M. Lousada, A.J. Johansson, T. Brinck, M. Jonsson, Mechanism of H_2O_2 Decomposition on Transition Metal Oxide Surfaces, J. Phys. Chem. C 116 (2012) 9533-9543.

[90] C.M. Lousada, M. Jonsson, Kinetics, Mechanism, and Activation Energy of H_2O_2 Decomposition on the Surface of ZrO_2, J. Phys. Chem. C 114 (2010) 11202-11208.

[91] S. Lin, M.D. Gurol, Catalytic Decomposition of Hydrogen Peroxide on Iron Oxide: Kinetics, Mechanism, and Implications, Environ. Sci. Technol. 32 (1998) 1417-1423.

[92] D. Fu, X. Zhang, P.G. Keech, D.W. Shoesmith, J.C. Wren, An electrochemical study of H_2O_2 decomposition on single-phase γ-FeOOH films, Electrochim. Acta 55 (2010) 3787-3796.

[93] S. Nilsson, M. Jonsson, H_2O_2 and Radiation Induced Dissolution of UO_2 and SIMFUEL pellets, J. Nucl. Mater. 410 (2011) 89-93.

[94] J.A. Navarro, M.A. de la Rosa, M. Roncel, F.F. de la Rosa, Carbon Dioxide-mediated Decomposition of Hydrogen Peroxide in Alkaline Solutions, J. Chem. Soc., Faraday Trans. 1. 80 (1984) 249-253.

[95] F.R. Duke, T.W. Haas, The Homogeneous Base-catalyzed Decomposition of Hydrogen Peroxide, J. Phys. Chem. 65 (1961) 304-306.

[96] O. Spalek, J. Balej, I. Paseka, Kinetics of the Decomposition of Hydrogen Peroxide in Alkaline Solutions, J. Chem. Soc., Faraday Trans. 1. 78 (1982) 2349-2359.

[97] D.E. Richardson, H. Yao, K.M. Frank, D.A. Bennett, Equilibria, Kinetics, and Mechanism in the Bicarbonate Activation of Hydrogen Peroxide: Oxidation of Sulfides by Peroxymonocarbonate, J. Am. Chem. Soc. 122 (2000) 1729-1739.

[98] T. Wu, J.D. Englehardt, A New Method for Removal of Hydrogen Peroxide Interference in the Analysis of Chemical Oxygen Demand, Environ. Sci. Technol. 46 (2012) 2291-2298.

[99] T.E. Eriksen, D.W. Shoesmith, M. Jonsson, Radiation Induced Dissolution of UO_2 Based Nuclear Fuel – A Critical Review of Predictive Modelling Approaches, J. Nucl. Mater. 420 (2012) 409-423.

[100] M. Jonsson, F. Nielsen, O. Roth, E. Ekeroth, S. Nilsson, M.M. Hossain, Radiation Induced Spent Nuclear Fuel Dissolution under Deep Repository Conditions, Environ. Sci. Technol. 41 (2007) 7087-7093.

[101] L. Wu, Y. Beauregard, Z. Qin, S. Rohani, D.W. Shoesmith, A Model for the Influence of Steel Corrosion Products on Nuclear Fuel Corrosion under Permanent Disposal Conditions, Corros. Sci. 61 (2012) 83-91.

[102] L. Wu, N. Liu, Z. Qin, D.W. Shoesmith, Modeling the Radiolytic Corrosion of Fractured Nuclear Fuel under Permanent Disposal Conditions, J. Electrochem. Soc. 161 (2014) E3259-E3266.

Chapter 2

2 Experimental Techniques and Details

In this chapter, the principles and experimental details of the techniques used in this project are briefly reviewed.

2.1 UO_2 Materials Studied in This Project

The UO_2 materials studied in chapters 5 and 7 are: 12.9 wt% Dy_2O_3 doped UO_2 (Dy-UO_2), 6.0 wt% Gd_2O_3 doped UO_2 (Gd-UO_2), 1.5 at% SIMFUEL and hyper-stoichiometric UO_{2+x}. Gd-UO_2 was supplied by Cameco (Port Hope, Canada) and the other materials were supplied by Atomic Energy of Canada Limited (AECL, Chalk River, Canada)*. All these materials were received in pellet form.

The microstructure of Dy-UO_2 and Gd-UO_2 were studied by SEM, EDX and Raman spectroscopy in Reference [1]. Both materials showed a rough and porous surface. The grain boundaries are not obvious because of the polishing (Fig. 2.1). EDX maps show a homogeneous distribution of the doping elements in the UO_2 matrix (Fig. 2.2). No accumulation of Gd (as Gd_2O_3) or Dy (as Dy_2O_3) was observed, and Gd and Dy were both uniformly distributed as dopants.

SIMFUEL is an analogue of CANDU spent nuclear fuel made of natural UO_2 doped with non-radioactive fission products to replicate the chemical effects of in-reactor burnup [2, 3]. Doping elements include up to11 elements, which can be divided into three groups: (1) elements which dissolve in the UO_2 matrix (Sr, Y, Ce, Nd, La, Zr) and significantly increase the conductivity; (2) elements which are stable as oxides but incompatible with the UO_2 matrix (Zr, Mo, Ba) and separate into precipitates, which tend to have the general composition ABO_3 and to adopt a cubic perovskite-type structure; (3) noble metal elements which congregate in alloy precipitates, referred to as ε-particles (Mo, Pd, Rh, Ru).

---

* AECL now is Canadian Nuclear Laboratories.

For the hyper-stoichiometric UO_{2+x} materials, the surface composition is not uniform, the x in UO_{2+x} represents the average degree of the non-stoichiometry. Fig. 2.3 shows the surface morphology of the $UO_{2.1}$ surface in Reference [4]. Grain A (Fig. 2.3) represents a smooth flat grain with an approximate O/U ratio of 2.01; grain B with a very shallow stepped pattern has a slightly hyper-stoichiometric composition of $UO_{2.15}$; grain C with a pronounced stepped pattern of grain ridges oriented horizontally has a stoichiometry of x ~0.22; grain D is a highly non-stoichiometric spiral-like grain with x ~0.31. The degree of non-stoichiometry is determined approximately by EDX analysis.

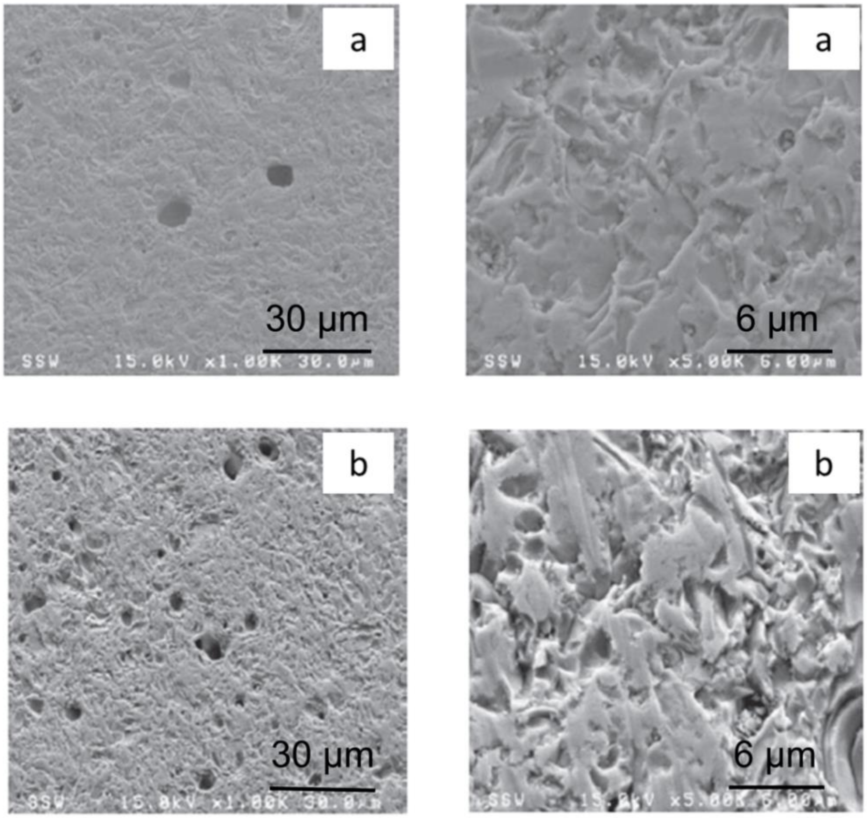

Figure 2.1: SEM micrographs recorded on a polished (a) Gd-doped UO_2 and (b) Dy-doped UO_2 electrode.

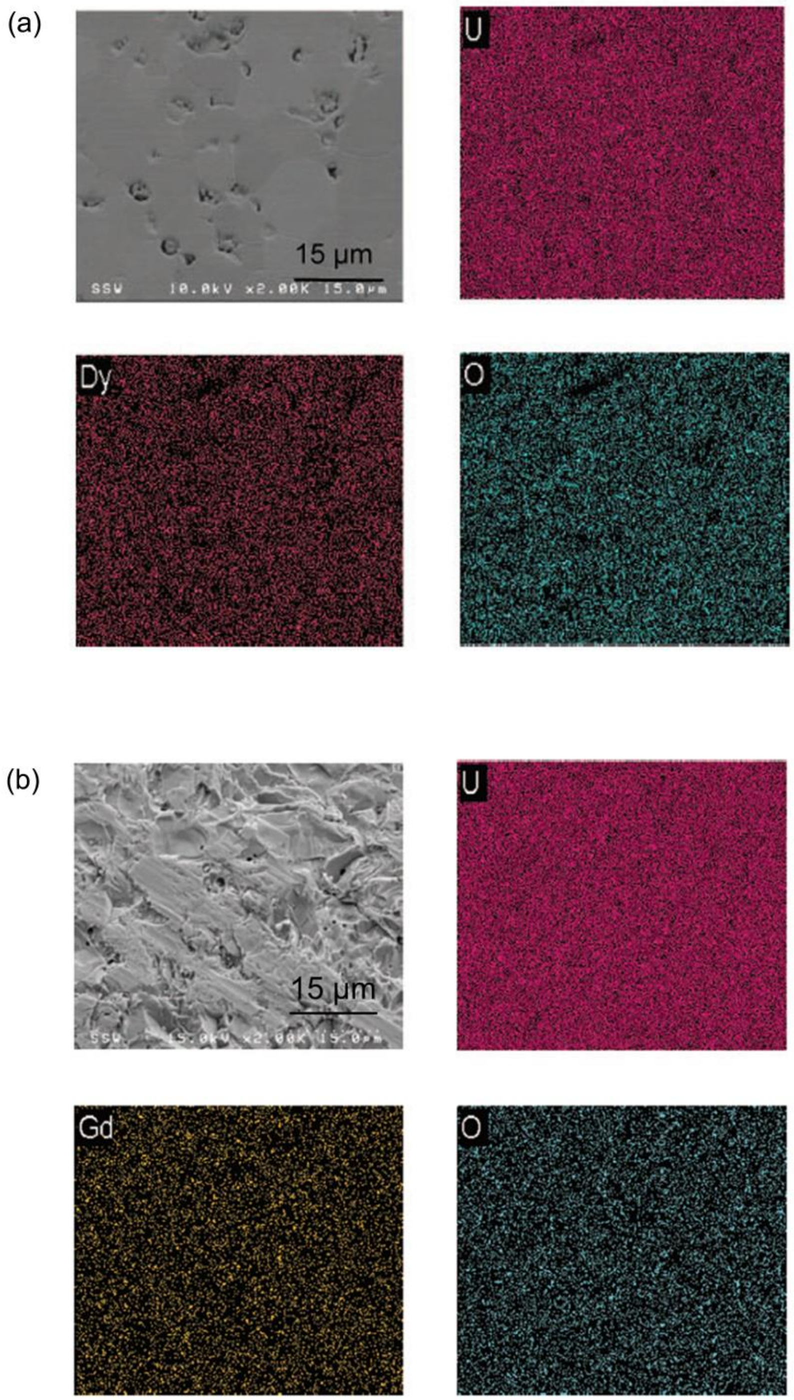

Figure 2.2: EDX maps recorded on Dy-doped UO_2 (a) and Gd-UO_2 (b) (from Reference [1]).

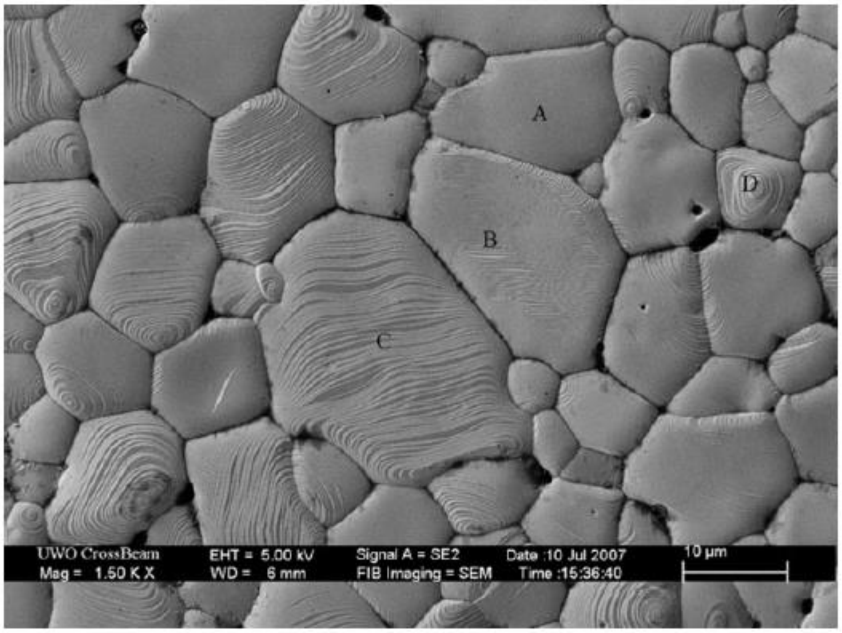

Figure 2.3: Surface morphology of the $UO_{2.1}$ surface determined by SEM [4].

The $(U_{1-y}Gd_y)O_2$ (y = 0.01-0.10) materials studied in chapter 6 were synthesized and characterized at the Korean Atomic Energy Research Institute (Daejeon, South Korea). The surface morphology and microstructure of these materials will be discussed in detail in chapter 6.

2.2 Electrochemical Experimental Design

2.2.1 Electrochemical Cell

All electrochemical measurements were performed in a standard three-electrode cell, as shown schematically in Fig. 2.4. The cell contained one central chamber with two side arms separated from the main chamber by glass frits. A commercial saturated calomel reference electrode (SCE, Fisher Scientific) was placed in one side arm and connected to the central chamber by a Luggin capillary, the tip of which was located near the surface of the working electrode. All potentials (E) in this thesis are quoted on the SCE scale (+0.242 V vs. the standard hydrogen electrode). The counter electrode was a Pt sheet (99.9% pure, Sigma-Aldrich), spot-welded to a Pt wire and placed in the other side arm of the cell. A gas tube with a fritted tip was inserted and used to de-aerate the solution. All experiments were performed under an Ar atmosphere at room temperature (~25°C). The cell was placed in a grounded Faraday cage to minimize external noise. A Solartron model 1287 potentiostat was used to apply potentials and record current responses. Corrware software (Scribner Associates) was used to control the potentiostat and analyze the data.

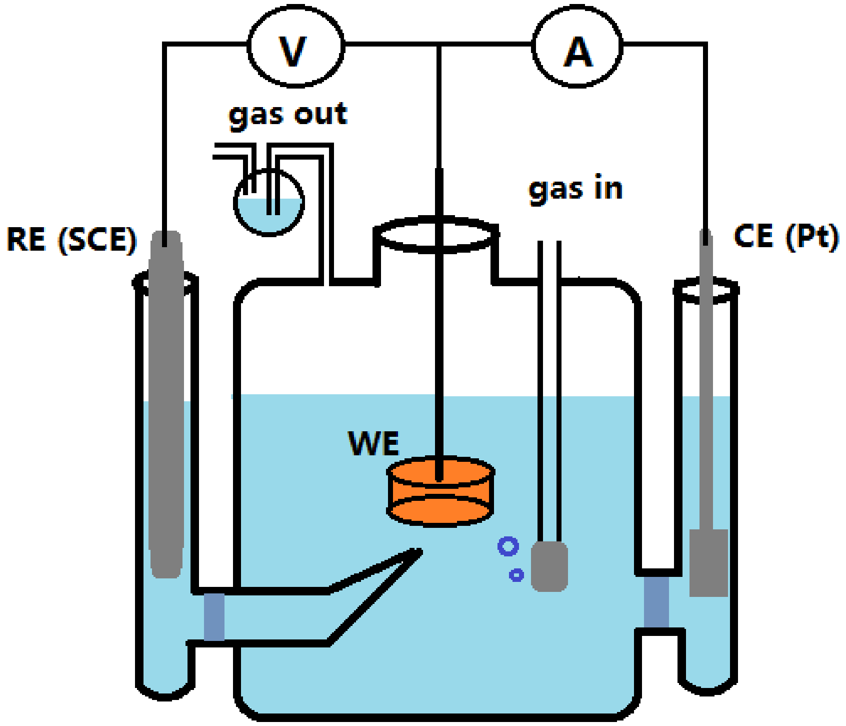

Figure 2.4: Schematic illustration of the three electrode electrochemical cell.

2.2.2 Solutions

All solutions were prepared using deionized water with a resistance of 18.2 (MΩ·cm) purified by a Millipore milli-Q-plus unit. The base electrolyte was 0.1 mol L^{-1} NaCl. Some solutions also contained carbonate and phosphate, the details being given in the relevant chapters. The solution pH was adjusted to the desired value with NaOH (Caledon Chemical). An Orion model 250A+ pH meter and an Orion 91-07 Triode pH/ATC probe were used to monitor pH before the electrochemical measurements. All solutions were deaerated with Ar (ultra-high purity, Praxair) for 60 minutes prior to each experiment, and purging was continued throughout the experiments.

2.2.3 Working Electrode

Disks were cut from the pellets supplied. To prevent cracking of this fragile ceramic material during cutting, the pellet was first mounted in a transparent epoxy (BUEHLER SAMPL-KWICK

No.20-3562 powder and No. 20-3564 liquid, mixed in a ratio of 2:1 by volume). The mounted pellet was then cut into disks, 2-3 mm in thickness, and the epoxy then removed. A thin layer of Cu was electroplated on one side of the disk to facilitate electrical contact to an external measuring device. The Cu-plating procedure is illustrated in Fig. 2.5. The disk was secured in the end of a piece of rubber tubing and placed in a 0.1 mol L^{-1} $CuSO_4$ solution. Mercury was carefully poured into the tubing, and then a conductive wire inserted to connect the mercury to the negative terminal of the DC power supply (GPR-30H10D) making it the cathode in a two electrode cell. A piece of polished Cu metal, attached to the positive terminal of the power supply, acted as the anode. A 10 mA current was applied for 10 minutes to produce a thin, evenly-distributed Cu layer on the UO_2 surface.

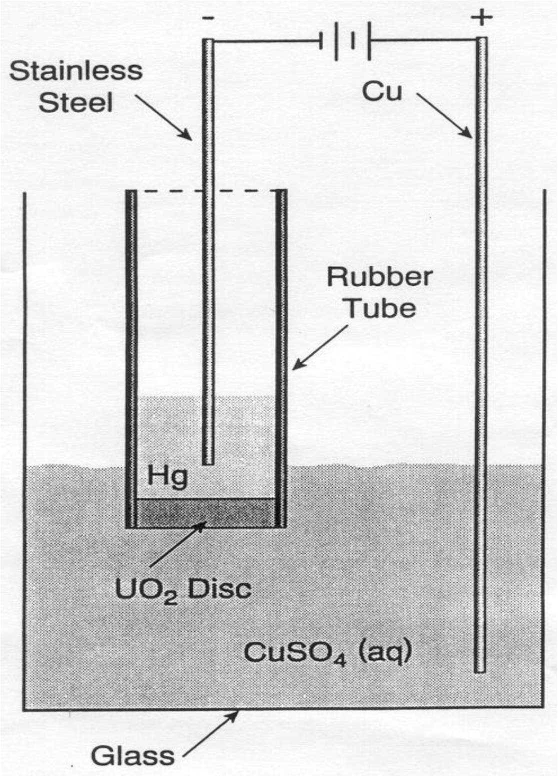

Figure 2.5: Schematic illustration of the experimental arrangement used to electroplate Cu on one side of a UO_2 disk [5].

Fig. 2.6 shows the design of the UO_2 electrode. A round steel disk was glued to the Cu plated side of UO_2 disk with conducting silver epoxy (MG Chemicals 8331), and attached to a steel shaft.

The electrode was then set in a sealing resin (Hysol EE 4183 and HD 3561) so that only one circular face of the electrode would be exposed to solution.

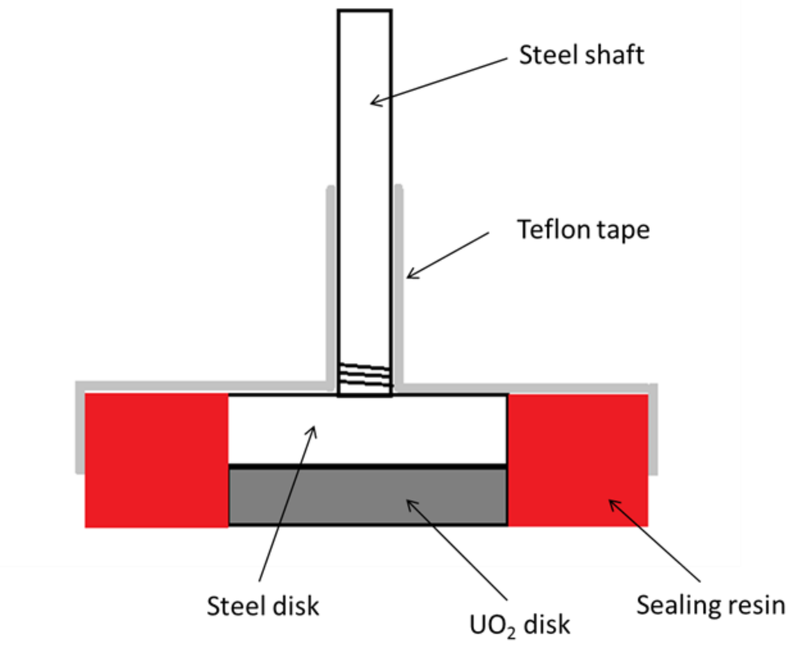

Figure 2.6: Design of the UO_2 electrode [6].

Fig. 2.7 shows the image of the electrode face that would be exposed to solution. Prior to the start of each experiment, the electrode was cleaned by polishing (with 1200 grit SiC paper) and sonication, and then rinsed with deionized water.

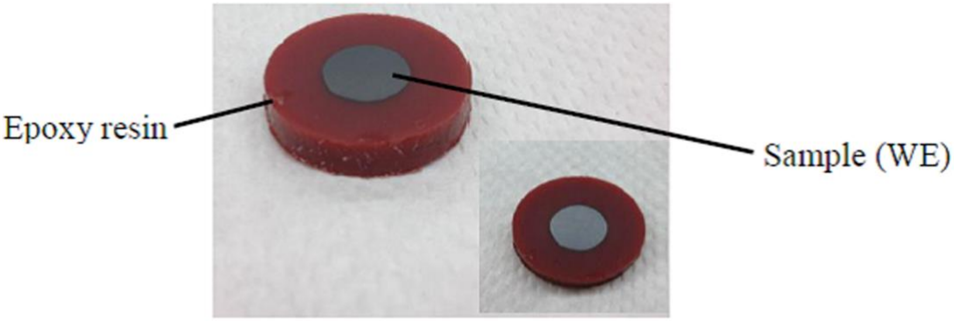

Figure 2.7: Image of a working electrode [7].

2.2.4 Corrosion Potential (E_{CORR}) Measurements

The corrosion of UO_2 in aqueous solution is an electrochemical reaction in which the oxidative dissolution of UO_2 is coupled with the reduction of an available oxidant [8],

$$UO_2 + Ox \rightarrow UO_2^{2+} + Red \tag{2.1}$$

This reaction can be separated into two half-reactions,

$$UO_2 \rightarrow UO_2^{2+} + 2e \qquad (E_e)_{UO_2^{2+}/UO_2} \tag{2.2}$$

$$Ox + ne \rightarrow Red \qquad (E_e)_{Ox/Red} \tag{2.3}$$

where $(E_e)_{UO_2^{2+}/UO_2}$ and $(E_e)_{Ox/Red}$ are the equilibrium potentials for the anodic and cathodic half-reactions ((2.2) and (2.3) respectively), given by the Nernst equation. Since each half-reaction involves an electron transfer, the kinetics can be described by the Butler-Volmer equation [9] as illustrated in Fig. 2.8,

$$i = i_0[\exp\{\frac{\alpha nF}{RT}(E - E_e)\} - \exp\{-\frac{(1-\alpha)nF}{RT}(E - E_e)\}] \tag{2.4}$$

where i_0 is the exchange current density, α is the transfer coefficient, F is Faraday's constant, R is the gas constant, T is the temperature and E is the applied potential. At the equilibrium potential ($E = E_e$), there is no measurable current flow.

In a corrosion process, the anodic and cathodic reactions are coupled together at the corrosion potential (E_{CORR}) which must lie between the equilibrium potentials for the two half-reactions, Fig. 2.8. The overall current is the sum of the currents for the two half reactions and has the form of a modified Butler-Volmer equation (2.5),

$$i = i_{CORR}[\exp\{\frac{\alpha nF}{RT}(E - E_{CORR})\} - \exp\{-\frac{(1-\alpha)nF}{RT}(E - E_{CORR})\}] \tag{2.5}$$

At E_{CORR}, the anodic and cathodic currents are equal and opposite in sign, and the overall measurable current is, therefore, zero.

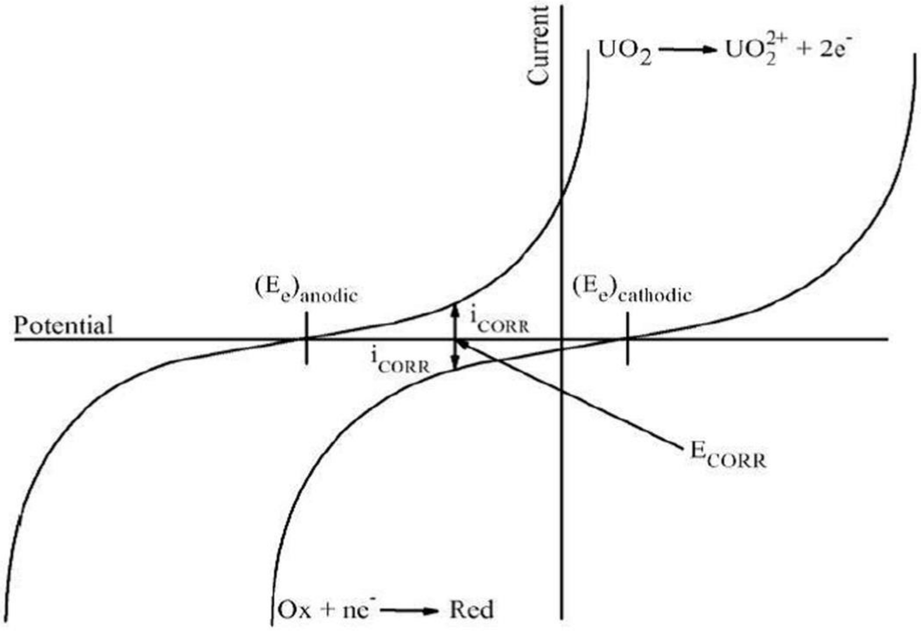

Figure 2.8: Current-potential relationships for the UO_2 dissolution and the oxidant reduction reactions.

Cyclic voltammetry (CV) is a potentiodynamic technique that allows the general electrochemical reactivity of a system to be examined in a fast and simple manner. As shown in Fig. 2.9, in a CV, the potential is scanned at a constant rate (v_s), from a negative limit (E_1) to a positive limit (E_2) (forward scan), and then back to E_1 (reverse scan), and the current (i) recorded and plotted as a function of potential. During CV scans, oxidative processes appear as positive currents, while reduction processes appear as negative currents.

Integration of the areas in a CV yield the charge (Q) consumed by oxidation (Q_A) or reduction (Q_C) reactions that have occurred. The charge (Q) is given by,

$$Q = \int i dt = \int i \frac{dt}{dE} dE = \frac{1}{v_S} \int i dE \qquad (2.6)$$

Figure 2.10 shows a schematic CV and the integrated areas between the potential limits E_i and E_f. Note that Q_A also includes the anodic charge accumulated on the reverse scan. The difference between Q_A and Q_C ($Q_A - Q_C$) can be taken as a measure of the amount of oxidized material lost by dissolution and, hence, unavailable for reduction on the reverse scan.

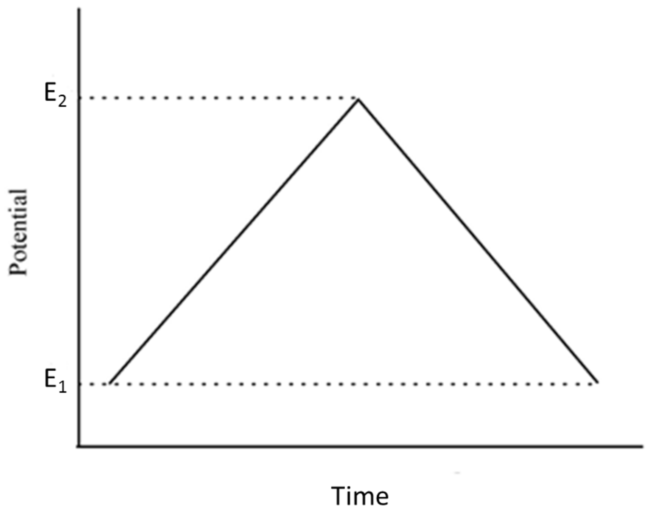

Figure 2.9: Potential-time profile for a CV in which the potential is scanned from $E_1$to E_2, and then back to E_1.

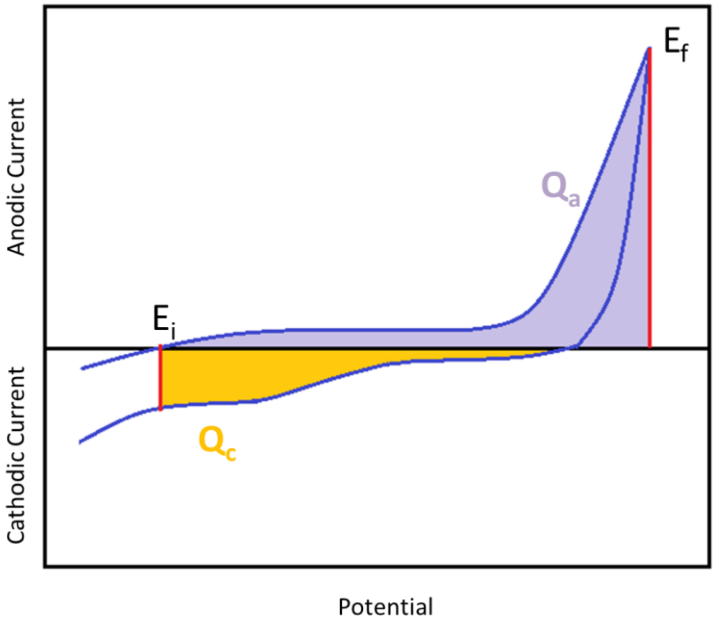

Figure 2.10: A schematic CV showing the integrated areas Q_A and Q_C. The lower limit of integration is the threshold for the onset of water reduction.

In potentiostatic experiments a constant potential (E) was applied to the working electrode for a specific time period, and the measured current plotted verses time. If the measured current is anodic, the surface of the working electrode is being oxidized, and a cathodic stripping voltammogram (CSV) can be used to determine the consequences of a period of oxidation, as shown in Fig. 2.11. By scanning the potential from E back to the negative limit and recording the reduction current as a function of potential, the extent of oxidation can be determined, provided that it leads to reducible surface films or deposits.

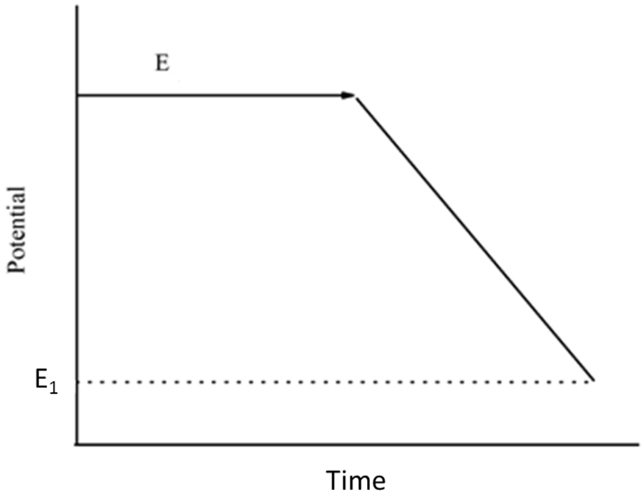

Figure 2.11: Potential-time profile for a potentiostatic oxidation at E followed by a CSV when the potential is scanned from E back to E_1.

2.3 X-ray Photoelectron Spectroscopy (XPS)

2.3.1 Basic Principles of XPS

XPS was employed in this project to quantitatively determine the oxidation states of uranium on the surface of the UO_2 electrodes after electrochemical treatment. XPS is a surface sensitive technique, which can provide atomic and molecular information about the outer 3 to 10 nm of a surface. During the measurement, the sample surface is irradiated with low energy X-rays and photoelectrons are ejected from the core and valence levels of the atoms in the surface (Fig. 2.16).

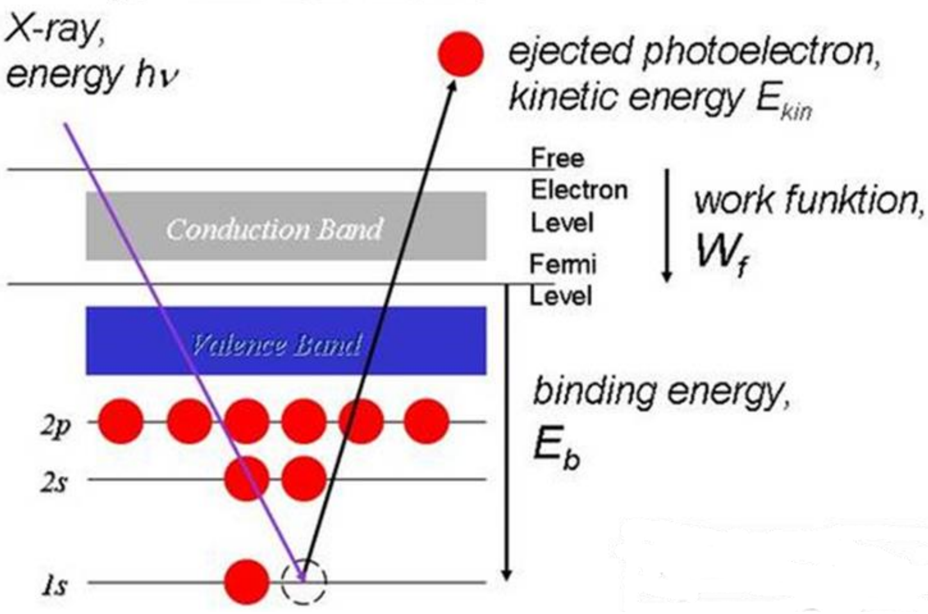

Figure 2.12: Schematic representation of the excitation of a core level electron, and the subsequent generation of a photoelectron.

The kinetic energy of the photoelectron (E_{kin}) is the difference between the energy of the X-ray (hν) and the binding energy of the electron (E_b) plus the work function (W_f, the minimum energy required to extract an electron from a surface into a vacuum),

$$E_{kin} = h\nu - (E_b + W_f) \tag{2.12}$$

Since electrons excited within the sample have a low inelastic mean-free path, only photoelectrons originating at depths between 0.5 to 3 nm can escape from the surface, making XPS a surface sensitive technique.

For an element, there is a characteristic binding energy associated with each core atomic orbital. Thus, each element will give rise to a characteristic set of peaks in the photoelectron spectrum at kinetic energies determined by the photon energy and the respective binding energies. The intensity of the peaks is related to the concentration of that element within the analyzed region. The precise binding energy of an electron depends not only upon the energy level from which photoemission occurs, but also upon the oxidation state of the atom and its chemical environment. These subtle differences in energy levels appear as small shifts on the binding energy scale.

Distinct chemical states can be determined by obtaining high-resolution spectra and using peak fitting programs to deconvolute the spectra yielding the percent composition of each state.

In addition to the main peaks in a photoelectron spectrum, there are a number of satellite peaks. These shake-up peaks are formed when the outgoing electron interacts with a valence electron and excites it to a higher energy level. As a consequence the energy of the core electron is reduced and a satellite structure appears a few eV below the core level position on the KE scale. The position of the satellite structure can be used to confirm the change in oxidation state of the element. Details are given in the following section.

2.3.2 Experimental Details of XPS

Spectra were collected on a Kratos Axis NOVA spectrometer using a monochromatic Al K_α (1486.6 eV) source. The work function of the instrument was calibrated to give a binding energy of 83.96 eV for the Au $4f_{7/2}$ line for metallic gold and the spectrometer dispersion was adjusted to give a binding energy of 932.62 eV for the Cu $2p_{3/2}$ line of metallic Cu. Survey scans were carried out for the energy range 0-1100 eV on an analysis area of 300 × 700 μm^2 with a pass energy of 160 eV. High resolution analyses were carried out on an analysis area of 300 × 700 μm^2 with a pass energy of 20 eV. Spectra were charge-corrected to the main line of the C_{1s} spectrum set to be at 285.0 eV. Spectra were analyzed using CasaXPS software (version 2.3.14).

The U 4f peaks are the strongest and most resolved peaks in the XPS spectrum of U [11], and are commonly used to analyze the oxidation state of U on the surface [12-14]. High-resolution scans were performed for the spectral region including the U $4f_{5/2}$ and U $4f_{7/2}$ peaks and their satellites, and the U 5f valence band region. These peaks were then resolved into contributions from U^{IV}, U^{V}, and U^{VI}, and the fractions of oxidation states on the electrode surface determined from the fitted spectra. The structure of the valence band region was used to check the validity of the fit. All high-resolution spectra were deconvoluted using a Shirley background correction. Gaussian-Lorentzian peak shapes were used: 50% Lorentzian for the main $4f_{7/2}$ and $4f_{5/2}$ peaks and 30% Lorentizian for the satellite peaks.

The fitting procedures were based on published reference spectra [7, 15-17]. The U $4f_{7/2}$ and U $4f_{5/2}$ peaks are located at 380 eV and 391 eV with the spin-orbital interaction separating them by

10.9 eV. While the binding energies for U^{IV}, U^{V}, and U^{VI} in the U $4f_{7/2}$ peak for mixed-valent U-compounds vary with the chemical composition of the compounds examined, the separations between the bands, reported in the literature, are relatively consistent; i.e., 0.5-0.9 eV between U^{IV} and U^{V} and 0.8-1.1 eV between U^{V} and U^{VI}. The satellite peaks associated with the U^{IV}, U^{V}, and U^{VI} components of the U $4f_{7/2}$ and the U $4f_{5/2}$ peaks are also characteristic of the U4f spectrum. The reported distance between the main peak and the satellite peak is relatively consistent, i.e., 6-7 eV for U^{IV}, 8-9 eV for U^{V} and 4 eV and 10 eV for U^{VI}.

2.4 X-ray Diffraction (XRD)

2.4.1 Basic Principles of XRD

XRD is a rapid analytical technique primarily used for the phase identification of crystalline materials and can provide information on unit cell dimensions [18]. For a crystalline solid, when an X-ray interferes with the lattice, the waves are scattered from lattice planes separated by the interplanar distance *d* (Fig. 2.17). When the scattered waves interfere constructively, they remain in phase since the difference between the path lengths of the two waves is equal to an integer multiple of the wavelength. The path difference between two waves undergoing interference is given by $2d\sin\theta$, where θ is the scattering angle. This leads to Bragg's law, which describes the condition for θ for the constructive interference to be at its strongest:

$$n\lambda = 2d\sin\theta \qquad (2.13)$$

where n is a positive integer and λ is the wavelength of the incident wave.

The lattice parameter (a) of a cubic structure can be calculated according to eq. 2.14, where h, k, l are the Miller indices of different planes.

$$d = \frac{\lambda}{2\sin\theta} = \frac{a}{\sqrt{h^2 + k^2 + l^2}} \qquad (2.14)$$

2.4.2 Experimental Details of XRD

XRD analyses were performed using a Bruker AXS D8 Advance X-ray Diffractometer. The wavelength of the incident X-ray was 1.5418Å (CuK_{α}), generated by electron bombardment of Cu.

XRD data were collected in the range 20º to 120º with a 0.02º step size. The lattice parameters of the samples were calculated from a refinement process using TOPAS program (Bruker Analytical X-Ray Systems).

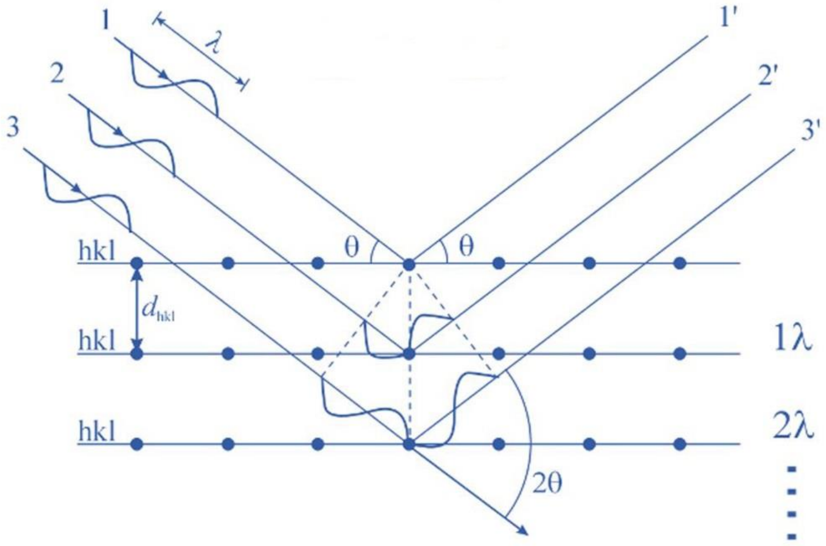

Figure 2.13: Visualization of the Bragg equation. Maximum scattered intensity is only observed when the phase shifts add to a multiple of the incident wavelength λ.

2.5 Raman Spectroscopy

2.5.1 Basic Principles of Raman Spectroscopy

Raman spectroscopy provides information about molecular vibrations that can be used for sample identification [19]. The technique involves shining a monochromatic light source (i.e. laser) on a sample and detecting the scattered light. The majority of the scattered light is of the same frequency as the excitation source, and is termed Rayleigh scattering. A very small amount of the scattered light is shifted in energy from the laser frequency due to interactions between the incident electromagnetic waves and the vibrational energy levels of the molecules in the sample (Fig. 2.18). Plotting the intensity of this “shifted” light versus frequency results in a Raman spectrum of the sample. Generally, Raman spectra are plotted with respect to the laser frequency such that the Rayleigh band lies at 0 cm^{-1}. On this scale, the band positions will lie at frequencies that correspond to the energy levels of different functional group vibrations.

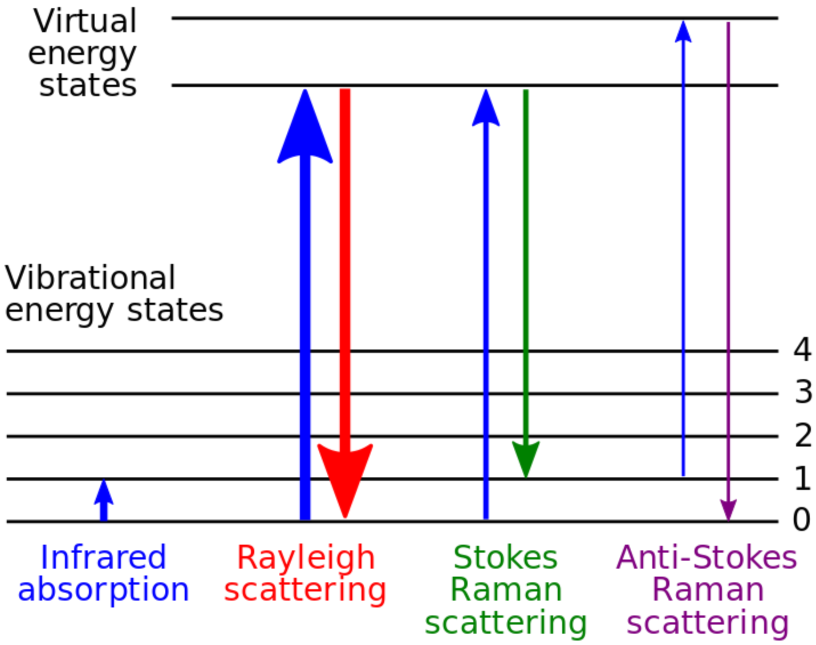

Figure 2.14: Energy level diagram showing the states involved in a Raman signal. The line thickness is roughly proportional to the signal strength from the different transitions.

Raman analyses were performed using an ANDOR Shamrock SR303i spectrometer. The samples were mounted on an Olympus microscope with a 50× lens, and excited using a HeNe laser with a wavelength of 632.8 nm which produces a focused beam of ~2 µm diameter at the sample surface. Each spectrum was measured for an exposure time of ~300 sec over the wavenumber range 400 to 1200 cm^{-1}. Repeated measurements were conducted at different locations on the electrode surfaces to ensure that bands do not show any shifts in vibrational frequencies. The Raman peaks were deconvoluted by Fityk (a curve fitting and peak fitting software).

2.6 References

[1] M. Razdan, D.W. Shoesmith, Influence of Trivalent-Dopants on the Structural and Electrochemical Properties of Uranium Dioxide (UO_2), J. Electrochem. Soc.161 (2014) H105-H113.

[2] P.G. Lucuta, R.A.Verrall, H. Matzke, B.J. Palmer, Microstructural Features of SIMFUEL - Simulated High Burnup UO_2-based Nuclear Fuel, J. Nucl. Mater. 178 (1991) 48-60.

[3] H. He, P.G. Keech, M.E. Broczkowski, J.J. Noël, D.W. Shoesmith, Characterization of the Influence of Fission Product Doping on the Anodic Reactivity of Uranium Dioxide, Can. J. Chem. 85 (2007) 702-713.

[4] H. He, D.W. Shoesmith, Raman Spectroscopic Studies of Defect Structures and Phase Transition in Hyper-stoichiometric UO_{2+x}, Phys. Chem. Chem. Phy. 12 (2010) 8108-8117.

[5] L. Wu, The Electrochemistry of Hydrogen Peroxide on Uranium Dioxide and the Modelling of Used Nuclear Fuel Corrosion under Permanent Disposal Conditions, PhD Thesis, Western University, London, ON, 2014.

[6] F. King, M.J. Quinn, N.H. Miller, The Effect of Hydrogen and Gamma Radiation on the Oxidation of UO_2 in 0.1 M NaCl solution, Report TR-99-27, Swedish Nuclear Fuel and Waste Management Co (SKB), Stockholm, 1999.

[7] M. Razdan, Electrochemical and Surface Compositional Studies on Uranium Dioxide, PhD Thesis, Western University, London, ON, 2013.

[8] D.W. Shoesmith, S. Sunder, W.H. Hocking, Electrochemistry of UO_2 Nuclear Fuel, in "Electrochemistry of Novel Materials", edited by J. Lipkowski, and P.N. Ross, VCH publishers, New York, 1994.

[9] A.J. Bard, L.R Faulkner, Electrochemical Methods: Fundamentals and Applications, 2nd Edition, J. Wiley & Sons, New York, 2001.

[10] P.G. Keech, J.S. Goldik, Z. Qin, D.W. Shoesmith, The Anodic Dissolution of SIMFUEL (UO_2) in Slightly Alkaline Sodium Carbonate/bicarbonate Solutions, Electrochim. Acta 56 (2011) 7923-7930.

[11] Y.A. Teterin, V.M. Kulakov, A.S. Baev, N.B. Nevzorov, I.V. Melnikov, V.A. Streltsov, L.G. Mashirov, D.N. Suglobov, A.G. Zelenkov, A Study of Synthetic and Natural Uranium Oxides by X-ray Photoelectron Spectroscopy, Phys. Chem. Miner. 7 (1981) 151-158.

[12] T.B. Scott, G.C. Allen, P.J. Heard, M.G. Randell, Reduction of U(VI) to U(IV) on the Surface of Magnetite, Geochim. Cosmochim. Acta 69 (2005) 5639-5646.

[13] A. Froideval, M. Del Nero, R. Barillon, J. Hommet, G. Mignot, pH Dependence of Uranyl Retention in a Quartz/solution System: an XPS Study, J. Colloid Interface Sci. 266 (2003) 221-235.

[14] R. Drot, E. Simoni, M. Alnot, J.J. Ehrhardt, Structural Environment of Uranium (VI) and Europium (III) Species Sorbed onto Phosphate Surfaces: XPS and Optical Spectroscopy Studies, J. Colloid Interf. Sci. 205 (1998) 410-416.

[15] M. Schindler, F.C. Hawthorne, M.S. Freund, P.C. Burns, XPS Spectra of Uranyl Minerals and Synthetic Uranyl Compounds. I: The U 4f Spectrum, Geochim. Cosmochim. Acta 73 (2009) 2471-2487.

[16] B.G. Santos, H.W. Nesbitt, J.J. Noël, D.W. Shoesmith, X-ray Photoelectron Spectroscopy Study of Anodically Oxidized SIMFUEL Surfaces, Electrochim. Acta, 49 (2004) 1863-1873.

[17] E.S. Ilton, J.-F. Boily, P.S. Bagus, Beam Induced Reduction of U(VI) during X-ray Photoelectron Spectroscopy: the Utility of the U4f Satellite Structure for Identifying Uranium Oxidation States in Mixed Valence Uranium Oxides, Surf. Sci. 601 (2007) 908-916.

[18] C. Suryanarayana, M.G. Norton, X-Ray Diffraction: A Practical Approach, Plenum press, New York, 1998.

[19] E. Smith, G. Dent, Modern Raman Spectroscopy- A Practical Approach, J. Wiley & Sons, Chichester, England, 2005.

Chapter 3

3 Roles of Radiolytic and Externally Generated H_2 in the Corrosion of Fractured Spent Nuclear Fuel [*]

3.1 Introduction

As discussed in chapter 1, two corrosion fronts will be established in a failed groundwater-containing container, one on the fuel surface and a second one on the surface of the carbon steel liner [1]. On the fuel surface, H_2O_2 (the key radiolysis product) has been shown to be the primary oxidant driving fuel corrosion [2]. Oxidation of fuel (U^{IV}) will produce the oxidized form (U^{VI}) with a considerably higher solubility than U^{IV}, leading to the release of radionuclides [3]. On the steel surface, corrosion can be sustained by reaction with water to produce Fe^{2+} and H_2.

Dissolved H_2 has been shown to suppress fuel corrosion and radionuclide release in a number of investigations on spent PWR (pressurized water reactor) and MOX (mixed oxide) fuels, fuel specimens doped with α-emitters to mimic “aged” fuels, SIMFUELs fabricated to simulate spent fuel properties, and unirradiated UO_2 pellets and powders [4-10]. Because at room temperature, the dissolved molecular H_2 is known to be chemically inert, these experiments confirm that the activation of H_2 by noble metals is a key mechanism in suppressing fuel oxidation [8-11].

Using the database generated by Jonsson et al., Wu et al. [12] developed a 1-dimensional model for fuel corrosion which includes the reactions involving H_2 and a full α-radiolytic reaction set. This model was subsequently expanded to account for the complex geometry of spent fuel, in particular the fracturing of the fuel pellets due to the thermal stress during the in-reactor irradiation and the cooling process on discharge from reactor [13]. This 2-D model showed that both radiolytically-produced H_2 ($(H_2)_{int}$) and H_2 from steel corrosion ($(H_2)_{ext}$) can inhibit fuel corrosion, although $(H_2)_{ext}$ would be expected to be the primary redox scavenger. However, the

---

[*] Chapter 3 has been published: Nazhen Liu, Linda Wu, Zack Qin, David W. Shoesmith, Roles of Radiolytic and Externally Generated H_2 in the Corrosion of Fractured Spent Nuclear Fuel, Environmental Science & Technology, 2016, 50, 12348.

transport of $(H_2)_{ext}$ to the fuel surfaces deep within fractures will be limited making it important to determine the role $(H_2)_{int}$ may play in suppressing fuel corrosion at these locations.

It is also judicious to examine the consequences of the absence of any $(H_2)_{ext}$, a scenario which is unlikely but could arise if the walls of the steel vessel become passivated [14]. Because separating the effects of $(H_2)_{int}$ and $(H_2)_{ext}$ experimentally would be difficult, if not impossible, we have used our model to separate them.

In this chapter, we have modified the published 2-D model to determine the separate effects of $(H_2)_{int}$ and $(H_2)_{ext}$ on the suppression of spent fuel corrosion for different fracture geometries, α-radiation dose rates, and concentration of external H_2. Our primary objective is to determine the relative importance of these two H_2 sources in determining the fuel corrosion rate and, hence, the radionuclide release rate inside a failed waste container.

3.2 Model Description

Under irradiation the fuel undergoes a number of microstructural and compositional changes involving the formation of rare earth (RE^{III}) elements and noble metal (ε) particles, which have been shown to influence its chemical reactivity under anticipated disposal conditions [1]. The RE^{III} elements cause an increase in the electrical conductivity of the fuel matrix [15, 16] and the noble metal particles, generally segregated to grain boundaries, can act as either cathodes or anodes (depending on the prevailing redox conditions in the exposure environment) galvanically-coupled to the conductive RE^{III}-doped UO_2 matrix.

Figure 3.1 illustrates the two corrosion fronts within the container and the main reactions involved in controlling redox conditions and, hence, the process of fuel corrosion. The model includes the following reactions.

(1) The production of H_2O_2 and H_2 by water radiolysis. This approach considers only the radiolytic production of these two molecular species as opposed to a full radiolysis model that would include the radical species as well (e.g., OH•, H•, etc.). Our previous comparison of this simplified model to the full model showed the simplified model overestimates the steady-state $[UO_2^{2+}]$ by ~20% at the bottom of a fracture (width = 0.1 mm, depth =1 mm); i.e., it overestimates the oxidizing effect of H_2O_2 compared to the reducing effect of H_2, making our calculations in this

paper conservative [13].

(2) The oxidative dissolution (corrosion) of UO_2 supported by H_2O_2 reduction on both the UO_2 surface (reaction 2a) [17] and noble metal particles (reaction 2b) [11].

(3) The reduction of oxidized surface species (U^V/U^{VI}) by H_2 oxidation on noble metal particles (reaction 3a) [18] and of dissolved UO_2^{2+} either by reaction with H_2 in solution (reaction 3b) [19] or with H_2 catalyzed on the fuel surface (reaction 3c) [20].

(4) the scavenging of H_2O_2 in homogeneous solution by reaction with Fe^{2+} [21].

(5) The reaction of H_2O_2 with H_2 catalyzed by noble metal particles [22] and (6) the decomposition of H_2O_2 to O_2 and H_2O [17].

The kinetic details of these reactions, and their incorporation into the model have been described in Chapter 1. Dissolution as UO_2^{2+} is assumed to be unimpeded by the formation on the dissolving surface of corrosion product deposits (e.g., $UO_3{\cdot}2H_2O$), which could significantly influence the corrosion rate. This would be the case in groundwater containing sufficient HCO_3^- to completely complex and dissolve the UO_2^{2+} as $UO_2(HCO_3)_a^{2-a}$.

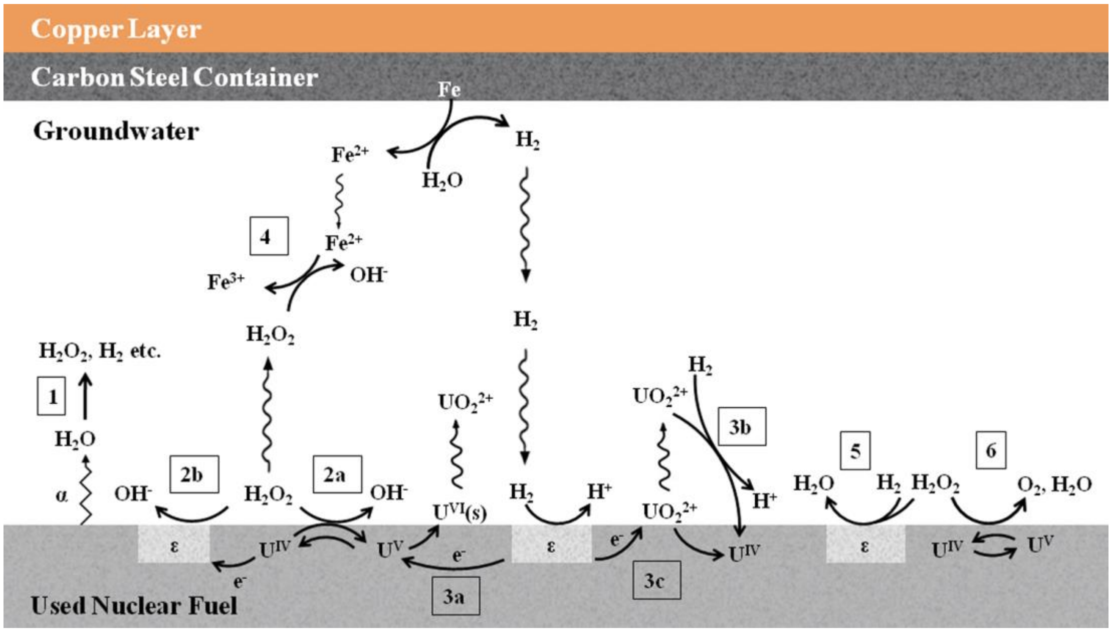

Figure 3.1: Schematic illustration of the reactions included in the model for the α-radiolytic corrosion of spent nuclear fuel [12].

Figure 3.2 shows a cross section of the fuel/solution interface illustrating the simplified geometry adopted to simulate radiolytic corrosion inside a fracture in a fuel pellet. Radiolysis is considered to occur uniformly within a thin layer of solution on the fuel surface with a thickness of 13 μm [23], given by the average penetration distance of α-radiation in water [24]. Beyond this layer no radiolysis products (H_2O_2, H_2 etc.) are produced. The boundary of the uniform radiation zone on the fuel surface is indicated by red dashed lines in Fig. 3.2. This is a simplification because the dose rate will actually non-uniformly distributed, the α-particles losing energy along the penetration path. We have previously calculated the consequences of assuming a uniform energy distribution rather than the actual exponential dose distribution and showed the simplification has only a marginal effect by exaggerating the corrosion rate by ~5% [23].

The diffusion zone (area indicated as light blue in Figure 3.2) is the H_2O layer on the fuel surface over which species can diffuse, and beyond which uniform concentrations are presumed to prevail. The consequences of varying this distance have been shown to be minor [23]. A similar diffusion zone will occur on the corroding steel surface as indicated by the narrow light blue zone at this surface in Figure 3.2. However, this zone is expected to be effectively nonexistent because the anticipated corrosion rate of steel (~0.1 μm/year) will be many orders of magnitude greater than that of the fuel [14]. The [H_2] and [Fe^{2+}] are uniform in the bulk solution (i.e., beyond the diffusion zone) and are assumed to depend on the corrosion behaviour of the steel vessel. The concentrations of all radiolytic species and fuel corrosion products are assumed to be zero in the bulk solution beyond the diffusion zone. The average α-dose rate used in all calculations is 9.03×10^5 Gy a^{-1} (Gy a^{-1}: the absorption of one joule of radiation energy per kilogram of matter per year), corresponding to CANDU fuel with a burnup of 220 MWh/kgU at 1000 years after discharge from reactor [24].

The mathematical model is numerically solved using COMSOL Multiphysics based on the finite element method. The model was simulated using the chemical engineering and the dilute species transportation modules (version 4.3.0.151, COMSOL Inc.). Since the groundwater between the two corrosion fronts is stagnant and contains an excess of inert ions, e.g., Na^+ and Cl^-, the rates of the various processes in the model can be considered governed by a series of diffusion-reaction equations without convection and migration. The rates of the various processes in the model are described by a series of one dimensional diffusion-reaction equations,

$$\frac{\partial c_i(x,t)}{\partial t} = D_i \frac{\partial^2 c_i(x,t)}{\partial x^2} + \sum_k R_k(i) \qquad (3.1)$$

where $c_i\,(x,t)$ is the concentration of species i at point x and time t, D_i is the diffusion coefficient of species i, and $R_k\,(i)$ is the reaction rate of species i in reaction k. At steady state, equation (3.1) reduces to

$$D_i \frac{\partial^2 c_i(x)}{\partial x^2} = -\sum_k R_k(i) \qquad (3.2)$$

suggesting a balance between the diffusion and reaction processes at steady state.

The values of the parameters used in calculations have been listed [13] and discussed in detail elsewhere [12, 13, 23]. Except in the case of the parameters discussed below, these previously listed values are used in all calculations.

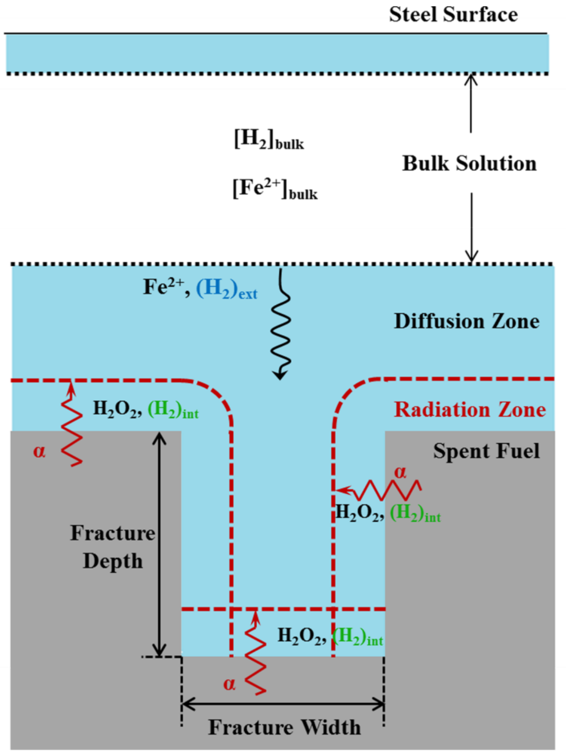

Figure 3.2: Model arrangement showing a cross-section of the fuel-solution interface for the simulation of radiolytic corrosion inside a fracture in a fuel pellet; the area in light blue indicates the diffusion zone.

3.3 The Kinetics of Redox-controlling Reactions

Reaction 3c (Fig. 3.1), the reduction of adsorbed UO_2^{2+} by H_2 catalyzed on the surface of noble metal particles, has been studied by Nilsson et al [20]. Based on experiments using Pd (to simulate noble metal particles) in an aqueous UO_2^{2+} solution with a H_2 atmosphere, it is claimed that the reaction rate is independent of the dissolved $[H_2]$ when varying the H_2 pressure between 1.5 and 40 bar, and can be represented by the rate equation (3.3) in which s_ε is the fractional surface coverage by ε-particles (taken to 0.01), and k_{3c} is the rate constant measured to be 1.5×10^{-5} m s^{-1} [20].

$$R_{3c} = k_{3c}\,[UO_2^{2+}]\,s_\varepsilon \tag{3.3}$$

The lowest $[H_2]$ used in this study was 1.17×10^{-3} mol L^{-1} (the solubility at a pressure of 1.5 bar). However, fuel corrosion kinetics are expected to be influenced by $[H_2]$ at much lower $[H_2]$. It is reasonable to assume that for a bimolecular process, the reaction kinetics would eventually depend on both $[H_2]$ and $[UO_2^{2+}]$. A total of three possible scenarios are plotted in different colors in Figure 3.3 showing how the kinetics of reaction 3c could change as the $[H_2]$ approaches zero: (1, red) the reaction could become first order with respect to H_2 immediately after the $[H_2]$ falls below the minimum concentration (1.17×10^{-3} mol L^{-1}) used in the published measurements; (2, green) the reaction could remain independent of $[H_2]$ to lower concentrations before becoming first order; and (3, blue) the rate could change nonlinearly with $[H_2]$. It is assumed the reaction kinetics become first order with respect to both H_2 and UO_2^{2+}, as indicated in (3.4),

$$R_{3c} = k'_{3c}\,[UO_2^{2+}]\,[H_2]\,s_\varepsilon \tag{3.4}$$

At low $[H_2]$ concentrations, this reaction will be controlled by the kinetics of the cathodic reaction. Because the reaction proceeds via H atoms formed on ε-particle surfaces, the use of this rate equation is equivalent to assuming that the coverage of the particle surfaces by H atoms is directly proportional to the $[H_2]$ in the solution. The rapid dissociation of H_2 required to validate this assumption is expected because the particles have high Ru, Rh, and Pd contents, all metals with high exchange current densities for the $H^+{-}H{-}H_2$ reaction [25].

To use rate equation (3.4) it is necessary to specify a value for the rate constant which has not been measured. In the model presented here, the first scenario (red) is adopted with the slope of the red line yielding a rate constant of $k'_{3c} = 1.3 \times 10^{-5}$ [$m^4\ s^{-1}\ mol^{-1}$]. This scenario is conservative from the perspective of fuel corrosion since the other two scenarios would yield larger rate constants which would lead to faster reduction of UO_2^{2+}.

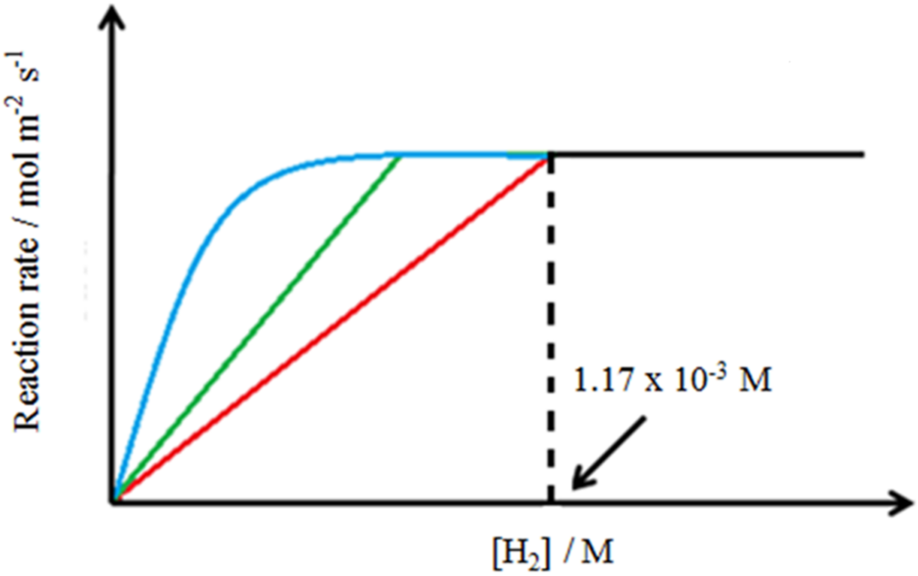

Figure 3.3: Three possible scenarios for the transition in reaction kinetics for reaction 3c when [H_2] approaches zero. The dashed line shows the lower bound of experimental measurements (1.17 × 10^{-3} mol L^{-1}), above which the reaction rate is independent of [H_2].

A similar approach has been adopted in selecting the rate constant for the reduction of H_2O_2 by H_2 catalyzed on noble metal particles (reaction 5 in Fig. 3.1), the rate of which has been shown to be independent of [H_2] over the pressure range 1 to 40 bar [22]. This leads to a modified reaction rate constant, $k'_5 = 2.8 \times 10^{-5}$ [$m^4\ s^{-1}\ mol^{-1}$]. The consequences of these adoptions are addressed in sensitivity calculations (Section 3.4.1.1).

3.4 Results and Discussion

3.4.1 The Critical Hydrogen Concentration ([H_2]$_{crit}$)

3.4.1.1 Influence of the Modified Reaction Rate Constant of Reaction 5 (k'_5) (Fig. 3.1)

The critical [H_2] ([H_2]$_{crit}$) is defined as the minimum [H_2]$_{bulk}$ required to completely suppress fuel corrosion when the [UO_2^{2+}] becomes zero. Consequently, the rate of reaction 3c (Fig. 3.1) is also zero due to the absence of the reagent UO_2^{2+}. Therefore, the incorporation of the modified reaction 3c will not influence $[H_2]_{crit}$. However, a modification of the rate constant of reaction 5 will influence $[H_2]_{crit}$. Figure 3.4 shows the $[H_2]_{crit}$ required to completely suppress fuel corrosion as a function of the adopted rate constant for reaction 5 (k'_5).

These calculations show that the $[H_2]_{crit}$ is almost independent of k'_5 in shallow fractures (i.e., 1 mm in depth) but increases and becomes progressively more dependent as the fracture deepens (3 mm to 9 mm in depth). For example, in a 9 mm deep fracture a decrease in the rate constant by two orders of magnitude (from 2.8×10^{-3} down to 2.8×10^{-5} m^4 s^{-1} mol^{-1}, the latter adopted as the default value in following calculations) results in an increase in $[H_2]_{crit}$ from 3.12 to 5.18 μmol L^{-1}. This can be attributed to the accumulation of H_2O_2 and H_2 within the fracture making the kinetics of reaction 5 more likely to dominate the corrosion behavior of the fuel. However, further decreases in k'_5 to values below the default value exert very little influence on $[H_2]_{crit}$, confirming that its adoption represents a conservative condition.

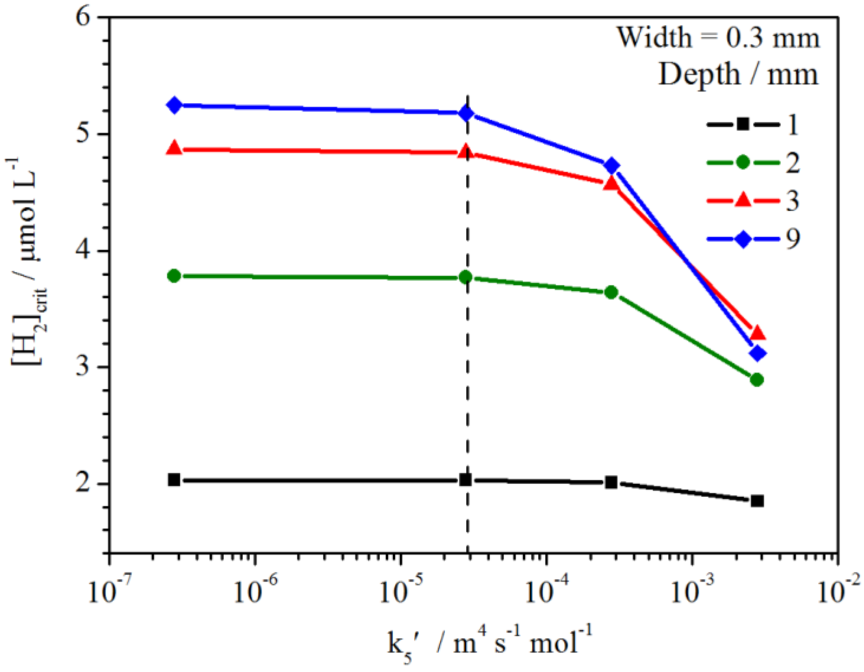

Figure 3.4: The critical $[H_2]$ ($[H_2]_{crit}$) as a function of the rate constant (k'_5) for reaction 5 (Fig. 3.1). Fracture width = 0.3 mm; fracture depth = 1, 2, 3 and 9 mm. All other model parameters are the default values. The vertical dashed line shows the default value for k'_5.

3.4.1.2 Influence of the Decomposition Ratio of H_2O_2 (reaction 6, Fig. 3.1)

A second reaction expected to exert a major influence on fuel corrosion is reaction 6, Fig. 3.1, the decomposition of H_2O_2 to O_2 and H_2O. While O_2 is also a potential fuel oxidant the rate constant for its reaction with UO_2 is ~200 times lower than that of H_2O_2 [2, 3]. Calculations suggest the inclusion of reactions involving O_2 have no significant additional effect on fuel corrosion [12] although this effect remains to be investigated in more detail. While fuel-surface-catalyzed H_2O_2 decomposition has been observed, no detailed kinetic analysis is presently available. Based on electrochemical measurements Wu et al. [26] demonstrated that H_2O_2 decomposition and UO_2 dissolution occur simultaneously and that decomposition could be the primary reaction pathway. These results are consistent with those of Pehrman et al. [17] who showed that surface-catalyzed decomposition accounted for 86% of the consumed H_2O_2 on UO_2 and 99.8% on a SIMFUEL pellet. Since the characteristics of the SIMFUEL were not specified in this study [17] we have adopted the value of 86% as the fraction of H_2O_2 uninvolved in fuel corrosion due to decomposition.

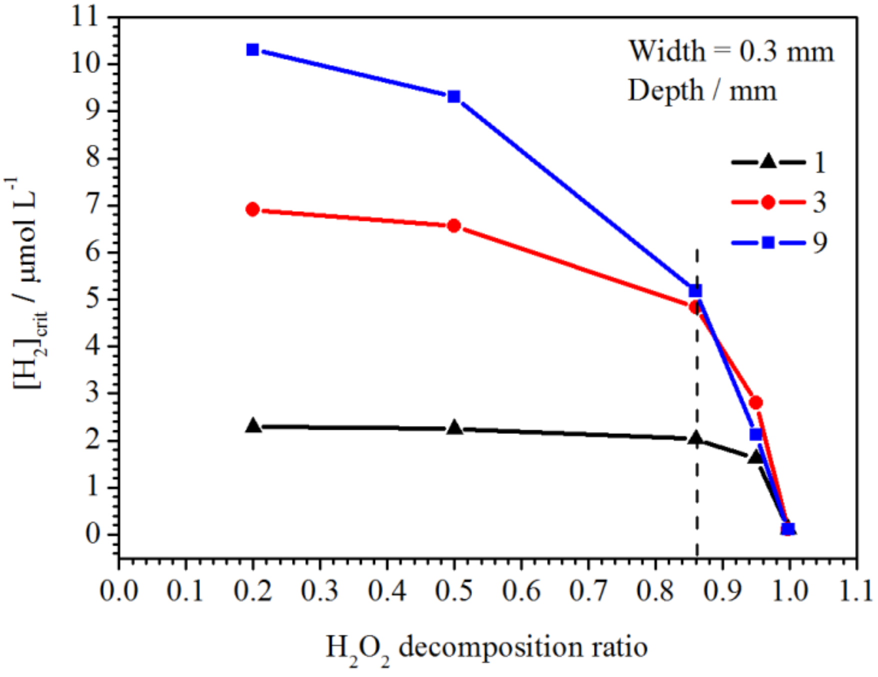

Figure 3.5: The critical $[H_2]$ ($[H_2]_{crit}$) as a function of the H_2O_2 decomposition ratio and the depth of the fracture (fracture width = 0.3 mm). All other model parameters have the default values. The vertical dashed line shows the default value for the ratio.

Figure 3.5 shows this reaction has a significant influence on $[H_2]_{crit}$, especially within a 9 mm deep fracture the demand for H_2 doubling when the decomposition ratio is decreased from the adopted default value to 0.2. This is not unexpected since undecomposed H_2O_2 at deep fracture locations will make the redox conditions considerably more oxidizing thereby increasing the demand for H_2 to suppress corrosion.

3.4.1.3 Influence of Time since Emplacement in the Repository

Since the α-radiation fields associated with the fuel decay as the fuel ages, $[H_2]_{crit}$ has been calculated as a function of decay time for a CANDU fuel bundle with a burnup of 220MWh/kgU, Fig. 3.6. As expected, the $[H_2]_{crit}$ decreases markedly with time since emplacement in the repository. The increase in the H_2 requirement over the first 50 years reflects the accumulation of α-emitters as a consequence of the short-term β/γ decay of radionuclides within the fuel [24]. In Fig. 3.6, there is an obvious increase of $[H_2]_{crit}$ when the depth of the fracture increases from 1 mm to 3 mm, especially in the first 1000 years. Further increase of $[H_2]_{crit}$ for deeper fractures is marginal. The calculation in the following section (3.4.2) demonstrates that this is due to the increasing influence of $[H_2]_{int}$.

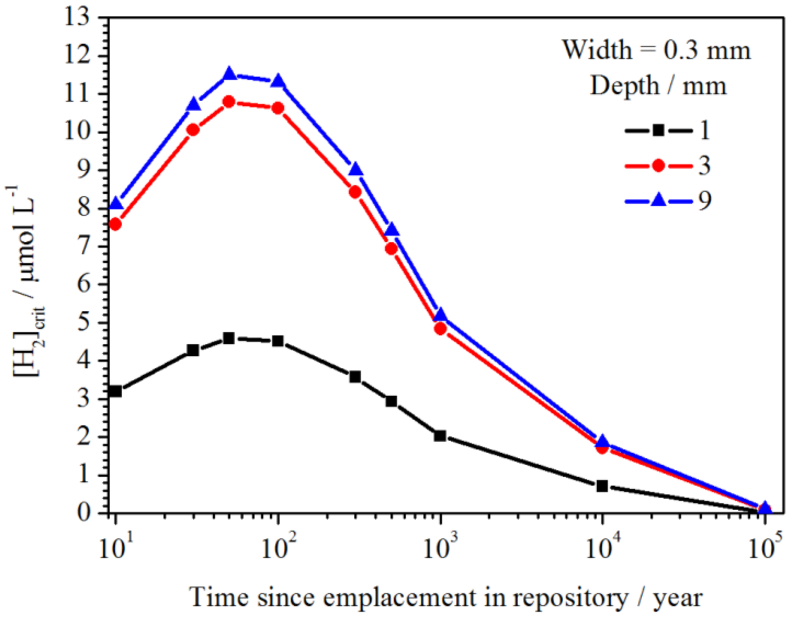

Figure 3.6: The critical $[H_2]$ ($[H_2]_{crit}$) as a function of time since emplacement in a repository. Fracture width = 0.3 mm; fracture depth = 1, 3 and 9 mm. All other model parameters have the default values.

3.4.1.4 Influence of Fracture Geometry

Figure 3.7 shows the $[H_2]_{crit}$ calculated for a range of fracture dimensions using the adopted rate constants and the fractional value for H_2O_2 decomposition. For wide fractures (i.e., with a width > 0.6 mm), $[H_2]_{crit}$ increases as the fracture depth increases. However, for narrow fractures (width < 0.6mm) $[H_2]_{crit}$ first increases then decreases as the fracture deepens, suggesting a significant suppression of fuel corrosion by the local accumulation of radiolytically-produced H_2, $(H_2)_{int}$. This hypothesis is supported by experiments performed on UO_2 in α-irradiated distilled water either open to, or closed from, the open atmosphere [27]. In the experiments, radiolytic H_2 was allowed to escape from the open system but to accumulate in the closed one. In the closed system the dissolved U concentration was suppressed to about one third of that observed in the open system due to the accumulation of radiolytical H_2.

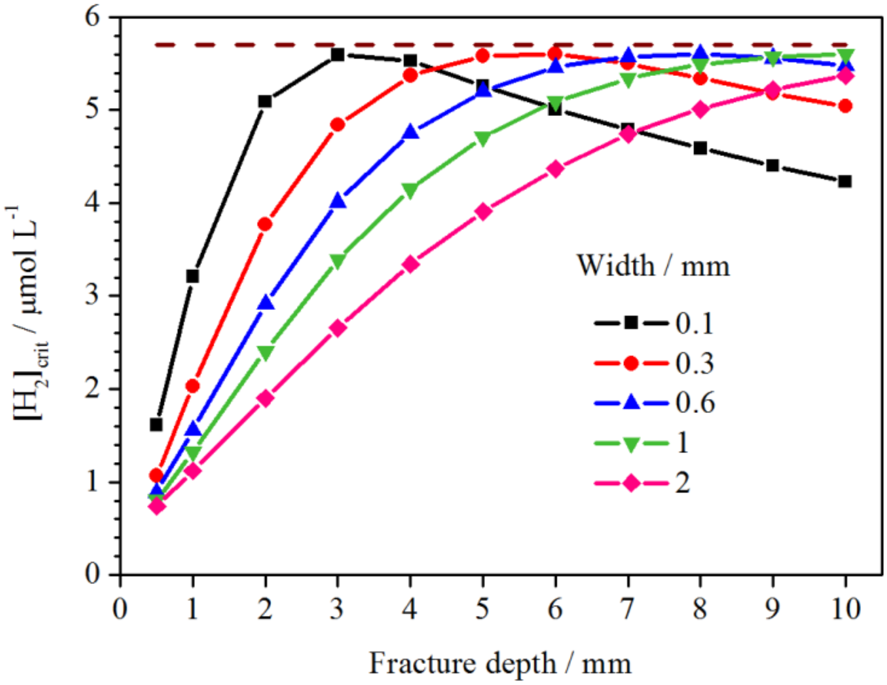

Figure 3.7: The critical $[H_2]$ ($[H_2]_{crit}$) in fractures with different widths and depths for CANDU spent fuel with a burnup of 220MWh/kgU at 1000 years after discharge from reactor. The dashed line indicates an upper limit, 5.7 µmol L^{-1}, for the $[H_2]_{crit}$. All other model parameters have the default values.

Figure 3.7 suggests the existence of an upper limit (5.7 µmol L^{-1}, as indicated by the horizontal dashed line) for the $[H_2]_{crit}$ for the anticipated range of possible fracture geometries. This value is ~17 times the $[H_2]_{crit}$ required on the planar unfractured surface (~0.33 μmol L^{-1}). This upper limiting value suggests that, if the corrosion of the carbon steel canister can produce a $[H_2]_{bulk} >$ 5.7 μmol L^{-1}, the corrosion of CANDU spent fuel with the reference burn-up level of 220 MWh/kgU should be completely suppressed.

3.4.2 The Separation of the Effects of Internal and External H_2 on the Corrosion of a Fracture Wall

The plots in Fig. 3.7 indicate a significant role for $[H_2]_{int}$ in the suppression of corrosion in narrow and deep fracture locations. This offers the prospect that the demand for $(H_2)_{ext}$ will be considerably lower than expected and the limitations on its transport to these deep locations will not prevent the suppression of fuel corrosion. The separation of the influences of $(H_2)_{int}$ and $(H_2)_{ext}$ is experimentally extremely difficult but can be investigated via modelling.

Figure 3.8 shows the individual and combined influences of $(H_2)_{int}$ and $(H_2)_{ext}$ on the corrosion of the walls of a narrow and relatively deep fracture (width = 0.3 mm, depth = 6 mm). As expected the combined influence leads to a lower corrosion rate, Fig. 3.8 A, the flux difference between the black ($(H_2)_{int} + (H_2)_{ext}$) and orange ($(H_2)_{ext}$ only) lines defining the effect of $(H_2)_{int}$ (shown in green in Fig. 3.8 A) on the corrosion rate. Similarly, the difference between the red ($(H_2)_{int}$ only) and black ($(H_2)_{int} + (H_2)_{ext}$) lines defines the influence of $(H_2)_{ext}$ (shown in blue in Fig. 3.8 B).

Because the separate H_2 effects on the corrosion rate should be proportional to their respective concentrations, the ratio of $[H_2]_{int}$ to the $[H_2]_{total}$ (total of $(H_2)_{int} + (H_2)_{ext}$) along the wall of the fracture defines the fractional influence of $(H_2)_{int}$. Similarly, the ratio $[H_2]_{ext}/[H_2]_{total}$ along the wall of the fracture defines the fractional influence of $(H_2)_{ext}$. These fractions are plotted in Fig. 3.8 C. These calculations demonstrate that the effects of $(H_2)_{int}$ and $(H_2)_{ext}$ can be modeled via either the flux difference or the ratio of their respective concentrations at a specific location. In the calculations below, the effects are simulated by comparing the respective concentrations.

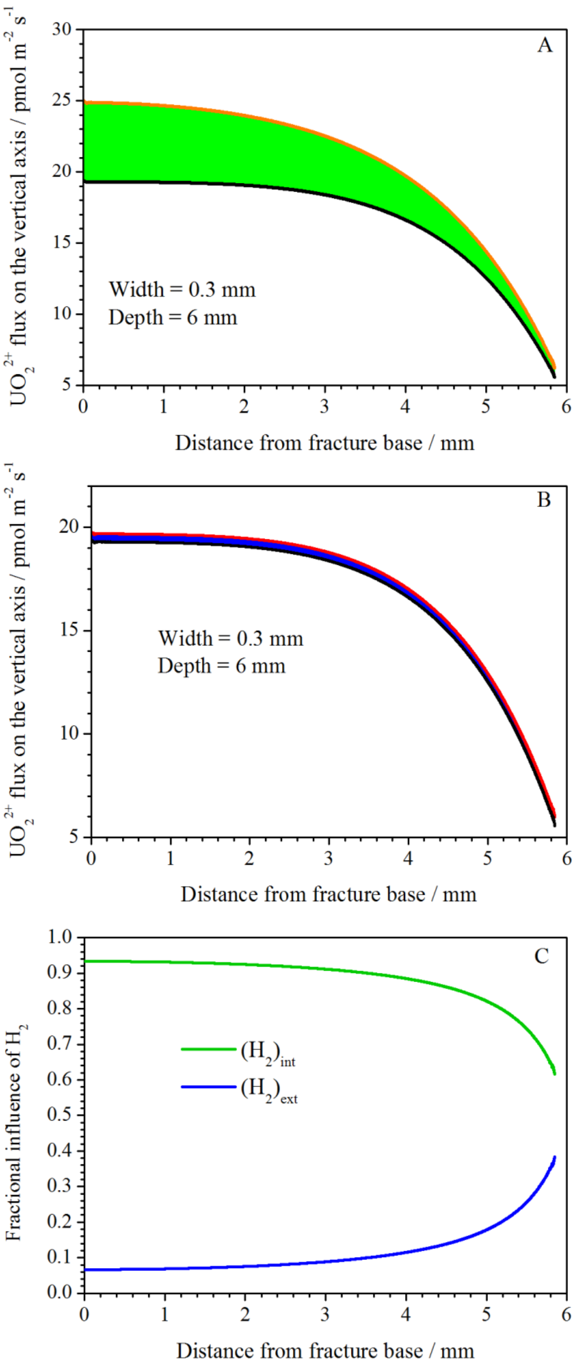

Figure 3.8: (A, B) the calculated flux of UO_2^{2+} in the direction normal to the wall of a narrow and deep fracture as a function of the distance from the base of the fracture; (C) the calculated fractional influence of H_2 from both sources based on a comparison of the respective concentrations. Fracture depth = 6 mm and fracture width = 0.3 mm, the $[H_2]_{bulk}$ = 10^{-7} mol L^{-1}. All other model parameters have their default values.

Fuel corrosion cannot be totally suppressed with only internal H_2 for both planar and fractured spent fuel with the dose rate of 9.03×10^5 Gy a^{-1}. For a planar fuel surface, when the corrosion of carbon steel could sustain $[H_2]_{bulk} \geq 0.33$ μmol L^{-1} (the $[H_2]_{crit}$), with the help of external H_2, the fuel corrosion can be totally suppressed. When we set the $[H_2]_{bulk} = 0.1$ μmol L^{-1}, the internal H_2 takes only 8.7% of the responsibility in suppressing fuel corrosion. For a fractured spent fuel (width = 0.3 mm, depth =6 mm), when the corrosion of carbon steel could sustain $[H_2]_{bulk} \geq 5.60$ μmol L^{-1} (the $[H_2]_{crit}$), the fuel corrosion can be totally suppressed. When we set the $[H_2]_{bulk} = 0.1$ μmol L^{-1}, the internal H_2 takes ~94% of the responsibility in suppressing fuel corrosion at the bottom of the fracture and ~60% at the mouth of the fracture (Fig. 3.8 C). The comparison shows the fractured spent fuel needs a higher $[H_2]_{bulk}$ to totally suppress fuel corrosion, and internal H_2 plays a much more important role of suppressing corrosion for the fractured fuel surface than it does on a planar surface.

3.4.2.1 Influence of Fracture Depth

Figure 3.9 shows the concentration profiles for $(H_2)_{int}$ for fractures with different depths (0.5, 1, 3 and 6 mm) and a constant width (0.6 mm). As the fracture becomes deeper, $(H_2)_{int}$ accumulates at the bottom of the fracture as its loss by diffusion out of the fracture becomes limited.

Figure 3.10 shows the fractions of $(H_2)_{int}$ and $(H_2)_{ext}$ used in suppressing corrosion as a function of the normalized distance from the base of fractures of various depths. In this case, the bulk $[H_2]$ (supplied by steel canister corrosion) is low (10^{-8} mol L^{-1}) and the fuel has a relatively high dose rate (9.03×10^5 Gy a^{-1}) (producing radiolytic H_2). Thus, for the geometries tested, the radiolytic H_2 ($(H_2)_{int}$) is always more important than H_2 from steel corrosion ($(H_2)_{ext}$). As the fracture becomes deeper the influence of $(H_2)_{int}$ in suppressing corrosion of the walls of the fracture becomes dominant increasing from ~70% (0.5 mm depth) to ~98% (6 mm depth).

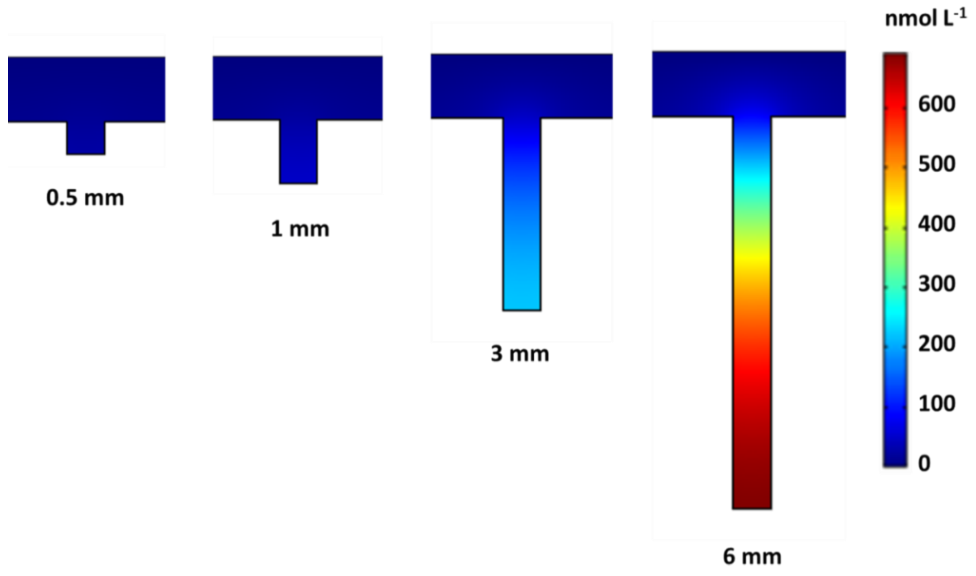

Figure 3.9: Concentration profiles for $(H_2)_{int}$ in fractures with different depths (0.5, 1, 3 and 6 mm) and a constant width (0.6 mm); $[H_2]_{bulk} = 10^{-8}$ mol L^{-1}; all other model parameters have the default values. A schematic description of the fracture is shown in Fig. 3.2.

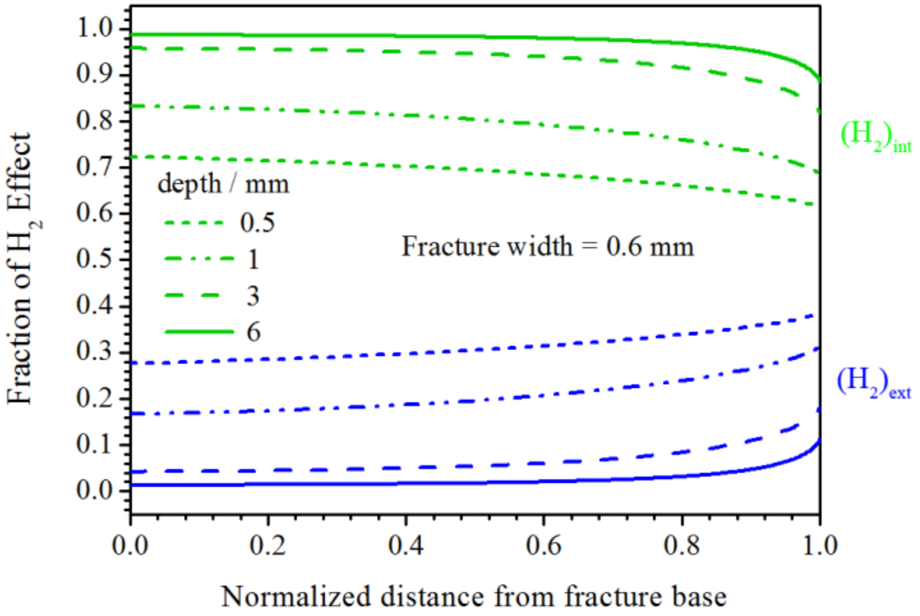

Figure 3.10: The fractional influences of $(H_2)_{int}$ (green) and $(H_2)_{ext}$ (blue) for different fracture depths (0.5, 1, 3, and 6 mm) with a constant fracture width (0.6 mm); $[H_2]_{bulk}$ = 10^{-8} mol L^{-1}; all other model parameters have the default values.

3.4.2.2 Influence of the Fracture Width

Figure 3.11 shows the concentration profiles of $(H_2)_{int}$ for fractures with different widths (0.6, 0.3 and 0.1 mm) and a constant depth (3 mm). As the fracture gets narrower, there is a greater accumulation of the $(H_2)_{int}$ within the fracture, resulting in an increasing fraction of the $(H_2)_{int}$ effect as shown in Fig. 3.12.

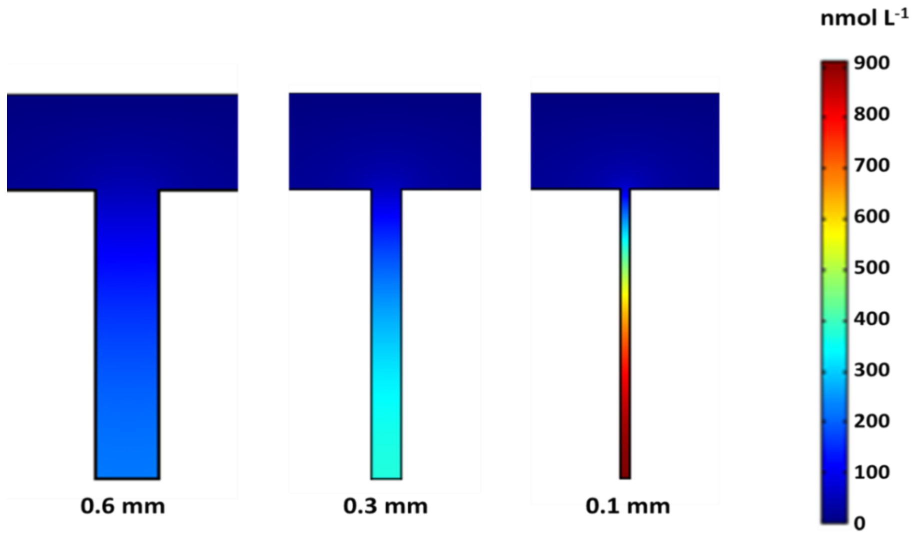

Figure 3.11: Concentration profiles for $(H_2)_{int}$ in fractures with different widths (0.1, 0.3 and 0.6 mm) and a constant depth (3 mm); $[H_2]_{bulk} = 10^{-8}$ mol L^{-1}; all other model parameters have the default values. A schematic description of the fracture is shown in Fig. 3.2.

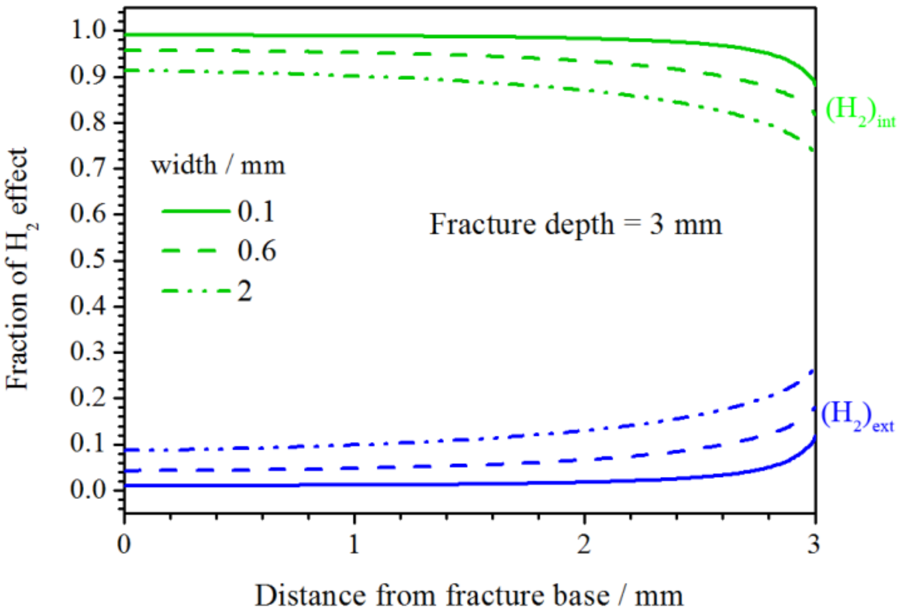

Figure 3.12: The fractional influences of $(H_2)_{int}$ (green) and $(H_2)_{ext}$ (blue) for different fracture widths (0.1, 0.6, and 2 mm) with a constant fracture depth (3 mm); $[H_2]_{bulk} = 10^{-8}$ mol L^{-1}; all other model parameters have the default values.

3.4.3 The Influence of the $[H_2]_{bulk}$ and the α-radiation Dose Rate

By changing the $[H_2]_{bulk}$ and the α-radiation dose rate, the production of $(H_2)_{int}$ and $(H_2)_{ext}$ are changed respectively. Figure 3.13 shows the fractional influence of $(H_2)_{ext}$ at different $[H_2]_{bulk}$. For a shallow fracture in Fig. 3.13 A, as the $[H_2]_{bulk}$ increases from 10^{-8} to 10^{-7} mol L^{-1}, the fractional influence of $(H_2)_{ext}$ increases markedly, from ~20% to ~70%. However, for a deep fracture in Fig. 3.13 B, when the $[H_2]_{bulk}$ increases to the same extent, the fractional influence of $(H_2)_{ext}$ increases only from ~1% to ~12% at the base of the fracture.

The rate of production of $(H_2)_{int}$ will be determined by the α-radiation dose rate which will decay with time. For a shallow fracture (depth = 1 mm, width = 0.6 mm) with $[H_2]_{bulk} = 10^{-8}$ mol L^{-1}, a change in the dose rate from 2.03×10^6 to 1.80×10^4 Gy a^{-1}, the fractional influence of $(H_2)_{int}$ decreases from ~90% to ~10%. Such a decrease in dose rate (for CANDU spent fuel with a burnup of 220 MWh/kgU) represents the change expected for fuel aged 50 years to 10^5 years (after discharge from the reactor).

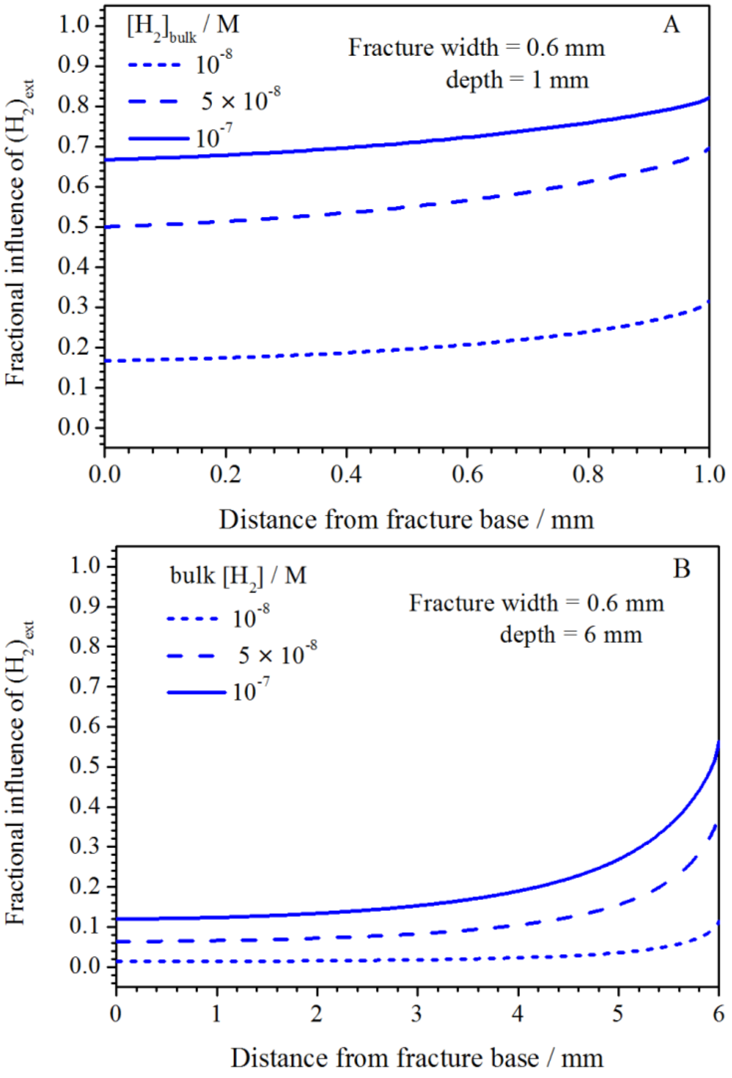

Figure 3.13: The fractional influences of $(H_2)_{ext}$ for different $[H_2]_{bulk}$: A – a shallow fracture (depth = 1 mm, width = 0.6 mm); B – a deep fracture (depth = 6 mm, width = 0.6 mm); all other model parameters have the default values.

3.4.4 The Separation of the Internal and External H_2 Effect at the Base of a Fracture

The most inaccessible location to $(H_2)_{ext}$ is at the base of a fracture, in particular in the corners where the radiation dose rate is the highest with contribution from both base and wall surfaces, Fig. 3.2. This doubling however yields only a minor influence on the corrosion rate of the base, thus, in the following calculations, the corrosion rate at the middle point of the base is taken to represent the corrosion rate on the base of a fracture.

Figure 3.14 shows the UO_2^{2+} flux (corrosion rate) at the base of a narrow (A) and a wide (B) fracture as a function of the depth. The total flux indicates the corrosion rate that would prevail if H_2 had no influence. Since H_2O_2 loss by transport out of a fracture would be more limited in a narrow fracture (Fig. 3.14 A), the corrosion rate is higher for a narrow compared to a wide fracture (Fig. 3.14 B). The decreases in rate due to $(H_2)_{int}$ and $(H_2)_{ext}$ are shown in green and blue, respectively. The influence of $(H_2)_{int}$ is very sensitive to the fracture geometry which becomes more important within a deeper and narrower fracture when the diffusive transport of H_2 out of the fracture becomes limited.

While the fractional effect of $(H_2)_{ext}$ is influenced by geometry (as described in section 3.4.2.1 and 3.4.2.2), its influence in suppressing the corrosion rate at the base of the fracture (indicated in blue in Fig. 3.14) is effectively insensitive to fracture geometry. This can be attributed to the low $[H_2]_{bulk}$ used in this calculation and the relatively high diffusion coefficient for H_2. Figure 3.15 clearly demonstrate that when $[H_2]_{bulk}$ increases, the $(H_2)_{ext}$ has a higher effect (blue) on suppressing the corrosion rate. The influence of $(H_2)_{int}$ remains unchanged (green) since the radiation dose rate and fracture geometry remain the same.

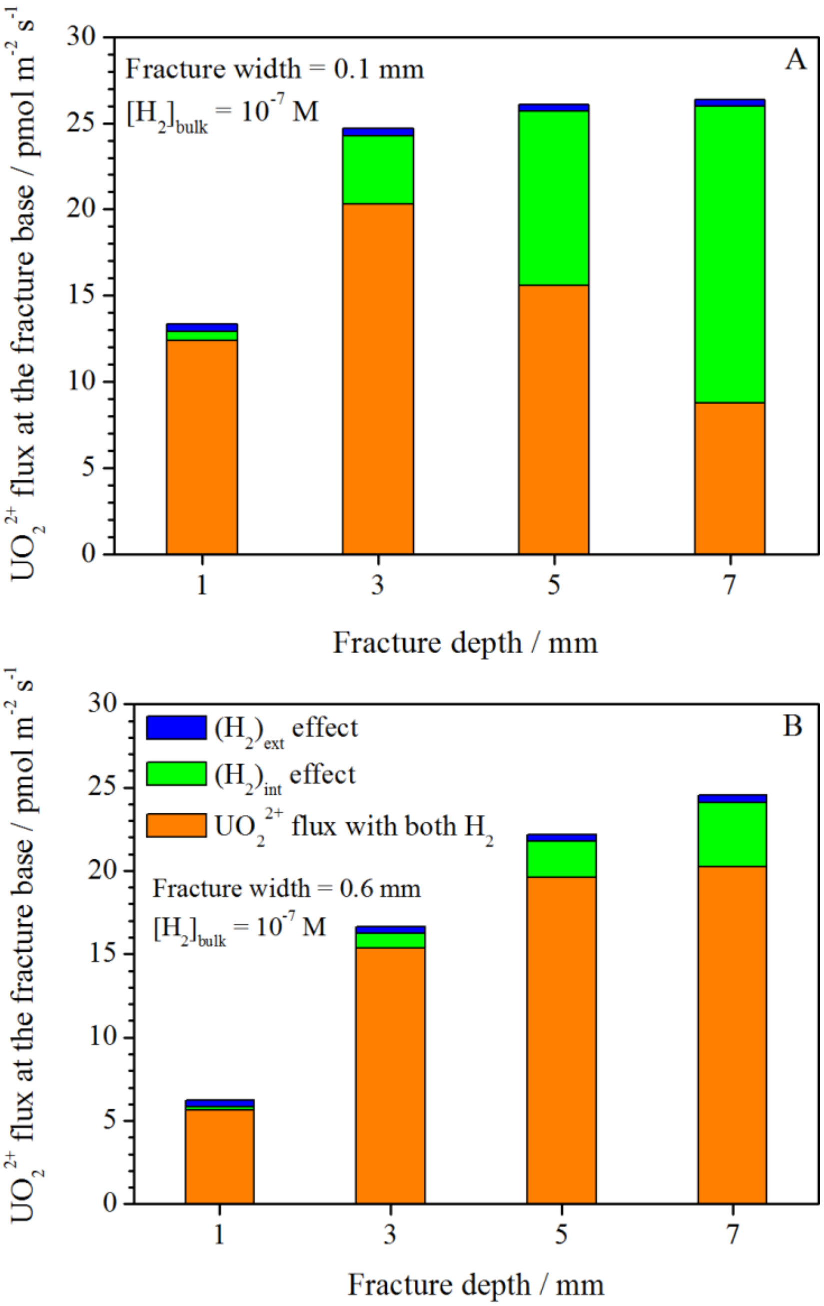

Figure 3.14: The UO_2^{2+} flux (corrosion rate) at the bottom of a fracture as a function of fracture depth for a narrow (A) and wide (B) fracture: orange - the flux with both $(H_2)_{int}$ and $(H_2)_{ext}$: green – the flux suppressed by $(H_2)_{int}$: blue – the flux suppressed by (($H_2)_{ext}$.

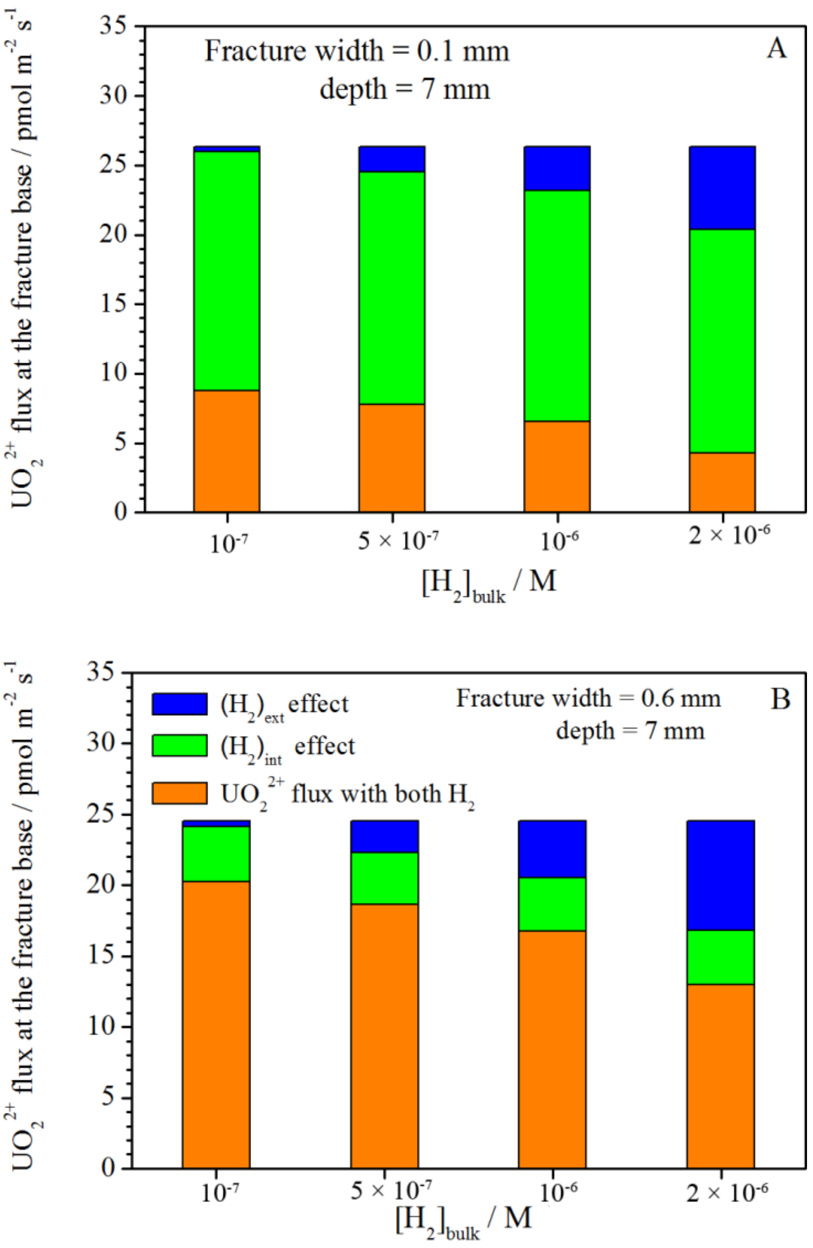

Figure 3.15: The UO_2^{2+} flux (corrosion rate) at the base of a fracture as a function of the $[H_2]_{bulk}$ for a narrow fracture (A) and a wide fracture (B); orange – the flux with both $(H_2)_{int}$ and $(H_2)_{ext}$; green – the flux suppressed by $(H_2)_{int}$; blue – the flux suppressed by $(H_2)_{ext}$.

3.5 Summary and Conclusions

A previously developed 2-D model for the corrosion of spent nuclear fuel inside a failed Cu-coated steel nuclear waste container emplaced in a geologic repository has been adapted to consider the influence of the redox-controlling reactions occurring within fractures in the fuel. The importance of the fractures is that they can act as locations at which H_2O_2, produced by the α-radiolysis of H_2O, can accumulate and be partially isolated from the redox scavengers (H_2, Fe^{2+}) produced by corrosion of the steel vessel, thereby leading to an increase in fuel corrosion rate.

A number of reactions have been shown able to moderate the influence of H_2O_2 leading to a reduction in corrosion rate. These include the surface-catalyzed decomposition of H_2O_2 to H_2O and the much less reactive oxidant, O_2, and a number of reactions involving H_2 (produced either by α-radiolysis or by corrosion of the steel vessel) which can both directly suppress the corrosion of UO_2 and consume H_2O_2 in reactions catalyzed on the noble metal particles present in the fuel matrix.

The catalytic decomposition of H_2O_2 has been shown to be a key reaction in moderating the corrosion of the fuel, although a fully developed kinetic model is not presently available. For the remaining undecomposed H_2O_2, the model suggests that, for CANDU fuel with moderate in-reactor burnup, only micromolar concentrations of dissolved H_2 are required to completely suppress fuel corrosion and that, even within deep fractures in the fuel, the “demand” for H_2 is only approximately 17 times that required on the outer planar surface of the fuel.

By separating the influences on corrosion of radiolytic H_2 ($(H_2)_{int}$) and H_2 from steel corrosion ($(H_2)_{ext}$) the model shows their relative influence is strongly affected by the dimensions of fractures in the fuel and by the amount of H_2 produced by corrosion. If only small amounts of H_2 are produced by steel corrosion then radiolytic H_2 exerts the dominant influence on fuel corrosion since the transport of $(H_2)_{int}$ out of the fracture is limited especially if it is deep and narrow. Even when larger amounts of H_2 are produced by steel corrosion, radiolytic H_2 remains the dominant reductant suppressing fuel corrosion in deep narrow fractures.

A number of mechanistic details and kinetic deficiencies remain unresolved. The kinetics of reactions involving H_2, H_2 and H_2O_2 and the decomposition of H_2O_2 (to O_2 and H_2O) are not known within the concentration ranges important for spent nuclear fuel. While these deficiencies may be covered by conservative assumptions in the calculations presented, they preclude any attempts to validate the model.

3.6 Reference

[1] D.W. Shoesmith, Used Fuel and Uranium Dioxide Dissolution Studies – A Review, report NWMO TR-2007-03, Nuclear Waste Management Organization, Toronto, ON, 2007.

[2] E. Ekeroth, O. Roth, M. Jonsson, TheRelative Impact of Radiolysis Products in Radiation Induced Oxidative Dissolution of UO_2, J. Nucl. Mater. 355 (2006) 38-46.

[3] D.W. Shoesmith, Fuel Corrosion Processes under Waste Disposal Conditions, J. Nucl. Mater. 282 (2000) 1-31.

[4] P. Carbol, J. Cobos-Sabate, J. Glatz, C. Ronchi, V. Rondinella, D.H. Wegen, T. Wiss, A. Loida, V. Metz, B. Kienzler, K. Spahiu, B. Grambow, J. Quinones, A. Martinez Esparza Valiente, The Effect of Dissolved Hydrogen on the Dissolution of ^{233}U Doped UO_2(s), High Burn-up Spent Fuel and MOX Fuel, Report TR-05-09, Swedish Nuclear Fuel and Waste Management Co (SKB), Stockholm, 2005.

[5] S. Rollin, K. Spahiu, U.-B. Eklund, Determination of Dissolution Rates of Spent Fuel in Carbonate Solutions under Different Redox Conditions with a Flow-through Experiment, J. Nucl. Mater. 297 (2001) 231-243.

[6] D.W. Shoesmith, The Role of Dissolved Hydrogen on the Corrosion/dissolution of Spent Nuclear Fuel, Report NWMO TR-2008-19, Nuclear Waste Management Organization, Toronto, ON, 2008.

[7] M.E. Broczkowski, D. Zagidulin, D.W. Shoesmith, The Role of Dissolved Hydrogen on the Corrosion/dissolution of Spent Nuclear Fuel, in: "Nuclear Energy and the Environment", American Chemical Society Symposium, 2010, Vol.1046, Chapter 26, pp. 349-380.

[8] M.E. Broczkowski, P.G. Keech, J.J. Noël, D.W. Shoesmith, Corrosion of Uranium Dioxide Containing Simulated Fission Products in Dilute Hydrogen Peroxide and Dissolved Hydrogen, J. Electrochem. Soc. 157 (2010) C275-C281.

[9] M.E. Broczkowski, J.J. Noël, D.W. Shoesmith, The Inhibiting Effects of Hydrogen on the Corrosion of Uranium Dioxide under Nuclear Waste Disposal Conditions, J. Nucl. Mater. 346 (2005) 16-23.

[10] M.E. Broczkowski, J.J. Noël, D.W. Shoesmith, The Influence of Dissolved Hydrogen on the Surface Composition of Doped Uranium Dioxide under Aqueous Corrosion Conditions, J. Electroanal. Chem. 602 (2007) 8-16.

[11] M. Trummer, O. Roth, M. Jonsson, H_2 Inhibition of Radiation Induced Dissolution of Spent Nuclear Fuel, J. Nucl. Mater. 383 (2009) 226-230.

[12] L. Wu, Z. Qin, D.W. Shoesmith, An Improved Model for the Corrosion of Used Nuclear Fuel Inside a Failed Waste Container under Permanent Disposal Conditions, Corros. Sci. 84 (2014) 85-95.

[13] L. Wu, N. Liu, Z. Qin, D.W. Shoesmith, Modeling the Radiolytic Corrosion of Fractured Nuclear Fuel under Permanent Disposal Conditions, J. Electrochem. Soc. 161 (2014) E3259-E3266.

[14] S.L.W. Hill, N. Liu, Z. Qin , D. Zagidulin, D.W. Shoesmith, Interactions between Carbon Steel and UO_2 Corrosion Fronts inside a Failed Nuclear Waste Container, Proceedings of the 17th International Conference on Environmental Degradation of Materials in Nuclear Power Systems − Water Reactors; Ottawa, Ontario, August 9−13, 2015;Canadian Nuclear Society (CNS): Toronto, 2015.

[15] M. Razdan, D.W. Shoesmith, Influence of Trivalent-Dopants on the Structural and Electrochemical Properties of Uranium Dioxide (UO_2), J. Electrochem. Soc. 161 (2014) H105-H113.

[16] D.W. Shoesmith, S. Sunder, W.H. Hocking, Electrochemistry of UO_2 Nuclear Fuel, in "Electrochemistry of Novel Materials", edited by J. Lipkowski, and P.N. Ross, VCH publishers, New York, 1994.

[17] R. Pehrman, M. Trummer, C.M. Lousada, M. Jonsson, On the Redox Reactivity of Doped UO_2 Pellets – Influence of Dopants on the H_2O_2 Decomposition Mechanism, J. Nucl. Mater. 430 (2012) 6-11.

[18] M. Trummer, S. Nilsson, M. Jonsson, On the Effects of Fission Product Noble Metal Inclusions on the Kinetics of Radiation Induced Dissolution of Spent Nuclear Fuel, J. Nucl. Mater. 378 (2008) 55-59.

[19] E. Ekeroth, M. Jonsson, T.E. Eriksen, K. Ljungqvist, S. Kovács, I. Puigdomenech, Reduction of UO_2^{2+} by H_2, J. Nucl. Mater. 334 (2004) 35-39.

[20] S. Nilsson, M. Jonsson, On the Catalytic Effect of Pd(s) on the Reduction of $UO_2^{2+}$with H_2 in Aqueous Solution, J. Nucl. Mater. 374 (2008) 290-292.

[21] F.J. Millero, S. Sotolongo, The Oxidation of Fe(Ⅱ) with H_2O_2 in Seawater, Geochim. Cosmochim. Acta 53 (1989) 1867-1873.

[22] S. Nilsson, M. Jonsson, On the Catalytic Effects of UO_2(s) and Pd(s) on the Reaction between H_2O_2 and H_2 in Aqueous Solution, J. Nucl. Mater. 372 (2008) 160-163.

[23] L. Wu, Y. Beauregard, Z. Qin, S. Rohani, D.W. Shoesmith, A Model for the Influence of Steel Corrosion Products on Nuclear Fuel Corrosion under Permanent Disposal Conditions, Corros. Sci. 61 (2012) 83-91.

[24] F. Garisto, D.H. Barber, E. Chen, A. Inglot, C.A. Morrison, Alpha, Beta and Gamma Dose Rates in Water in Contact with Used CANDU Fuel, Report NWMO TR-2009-27, Nuclear Waste Management Organization, Toronto, ON, 2009.

[25] J.K. Norskov, T. Bligaard, A. Logadottir, J. R. Kitchin, J. G. Chen, S. Pandelov, U. Stimming, Trends in the Exchange Current for Hydrogen Evolution, J. Electrochem. Soc. 152 (2005) J23-J26.

[26] L. Wu, D.W. Shoesmith, An Electrochemical Study of H_2O_2 Oxidation and Decomposition on Simulated Nuclear Fuel (SIMFUEL), Electrochim. Acta 137 (2014) 83-90.

[27] A. Traboulsi, J. Vandenborre, G. Blain, B. Humbert, J. Barbet, M. Fattahi, Radiolytic Corrosion of Uranium Dioxide: Role of Molecular Species, J. Phys. Chem. C 118 (2014) 1071-1080.

Chapter 4

4 Modelling the Radiolytic Corrosion of α-emitter doped UO_2 and Spent Nuclear Fuel

4.1 Introduction

Since α-radiolysis of water is the dominant oxidant for spent fuel oxidation/dissolution (corrosion) inside a failed waste nuclear container, the influence of the α-dose rate on the corrosion of UO_2 materials has been extensively studied [1-8]. The corrosion rates as a function of α-dose from a wide range of studies have been discussed in detail and summarized [9]. These measurements were conducted on a wide variety of specimens including ^{233}U-doped UO_2, ^{238}Pu-doped UO_2, ^{225}Ac-doped UO_2, UO_2 fuel pellets, SIMFUEL and some spent fuel. Fig. 4.1 shows that, while significant variability exists, a clear trend of increasing corrosion rate with increasing α-source strength was established. It was suggested that a specific activity threshold existed below which the corrosion rate became independent of α-activity. Inspection of Figure 4.1 suggests this threshold, if it exists, would be in the activity source strength range 0.1 to 1 MBq/gUO_2.

Within this compilation three sets of data, marked A, B and C, cannot be considered to fit the linear relationship. For A, corrosion rates were calculated based on impedance measurements which required the compensation of the resistance in low conductivity materials. This leads to large errors and an overestimation of the rates. The value labeled B was measured in a clay environment, known to contain reducing species. The values labeled C were measured on ^{238}Pu-doped specimens and it has been suggested, but not proven, that the low rates indicate a stabilizing influence of Pu on the UO_2 matrix. A fit to this data, indicated by the red line in the figure, yields a relationship between corrosion rate and α-activity,

$$\text{Corrosion Rate [mg (UO}_2\text{) m}^{-2}\text{ d}^{-1}] = 4.35\times 10^{-3}\times \text{ Activity [MBq g}^{-1}\text{ (UO}_2\text{)]}$$

This relationship has been used by the Nuclear Waste Management Organization (Toronto) in performance assessment studies [10].

In this chapter, an attempt is made to use this data to validate the model we have developed for fuel corrosion inside a failed waste container [11-13]. The model is then used to evaluate a number of scenarios which could occur within a failed container. Of particular interest is the influence of O_2 which can be produced by both decomposition of H_2O_2 and water radiolysis. In many of the experiments performed to produce the rates plotted in Figure 4.1 the system was open and/or the solution purged of O_2. However, it is possible that O_2 formed within a container could be, at least partially, retained, yielding a closed system within which O_2 could act as an additional oxidant driving fuel corrosion.

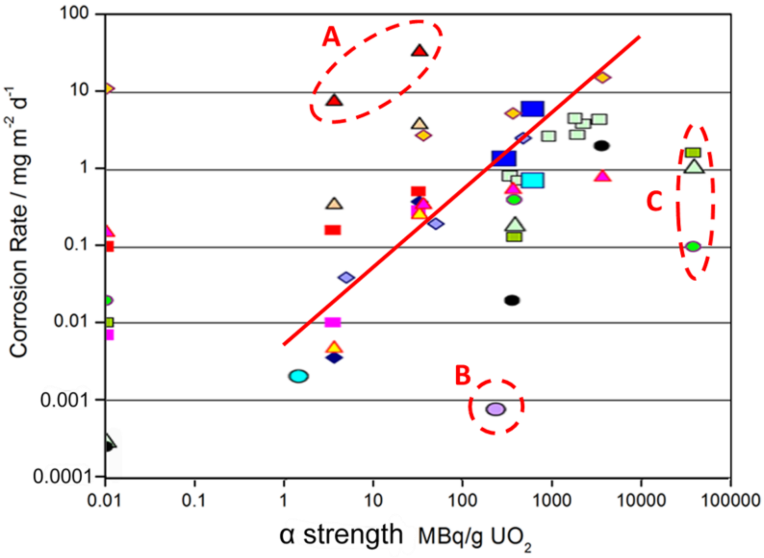

Figure 4.1: Corrosion rates of α-emitter doped UO_2, non-doped UO_2 (0.01 MBq/g), SIMFUEL and some spent fuel [9]. The red line indicates a linear least squares fit to the data from [10]. The values marked A, B and C are discussed in the text.

4.2 Model Calculations

4.2.1 Conversion of α-source Strength to α-dose Rate

In Fig. 4.1 the corrosion rates are plotted as a function of α-source strength. This must be converted to the α-dose rate to the water layer adjacent to the UO_2 surface which is used in the model to calculate the rate of production of radiolytic species. The rate of radiolytic production for species i can be calculated according to equation 4.1,

$$R_i(\text{mol}\,\text{m}^{-3}\text{s}^{-1}) = \text{D}_\text{R} \times \text{g}_i \times \rho_{\text{H}_2\text{O}} \tag{4.1}$$

where D_R is the dose rate representing the rate of energy deposited per unit of mass of water in this case, g_i is the g-value of species *i*, and ρ_{H_2O} is the density of water.

For α-radiation the dose rate near the solid surface and the energy fraction transferred into the solution can be approximately estimated from geometric considerations. Since the range of α-particles in UO_2 is only ~14μm, only a fraction of the α-emissions within this range can reach the adjacent liquid to form radiolytic products [9]. For a 1 MBq / g (UO_2) doped UO_2 material, the energy deposited in the UO_2 layer with a thickness of 14 μm is 1.425×10^{-8} J cm^{-2} s^{-1} (equation 4.2). Depending on the depth within the solid at which the decay occurs it can be calculated that only 18.8% of this energy can be absorbed by the adjacent H_2O [9].

The geometrical distribution of α-dose rate in an H_2O layer has been found to follow an exponential decay with distance from the fuel surface [14, 15]. Wu studied the influence of dose rate distributions on calculated corrosion rates, and justified the use of a simplified uniform distribution of α-dose rate [11]. Using this simplified approach, the mean dose rate to the adjacent water layer (30 μm) can be calculated to be 8.93×10^{-4} Gy s^{-1} for a 1 MBq / g(UO_2) (equation 4.3).

$$1\frac{\mathrm{MBq}}{\mathrm{g(UO_2)}} = 10.97\times10^{6}(\mathrm{Bq\,cm^{-3}})\times5.8\times10^{6}(\mathrm{eV})\times1.6\times10^{-19}(\mathrm{J\,eV^{-1}})\times0.0014(\mathrm{cm})$$
$$=1.425\times10^{-8}(\mathrm{J\,cm^{-2}s^{-1}}) \qquad (4.2)$$

$$18.8\%\times1.425\times10^{-8}(\mathrm{J\,cm^{-2}s^{-1}})\Big/10^{-3}(\mathrm{Kg\,cm^{-3}})\times0.003\,(\mathrm{cm})$$
$$=8.93\times10^{-4}(\mathrm{Gy\,s^{-1}}) \qquad (4.3)$$

4.2.2 Modelling α-emitter doped UO_2 Corrosion (open system) [9]

To simulate the experiments made on α-emitter doped UO_2 specimens we have modified our model to include only the reactions shown in Fig. 4.2. A more extensive discussion of the reactions incorporated in the model has been published elsewhere [13].

(1) The production of H_2O_2 and H_2 by water radiolysis in the radiation zone (reaction 1). This approach considers only the radiolytic production of these two molecular species as opposed to a full radiolysis model that would include the radical species as well (e.g., OH•, H•, etc.). Our

previous comparison of this simplified model to the full model showed the simplified model overestimates the steady-state [UO_2^{2+}] by ~20% at the bottom of a fracture (width = 0.1 mm, depth =1 mm); i.e., it slightly overestimates the oxidizing effect of H_2O_2 compared to the reducing effect of H_2. This makes our calculations conservative with respect to the calculated corrosion rates.

(2) The oxidative dissolution (corrosion) of UO_2 supported by H_2O_2 reduction on the UO_2 surface (reaction 2);

(3) The decomposition of H_2O_2 to O_2 and H_2O catalyzed on the UO_2 surface (reaction 3);

(4) The reduction of dissolved UO_2^{2+} by reaction with H_2 in solution (reaction 4);

(5) The oxidative dissolution (corrosion) of UO_2 supported by O_2 reduction on the UO_2 surface (reaction 5). The cathodic reduction of O_2 on UO_2 is ~200 times slower than that of H_2O_2 since the rate of the first electron transfer in the overall four electron reaction ($O_2 + 2H_2O + 4e^- \rightarrow 4OH^-$) is rate-determining. The kinetics of this reaction have been well studied and the results and mechanism discussed elsewhere [16].

The dissolution as UO_2^{2+} is assumed to be unimpeded by the formation on the dissolving surface of corrosion product deposits (e.g., $UO_3{\cdot}2H_2O$), which could significantly influence the corrosion rate. The avoidance of deposits would be expected in groundwater containing sufficient HCO_3^- to completely complex and dissolve the UO_2^{2+} as $UO_2(HCO_3)_a^{2-a}$.

The dissolution experiments plotted in Fig. 4.1 were normally performed in a glove box to simulate the oxygen-free environment of the permanent waste disposal condition [9]. This would constitute an open-system since the gases generated directly or indirectly by α-radiolysis, such as O_2 and H_2, would be removed by the vacuum pump which is part of the purification system of the glove box. Thus, at the boundary of the water layer (shown as a dashed line in Fig. 4.2), the [H_2] and [O_2] were set to be 0, indicating the gaseous species will be evacuated from the system. However, H_2O_2 and UO_2^{2+} will stay in the system, so the flux of these two species ($J_{H_2O_2}$, $J_{UO_2^{2+}}$) were set to be 0. Sensitivity tests show the calculated corrosion rate on the UO_2 surface is not sensitive to the thickness of the water layer, and a value of 1 mm was chosen as the default value.

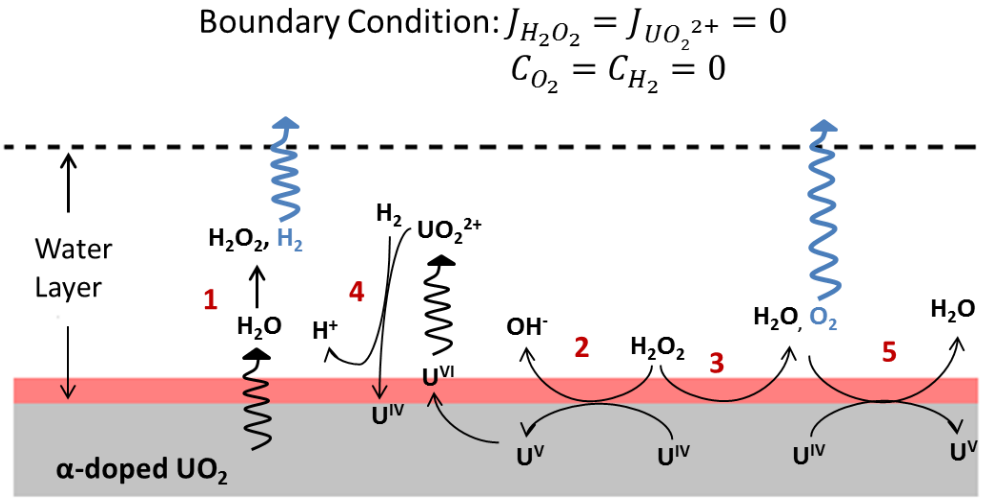

Figure 4.2: Chemical reactions included in the model to simulate the corrosion of α-emitter doped UO_2 [9]. The pink area indicates the radiation zone; i.e., the zone within which radiolytic oxidants are produced.

4.2.3 Modelling α-emitter doped UO_2 Corrosion (closed system)

Under permanent waste disposal conditions which involve multiple barriers to inhibit transport processes it is possible that a groundwater-containing failed container could be, at least partially, resealed by steel corrosion products as illustrated schematically in Fig. 4.3. In addition, although very unlikely [17], the inner surface of the steel container could be passivated which would eliminate the supply of redox scavengers produced by steel corrosion (Fe^{2+} and H_2) that our previous calculations show have a significant influence on the redox conditions within the container [11-13]. This would constitute a closed system in which H_2 (produced by H_2O radiolysis) and O_2 (produced by the decomposition of H_2O_2) would be trapped within the container. To simulate this situation, the flux of all species ($J_{H_2O_2}$, $J_{UO_2^{2+}}$, J_{H_2}, J_{O_2}) was set to 0 on the boundary of the H_2O layer, as illustrated schematically in Fig. 4.4.

This model enables us to evaluate the consequences of O_2 retention in the experiments on α-emitter doped UO_2 [9] and also to address the consequences of the deactivation of the noble metal (ε) particles (by surface contamination or the accumulation of deposits). Many studies have shown that these particles can act as catalysts to control the rate of redox reactions on the surfaces of simulated spent fuels (SIMFUEL) [18-20].

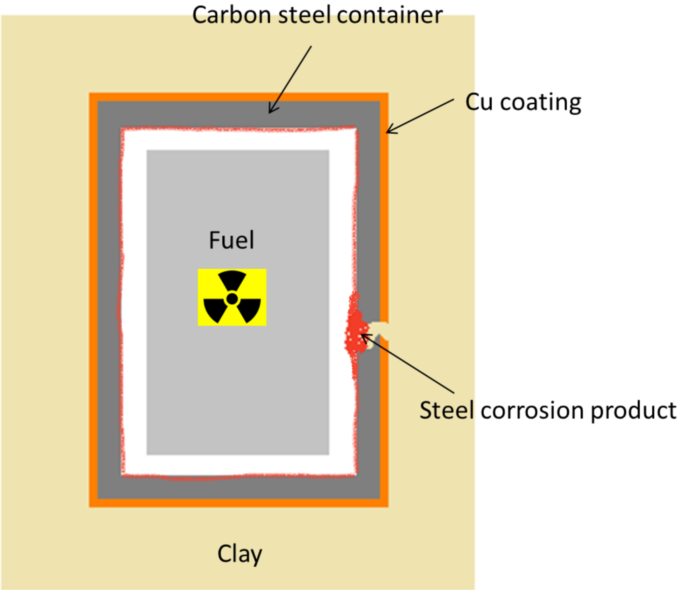

Figure 4.3: Schematic showing the passivated inner surface of the steel container, and the failed part of the waste container sealed by the steel corrosion product.

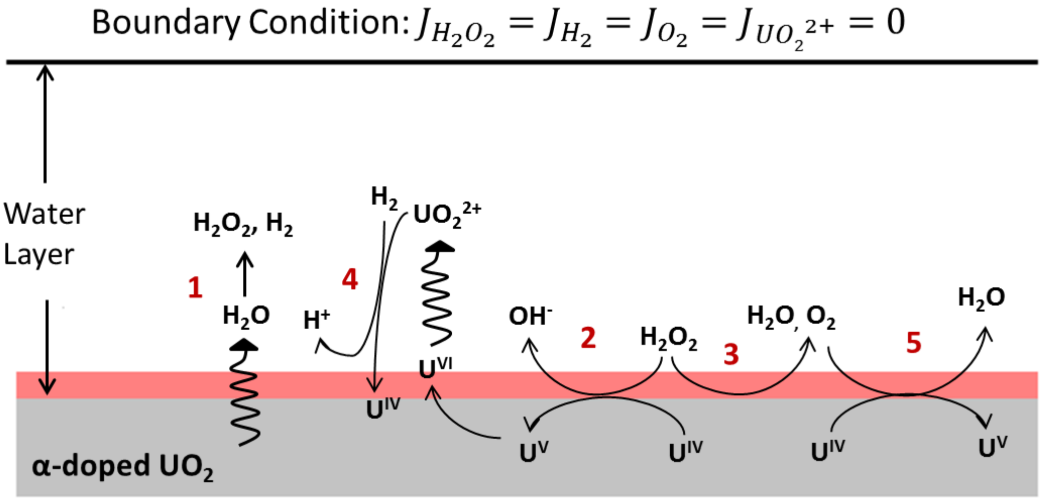

Figure 4.4: Chemical reactions included in the model to simulate the corrosion of α-emitter doped UO_2 in a closed system. The pink area indicates the radiation zone.

4.2.4 Modelling the Corrosion of Spent Nuclear Fuel (closed system)

A less conservative and more realistic approach to evaluating the corrosion of fuel inside a resealed container is to include reactions which can occur on the surface of ε particles [21]. These particles can act as catalysts for reactions involving H_2O_2 (which would accelerate fuel corrosion) and H_2 (which would suppress corrosion) [22]. Figure 4.5 shows the chemical reactions included in the model. The reactions added to those shown in Fig 4.4 to address the effect of the ε particles are: (i) the oxidative dissolution (corrosion) of UO_2 supported by H_2O_2 reduction catalyzed on ε particles (reaction 2' in Fig. 4.5); (ii) the reduction of oxidized surface species (U^V/U^{VI}) by H_2 oxidation on ε particles (reaction 4' in Fig. 4.5); (iii) the reduction of dissolved UO_2^{2+} by reaction with H_2 on ε particles (reaction 4'' in Fig. 4.5); and (iv), the reaction of H_2O_2 with H_2 catalyzed by ε particles leading to the reformation of H_2O (reaction 6 in Fig. 4.5).

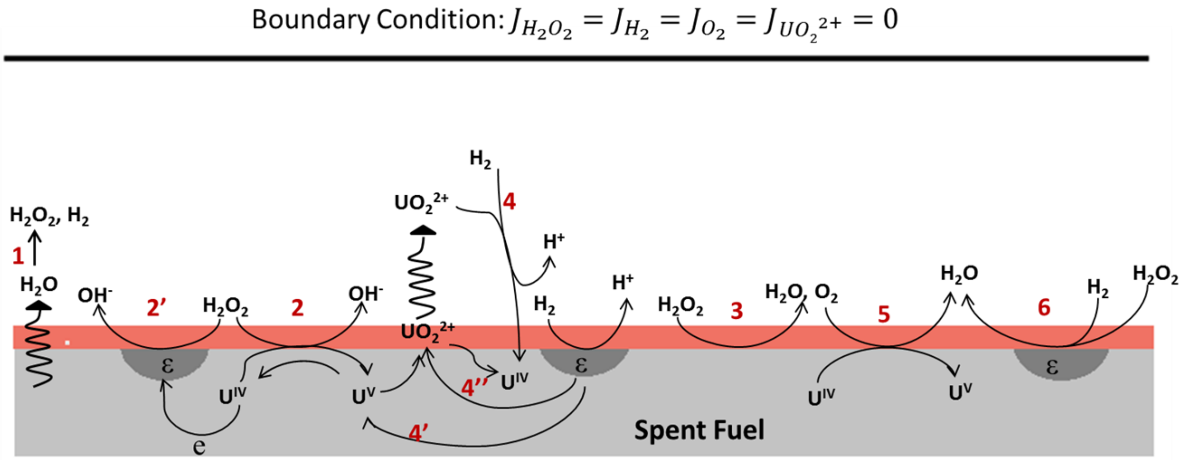
Boundary Condition: $J_{H_2O_2} = J_{H_2} = J_{O_2} = J_{UO_2^{2+}} = 0$

Figure 4.5: Chemical reactions included in the model to simulate the corrosion of spent nuclear fuel in a closed system. The pink area indicates the radiation zone.

4.2.5 Modelling Procedure and Default Parameter Values

The models outlined above were solved numerically using COMSOL Multiphysics, a commercial simulation package based on the finite element method. The model was simulated using the diluted species transportation module of COMSOL Multiphysics (version 5.2a).The default values of the simulation parameters are summarized and referenced in Table 4.1 [12, 13].

Table 4.1: Default values of simulation parameters

Parameter	Symbol	Value	Units
Water layer thickness [a]	L	1	mm
Radiation zone thickness [9]	b	30	μm
ε-particle coverage	s_ε	0.01	
g-value of H_2O_2 [12]	$g_{H_2O_2}$	0.1248	μmol J^{-1}
g-value of H_2 [12]	g_{H_2}	0.1248	μmol J^{-1}
UO_2 pellet oxidation rate constant in H_2O_2 [23]	k_2	1.0×10^{-8}	m s^{-1}
H_2O_2/UO_2 surface reaction rate constant on ε [24]	$k_{2'}$	6.92×10^{-6}	m s^{-1}
H_2O_2 surface-catalyzed decomposition rate constant [12, 23]	k_3	6.14×10^{-8}	m s^{-1}
H_2/UO_2^{2+} bulk reaction rate constant [25]	k_4	3.6×10^{-9}	L mol^{-1} s^{-1}
H_2/U^{VI} surface reaction rate constant on ε [26]	$k_{4'}$	4×10^{-7}	m s^{-1}
H_2/UO_2^{2+} surface reaction rate constant on ε [27], [c]	$k_{4''}$	1.3×10^{-5}	m^4 s^{-1} mol^{-1}
UO_2 pellet oxidation rate constant by O_2 [b]	k_5	5×10^{-11}	m s^{-1}
H_2/H_2O_2 surface reaction rate constant on ε [28], [c]	k_6	2.8×10^{-5}	m^4 s^{-1} mol^{-1}

[a] The calculated corrosion rate on the UO_2 surface is not dependent on the thickness of the water layer: 1 mm is chosen to be the default value.

[b] Since studies show that the oxidation of UO_2 to $UO_{2:33}$ is ~200 times faster in H_2O_2 than in a solution containing an equal concentration of O_2 [16], k_5 is calculated based on k_2.

[c] Modified reaction rate constants [29] based on the work in Reference [27, 28].

4.3 Results and Discussion

4.3.1 Corrosion of α-emitter doped UO_2 (open system)

Using the reaction scheme shown in Fig. 4.2, the relationship between fuel corrosion rate and α-source strength was calculated. The simulations yield steady-state corrosion rates for UO_2 after a short initial period. As shown in Fig. 4.6 the calculated steady-state corrosion rates are in good agreement with the published experimental data [9], except at α-source strengths > 10^4 MBq / g (UO_2). As discussed above the rates measured at these high dose rates may be governed by features not incorporated into the model.

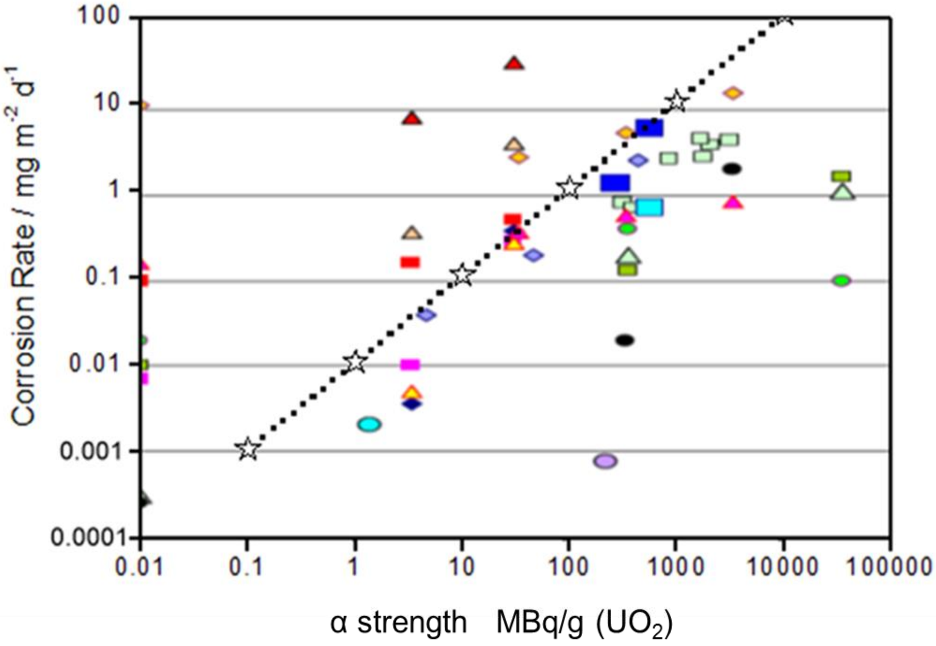

Figure 4.6: Comparison of experimental corrosion rates for α-emitter doped UO_2, non-doped UO_2 (0.01 MBq/g) and spent fuel with simulation results (stars).

In an open system, from which O_2 could be evacuated, the main oxidant driving the corrosion of UO_2 is H_2O_2, whose production rate is constant at a given α-dose rate to H_2O (equation 4.1). Once the steady-state corrosion rate is established, the production and consumption of H_2O_2 will be balanced, and the [H_2O_2] will be constant. Sensitivity calculations show that the rate constant for reaction 2 (k_2) does not influence the steady-state corrosion rate, only the time required to achieve it. Fig. 4.7 confirms that the production rate of H_2O_2 (calculated using equation 4.1) is directly proportional to the simulated corrosion rate of UO_2; i.e., the steady-state corrosion rate is determined by the production rate of H_2O_2 irrespective of the reactivity of the UO_2 surface.

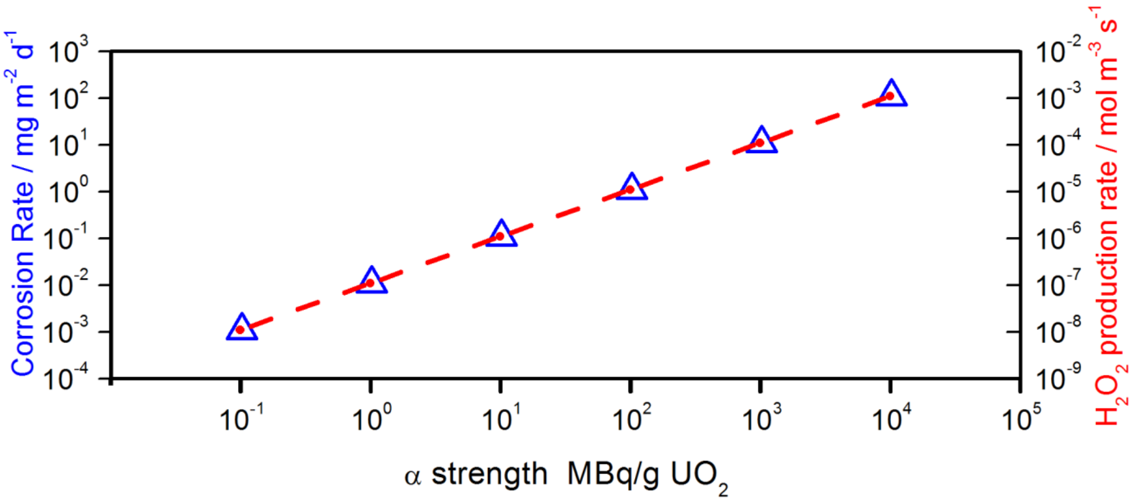

Figure 4.7: Comparison of the production rate of H_2O_2 (calculated by equation 4.1) with the simulated steady-state corrosion rate of UO_2 (calculated by the model) as a function of α-activity.

4.3.2 Corrosion of α-emitter doped UO_2 (closed system)

The good agreement between the simulated and experimental rates (Fig 4.6) gives us confidence that our model can be used to simulate the consequences of various failure scenarios, in particular the closed systems described above (sections 4.2.3 and 4.2.4). Since both H_2O_2 and O_2 will cause UO_2 corrosion the contribution to fuel corrosion will be determined by the relative concentrations of these two oxidants. For the reaction set incorporated into this model, this balance will be controlled by the rates of reaction of O_2 and H_2O_2 with UO_2 and the kinetics of the H_2O_2 decomposition reaction. Implicit in this statement is the assumption that the importance of O_2 produced by H_2O_2 decomposition will be much greater than that produced radiolytically. The corrosion rates due to H_2O_2 and O_2 can be calculated using rate equations 4.4 and 4.5, respectively.

$$R_{2,\,UO_2^{2+}} = k_2[H_2O_2] \tag{4.4}$$

$$R_{5,\,UO_2^{2+}} = 2k_5[O_2] \tag{4.5}$$

The kinetics of H_2O_2 decomposition, however, remains undetermined. Consequently, in the model the extent of decomposition is expressed as a ratio.

The consequences of a closed system were simulated using the reaction scheme shown in Fig. 4.4. Fig. 4.8 compares the simulated steady-state corrosion rates for α-emitter doped UO_2 in open and closed systems. In a closed system, the steady-state corrosion rate is almost one order of magnitude higher, indicating that the effect of O_2 (reaction 5 in Fig. 4.4) should not be underestimated in a closed system. Even though the reaction rate constant for reaction 5 (UO_2 oxidation by O_2) is ~200 times smaller than that for reaction 2 (UO_2 oxidation by H_2O_2) [16], the effect of O_2 is significant since the steady-state $[O_2]$ is higher than the $[H_2O_2]$ in a closed system. It is possible, therefore, that some of the variability in the corrosion rates plotted in Fig. 4.1, which are compiled from a wide range of experiments by many authors, reflect differences in the O_2 contents in the exposure solutions used.

In the model, the H_2O_2 decomposition ratio is defined as the fraction or percentage of the H_2O_2 decomposed. A value of 86% for the percentage decomposed on the surface of a UO_2 pellet has been published [23]. This decomposition ratio is important in regulating the $[O_2]$ and $[H_2O_2]$ and influences the respective contributions to corrosion by the two oxidants. Table 4.2 summarizes the simulated $[O_2]$ and $[H_2O_2]$ (calculated by model) when the steady-state corrosion rate is established for different H_2O_2 decomposition ratios. The corrosion rates due to H_2O_2 and O_2, calculated using equations 4.4 and 4.5 vary with the decomposition ratio as expected. However, the extent of decomposition of H_2O_2 to O_2 does not influence the total corrosion rate in a closed system. The decomposition of H_2O_2 produces O_2 ($2H_2O_2 \rightarrow 2H_2O+O_2$), as a second oxidant, O_2 will oxidize UO_2 ($2UO_2 + O_2 \rightarrow 2UO_2^{2+}$), the equations show the decomposition of H_2O_2 will not influence the ratio between H_2O_2 and UO_2^{2+} ($H_2O_2 + UO_2 \rightarrow UO_2^{2+} + 2OH^-$). Since the steady-state corrosion rate is dependent on the production rate of H_2O_2, the decomposition ratio will only influence the time required to reach the steady-state corrosion rate. As the H_2O_2 decomposition ratio increases, more time is needed to establish the steady-state condition.

In these calculations the only influence of H_2 is on the reduction of UO_2^{2+} (reaction 4) [25], a reaction which will not influence radionuclide release but only lower the concentration of dissolved UO_2^{2+}. However, a significant literature is available indicating that radiolytic H_2 is reactive as a reductant on UO_2 surfaces in the presence of α-radiation. Using a thin layer electrochemical cell to confine the radiolysis products from an external α-source to a 25μm layer of solution at a UO_2 disc surface (i.e., a partially closed system) Wren et al. [8] showed that while the oxidizing influence of radiolytic H_2O_2 was dominant the rate of surface oxidation of the UO_2 was slowed by the influence of radiolytic H_2. Traboulsi et al [30] compared the radiolytic corrosion of UO_2 in open and closed systems in H_2O irradiated with a $^{4}He^{2+}$ beam and found that corrosion was significantly suppressed when H_2 was present. In both these studies only the H_2O or solution was irradiated not the UO_2 itself. While the exact mechanism remains uncertain the influence of H_2 was thought to involve a surface reaction. However, no usable kinetic parameters, enabling H_2 effects to be incorporated in our model, were measured.

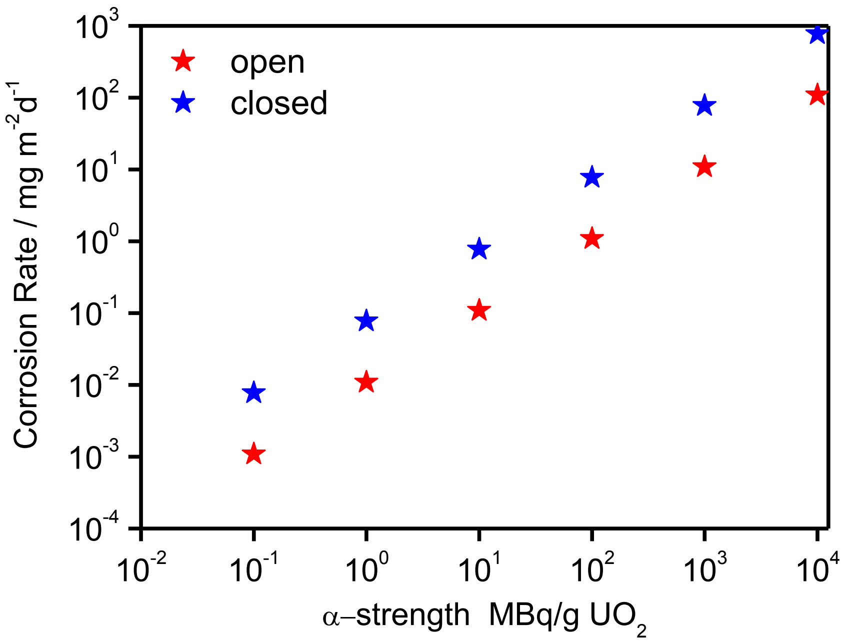

Figure 4.8: Comparison of the simulated steady-state corrosion rate of α-emitter doped UO_2 in open and closed system.

Table 4.2: Comparison of the effects of H_2O_2 and O_2 on fuel corrosion for different H_2O_2 decomposition ratios, Dose rate = 8.93 × 10^{-3} Gy s^{-1}.

	H_2O_2 decomposition ratio		
	50%	**86%**	**95%**
$[H_2O_2]$ [a]	1.668×10^{-6}	4.672×10^{-7}	1.668×10^{-7}
UO_2 corrosion rate [b] by H_2O_2	1.668×10^{-11}	4.672×10^{-12}	1.668×10^{-12}
$[O_2]$ [a]	2.107×10^{-5}	3.623×10^{-5}	4.003×10^{-5}
UO_2 corrosion rate [b] by O_2	1.669×10^{-11}	2.869×10^{-11}	3.170×10^{-11}
Total UO_2 corrosion rate [c]	3.34×10^{-11}	3.34×10^{-11}	3.34×10^{-11}

[a] The unit of concentration is mol L^{-1}, the values are calculated by the model.

[b] The unit of corrosion rate is mol m^{-2} s^{-1}, the values are calculated by equation 4.4 and 4.5.

[c] The unit of corrosion rate is mol m^{-2} s^{-1}, the value is calculated by the model.

4.3.3 Corrosion of Spent Nuclear fuel (closed system)

A number of key differences exist between α-emitter doped UO_2 and spent fuel (commonly investigated in the form of SIMFUEL). The two key differences likely to influence fuel corrosion are lattice doping by rare earth (RE^{III}) fission products and the presence of noble metal (ε) particles. Doping with rare earths has been shown to suppress the reactivity of fuel [Chapter 5 and 6], [31] [32]. However, the calculations presented in section 4.3.1 show that the α-radiation dose rate, which controls the rate of production of radiolytic species is the key parameter controlling the fuel corrosion rate making any influence of lattice doping on reactivity minor. By contrast, as noted above (section 4.2.3), the noble metal particles exert a significant influence on fuel corrosion.

The consequences of a closed system on spent fuel corrosion were simulated using the reaction scheme in Fig. 4.5. In this case, when reactions involving H_2 are included a steady-state corrosion rate cannot be achieved. Figure 4.9 shows the simulated corrosion rates calculated as a function of time using the reaction scheme in Fig 4.5, an α-dose rate = 8.93×10^{-3} Gy s^{-1} and an H_2O_2 decomposition percentage of 86%. After initially increasing rapidly the rate begins to steadily decrease to insignificant values. Fig. 4.10 shows the simulated [H_2], [H_2O_2] and [O_2] at the fuel surface for the same dose rate. Over the first 10 hours, the accumulation of H_2 is insufficient to overcome the oxidizing effect of H_2O_2 resulting in the increase in corrosion rate. With time, as [H_2] increases, the corrosion rate is suppressed. After 50 hours, the [H_2] at the fuel surface is ~20 times the [H_2O_2]. In addition, despite the [O_2] at the fuel surface being ~5 times that of [H_2O_2] after 50 hours, H_2O_2 remains the dominant oxidant due to the high rate constant for its reaction with UO_2 compared to that of O_2. These results clearly demonstrate that the accumulation of radiolytic H_2 in a closed system will radically suppress the fuel corrosion process.

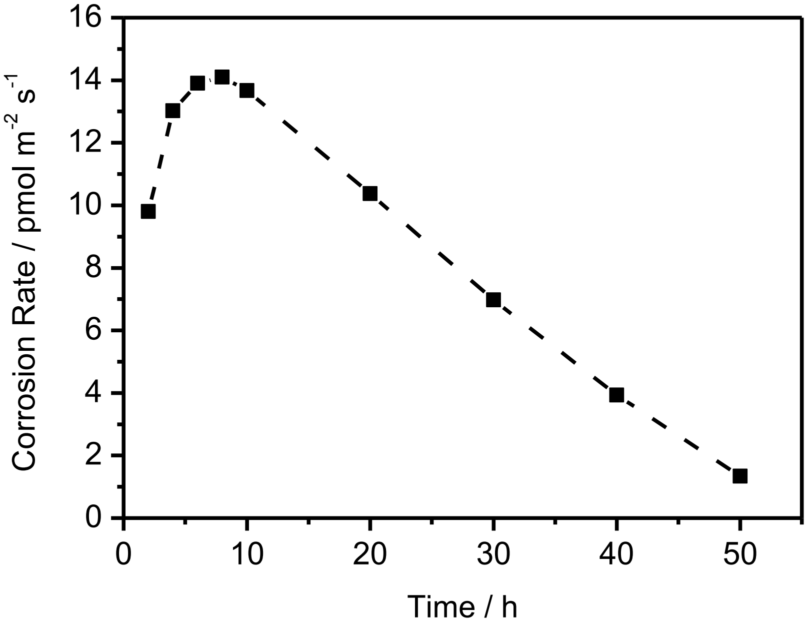

Figure 4.9: The simulated corrosion rates of spent nuclear fuel (α-dose rate = 8.93×10^{-3} Gy s^{-1}) as a function of time. All other model parameters have the default values (Table 4.1).

Fig. 4.11 compares the simulated corrosion rates as a function of time for different H_2O_2 decomposition ratios. As the decomposition ratio decreases, the corrosion rates increases, since oxidation by H_2O_2 is more rapid than by O_2. As a consequence the radiolytic H_2 takes longer to suppress the corrosion rate.

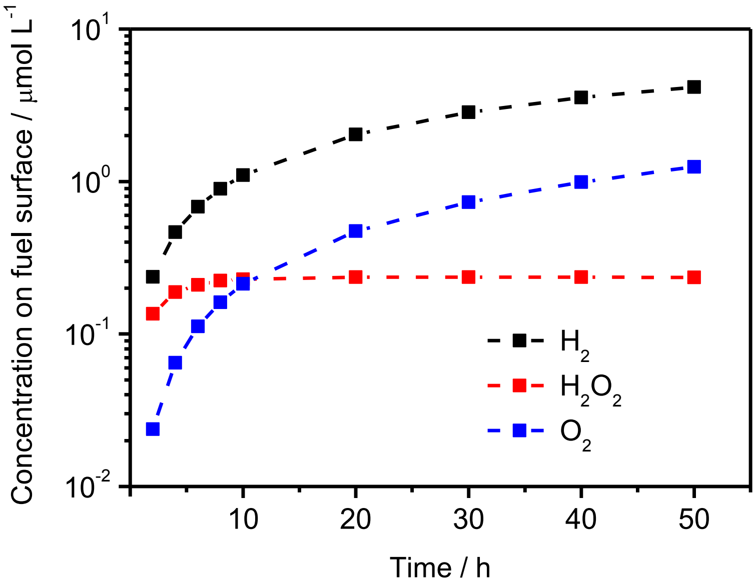

Figure 4.10: The simulated [H_2], [H_2O_2] and [O_2] at the fuel surface (α-dose rate = 8.93 × 10^{-3} Gy s^{-1}) as a function of time. All other model parameters have the default values (Table 4.1).

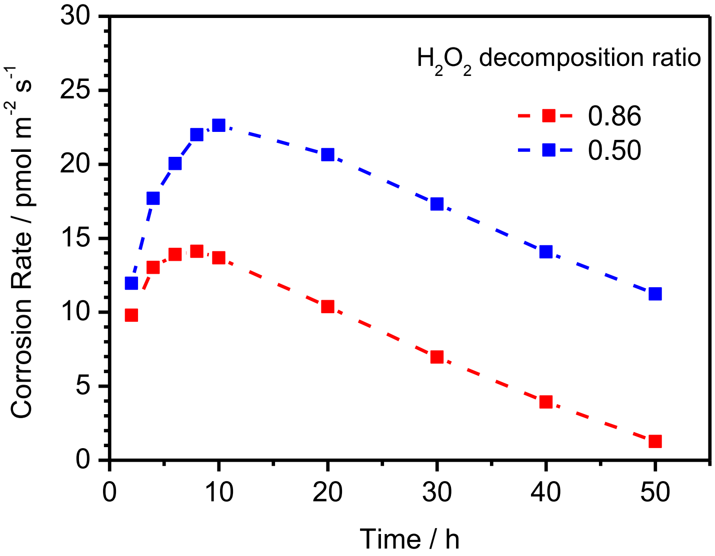

Figure 4.11: The simulated corrosion rates of spent nuclear fuel (α-dose rate = 8.93 × 10^{-3} Gy s^{-1}) as a function of time for different H_2O_2 decomposition ratios. All other model parameters have the default values (Table 4.1).

Figure 4.12 compares the simulated corrosion rates as a function of time for different coverages by ε-particles which can catalyze both H_2O_2 reduction and H_2 oxidation reactions. At short times there is a slight increase in corrosion rate since H_2O_2 initially plays a dominant role in controlling the surface redox conditions with Reaction 2' (Fig. 4.5) being accelerated leading to the increased corrosion rate. However, at longer times as the [H_2] increases the increased surface area of available ε particles allows reactions 4' and 4'' (Fig 4.5) to dominate leading to a very rapid decrease in corrosion rate.

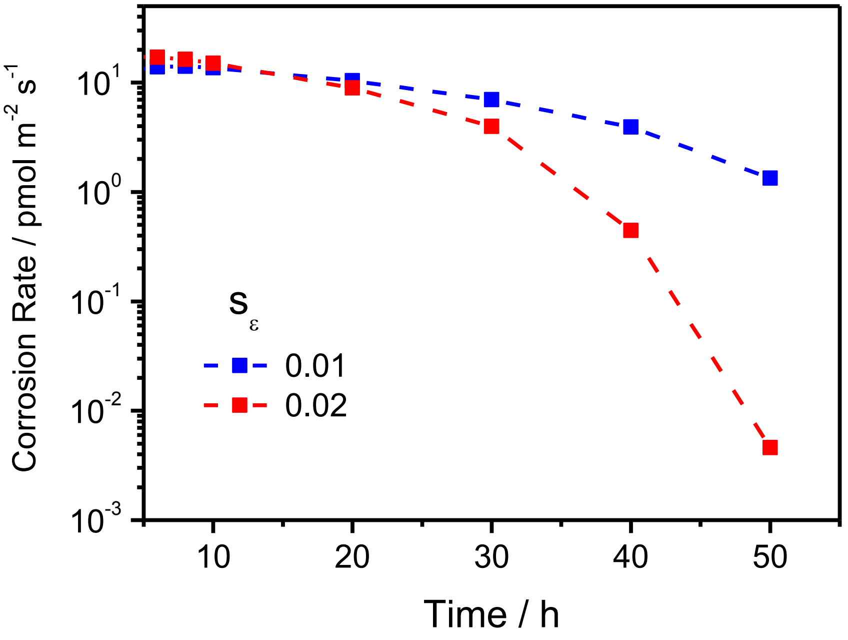

Figure 4.12: The simulated corrosion rates of spent nuclear fuel (α-dose rate = 8.93 × 10^{-3} Gy s^{-1}) as a function of time for different ε-particle coverages. All other model parameters have the default values (Table 4.1).

4.4 Summary and Conclusions

The calculated steady-state corrosion rates are in good agreement with published dissolution rates measured on a range of α-emitter doped UO_2 and spent fuel specimens.

The value of the rate constant for the reaction of H_2O_2 with UO_2 does not influence the calculated steady-state corrosion rate, only the time required to achieve the steady-state value. This demonstrates that the corrosion rate is determined by the radiolytic production rate of H_2O_2 irrespective of the reactivity of the fuel surface.

Calculations of corrosion rates for α-emitter doped UO_2 in a closed system demonstrate that the accumulation of O_2, primarily from H_2O_2 decomposition lead to an increase in corrosion rate. This reflects the fact that, even though the rate constant for the reaction of O_2 is ~200 times less than that of H_2O_2, the effect of O_2 can be significant since the steady-state $[O_2]$ can be greater than that of H_2O_2 in a closed system. However, this calculation does not include the influence of radiolytic H_2 which could suppress the corrosion rate.

When the influence of H_2 as a reductant reacting on noble metal (ε) particles is included, the model can be used to predict the corrosion rates of spent fuel. No steady-state corrosion rate can be established due to the accumulation of radiolytic H_2 with time, and the corrosion rate will decrease with time. The dose rate, H_2O_2 decomposition ratio, and the coverage of ε particles will influence the time needed for the corrosion rate to decrease to a negligible level, confirming that corrosion of spent fuel in a closed system should be severely restricted by radiolytic H_2.

4.5 References

[1] K. Ollila, E. Myllykylä, M. Tanhua-Tyrkkö, T. Lavonen, Dissolution Rate of Alpha-doped UO_2 in Natural Groundwater, J. Nucl. Mater. 442 (2013) 320-325.

[2] S. Stroes-Gascoyne, F. Garisto, J.S. Betteridge, The Effects of Alpha-radiolysis on UO_2 Dissolution Determined from Batch Experiments with ^{238}Pu-doped UO_2, J. Nucl. Mater. 346 (2005) 5-15.

[3] T. Mennecart, C. Cachoir, K. Lemmens, Influence of the Alpha Radiation on the UO_2 Dissolution in High pH Cementitious Waters, J. Radioanal. Nucl. Chem. 304 (2014) 61-66.

[4] K. Ollila, Influence of Radiolysis on UO_2 Fuel Matrix Dissolution Under Disposal Conditions, Working Report 2011-27, Posiva Oy, Eurajoki, Finland, 2011.

[5] T. Mennecart, B. Grambow, M. Fattahi, Z. Andriambololona, Effect of Alpha Radiolysis on Doped UO_2 Dissolution under Reducing Conditions, Radiochim. Acta 92 (2004) 611-615.

[6] V.V. Rondinella, Hj. Matzke, J. Cobos, T. Wiss, Leaching Behaviour of UO_2 Containing α-emitting Actinides, Radiochim. Acta 88 (2000) 527-531.

[7] J. Cobos, L. Havela, V. V. Rondinella, J. De Pablo, T. Gouder, J. P. Glatz, P. Carbol, H. Matzke, Corrosion and Dissolution Studies of UO_2 Containing α-emitters, Radiochim. Acta 90 (2002) 597-602.

[8] J.C. Wren, D.W. Shoesmith, S. Sunder, Corrosion Behavior of Uranium Dioxide in Alpha Radiolytically Decomposed Water, J. Electrochem. Soc. 152 (2005) B470-B481.

[9] C. Poinssot, C. Ferry, et al., Spent Fuel Stability under Repository Conditions – Final Report of the European Project, Report CEA-R-609, European Commission, 2005.

[10] M. Gobien, F. Garisto, E. Kremer, Fifth Case Study: Reference Data and Codes, report NWMO TR-2013-05, Nuclear Waste Management Organization, Toronto, ON, 2013.

[11] L. Wu, Y. Beauregard, Z. Qin, S. Rohani, D.W. Shoesmith, A Model for the Influence of Steel Corrosion Products on Nuclear Fuel Corrosion under Permanent Disposal Conditions, Corros. Sci. 61 (2012) 83-91.

[12] L. Wu, N. Liu, Z. Qin, D.W. Shoesmith, Modeling the Radiolytic Corrosion of Fractured Nuclear Fuel under Permanent Disposal Conditions, J. Electrochem. Soc. 161 (2014) E3259-E3266.

[13] L. Wu, Z. Qin, D.W. Shoesmith, An Improved Model for the Corrosion of Used Nuclear Fuel Inside a Failed Waste Container under Permanent Disposal Conditions, Corros. Sci. 84 (2014) 85-95.

[14] M. Jonsson, F. Nielsen, O. Roth, E. Ekeroth, S. Nilsson, M.M. Hossain, Radiation Induced Spent Nuclear Fuel Dissolution under Deep Repository Conditions, Environ. Sci. Technol. 41 (2007) 7087-7093.

[15] F. Nielsen, M. Jonsson, Geometrical α- and β-dose Distributions and Production Rates of Radiolysis Products in Water in Contact with Spent Nuclear Fuel, J. Nucl. Mater. 359 (2006) 1-7.

[16] D.W. Shoesmith, Fuel Corrosion Processes under Waste Disposal Conditions, J. Nucl. Mater. 282 (2000) 1-31.

[17] S.L.W. Hill, N. Liu, Z. Qin , D. Zagidulin, D.W. Shoesmith, Interactions between Carbon Steel and UO_2 Corrosion Fronts inside a Failed Nuclear Waste Container, Proceedings of the 17th International Conference on Environmental Degradation of Materials in Nuclear Power Systems − Water Reactors; Ottawa, Ontario, August 9−13, 2015;Canadian Nuclear Society (CNS): Toronto, 2015.

[18] M.E. Broczkowski, P.G. Keech, J.J. Noël, D.W. Shoesmith, Corrosion of Uranium Dioxide Containing Simulated Fission Products in Dilute Hydrogen Peroxide and Dissolved Hydrogen, J. Electrochem. Soc. 157 (2010) C275-C281.

[19] H. He, M. Broczkowski, K. O'Neil, D. Ofori, O. Semenikhin, D.W. Shoesmith, Corrosion of Nuclear Fuel (UO_2) Inside a Failed Nuclear Waste Container, report NWMO TR-2012-09, Nuclear Waste Management Organization, Toronto, ON, 2012.

[20] M. Razdan, D.W. Shoesmith, The Influence of Hydrogen Peroxide and Hydrogen on the Corrosion of Simulated Spent Nuclear Fuel, Faraday Discuss. 180 (2015) 283-299.

[21] D.W. Shoesmith, Used Fuel and Uranium Dioxide Dissolution Studies – A Review, report NWMO TR-2007-03, Nuclear Waste Management Organization, Toronto, ON, 2007.

[22] M.E. Broczkowski, J.J. Noël, D.W. Shoesmith, The Inhibiting Effects of Hydrogen on the Corrosion of Uranium Dioxide under Nuclear Waste Disposal Conditions, J. Nucl. Mater. 346 (2005) 16-23.

[23] R. Pehrman, M. Trummer, C.M. Lousada, M. Jonsson, On the Redox Reactivity of Doped UO_2 Pellets – Influence of Dopants on the H_2O_2 Decomposition Mechanism, J. Nucl. Mater. 430 (2012) 6-11.

[24] M. Trummer, O. Roth, M. Jonsson, H_2 Inhibition of Radiation Induced Dissolution of Spent Nuclear Fuel, J. Nucl. Mater. 383 (2009) 226-230.

[25] E. Ekeroth, M. Jonsson, T.E. Eriksen, K. Ljungqvist, S. Kovács, I. Puigdomenech, Reduction of UO_2^{2+} by H_2, J. Nucl. Mater. 334 (2004) 35-39.

[26] M. Trummer, S. Nilsson, M. Jonsson, On the Effects of Fission Product Noble Metal Inclusions on the Kinetics of Radiation Induced Dissolution of Spent Nuclear Fuel, J. Nucl. Mater. 378 (2008) 55-59.

[27] S. Nilsson, M. Jonsson, On the Catalytic Effect of Pd(s) on the Reduction of $UO_2^{2+}$with H_2 in Aqueous Solution, J. Nucl. Mater. 374 (2008) 290-292.

[28] S. Nilsson, M. Jonsson, On the Catalytic Effects of UO_2(s) and Pd(s) on the Reaction between H_2O_2 and H_2 in Aqueous Solution, J. Nucl. Mater. 372 (2008) 160-163.

[29] N. Liu, L. Wu, Z. Qin, D.W. Shoesmith, Roles of Radiolytic and Externally Generated H_2 in the Corrosion of Fractured Spent Nuclear Fuel, Environ. Sci. Technol. 50 (2016) 12348-12355.

[30] A. Traboulsi, J. Vandenborre, G. Blain, B. Humbert, J. Barbet, M. Fattahi, Radiolytic Corrosion of Uranium Dioxide: Role of Molecular Species, J. Phys. Chem. C 118 (2014) 1071-1080.

[31] M. Razdan, D.W. Shoesmith, The Electrochemical Reactivity of 6.0 wt% Gd-Doped UO_2 in Aqueous Carbonate/Bicarbonate Solutions, J. Electrochem. Soc. 161 (2014) H225-H234.

[32] D.W. Shoesmith, The Chemistry/Electrochemistry of Spent Nuclear Fuel as a Wasteform, in "Uranium: Cradle to Grave", edited by P. Burns, and G. Sigmon, Mineralogical Society of Canada, Short Course Series Vol 43, 337-368 (2013).

Chapter 5

5 The Electrochemical Study of Dy Doped UO_2 in Slightly Alkaline Sodium Carbonate/bicarbonate and Phosphate Solutions

5.1 Introduction

The reactivity of the UO_2 matrix, and how it is modified by in-reactor irradiation is very important in determining fuel corrosion and, hence, radionuclide release rates. The key changes likely to influence the chemical reactivity of the fuel are the rare earth (RE) doping of the matrix, the presence of noble metal particles and the development of non-stoichiometry [1]. Considerable experimental evidence exists to show that fission product and actinide-lanthanide doping have a significant effect on the kinetics of air oxidation of the fuel [2, 3]. Choi et al. investigated the oxidation of UO_2 based SIMFUELs (1.5, 3.0, 4.0, 6.0 and 8.0 at%) and showed that oxidation of the 6 at% and 8 at% SIMFUELs yielded a cubic phase and increased simulated burnup resulted in longer U_3O_8 formation times at 250 °C [4]. Kim et al. studied the effect of Gd^{III} on the air oxidation of doped UO_2 by thermogravimetry and XRD analysis. The results revealed that the degree of oxidation from UO_2 to U_3O_8 decreased linearly with increasing content of Gd, and proposed that the Gd dopant inhibited the initial oxidation kinetics from UO_2 to U_4O_9 and prevented the complete oxidation to U_3O_8 [5]. Talip et al. studied the air oxidation of lanthanum doped UO_2 at 500 K and concluded that La doping caused a lattice expansion which could increase diffusion of O^{2-} ions in the UO_2 matrix, leading to a prompt air oxidation process which stops with the formation of an M_4O_9 phase [6].

In aqueous solution, Razdan et al. showed that the anodic oxidation/dissolution mechanism on Gd-UO_2 is similar to that observed on SIMFUELs, although the overall reactivity of Gd-UO_2 was significantly lower. This was attributed to the presence of Gd^{III}-O_v (O_v: oxygen vacancy) clusters which would reduce the availability of the O_v required to accommodate excess O^{2-} ions when oxidation occurred [7, 8]. Since there has been a continuous trend toward higher in-reactor fuel burn-up [9], the extent of doping and its influence on reactivity are becoming more important.

Non-stoichiometry has been shown to exert a major influence on UO_2 reactivity. Scanning electrochemical microscopy studies [10] showed that the reactivity increased substantially with highly non-stoichiometric UO_2 (~$UO_{2.25}$) being $\geq 10^3$ more reactive than close-to-stoichiometric UO_2. While the exact mechanistic details of the anodic reaction remain unresolved, the extent of oxidation on a surface close to stoichiometry appears to be limited by low interstitial O (O_I) mobility within the matrix. At higher degrees of non-stoichiometry, the formation of defect clusters [11] appears to enhance O_I mobility in the matrix leading to an increase in oxidation rate.

Corrosion rates will also depend on groundwater composition, which will be determined by its origin in the host rock. For relevant Canadian conditions (in crystalline rock) it is expected to be $Ca^{2+}/Na^{+}/Cl^{-}/SO_4^{2-}$ dominated [12]. It may also contain small amounts of HCO_3^{-}/CO_3^{2-} (10^{-4} to 10^{-3} mol L^{-1}), the key groundwater constituent, since it will increase $[UO_2]^{2+}$ solubility by complexing the uranyl ion leading to an acceleration of UO_2 corrosion rates [13].

In this study we have investigated the electrochemical reactivity of Gd_2O_3 (6.0 wt%) and Dy_2O_3 (12.9 wt%) doped UO_2. While all rare earth dopants are not expected to have an identical effect on UO_2, this comparison offers an opportunity to determine their influence on the oxidative behavior of UO_2 in an aqueous environment. We also compared the reactivity of rare earth doped UO_2 with close-to-stoichiometric $UO_{2.002}$ and SIMFUEL. SIMFUELs are UO_2 pellets doped with 11 non-radioactive elements (Ba, Ce, La, Sr, Mo, Y, Zr, Rh, Pd, Ru, Nd) to replicate the chemical effects of in-reactor irradiation, and have been well characterized and studied [14, 15].

5.2 Experimental

5.2.1 Electrode Material and Preparation

Experiments were performed on $UO_{2.002}$, 1.5 at% SIMFUEL, 6.0 wt% Gd_2O_3 doped UO_2 (Gd-UO_2) and 12.9 wt% Dy_2O_3 doped UO_2 (Dy-UO_2) electrodes. Pellets of $UO_{2.002}$, SIMFUEL and Dy-UO_2 were fabricated and supplied by Canadian Nuclear Laboratories, Chalk River, Canada. The Gd-UO_2 was supplied by Cameco (Port Hope, Canada). SEM images have been published elsewhere [8, 10]. EDX analyses showed the RE^{III} dopants were homogeneously distributed throughout the matrix [8]. The pellets were cut into 2 mm thick disks and fabricated into electrodes using the previously published procedure [16, 17].

5.2.2 Electrochemical Cell and Equipment

Experiments were performed in a standard three-electrode cell. A commercial saturated calomel reference electrode (SCE) (+0.242 V vs. the standard hydrogen electrode) was used, and a Pt foil, spot-welded to a Pt wire, was employed as the counter electrode. All potentials are quoted on the SCE scale. All electrochemical experiments were carried out using a Solartron model 1287 potentiostat to control applied potentials and record current responses. The current interrupt method was employed to compensate the electrode resistance. Corrware (Scribner Associates) was used to analyze the data.

5.2.3 Electrochemical Procedure

Prior to each experiment, electrodes were polished on wet 1200 grit SiC paper and rinsed with distilled deionized water. Subsequently, the electrodes were electrochemically reduced at −1.2 V for 5 min (vs. SCE) to remove any air-formed oxides or organic contaminants present on the surface. Cyclic voltammetric (CV) experiments were performed by scanning the potential from −1.2 V to an anodic limit of ≤ 0.4 V and back at a scan rate of 10 mV s^{-1}. In potentiostatic experiments electrodes were held at a constant applied potential for 1 hour.

5.2.4 Solution Preparation

Solutions were prepared using distilled deionized water (resistivity $\rho = 18.2$ MΩ cm) purified using a Millipore Milli-Q plus unit which removes organic and inorganic impurities. The base electrolyte was 0.1 mol L^{-1} NaCl. The carbonate and phosphate concentrations were adjusted with Na_2CO_3/$NaHCO_3$ (Caledon) and $NaHPO_4$ (Caledon). The total carbonate concentration ($[CO_3]_T = [HCO_3^-] + [CO_3^{2-}]$) ranged from 1×10^{-2} to 2×10^{-1} mol L^{-1}. The total phosphate concentration ($[PO_4]_T = [H_2PO_4^-] + [HPO_4^{2-}] + [PO_4^{3-}]$) was 0.05 mol L^{-1}. The solution pH was set to 10 and measured with an Orion model 720A pH meter. At this pH HCO_3^- and CO_3^{2-} will be present at approximately equal concentrations ($pK_a = 10.3$). For phosphate the dominant anion will be HPO_4^{2-} ($pK_{a2} = 7.21$ and $pK_{a3} = 12.36$). Prior to an experiment the solution in the cell was purged with Ar (Praxair) for an hour and purging was maintained throughout the experiment.

5.2.5 XPS Analysis

Between the electrochemical and XPS analysis, the sample was rinsed with distilled deionized water, dried by Ar and kept in Ar. XPS spectra were recorded on a Kratos Axis NOVA spectrometer using an Al K_α monochromatic high energy ($h\nu$ =1486.6 eV) radiation source. The work function of the instrument was set to give a value of 83.96 eV for the binding energy (BE) of the Au ($4f_{7/2}$) line of metallic Au. The spectrometer dispersion was adjusted to give a BE of 932.62 eV for the Cu $2p_{3/2}$ line of Cu metal. Charge neutralization was used on all specimens. The C 1s peak at 285.0 eV was used as a standard to correct for surface charging when required. All spectra were analyzed using CasaXPS software (version 2.3.14) and involved a 50% Gaussian and 50% Lorentzian fitting routine with a Shirley background correction. The procedure used to deconvolute the U4f spectra into contributions from U^{IV}, U^{V} and U^{VI} has been described elsewhere [18]. The satellite structures close to the $U4f_{5/2}$ peak, and the valence band region were used to check the validity of the spectral fit.

5.2.6 Current-sensing Atomic Force Microscopy (CS-AFM)

A DC bias potential is applied to the microscope probe tip while the specimen (in the present case $UO_{2.002}$) is held at ground potential and the current passing through the tip and the specimen measured. Both topographic and conductivity images are then generated simultaneously by scanning the tip across the surface allowing correlation of the surface features and the local conductivity [19]. CS-AFM images were obtained using a Multimode AFM (Veeco) equipped with a Nanoscope IV controller and a CS-AFM extension module. Samples were mounted on a metal disk, and Cu tape was applied to the sides and the front of the pellet to ensure electrical contact. Imaging was performed in the contact mode using DDESP conducting diamond coated AFM probes (Nanoworld, 40 N/m). Topographic and current images were acquired simultaneously to correlate the surface features and local conductivity. Further details of CS-AFM measurements can be found in [20].

5.3 Results and Discussion

5.3.1 Voltammetry

Previous studies have shown that the anodic oxidation of UO_2 involves two stages, matrix oxidation ($UO_2 \rightarrow U^{IV}_{1-2x}U^{V}_{2x}O_{2+x}$) and further oxidation of the matrix to soluble U^{VI} as $U^{VI}O_2^{2+}$ ($U^{VI}O_2(CO_3)_x^{(2-2x)+}$ in HCO_3^-/CO_3^{2-} solutions) [21]. Fig. 5.1A shows a series of CVs recorded on Dy-UO_2 to different anodic potential limits in 0.1 mol L^{-1} NaCl + 0.01 mol L^{-1} $(CO_3)_T$. When the anodic potential limit is < −0.4 V, a very shallow anodic current is observed on the forward scan leading to an equally shallow cathodic current on the reverse scan indicating a reversible oxidation of surface states. It has been suggested this occurs at slightly non-stoichiometric grain boundaries [13]. When the anodic limit is extended to more positive values oxidation (reaction 5.1) and anodic dissolution (reactions 5.2 and 5.3) occur more extensively across the surface [22].

$$U^{IV}O_2 \rightarrow U^{IV}_{1-2x}U^{V}_{2x}O_{2+x} + 2xe^- \qquad (5.1)$$

$$U^{IV}_{1-2x}U^{V}_{2x}O_{2+x} + CO_3^{2-} \rightarrow U^{VI}O_2CO_3 + (2\text{-}2x)e^- \qquad (5.2)$$

$$U^{VI}O_2CO_3 + (x-1)CO_3^{2-} \rightarrow U^{VI}O_2(CO_3)_x^{(2-2x)+} \qquad (5.3)$$

The extent of oxidation can be gauged from the size and breadth of the reduction peak observed on the reverse scan.

Figure 5.1B shows a similar series of experiments conducted on the close-to-stoichiometric $UO_{2.002}$. The current on the anodic scan is enhanced with observable anodic oxidation (and an accompanying cathodic reduction on the reverse scan) observed for potentials ≤ −0.6 V.

The anodic charge leading to dissolution (Q_D) was calculated as the difference between the anodic (Q_A) and cathodic (Q_C) charges obtained by integrating series of such CVs for all four electrodes between a potential for the onset of water reduction and the anodic potential limit for that particular scan. Given the ceramic nature of the electrode it is recognized that a significant charging current will be recorded in these CVs. However, since the scan rate is the same on the forward and reverse scans the charging current will be equal for both scan directions. While this will render the absolute charge values only approximate they will remain quantitatively comparable.

For Dy-UO_2 and Gd-UO_2 no measurable charge, Q_D, for anodic dissolution was detected for potentials < −0.1 V (Fig. 5.2). These results show that the $U^{IV}_{1-2x}U^{V}_{2x}O_{2+x}$ layer formed is stabilized by this level of RE^{III} doping as indicated, but not demonstrated, previously [7, 18]. For SIMFUEL, anodic dissolution is detected for potentials > −0.3 V (Fig. 5.2) confirming a less stabilizing influence of the lower level of RE^{III} doping in this material. At higher potentials, when anodic dissolution is the dominant reaction, Q_D is in the order

SIMFUEL > Gd-UO_2 > Dy-UO_2

although the differences, especially between the latter two materials, are minor. Based on Raman spectroscopic and XPS analyses, this suppression of anodic dissolution has been attributed to the formation of RE^{III}-O_V clusters. It was proposed that these clusters protect the fluorite lattice against the destabilizing formation of tetragonal distortions by reducing the availability of (O_V)s required for oxidation and dissolution to proceed [8].

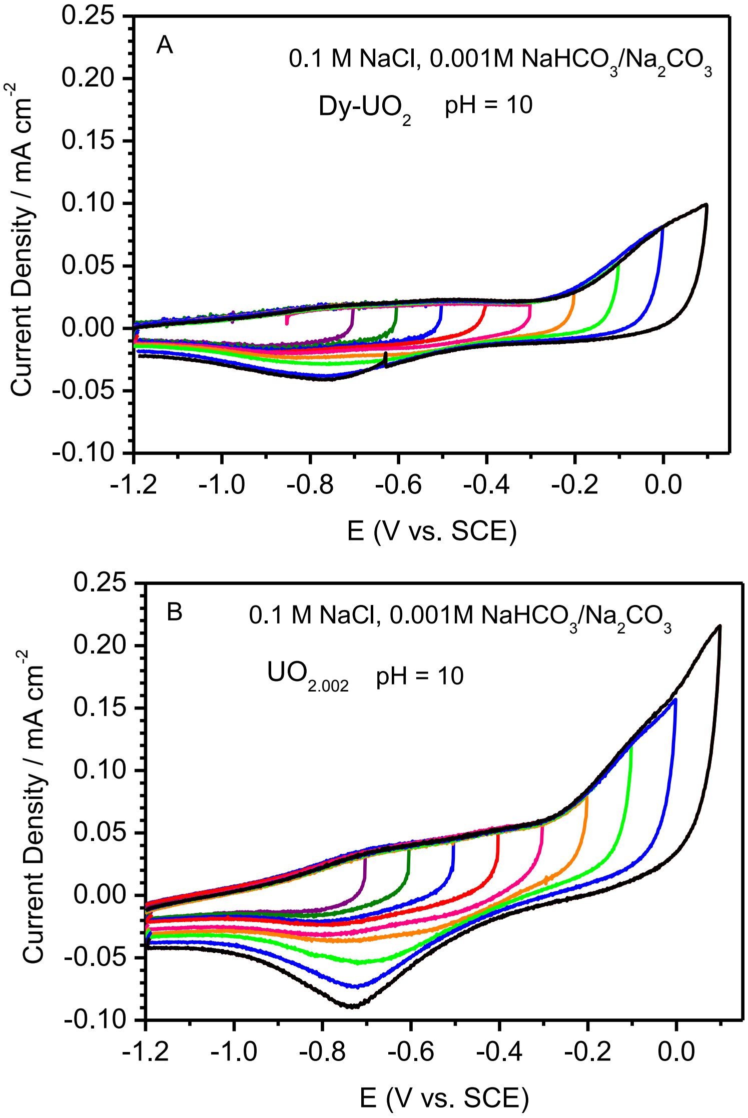

Figure 5.1: CVs recorded on Dy-UO_2 (A) and $U_{2.002}$ (B) at a scan rate of 10 mV s^{-1} in Ar-purged 0.1 mol L^{-1} NaCl containing 0.01 mol L^{-1} $[CO_3]_T$ to different anodic potential limits at pH 10.

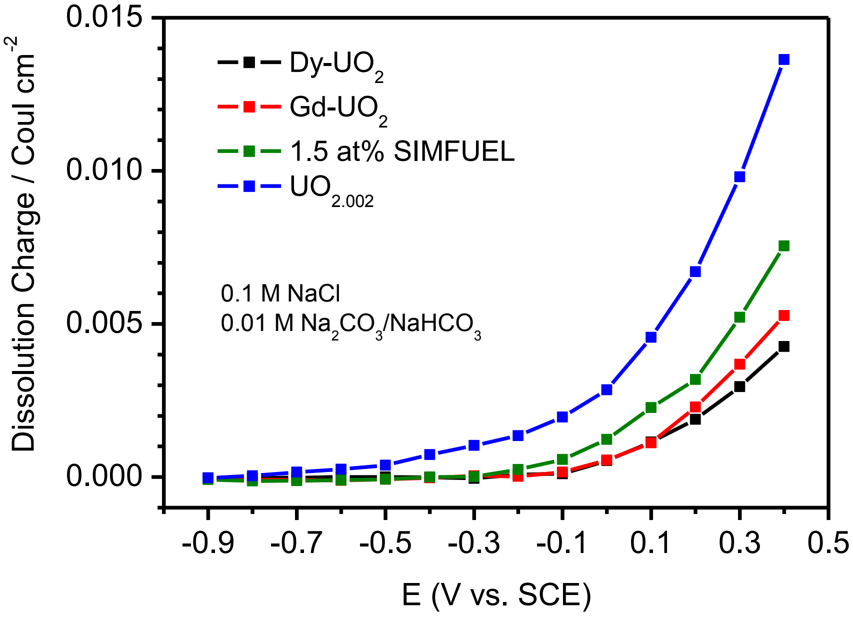

Figure 5.2: Q_D (dissolution charge) calculated for four UO_2 materials in 0.1 mol L^{-1} NaCl containing 0.01 mol L^{-1} $[CO_3]_T$ (pH = 10).

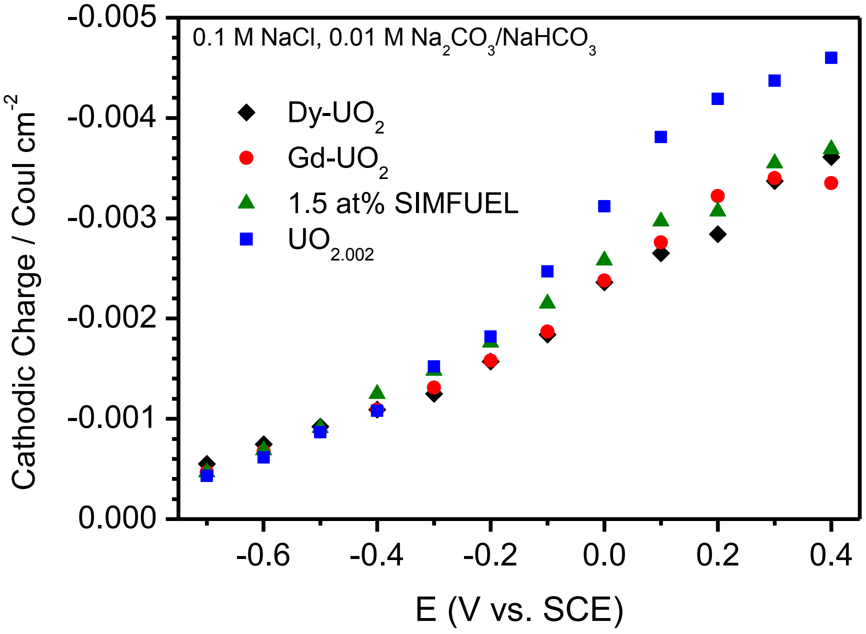

Figure 5.3: Cathodic charge (Q_C) obtained by integration of CVs recorded in 0.1 mol L^{-1} NaCl containing 0.01 mol L^{-1} $[CO_3]_T$ (pH = 10).

Figure 5.3 shows the influence of the anodic potential limit on the extent of oxidation of the surface as indicated by the charge (Q_C) required to cathodically reduce it. For all electrodes, irrespective of the doping level or the presence of minor non-stoichiometry, the extent of surface oxidation increases for potentials > −0.2 V indicating that the onset of matrix dissolution is accompanied by the enhanced formation of the $U^{IV}_{1-2x}U^{V}_{2x}O_{2+x}$ layer as will be demonstrated below by XPS.

For $UO_{2.002}$, dissolution starts at potentials as low as −0.7 V, Figure 5.2. Previous results have shown that oxidation of non-stoichiometric UO_2 does occur at sub-thermodynamic potentials [13, 23]. This was attributed to the association of randomly distributed O interstitial (O_I) defects into clusters as the degree of non-stoichiometry increased [24]. While the exact anodic oxidation mechanism remains unresolved, the higher O_I mobility in the non-stoichiometric matrix appears to lead to a deeper and more extensive surface oxidation. However, for a degree of non-stoichiometry of $x = 0.002$, Raman spectroscopic studies [25] show the anion sub-lattice should be only slightly distorted by the small number of O_I expected to be randomly distributed within the fluorite matrix at this degree of non-stoichiometry. Consequently, any influence on anodic reactivity would be expected to be minimal especially at sub-thermodynamic potentials.

5.3.2 Current Sensing-AFM

Figure 5.4 shows representative 20μm by 20μm CS-AFM topographic and current images of the $UO_{2.002}$ surface, with the resolution optimized for the current rather than the topographic maps. In the topographic map, raised areas are light in color and depressed areas darker. Black areas on the surface show the locations of voids (i.e., missing grains). The conductivity map is color-coded according to standard AFM practice with conductive regions shown as bright and regions of lower conductivity as dark. Comparison of the images reveals a correlation between topography and local conductivity, with regions of increased conductivity associated with grain boundaries and grain edges at the location of voids. Since the electrical conductivity of UO_{2+x} increases with the degree of non-stoichiometry, these variations indicate differences in composition associated with the grain boundaries and edges. While the nominal composition is $UO_{2.002}$, it is likely these locations are significantly more non-stoichiometric and, hence, the locations of the sub-thermodynamic oxidation and anodic dissolution sites.

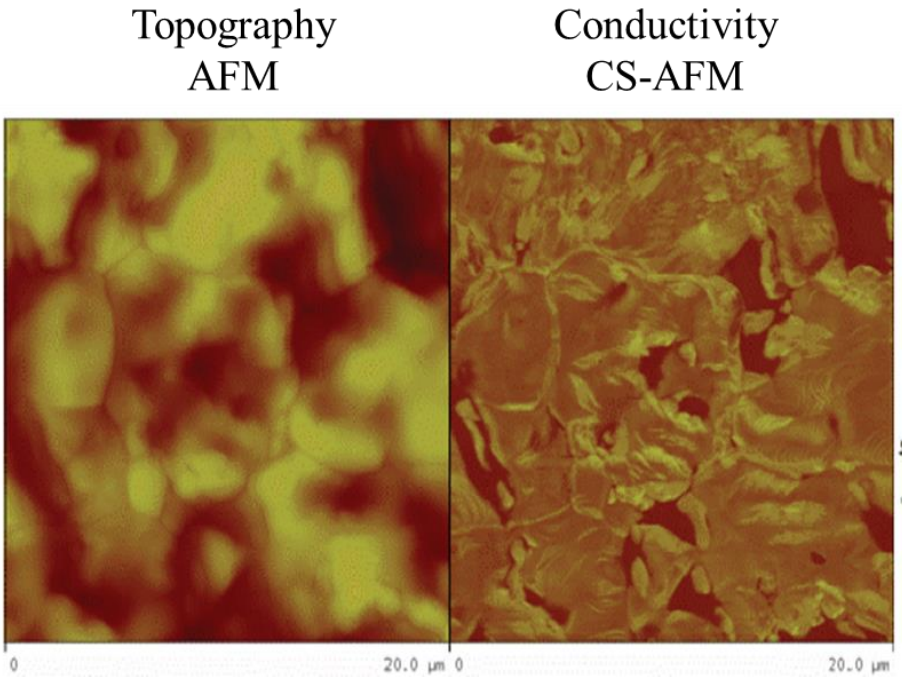

Figure 5.4: AFM, CS-AFM analyses recorded on the $UO_{2.002}$ specimen. The CS-AFM image is color-coded according to standard AFM practice with conducting regions shown as bright, and regions of lower activity as dark areas. The height range in the AFM image is 2000 nm, the current range in the CS-AFM image is 20000 pA.

5.3.3 Voltammetry in HCO_3^-/CO_3^{2-} and HPO_4^{2-}

Figure 5.5 shows a series of CVs recorded on the Dy-UO_2 electrode in solutions containing various $[CO_3]_T$. The very shallow anodic current at low potentials attributed to the oxidation of surface states (discussed above) appears independent of the $[CO_3]_T$. For potentials > −0.2 V the current is increased by the addition of HCO_3^-/CO_3^{2-} but only marginally dependent on $[CO_3]_T$ for potentials ≤ 0 V. This confirms that once dissolution is possible (Figure 5.2) it is accelerated by complexation with HCO_3^-/CO_3^{2-} to yield $U^{VI}O_2(CO_3)_x^{(2-2x)+}$. At potentials ≥ 0.1V the current becomes less dependent on potential but more dependent on $[CO_3]_T$. These observations are consistent with a previous electrochemical impedance spectroscopy study performed on SIMFUEL (1.5 at% burnup) [22]. This study showed that at low potentials, the overall anodic dissolution reaction was controlled by the first electron transfer step to produce an adsorbed U^V intermediate, $(U^VO_2HCO_3)_{ads}$. At higher potentials, when the current became less dependent on potential but more dependent on $[CO_3]_T$, this intermediate was converted to an adsorbed U^{VI} state, ($U^{VI}O_2CO_3$), with the overall dissolution process becoming controlled by the chemical dissolution of this adsorbed intermediate, reaction 5.3. The decrease in size of the reduction peaks on the reverse scan in HCO_3^-/CO_3^{2-} solutions is consistent with an enhanced dissolution process leading to a thinning of the oxide layer retained on the surface. As noted previously on Gd-doped UO_2 [7], when no HCO_3^-/CO_3^{2-} is present there are two reduction peaks, possibly reflecting the dual phase nature of the surface film, the $U^{IV}_{1-2x}U^{V}_{2x}O_{2+x}$ layer being reduced at ~−0.7 V (peak 1 in Fig. 5.5) and the $U^{VI}O_3 \cdot yH_2O$ being reduced at −0.8 V to −0.9 V (peak 2 in Fig. 5.5). When HCO_3^-/CO_3^{2-} is present both these peaks are reduced in size indicating an enhanced dissolution as U^{VI} and a thinner U^{IV}/U^{V} surface layer.

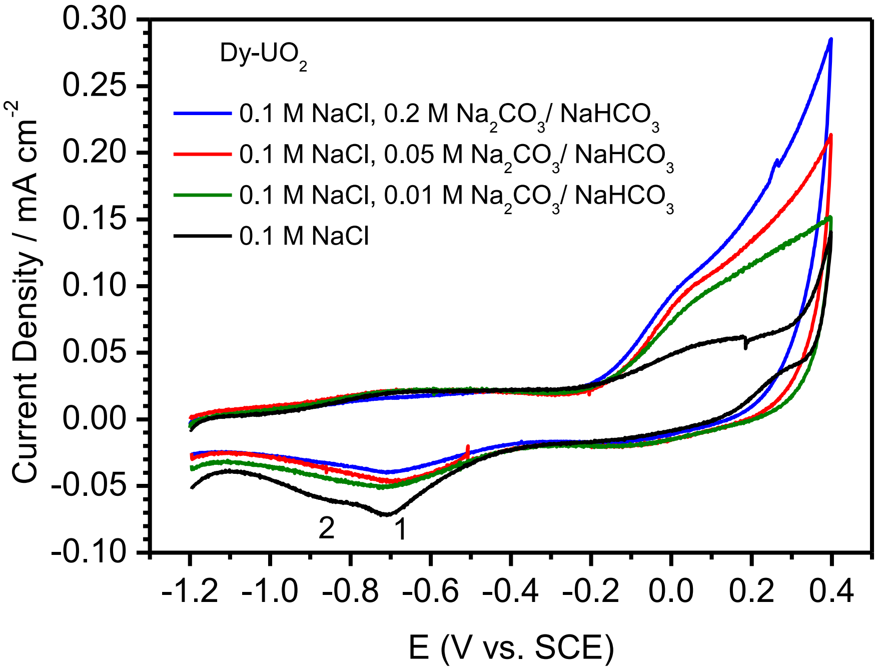

Figure 5.5: CVs recorded on Dy-UO_2 in Ar-purged 0.1 mol L^{-1} NaCl containing various $[CO_3]_T$ at pH = 10; electrode rotation rate 16.7 Hz; scan rate = 10 mV s^{-1}.

Figure 5.6 compares CVs recorded in HCO_3^-/CO_3^{2-} and HPO_4^{2-}. At very low potentials (−0.8 V to −0.4 V) the current recorded in the HPO_4^{2-} solution is marginally, and possibly insignificantly, lower than that recorded in HCO_3^-/CO_3^{2-}. For potentials ≥ −0.2 V, the current in HPO_4^{2-} exhibits a similar form to that observed in HCO_3^-/CO_3^{2-} but is considerably lower. On the reverse scan the size of the peaks for the reduction of surfaced oxidized layers are significantly enhanced in the HPO_4^{2-} solution indicating the presence of thicker oxidized surface layers. Integration of these plots to determine values of Q_A, Q_C and Q_D (= $Q_A - Q_C$) shows the development of a thicker surface layer is accompanied by a significant decrease in the extent of dissolution (2.3 mC cm^{-2} in HPO_4^{2-} compared to 5.9 mC cm^{-2} in HCO_3^-/CO_3^{2-}). This is not surprising since the solubility of U^{VI} is significantly lower in HPO_4^{2-}, the solubility product for uranyl orthophosphate $((U^{VI}O_2)_3(PO_4)_2(H_2O)_4$ being −49 to −53.3 compared to −13 to −15 for rutherfordine ($U^{VI}O_2CO_3$) [26].

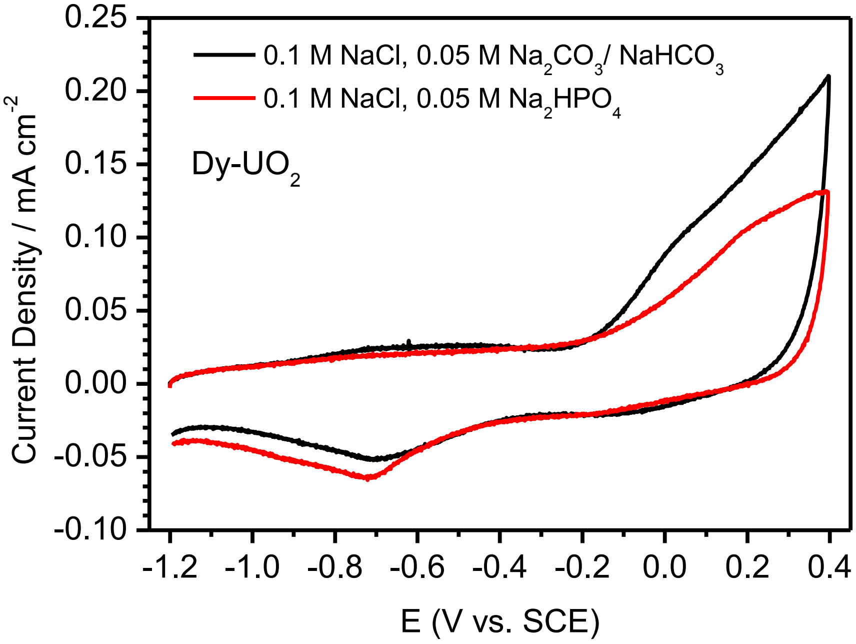

Figure 5.6: CVs recorded on Dy-UO$_2$ at a scan rate of 10 mV s^{-1} in 0.1 mol L^{-1} NaCl containing 0.05 mol L^{-1} of $[CO_3]_T$ or 0.05 mol L^{-1} $[PO_4]_T$ at pH = 10.

5.3.4 Potentiostatic Oxidation

To investigate film formation processes in more detail a series of potentiostatic oxidations (1 hour in duration) were performed in both solutions at various applied potentials over the range −0.9 V to 0.35 V, Figure 5.7. At low potentials the currents rapidly decay to very low values and are noisy. A better comparison can be made by comparing the charges obtained by integration of the current-time plots at these low potentials. Figure 5.8 compares the charges obtained in both solutions at

−0.4 V. In the HCO_3^-/CO_3^{2-} solution the charge is positive and increasing slowly indicating the occurrence of a slow oxidation process. By contrast, in the HPO_4^{2-} solution an initial slight oxidation is overcome by a linearly increasing cathodic charge indicating the electrode is supporting a cathodic reaction, with the reduction of H_2O being the only available option.

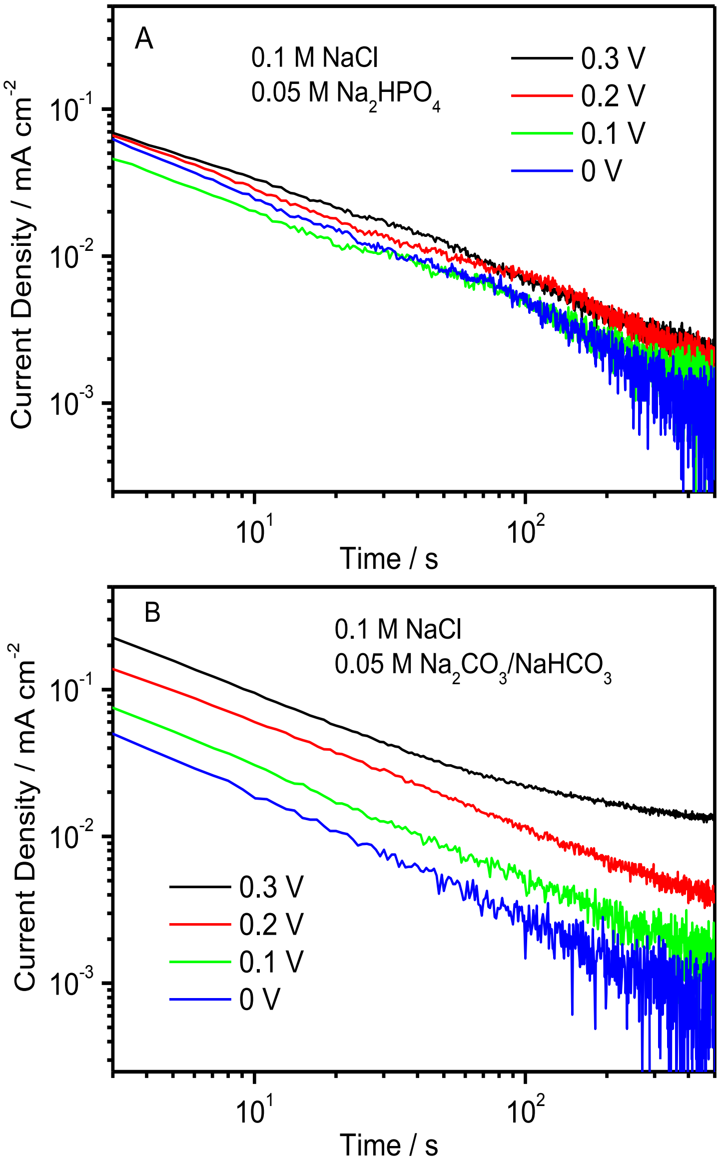

Figure 5.7: Potentiostatic current-time curves recorded on Dy-UO_2 for 1 hour in Ar-purged 0.1 mol L^{-1} NaCl with HPO_4^{2-} (A) ($[PO_4]_T$ = 0.05 mol L^{-1}) or HCO_3^-/CO_3^{2-} (B) ($[CO_3]_T$ = 0.05 mol L^{-1}), pH= 10. In both solutions the current becomes very noisy after 500 s and not shown for clarity.

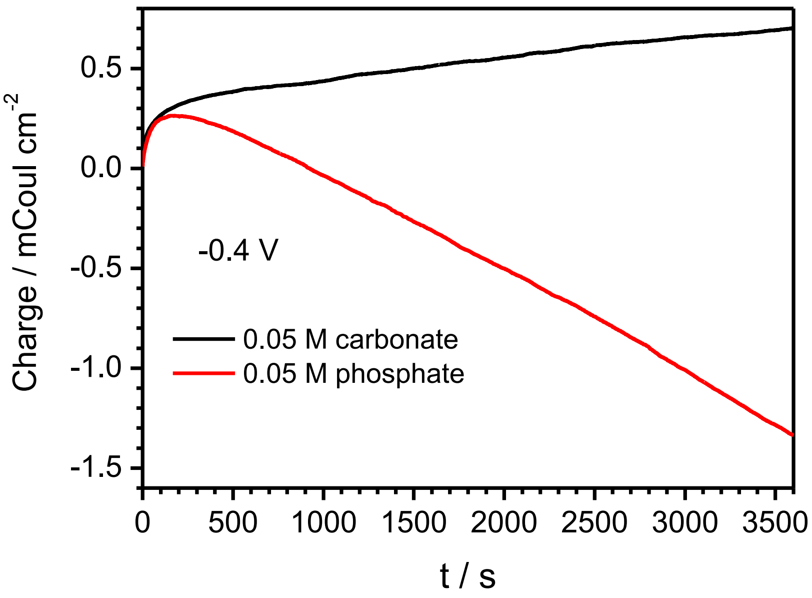

Figure 5.8: Charge as a function of time for potentiostatic polarization of Dy-UO_2 at −0.4 V in 0.1 mol L^{-1} NaCl + 0.05 mol L^{-1} $[CO_3]_T$ or $[PO_4]_T$ solutions.

At more positive potentials when both surface oxidation and anodic dissolution are anticipated (0 V to 0.3 V) the currents recorded in HCO_3^-/CO_3^{2-} and HPO_4^{2-} exhibit significant differences. In HCO_3^-/CO_3^{2-} solution (Fig. 5.7B), the currents are dependent on potential and decay with time. At low potentials (i.e., 0 V and 0.1 V) the current decreases linearly on a logarithmic scale consistent with the formation of a current-inhibiting surface oxide. At higher potentials (i.e., 0.2 V and 0.3 V) a similar linear decay in the logarithmic current-time plots is observed with the slope being the same at all potentials. This behaviour indicates formation of the $U^{IV}_{1-2x}U^{V}_{2x}O_{2+x}$ layer occurs at a potential independent rate with a steady-state potential-independent dissolution current. At the highest potential applied (0.3 V) the current approaches a steady-state value consistent with control of the overall anodic reaction process by the chemical dissolution rate of a surface $U^{VI}O_2CO_3$ film. In HPO_4^{2-}solution, the current also decays linearly on a log-log scale but is only marginally dependent on potential indicating the formation of the $U^{IV}_{1-2x}U^{V}_{2x}O_{2+x}$ layer occurs unaccompanied by significant dissolution. This claim is supported by the behaviour observed at longer times when the slope increases in contrast to the behaviour observed in HCO_3^-/CO_3^{2-} solution. This decrease has been observed previously on SIMFUEL in solutions with no added anions and attributed to the accumulation of a U^{VI} deposit [16]. In the HPO_4^{2-} solution this deposit would be uranyl phosphate.

5.3.5 XPS Analyses

Following potentiostatic oxidations, the electrode surfaces were analyzed by XPS. Examples of the fitted and deconvoluted spectra recorded at a number of potentials are shown in Figure 5.9. Although not shown the validity of the fitting and deconvolution process was confirmed by similarly fitting the U4f$_{5/2}$ peak and the satellite structures associated with these peaks.

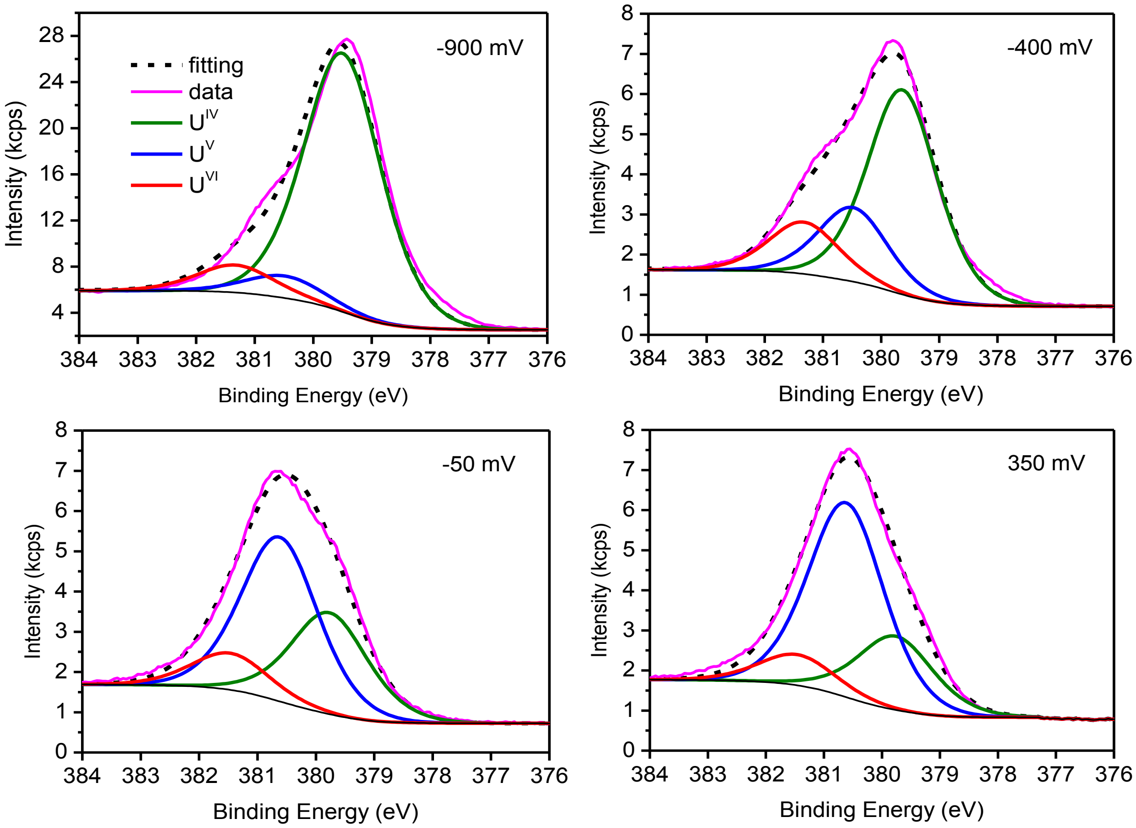

Figure 5.9: The U 4f$_{7/2}$ XPS peak resolved into contributions from U^{IV}, U^{V} and U^{VI} for surfaces anodically oxidized at −900, −400, −50 and 350 mV in 0.1 mol L^{-1} NaCl containing 0.05 mol L^{-1} $[CO_3]_T$ for 1 hour at pH = 10.

Figure 5.10 shows the fractions of all three oxidation states as a function of applied potential in

HCO_3^-/CO_3^{2-} solution. A number of regions of behaviour are observed. For potentials < −0.5 V the surface composition is dominated by U^{IV} with the content of oxidized states U^V/U^{VI} remaining very low. Although minor and not well resolved there appears to be a slight increase in the extent of oxidation of the surface over this potential range, consistent with the electrochemical oxidation of surface states indicated in the voltametric scan (Figures 5.1 and 5.5). Over the potential range −0.5 V to −0.2 V a clear oxidation of the surface is observed attributable to the formation of the $U^{IV}_{1-2x}U^V_{2x}O_{2+x}$ layer with the results in Figure 5.2 indicating the formation of this surface layer is not accompanied by significant dissolution. For potentials > −0.2 V (up to 0 V) the extent of oxidation of the surface increases markedly indicated by the more rapid increase in U^V content of the surface with potential with the results in Figure 5.2 showing this is accompanied by the onset of dissolution. Since the surface content of U^{VI} changes only marginally, as expected since it would be expected to dissolve as $U^{VI}O_2(CO_3)_2^{2-}$, this enhanced oxidation can be attributed to the thickening of the $U^{IV}_{1-2x}U^V_{2x}O_{2+x}$ layer in agreement with the increase in cathodic charge for film reduction, Figure 5.3.

A possible explanation for this coincidence in enhanced matrix oxidation and the onset of dissolution is that a potential of ~−0.2 V is a threshold for the onset of tetragonal lattice distortions leading to the destabilization of the fluorite lattice. That such a change occurs as the degree of non-stoichiometry increases has been demonstrated by Raman spectroscopy on specimens with different non-stoichiometries [25]. The transformation was found to occur at a composition of approximately $U^{IV}_{0.7}U^V_{0.3}O_{2+x}$ and involved the formation of defect clusters in the transformed lattice. In addition scanning electrochemical microscopy measurements on surface locations with different degrees of non-stoichiometry demonstrated that beyond an intermediate composition in this range the rate and depth of anodic oxidation increased markedly [27]. Figure 5.11 attempts to illustrate this transformation from shallow oxidation involving randomly distributed O_Is to deeper oxidation involving the formation of defect clusters accompanied by dissolution.

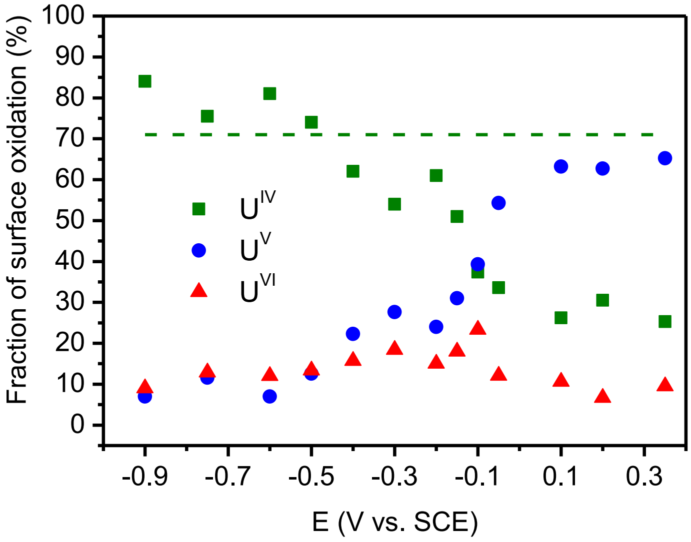

Figure 5.10: Relative fractions of U oxidation states as a function of applied potential recorded on Dy-UO$_2$ after 1 h oxidation in 0.1 mol L^{-1} NaCl + 0.05 mol L^{-1} [CO$_3$]$_T$ at pH = 10. The dash line shows the fraction of U^{IV} on a freshly polished Dy-UO$_2$ surface.

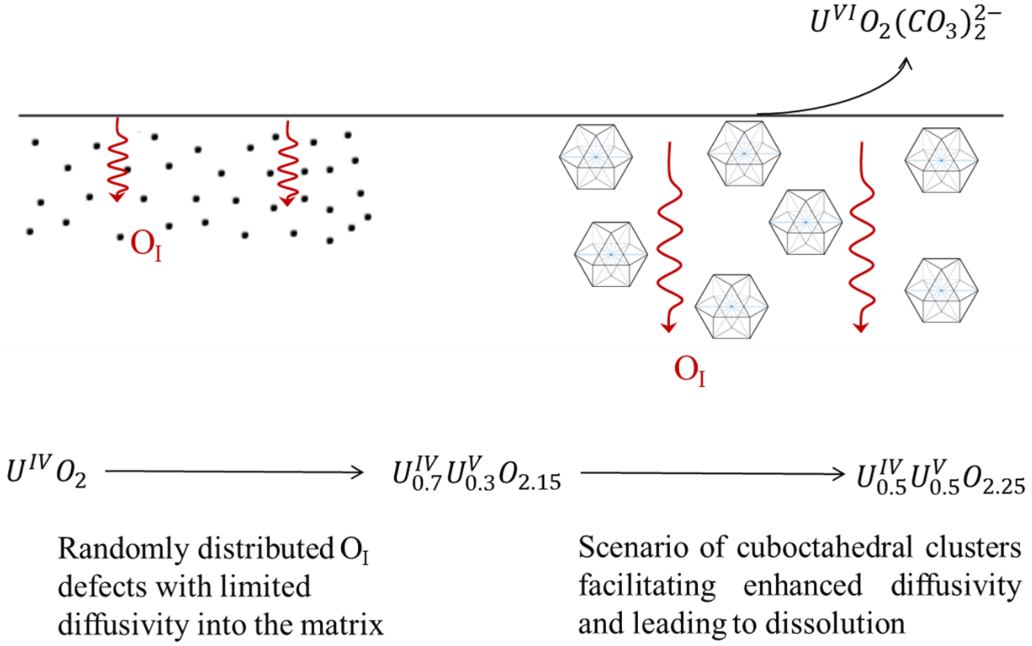

Figure 5.11: Schematic illustrating the influence of major tetragonal distortions leading to the extensive formation of cuboctahedral clusters and the onset of dissolution.

Figure 5.12 compares the U^{IV}, U^{V} and U^{VI} contents of the surface in HCO_3^{-}/CO_3^{2-} and HPO_4^{2-} solutions with representative examples of fitted spectra shown in Figure 5.13. There are a number of regions in which the behaviour is different in the two solutions. In the potential range −0.6 V to −0.3 V the extent of oxidation of the surface in HPO_4^{2-} is considerably lower than in HCO_3^{-}/CO_3^{2-}. This difference is predominantly in the U^{IV} and U^{V} contents, the U^{VI} contents of the surface being identical and low, and may reflect the ability of HCO_3^{-}/CO_3^{2-} to enhance surface oxidation by stabilizing the U^{V} state. This would be consistent with the demonstrated ability of HCO_3^{-}/CO_3^{2-} to stabilize this oxidation state against disproportionation to U^{IV} and $U^{VI}O_2^{2+}$ in solution [28].

At potentials > −0.2 V the U^{V} content of the surface is also considerably higher after oxidation in HCO_3^{-}/CO_3^{2-} but that of U^{VI} markedly lower, Figure 5.12. This is consistent with the electrochemical results which demonstrate enhanced dissolution of the U^{VI} state in HCO_3^{-}/CO_3^{2-} but the suppression of dissolution by the accumulation of insoluble U^{VI} in the HPO_4^{2-} solution. The threshold around −0.2 V for the introduction of tetragonal distortions leading to anodic dissolution is obscured in the HPO_4^{2-} solution by the suppression of the formation of the $U^{IV}_{1-2x}U^{V}_{2x}O_{2+x}$ layer at low potentials and the more rapid conversion of this layer to $U^{VI}O_2HPO_4$ at higher potentials.

At the highest potentials (0.3 V and 0.35 V) the surface achieves a steady-state composition in HCO_3^{-}/CO_3^{2-} with a high U^{V} and low U^{VI} content confirming that that anodic dissolution as $U^{VI}O_2(CO_3)_2^{2-}$ occurs on a $U^{IV}_{1-2x}U^{V}_{2x}O_{2+x}$ surface with a potential-independent composition. In the case of HPO_4^{2-} a slight increase in U^{VI} and marked decrease in U^{V} is accompanied by an increase in U^{IV} suggesting a conversion of the U^{V} in the $U^{IV}_{1-2x}U^{V}_{2x}O_{2+x}$ layer to U^{VI}.

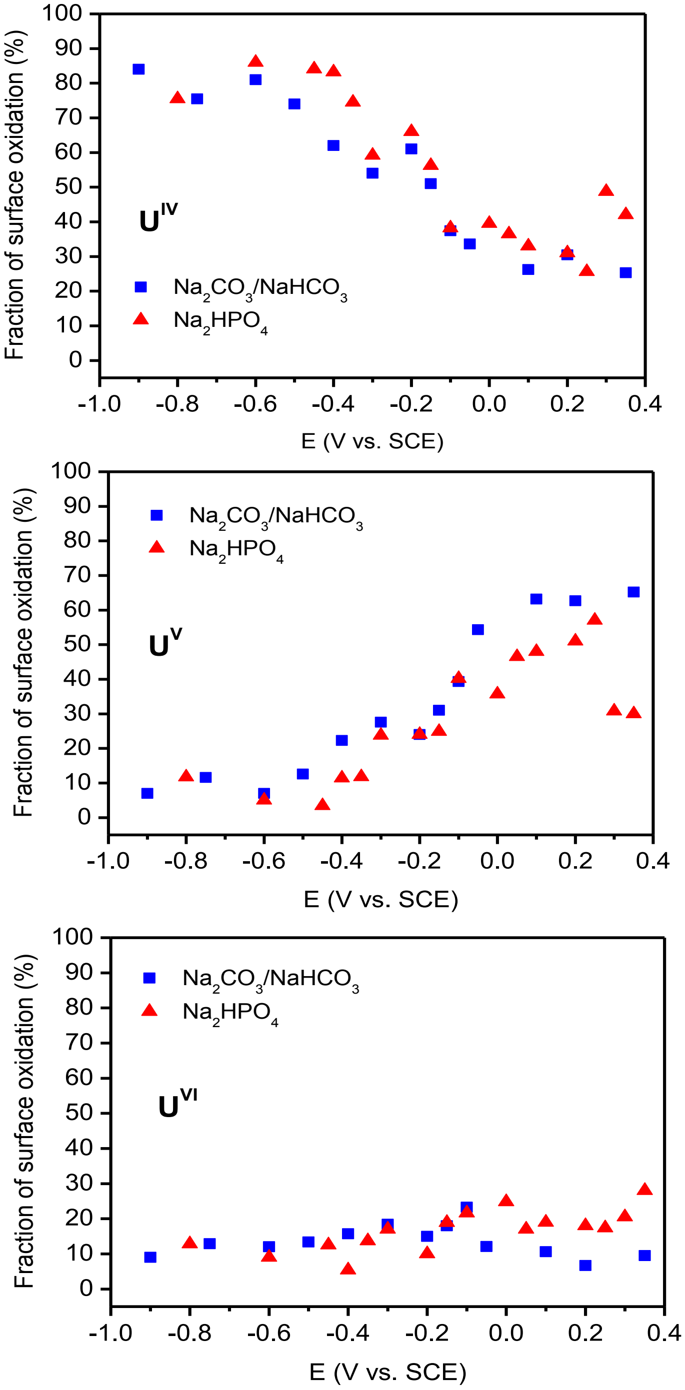

Figure 5.12: Relative fractions of U oxidation states as a function of applied potential recorded for Dy-UO$_2$ after 1 hour oxidation in 0.1 mol L^{-1} NaCl + 0.05 mol L^{-1} [CO$_3$]$_T$ or [PO$_4$]$_T$ solutions at pH = 10.

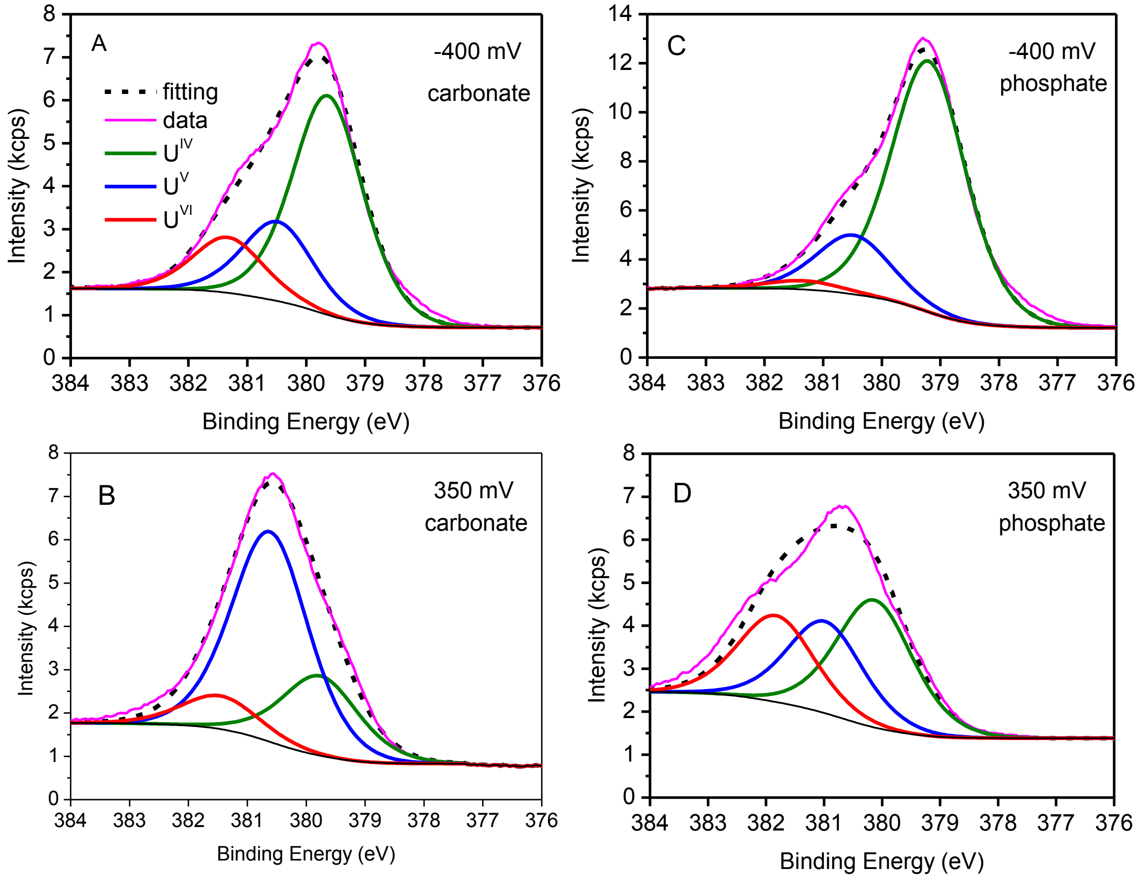

Figure 5.13: The U 4f$_{7/2}$ XPS peak resolved into contributions from U^{IV}, U^{V} and U^{VI} for surfaces anodically oxidized at −400 and 350 mV in 0.1 mol L^{-1} NaCl containing 0.05 mol L^{-1} [CO$_3$]$_T$ (A, B) or [PO$_4$]$_T$ (C, D) for 1 hour at pH = 10.

5.3.6 Cathodic Stripping Voltammetry

Figure 5.14 shows cathodic stripping voltammograms (CSV) recorded after potentiostatic oxidations for 1 hour at various potentials. That oxidation is either enhanced by HCO_3^-/CO_3^{2-} or suppressed by HPO_4^{2-} is confirmed by the smaller cathodic reduction peak observed in HPO_4^{2-} after anodic oxidation at –0.2 V, Figure 5.14A. An increase in oxidation potential to 0 V (Figure 5.14B) shows that peak 2 (resolved here only as a shoulder) for the reduction of a U^{VI} layer is enhanced in HPO_4^{2-} consistent with the XPS results. As the potential is increased further (Figure 5.14C and D) the charge associated with the reduction of surface oxides changes only slightly in HCO_3^-/CO_3^{2-} as expected since the U^{VI} formed is readily dissolved. In the HPO_4^{2-} solution the current associated with peak 2 (reduction of U^{VI} deposits) is enhanced relative to that for peak 1 (reduction of $U^{IV}_{1-2x}U^{V}_{2x}O_{2+x}$) as expected since U^{VI} is insoluble in this solution. This change in the relative contributions from peaks 1 and 2 may also reflect the transformation of U^{V} in the $U^{IV}_{1-2x}U^{V}_{2x}O_{2+x}$ layer indicated by the XPS analyses after oxidation at potentials in this region or higher.

The origin of the small peak at ~−0.2 V is uncertain but it may be due to the reduction of adsorbed intermediates involved in the anodic reaction or to the retention of dissolved U^{VI} within rough locations on the electrode surface. The much larger current at the negative potential limit of the CSV in HPO_4^{2-} can be attributed to enhanced reduction of H_2O in this solution. The reasons for this enhancement are unclear but it precludes any quantitative comparison of film thicknesses in the two solutions.

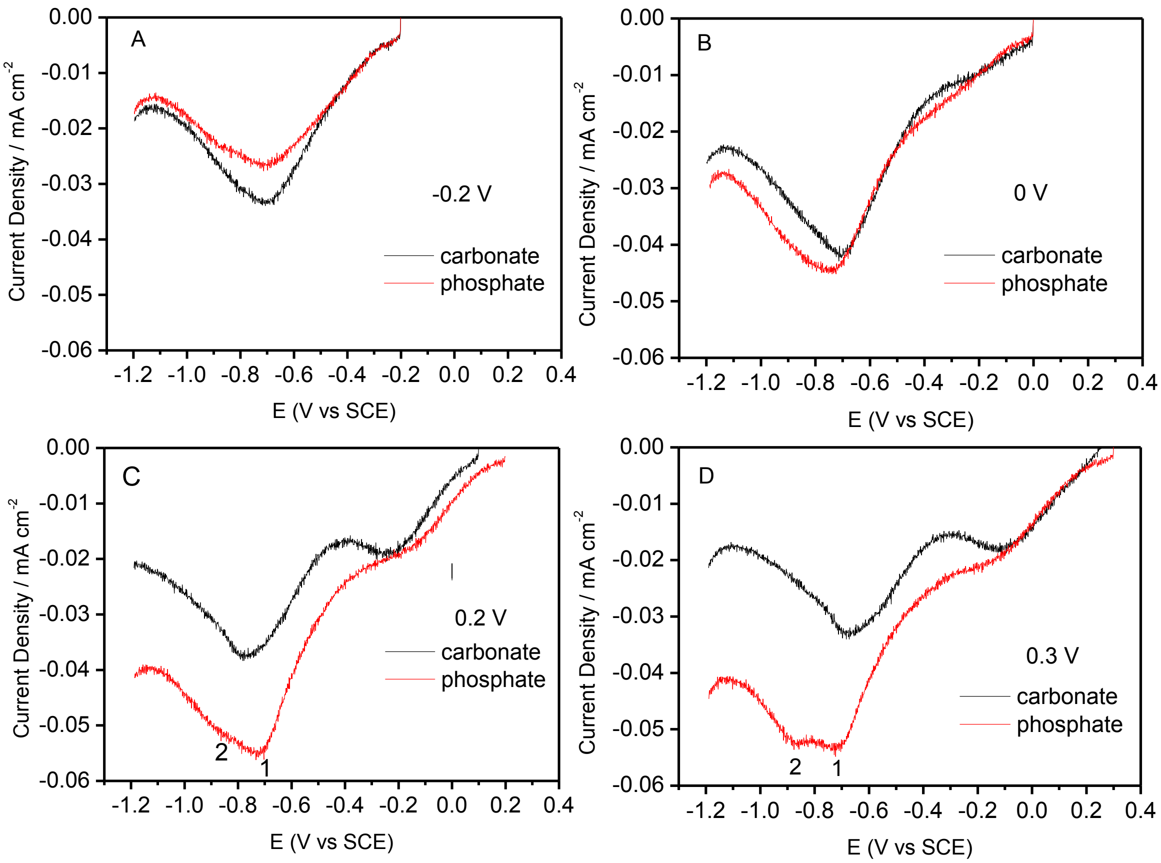

Figure 5.14: Cathodic stripping voltammograms (CSV) recorded on Dy-UO_2 after potentiostatic polarization for 1 hour at various potentials (−0.2, 0, 0.2 and 0.3 V) in an Ar-purged 0.1 mol L^{-1} NaCl solution with 0.05 mol L^{-1} $[CO_3]_T$ or $[PO_4]_T$, pH = 10.

5.4 Summary and Conclusions

A comparison of the anodic reactivity of the close-to-stoichiometric $UO_{2.002}$, SIMFUEL and Gd-doped and Dy-doped UO_2 specimens showed that rare earth doping stabilized the matrix against oxidation to $U^{IV}_{1-2x}U^{V}_{2x}O_{2+x}$ and its further oxidation to soluble U^{VI}. Once dissolution occurs the order of reactivity is $UO_{2.002}$ > SIMFUEL > Gd-UO_2 > Dy-UO_2. For $UO_{2.002}$ the composition is non-uniform with some surface locations being more non-stoichiometric and, hence, more reactive than others.

For the RE^{III}-doped UO_2 the onset of matrix dissolution is accompanied by the enhanced oxidation of the matrix to $U^{IV}_{1-2x}U^{V}_{2x}O_{2+x}$. This can be attributed to the onset of tetragonal lattice distortions as oxidation proceeds which leads to the clustering of defects, enhanced diffusion of O_I to deeper locations and destabilization of the fluorite lattice.

HCO_3^-/CO_3^{2-} and HPO_4^{2-} have significantly different effects on the matrix oxidation and dissolution processes. At low potentials HPO_4^{2-} suppresses matrix oxidation compared to the behaviour in HCO_3^-/CO_3^{2-}. This may be related to the ability of HCO_3^-/CO_3^{2-} to stabilize the U^V state. At higher potentials the oxidation to U^{VI} is promoted by HPO_4^{2-} but, compared to the behavior in HCO_3^-/CO_3^{2-}, dissolution is suppressed by the formation of an insoluble uranyl phosphate layer.

5.5 Reference

[1] H. He, M. Broczkowski, K. O’Neil, D. Ofori, O. Semenikhin, D.W. Shoesmith, Corrosion of Nuclear Fuel (UO_2) Inside a Failed Nuclear Waste Container, Report NWMO TR-2012-09, Nuclear Waste Management Organization, Toronto, ON, 2012.

[2] R.J. McEachern, P. Taylor, A Review of the Oxidation of Uranium Dioxide at Temperatures below 400°C, J. Nucl. Mater. 254 (1998) 87-121.

[3] L.E. Thomas, R.E. Einziger, H.C. Buchanan, Effect of Fission Products on Air-oxidation of LWR Spent Fuel, J. Nucl. Mater. 201 (1993) 310-319.

[4] J. Choi, R.J. McEachern, P. Taylor, D.D. Wood, The Effect of Fission Products on the Rate of U_3O_8 Formation in SIMFUEL Oxidized in Air at 250°C, J. Nucl. Mater. 230 (1996) 250-258.

[5] J.-G. Kim, Y.-K. Ha, S.-D. Park, K.-Y. Jee, W.-H. Kim, Effect of a Trivalent Dopant, Gd^{3+}, on the Oxidation of Uranium Dioxide, J. Nucl. Mater. (2001) 327-331.

[6] Z. Talip, T. Wiss, P.E. Raison, J. Paillier, D. Manara, J. Somers, R.J.M. Konings, Raman and

X-ray Studies of Uranium-Lanthanum-Mixed Oxides Before and After Air Oxidation, J. Am. Ceram. Soc. 98 (2015) 2278-2285.

[7] M. Razdan, D.W. Shoesmith, The Electrochemical Reactivity of 6.0 wt% Gd-Doped UO_2 in Aqueous Carbonate/Bicarbonate Solutions, J. Electrochem. Soc. 161 (2014) H225-H234.

[8] M. Razdan, D.W. Shoesmith, Influence of Trivalent-Dopants on the Structural and Electrochemical Properties of Uranium Dioxide (UO_2), J. Electrochem. Soc. 161 (2014) H105-H113.

[9] P.G. Boczar, J. Griffiths, I.J. Hastings, Extended Burnup in CANDU, AECL Research, Chalk River, Ontario, CA, 1991.

[10] H. He, Z. Qin, D.W. Shoesmith, Characterizing the Relationship between Hyperstoichiometry, Defect Structure and Local Corrosion Kinetics of Uranium Dioxide, Electrochim. Acta 56 (2010) 53-60.

[11] L. Desgranges, G. Baldinozzi, P. Simon, G. Guimbretière, A. Canizares, Raman Spectrum of U_4O_9: a New Interpretation of Damage Lines in UO_2, J. Raman Spectrosc. 43 (2012) 455-458.

[12] J. McMurry, Reference Water Compositions for a Deep Geological Repository in the Canadian Shield, Report 06819-REP-01200-10135-R01, Ontario Power Generation, Toronto, ON, 2004.

[13] D.W. Shoesmith, Fuel Corrosion Processes under Waste Disposal Conditions, J. Nucl. Mater. 282 (2000) 1-31.

[14] D.W. Shoesmith, Used Fuel and Uranium Dioxide Dissolution Studies – A Review, report NWMO TR-2007-03, Nuclear Waste Management Organization, Toronto, ON, 2007.

[15] P.G. Lucuta, R.A.Verrall, Hj. Matzke, B.J. Palmer, Microstructural Features of SIMFUEL - Simulated high burnup UO_2-based nuclear fuel, J. Nucl. Mater. 178 (1991) 48-60.

[16] B.G. Santos, H.W. Nesbitt, J.J. Noël, D.W. Shoesmith, X-ray Photoelectron Spectroscopy Study of Anodically Oxidized SIMFUEL Surfaces, Electrochim. Acta 49 (2004) 1863-1873.

[17] F. King, M.J. Quinn, N.H. Miller, The Effect of Hydrogen and Gamma Radiation on the Oxidation of UO_2 in 0.1 M NaCl solution, Report TR-99-27, Swedish Nuclear Fuel and Waste Management Co (SKB), Stockholm, 1999.

[18] M. Razdan, D.S. Hall, P.G. Keech, D.W. Shoesmith, Electrochemical reduction of hydrogen peroxide on SIMFUEL (UO_2) in acidic pH conditions, Electrochim. Acta 83 (2012) 410-419.

[19] K.D. O'Neil, H. He, P. Keech, D.W. Shoesmith, O.A. Semenikhin, Anisotropy of Local Electrical Conductivity of Hyper-stoichiometric Uranium Dioxide Revealed by Current-sensing Atomic Force Microscopy (CS-AFM), Electrochem. Commun. 10 (2008) 1805-1808.

[20] K.D. O'Neil, B. Shaw, O.A. Semenikhin, On the Origin of Mesoscopic Inhomogeneity of Conducting Polymers, J. Phys. Chem. B 111 (2007) 9253-9269.

[21] B.G. Santos, J.J. Noël, D.W. Shoesmith, The Effect of pH on the Anodic Dissolution of

SIMFUEL (UO_2), J. Electroanal. Chem. 586 (2006) 1-11.

[22] P.G. Keech, J.S. Goldik, Z. Qin, D.W. Shoesmith, The Anodic Dissolution of SIMFUEL (UO_2) in Slightly Alkaline Sodium Carbonate/bicarbonate Solutions, Electrochim. Acta 56 (2011) 7923-7930.

[23] H. He, R. Zhu, Z. Qin, P.G. Keech, Z. Ding, D.W. Shoesmith, Determination of Local Corrosion Kinetics on Hyper-Stoichiometric UO_{2+x} by Scanning Electrochemical Microscopy, J. Electrochem. Soc. 156 (2009) C87-C94.

[24] H.Y. Geng, Y. Chen, Y. Kaneta, M. Iwasawa, T. Ohnuma, M. Kinoshita, Point Defects and Clustering in Uranium Dioxide by LSDA+U Calculations, Phys. Rev. B 77 (2008) 104120.

[25] H. He, D.W. Shoesmith, Raman Spectroscopic Studies of Defect Structures and Phase Transition in Hyper-stoichiometric UO_{2+x}, Phys. Chem. Chem. Phy. 12 (2010) 8108-8117.

[26] D. Gorman-Lewis, P.C. Burns, J.B. Fein, Review of Uranyl Mineral Solubility Measurements, J. Chem. Thermodyn. 40 (2008) 335-352.

[27] H. He, Z. Ding, D.W. Shoesmith, The Determination of Electrochemical Reactivity and Sustainability on Individual Hyper-stoichiometric UO_{2+x} Grains by Raman Microspectroscopy and Scanning Electrochemical Microscopy, Electrochem. Commun. 11 (2009) 1724-1727.

[28] K. Mizuoka, I. Grenthe, Y. Ikeda, Structural and Kinetic Studies on Uranyl(V) Carbonate Complex Using ^{13}C NMR Spectroscopy, Inorg. Chem. 44 (2005) 4472-4474.

Chapter 6

6 Influence of Gd Doping on the Structure and Electrochemical Behavior of UO_2

6.1 Introduction

As discussed in chapter 5, the reactivity of the UO_2 matrix, and how it is modified by in-reactor irradiation, is important in determining fuel corrosion. One of the key changes likely to influence the chemical reactivity of the fuel is the rare earth (RE) doping of the matrix [1]. In chapter 5, the electrochemical reactivity of Dy_2O_3 (12.9 wt%) doped UO_2 is compared with Gd_2O_3 (6.0 wt%) doped UO_2, 1.5 at% SIMFUEL and $UO_{2.002}$. The Q_d (dissolution charge) values for the doped materials decrease in the order of SIMFUEL > Gd-UO_2 > Dy-UO_2, which is in the order of an increasing doping level.

Since all rare earth dopants are not expected to have an identical effect on UO_2, in this chapter, a series of $(U_{1-y}Gd_y)O_2$ materials (y = 0, 0.01, 0.03, 0.05, 0.07 and 0.10) are synthesized, characterized by XRD and Raman spectroscopy and the reactivity of the $(U_{1-y}Gd_y)O_2$ matrix investigated electrochemically. Since the key groundwater constituents likely to influence fuel dissolution are HCO_3^-/CO_3^{2-}, which will increase UO_2^{2+} solubility by complexing UO_2^{2+} [2], these studies are conducted in solutions containing HCO_3^-/CO_3^{2-}.

6.2 Experimental

6.2.1 Electrode Material and Preparation

$U_{1-y}Gd_yO_2$ pellets with various compositions (y = 0, 0.01, 0.03, 0.05, 0.07 and 0.10) were synthesized using a conventional solid-state process involving the mixing of oxide powders. Appropriate amounts of UO_2 and Gd_2O_3 (Aldrich, > 99.99%) powder were mixed and thoroughly blended in an agar mortar. The blended powders were then pressed into a disk-shaped pellet and sintered at 1700ºC for 18 h in a reducing atmosphere with flowing hydrogen. The sintered pellets were then cooled to room temperature in flowing hydrogen after annealing in the same atmosphere at 1200ºC for 12 h.

6.2.2 X-ray Diffraction

The X-ray diffraction (XRD) patterns of the pellets were measured with a Bruker AXS D8 Advance X-ray Diffractometer using Cu K_α radiation at room temperature. XRD data were collected from several locations on the sintered pellets to confirm the homogeneity in structure. The lattice parameters of the solid solution samples were determined over the 2θ range from 20° to 120° with 0.02° step size. The lattice parameters of the samples were calculated by a refinement process using the TOPAS program (Bruker Analytical X Ray Systems) with the $Fm\bar{3}m$ space group.

6.2.3 Raman Spectroscopy

The Raman spectroscopic measurements were carried out with an ANDOR Shamrock SR303i spectrometer, with active vibrations excited using a He-Ne laser with a wavelength of 632.8 nm. The laser, with a power of ~5mW, was focused onto the pellets using an Olympus microscope with a 50-fold magnification lens. This laser power was confirmed to be low enough to prevent surface oxidation of the pellets due to local heating effects by the laser beam. Raman spectra were acquired over the wavenumber range from 400 to 1200 cm^{-1} using an exposure time of 300 s. Spectra were collected from different locations on the surface of pellets to confirm their reproducibility and the homogeneity of composition.

6.2.4 Electrochemical Cell and Equipment

Experiments were performed in a standard three-electrode cell. A commercial saturated calomel reference electrode (SCE) (+0.242 V, 25°C vs. standard hydrogen electrode (SHE)) was used, and a Pt wire with a spot-welded Pt foil was employed as the counter electrode. All potentials were quoted on the SCE scale. All electrochemical experiments were carried out using a CHI-600D potentiostat to control applied potentials and record current responses.

6.2.5 Electrochemical Procedure

Prior to experiments, electrodes were prepared by polishing using wet 3000 grit SiC paper and rinsed with distilled deionized water. Subsequently, the electrodes were electrochemically reduced at −1.2 V for 5 min (vs. SCE) to remove any air-formed oxides or organic contaminants present on the surface. Before each measurement, the resistance of the system (mainly from the electrode and solution) was tested. At the test potential, no electrochemical reaction should occur. When the system was performing the test, it applied a potential step relative to the test potential, the test was passed only if the electrochemical cell can be considered equivalent to a solution resistance in series with a double layer capacitor. The resistance measured from the test was then compensated by the potentiostat in the following experiment.

6.2.6 Solution Preparation

Solutions were prepared using distilled deionized water (resistivity $\rho = 18.2$ MΩ·cm) purified using a Millipore Milli-Q plus unit which removes organic and inorganic impurities. The base electrolyte was 0.1 mol L^{-1} NaCl (Aldrich). The HCO_3^-/CO_3^{2-} concentrations were adjusted with Na_2CO_3 and $NaHCO_3$ (Aldrich). The total carbonate concentration ($[CO_3]_T = [HCO_3^-] + [CO_3^{2-}]$) was 0.05 mol L^{-1} with the pH maintained constant at 10 using an Orion model 720A pH meter. Prior to an experiment the solution in the cell was purged with Ar-gas (Shinhan Gas) for an hour and purging was then maintained throughout the experiment.

6.3 Results and Discussion

6.3.1 Surface Morphology

Figure 6.1 shows that the morphology of the surface for $U_{1-y}Gd_yO_2$ changes as the doping level increases from 0 to 3% but then remains unchanged up to 7%. Also a number of voids are visible on the surface, introducing the possibility that the reactivity may not be totally uniform.

6.3.2 XRD Analysis

The XRD patterns (not shown here) show that the specimens retain the fluorite structure and no XRD peaks for the monoclinic Gd_2O_3 impurity [3]. Figure 6.2 compares the lattice parameter as a function of Gd determined in this study with those measured by Kim [4], Ohmichi [5] and Baena [6]. The lattice parameter decreases as the Gd doping level increases. The lattice contraction could be caused by one or other (or both) of two charge compensation mechanisms; one involves the creation of U^V (the radius of U^{5+} ion (r = 0.088 nm) is smaller than that of the U^{4+} ion (0.1001 nm)), and the other the formation of (O_v)s (O_v: oxygen vacancy). He et al. studied the influence of fission product doping on the structure of SIMFUELs [7]. As the doping level increased, the XPS data indicated an increase in U^V content, while deconvolution of the Raman spectra indicated the increasing formation of RE^{III}-O_v clusters, suggesting either both charge compensation mechanisms are operative or they cannot be distinguished in SIMFUELs. Compared with the results of Ohmichi [5] and Baena [6], this work yields a slightly larger lattice parameter (Fig. 6.2), which could be attributable to a slight hypo-stoichiometry of our specimens [5]. According to the relationship between the degree of hypo-stoichiometry x (in $U_{1-y}Gd_yO_{2-x}$) and the lattice parameter (*a*) proposed by Ohmichi [5] (Eq. 6.1),

$$\frac{da}{dx} = 0.024 \pm 0.006\,(\text{nm}) \tag{6.1}$$

the degree of hypo-stoichiometry (x in $U_{1-y}Gd_yO_{2-x}$) in our specimens could be between 0.012 (y = 0) and 0.025 (y = 0.1).

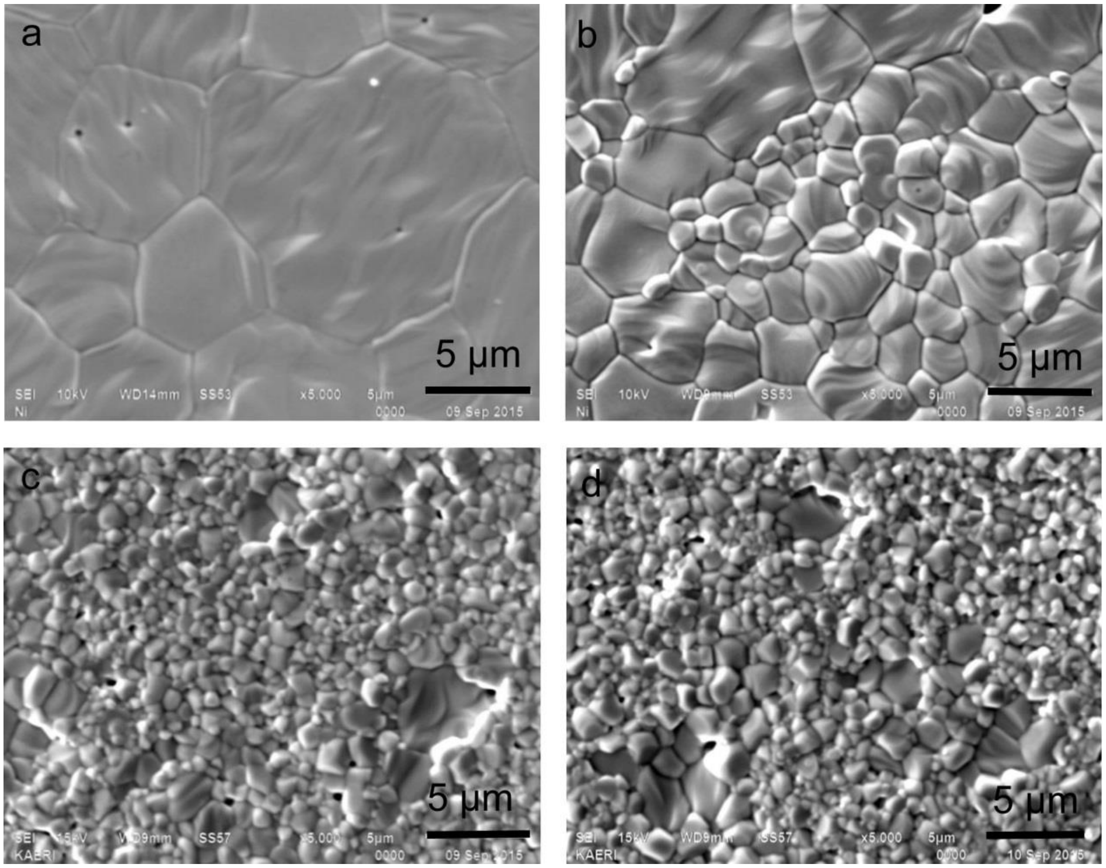

Figure 6.1: SEM images recorded on $U_{1-y}Gd_yO_2$ specimens (a, y = 0; b, y = 0.01; c, y = 0.03 and d, y = 0.07).

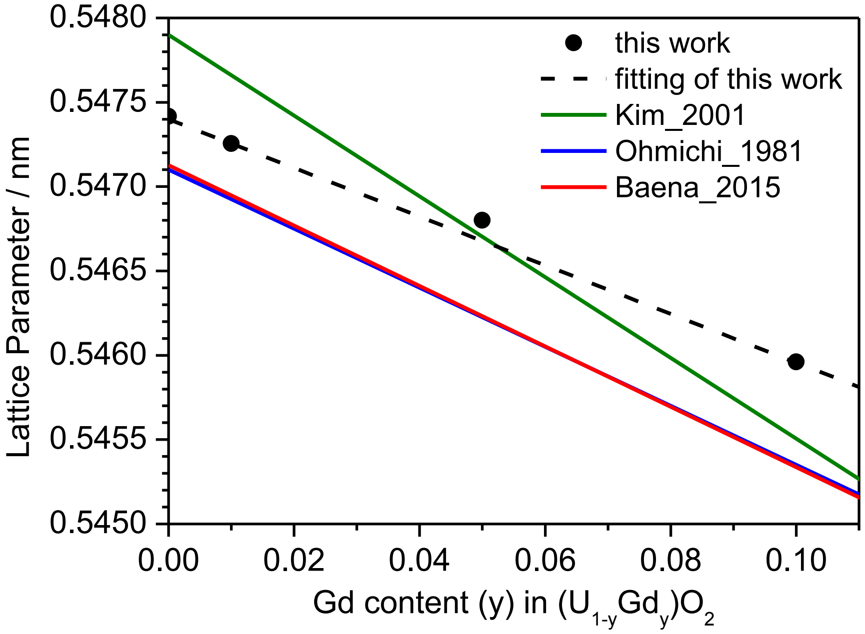

Figure 6.2: Lattice parameter of $U_{1-y}Gd_yO_2$ specimens as a function of Gd content.

6.3.3 Raman Spectroscopy

Raman spectroscopy has been commonly used to investigate the structure of the U-O system [7-13]. UO_2 has a cubic fluorite structure and belongs to the space group O_h ($Fm\bar{3}m$) and should generate a triply degenerate Raman active (T_{2g}) mode at ~445 cm^{-1}, assigned to the O-U stretch, and a band at ~1150 cm^{-1}, assigned as an overtone (2L-O) of the first order L-O phonon (~575 cm^{-1}). It has been suggested that the band at ~1150 cm^{-1} can be taken as a fingerprint for the quasi-perfect fluorite structure since its intensity decreases considerably as the defect structure due to increasing non-stoichiometry develops [12].

Figure 6.3 shows the Raman spectra of the $U_{1-y}Gd_yO_2$ specimens (y = 0, 0.01, 0.05 and 0.07). While all four exhibit a similar structure, the relative peak intensities differ considerably. For UO_2 (Fig. 6.3a), the peaks at 450 cm^{-1} and 1150 cm^{-1} are dominant compared to the broad band between 500-700 cm^{-1}, indicating the lattice is relatively defect free. As the extent of Gd doping increases, the relative intensity of the two bands at 445 cm^{-1} and 1150 cm^{-1} decrease with respect to the broad band (between 500-700 cm^{-1}), which has been attributed to UO_2 lattice damage, due to the formation of the defects caused by doping [7].

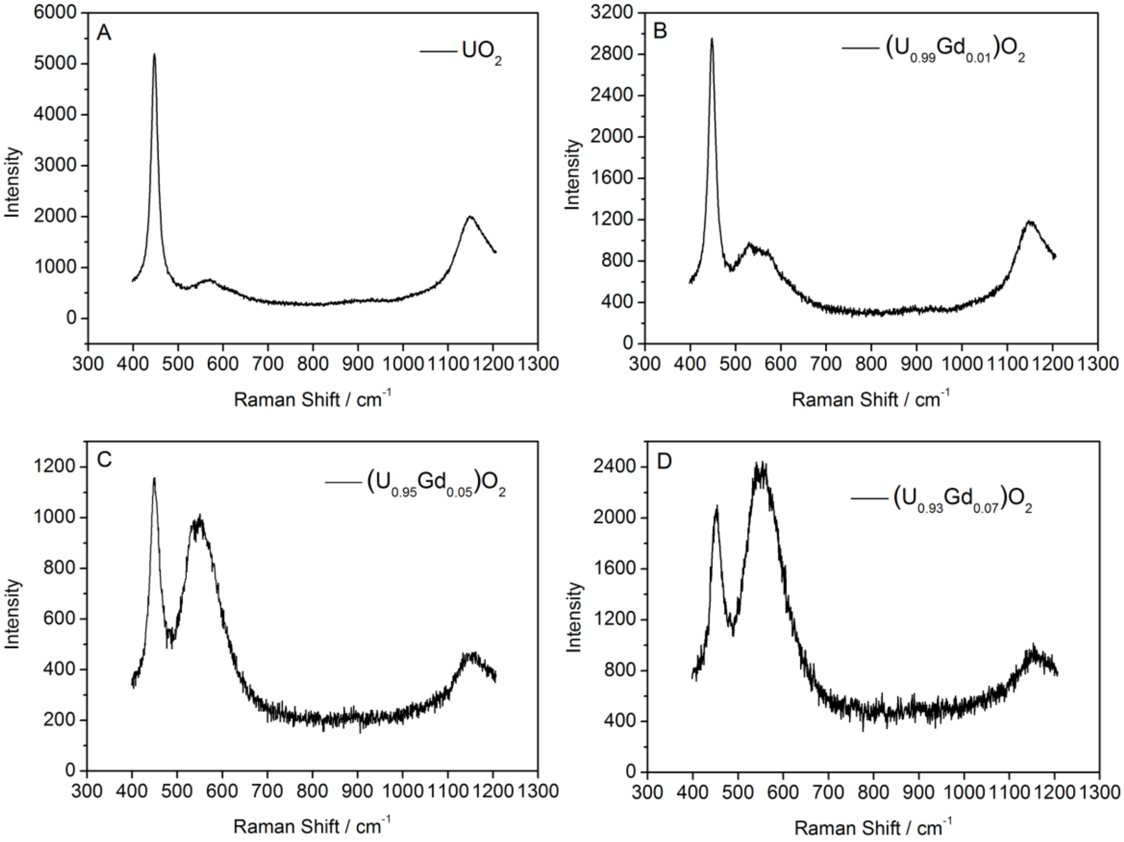

Figure 6.3: Raman spectra recorded on $U_{1-y}Gd_yO_2$ specimens (a, $y = 0$; b, $y = 0.01$; c, $y = 0.05$ and d, $y = 0.07$).

Li et al. [14] studied the defect sites for a series of dopants in $Ce_{0.8}M_{0.2}O_{2-\delta}$ solid solutions (CeO_2 has a similar fluorite lattice to UO_2) using Raman spectroscopy, and investigated the effects of different valence state and ionic radius of the dopants on the spectral features of these materials. A peak at ~560 cm^{-1}, observed on $Ce_{0.8}Pr_{0.2}O_{2-\delta}$ was assigned to the creation of oxygen vacancies (O_v), due to the difference in ionic valence states between Pr^{n+} (n = 3-4) and Ce^{4+}, because Pr^{n+} having a similar average ionic radius to Ce^{4+}. A peak at ~600 cm^{-1}, observed on $Ce_{0.8}Zr_{0.2}O_{2-\delta}$ was assigned to the formation of a ZrO_8-type complex, Zr^{4+} (0.084 nm) and Ce^{4+} (0.097 nm) having very different ionic radii. For $Ce_{0.8}Gd_{0.2}O_{2-\delta}$, two bands are observed simultaneously at approximately 560 and 600 cm^{-1}, suggesting the presence of both defect structures when both the oxidation state and the ionic radius of the dopant differ from that of the matrix cation. He et al.

studied the defect structures of hyper-stoichiometric UO_{2+x} using Raman spectroscopy [8], and demonstrated that a band at 630 cm^{-1} became increasingly more prominent as the O defect content increased. This 630 cm^{-1} band was assigned to the A_{1g} stretch due to the formation of cuboctahedral clusters. This assignment was confirmed by Desgranges et al [10]. Talip et al. [15] studied the La doped UO_2 and assigned the 630 cm^{-1} band to the formation of U_4O_9 under oxidation conditions.

The deconvolution of the broad band in our spectra is shown in Fig. 6.4. The 450 cm^{-1} peak is treated as Lorentzian while those at 540, 575 and 620 cm^{-1} are treated as Gaussian. The peak at 540cm^{-1} is not observed in UO_2 (Fig. 6.4a) but increases as the doping level increases, confirming it can be assigned to the creation of Gd^{III}- oxygen vacancy (O_v) clusters. The presence of O_v in UO_2 is consistent with the calculations of Park [15] and the observations of Desgranges who attributed a peak at this wavenumber (recorded on Nd-doped UO_2) to a local phonon mode associated with O_v-induced lattice distortion [16]. The intensity of the peak at 620 cm^{-1} also increases as the doping level increases suggesting the possible presence of MO_8-type complexes as claimed by Li et al. [14] when Gd was the dopant. As noted above the peak at 575 cm^{-1} is due to the first order L-O phonon and is associated with the close to perfect fluorite lattice.

Figure 6.5 shows the area ratios of the peak at 540, 575 and 620 cm^{-1} versus the T_{2g} peak (450 cm^{-1}). Since the T_{2g} peak is characteristic of the undisturbed fluorite lattice and the 540 cm^{-1} peak is related to the creation of O_v associated with the Gd^{III} doping, the ratio increases as the doping level increases. A similar trend in area ratio between the 620 cm^{-1} peak and the T_{2g} peak suggests an increase in importance of MO_8-type complexes as the lattice is disturbed by the Gd^{III} doping. The alternative assignment that a peak in this spectral region can be assigned to a hyperstoichiometric cuboctahedral cluster can be ruled out in our specimens which are close to stoichiometric and possibly slightly hypostoichiometric. The peak at 575 cm^{-1} was shown to be independent of doping level in a series of SIMFUELs investigated previously [7], however, in this study, the area ratio (A_{575}/A_{450}) increases as the doping level increases, which can be explained as a breakdown in selection rules as the presence of defects increases, making the forbidden first order L–O Raman scattering mode (575 cm^{-1}) allowed [8].

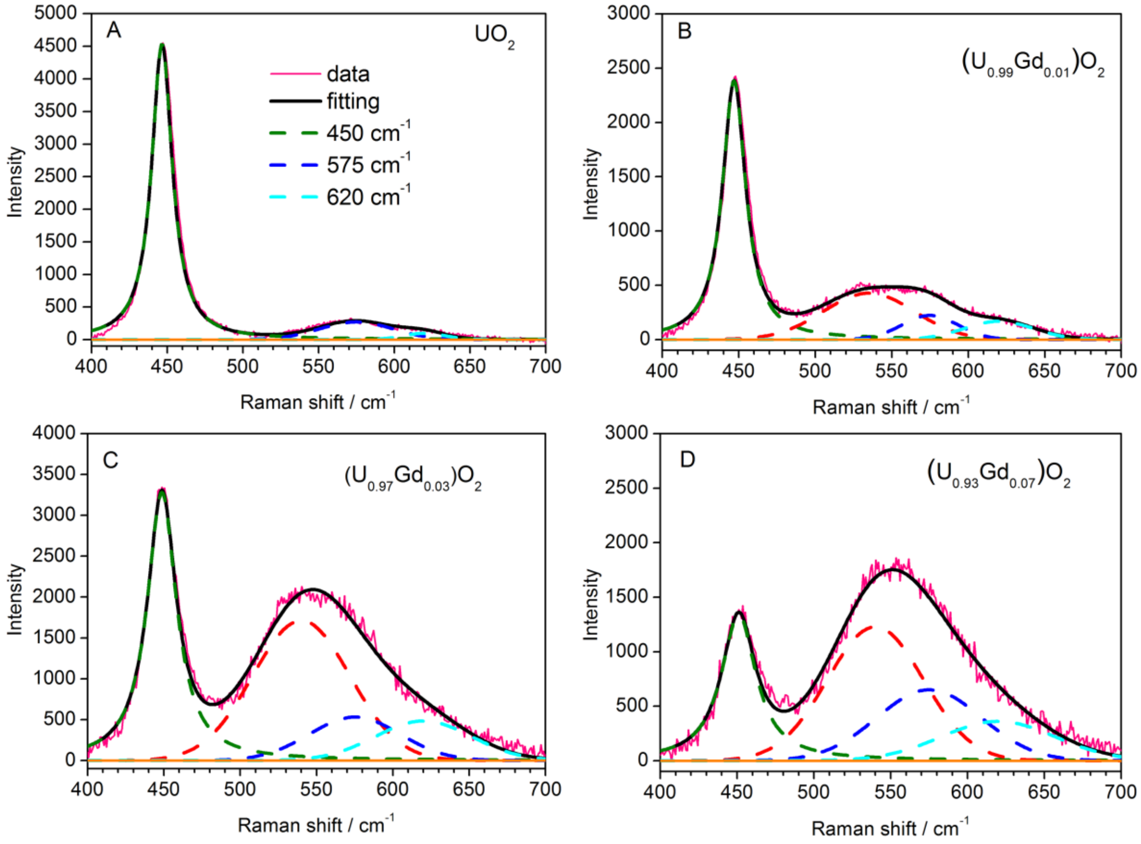

Figure 6.4: Deconvoluted Raman spectra of $U_{1-y}Gd_yO_2$ specimens (a, $y = 0$; b, $y = 0.01$; c, $y = 0.03$ and d, $y = 0.07$).

Whether or not MO_8-type clusters are present is uncertain since deconvolution of the Raman spectra was found to be very sensitive to the peak shape adopted when fitting the spectra. Figure 6.6 compares the deconvoluted Raman spectra for our $U_{0.93}Gd_{0.07}O_2$ specimen obtained using different assumed peak shapes. While the 450 cm^{-1} peak is treated as Lorentzian in both fits, the peaks at 540, 575 and 620 cm^{-1} are assigned as Gaussian peaks in Fig. 6.6a and Lorentzian peaks in Fig. 6.6b. In the latter case (Fig. 6.6b) the 620 cm^{-1} peak becomes marginal.

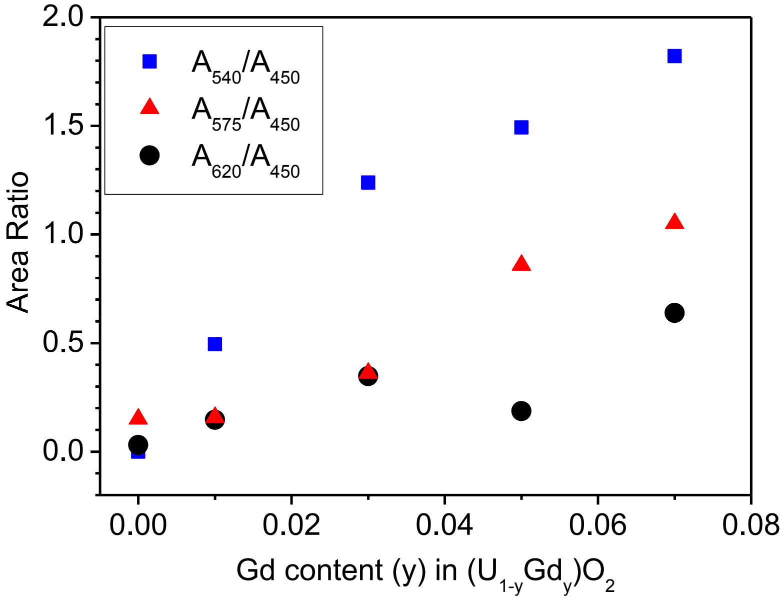

Figure 6.5: Area ratios of the Raman peaks recorded at 540 cm^{-1}, 575 cm^{-1} and 620 cm^{-1} versus the T_{2g} peak at 450 cm^{-1} as a function of the Gd doping level.

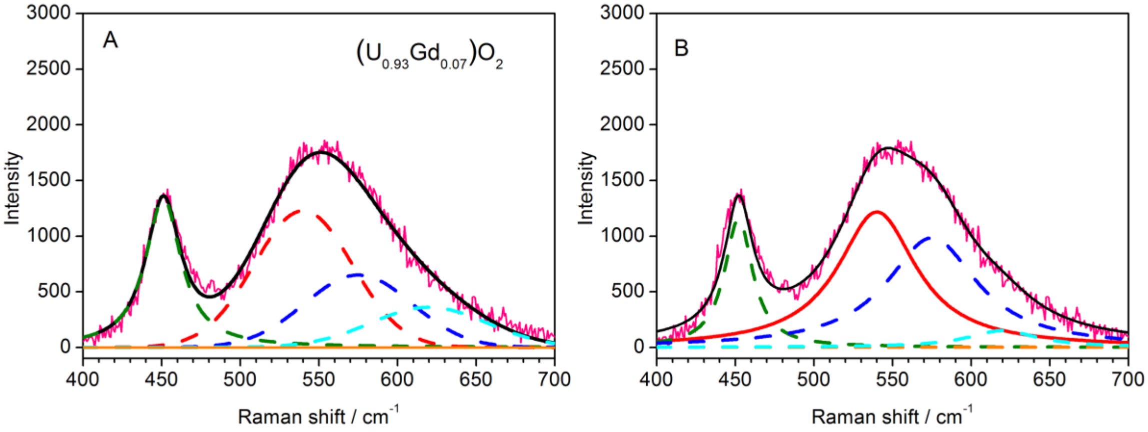

Figure 6.6: Deconvoluted Raman spectrums of $U_{0.93}Gd_{0.07}O_2$. The peaks at 540, 575 and 620 cm^{-1} are treated as Gaussian peaks in (a) and Lorentzian peaks in (b).

6.3.4 Electrochemical Study

When perfectly stoichiometric, UO_2 is best described as a Mott-Hubbard insulator. The introduction of electronic conductivity requires promotion of electrons from the occupied U 5f level to the conduction band which is a strongly activated process with a low probability at room temperature. However, replacement of a fraction of the U^{IV} ions with RE^{III} ions requires further ionization of the remaining uranium ions (to U^{V}) or the creation of oxygen vacancies (O_v) to maintain overall charge balance. The former creates mobile holes in the U 5f band, resulting in an increased conductivity [17]. Table 6.1 summarizes the total cell resistances for the four electrodes investigated, with the resistance being effectively the resistance of the $U_{1-y}Gd_yO_2$ electrode. As expected the undoped UO_2 has a relatively high resistance compared with the $(U_{0.99}Gd_{0.01})O_2$ electrode. However, increased doping leads to only a marginal further increase in conductivity. A possible explanation for this is that the expected increase in conductivity due to doping is offset by the lattice disorder introduced by Gd^{III}-O_v clustering.

Table 6.1: Resistance of the circuits (mainly from the electrodes) measured by the potentiostat in 0.1 mol L^{-1} NaCl with and without 0.05 mol L^{-1} $Na_2CO_3/NaHCO_3$.

Electrode [a]	Resistance (ohms) in 0.1 mol L^{-1} NaCl	Resistance (ohms) in 0.1 mol L^{-1} NaCl and 0.05 mol L^{-1} $Na_2CO_3/NaHCO_3$
UO_2	261.6	245.1
$(U_{0.99}Gd_{0.01})O_2$	53.1	38.6
$(U_{0.95}Gd_{0.05})O_2$	50.8	37.9
$(U_{0.90}Gd_{0.10})O_2$	51.2	37.4

[a] The $U_{1-y}Gd_yO_2$ pellets are ~0.8 cm in diameter and ~0.2 cm in height.

6.3.4.1 Cyclic Voltammetry

Figure 6.7 shows a series of CVs recorded on the undoped and Gd^{III}-doped UO_2 electrodes. As observed for SIMFUEL [18] and Gd-doped UO_2 [19], the electrodes exhibit similar stages of oxidation and reductions. On the positive scan, the current in region 1 can be attributed to the oxidation of a thin surface layer to a mixed U^{IV}/U^{V} oxide ($U^{IV}_{1-2x}U^{V}_{2x}O_{2+x}$) with a thickness limited by diffusion of O to sublattice locations. Oxidation at higher potentials (region 2 in Fig. 6.7) was attributed to the oxidation of this $U^{IV}_{1-2x}U^{V}_{2x}O_{2+x}$ layer to U^{VI}, most of which will dissolve as UO_2^{2+} complexed by HCO_3^-/CO_3^{2-}. On the reverse scan the extent of surface oxidation (not including the U dissolved) can be gauged by the size of the reduction peak 3.

Comparison of the CVs shows that the reactivity in region 1 is insensitive to the doping level and only decreased in region 2 at the highest doping level ($y = 0.1$). Similarly, on the reverse scan the current associated with the reduction of the surface does not vary significantly with doping level.

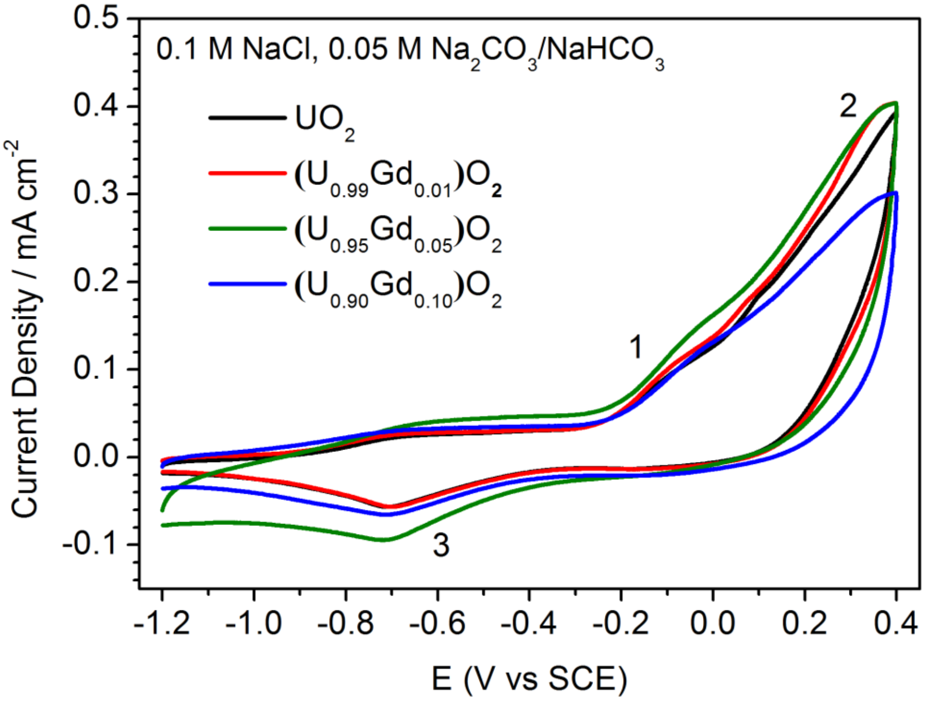

Figure 6.7: CVs recorded on freshly polished $(U_{1-y}Gd_y)O_2$ electrodes in an Ar-purged 0.1 mol L^{-1} NaCl with 0.05 mol L^{-1} $Na_2CO_3/NaHCO_3$ solution, pH = 10. The scan rate = 10 mV s^{-1}.

6.3.4.2 Potentiostatic Polarization

Since CVs are performed rapidly, they may not faithfully capture the differences in reactivity levels due to the doping. These differences may be more realistically assessed under steady-state conditions. Figure 6.8 shows potentiostatic polarization curves recorded on the $U_{0.95}Gd_{0.05}O_2$ electrode for potentials at the positive end of region 1 (0.1 V) and in region 2 (0.2 V to 0.5 V). At the two lowest potentials (0.1 V and 0.2 V) the current decreases linearly (on the logarithmic scale used) especially at the lowest potential. This is consistent with a loss in surface reactivity associated with the formation of a $U^{IV}{}_{1-2x}U^{V}{}_{2x}O_{2+x}$ thin surface layer. At longer times the current continues to decrease at 0.1 V but begins to stabilize at a steady-state value indicating the onset of region 2; i.e., the conversion of this layer to soluble $U^{VI}O_2{}^{2+}$. At 0.3 V and higher a steady state current independent of potential is much more rapidly achieved. As previously shown for 6 wt%

Gd-doped UO_2 steady-state, potential independent behavior can be attributed to the electrochemical formation of a $U^{VI}O_2CO_3$ surface layer (eq. 6.2),

$$U^{IV}{}_{1-2x}U^{V}{}_{2x}O_{2+x} + CO_3{}^{2-} \rightarrow U^{VI}O_2CO_3 + (2-2x)e^- \qquad (6.2)$$

with the subsequent chemically-controlled dissolution of this layer (eq. 6.3).

$$U^{VI}O_2CO_3 + CO_3{}^{2-} \rightarrow U^{VI}O_2(CO_3)_2{}^{2-} \qquad (6.3)$$

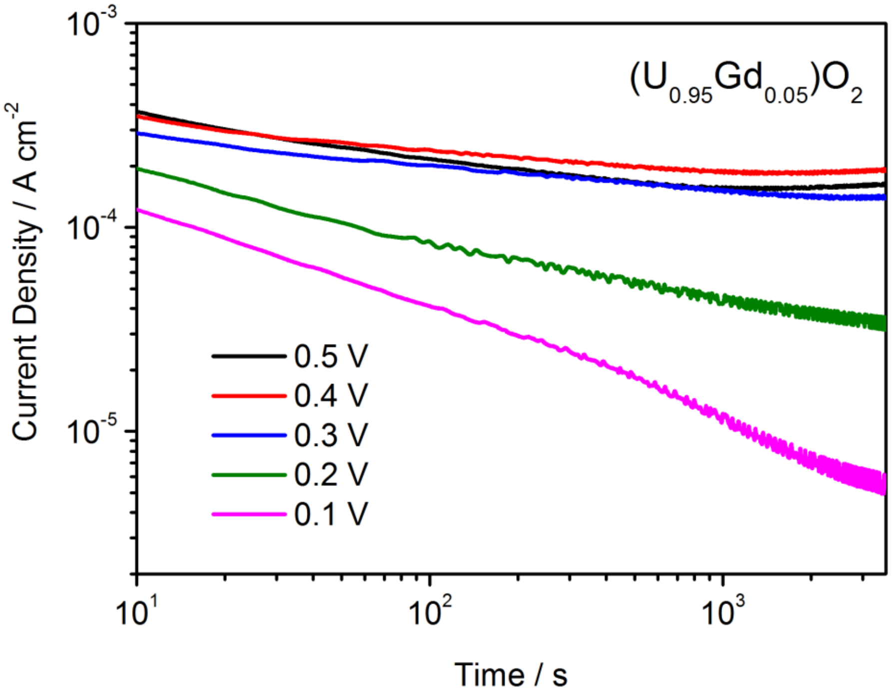

Figure 6.8: Potentiostatic current-time curves (plotted logarithmically) recorded on rotating a $(U_{0.95}Gd_{0.05})O_2$ electrode (16.67 Hz) for 1 h in Ar-purged 0.1 mol L^{-1} NaCl with 0.05 mol L^{-1} $NaHCO_3/Na_2CO_3$, pH = 10.

Figure 6.9 shows the steady-state currents recorded in region 2 as a function of the Gd content of the matrix. At low Gd contents (up to ~y = 0.03 to 0.05) the current, which is due to steady-state dissolution (as $U^{VI}O_2(CO_3)_2{}^{2-}$) is either independent of the doping level or increases slightly (at 0.3 V and 0.5 V). For $y \geq 0.05$ the current decreases with further increases in Gd content. Perhaps a more reliable measure of the influence of Gd-doping can be obtained by integrating the potentiostatic currents measured over the full 60 minute period. The total anodic charges obtained in this manner are shown in Figure 6.10. For anodic oxidation at a potential in region 1 (0.1 V) there is no observable influence of Gd content on the charge accumulated. This confirms that the formation of the thin $U^{IV}{}_{1-2x}U^{V}{}_{2x}O_{2+x}$ is not influenced by Gd-doping. At a slightly higher applied potential (0.2 V) when dissolution as $U^{VI}O_2(CO_3)_2{}^{2-}$ is occurring the trends observed for steady-state currents are confirmed, the charge either remaining constant or increasing slightly over the doping range $0.01 \leq y \leq 0.05$ and then decreasing with y at higher doping levels. ($y > 0.05$).

These effects can be interpreted based on the XRD and Raman spectroscopic observations. The XRD data shows that an increase in doping level leads to a contraction of the UO_2 lattice. This would be expected to inhibit the incorporation of O^{II} ions into interstitial sites (O_I) in the UO_2 fluorite lattice, which should inhibit the oxidation process. By contrast the increase in Gd^{III} content should also lead to an increase in the number of O_v which should increase the rate of oxidation by providing additional sites for the inclusion of O_I.

These changes in current and charge with Gd content suggest a competition between these two effects. The slight increase in current and charge could be taken to indicate a slight increase in anodic reactivity (for the second stage of oxidation) at low doping levels while the clear decrease in reactivity at higher doping levels could reflect the lattice contraction which is marked at the highest levels. It is also possible that the clear decrease, while only small, at higher doping levels demonstrates the formation of Gd^{III}-O_v clusters, as indicated by the changes in the Raman spectra with doping, a process that would also retard oxidation by decreasing the availability of the O_v required to accommodate additional O_I.

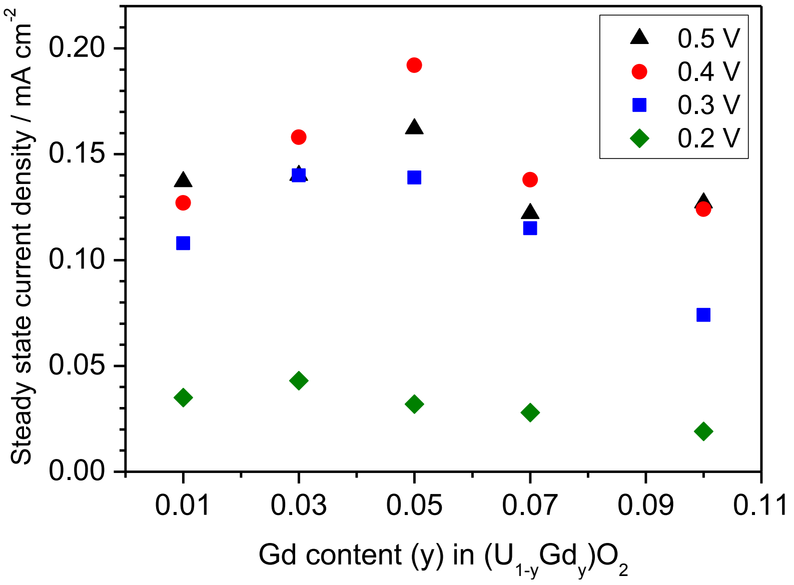

Figure 6.9: Steady-state current density of $(U_{1-y}Gd_y)O_2$ specimens determined potentiostatically at different potentials for 1 hour in 0.1 mol L^{-1} NaCl containing 0.05 mol L^{-1} $Na_2CO_3/NaHCO_3$.

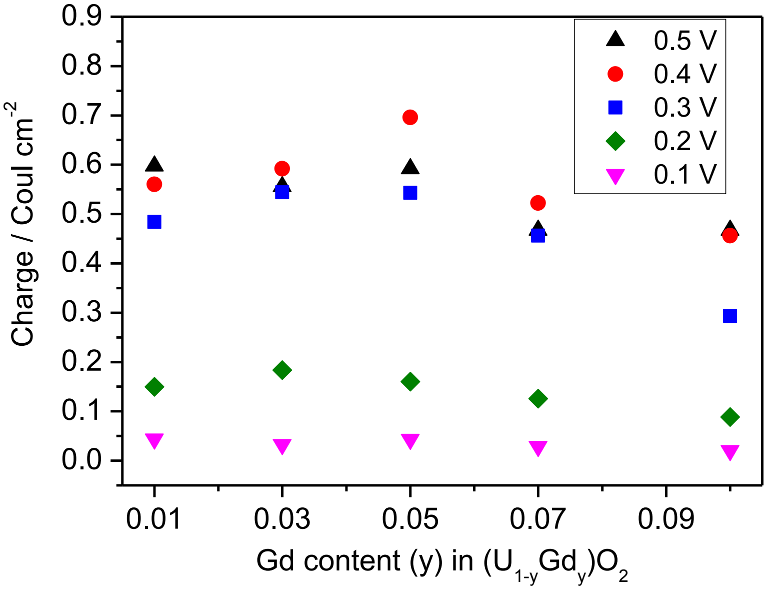

Figure 6.10: Total anodic charge obtained by integration of the current measured potentiostatically for 1 hour on $(U_{1-y}Gd_y)O_2$ electrodes at different potentials in 0.1 mol L^{-1} NaCl containing 0.05 mol L^{-1} $Na_2CO_3/NaHCO_3$.

6.4 Summary and Conclusions

A series of $(U_{1-y}Gd_y)O_2$ materials (y = 0, 0.01, 0.03, 0.05, 0.07 and 0.10) were characterized by XRD and Raman spectroscopy to study the influence of Gd^{III} doping on the structure of $(U_{1-y}Gd_y)O_2$ solid solutions. XRD shows that the materials retain a fluorite lattice, which contracts as the Gd content increases up to 10%. Raman spectroscopy shows that Gd^{III} doping distorts fluorite lattice structure leading to the formation of oxygen vacancies (O_v) and, possibly, MO_8-type complexes since both the oxidation state and ionic radius of Gd^{III} differ from those of U^{IV}.

The reactivity of the $(U_{1-y}Gd_y)O_2$ specimens were compared electrochemically. Oxidation of $(U_{1-y}Gd_y)O_2$ proceeded in two stages: (1) the oxidation of a thin surface layer to a mixed U^{IV}/U^{V} oxide ($U^{IV}_{1-2x}U^{V}_{2x}O_{2+x}$); (2) the oxidation of this $U^{IV}_{1-2x}U^{V}_{2x}O_{2+x}$ layer to U^{VI}, which dissolved as $U^{VI}O_2(CO_3)_2^{2-}$ in the carbonate-containing solution.

No influence of Gd content was observed on the first stage of oxidation. For the second stage, the anodic reactivity appeared to increase very slightly up to y = 0.05 possibly due to the formation of (O_v)s. At higher doping levels a clear decrease in reactivity was observed which could reflect the lattice contraction which becomes marked at these doping levels.

Overall the increase in doping does not exert a major effect on reactivity possibly due to this competition between an increase in the number of O_v and a contraction in the lattice constant.

6.5 References

[1] H. He, M. Broczkowski, K. O'Neil, D. Ofori, O. Semenikhin, D.W. Shoesmith, Corrosion of Nuclear Fuel (UO_2) Inside a Failed Nuclear Waste Container, Report NWMO TR-2012-09, Nuclear Waste Management Organization, Toronto, ON, 2012.

[2] D.W. Shoesmith, Fuel Corrosion Processes under Waste Disposal Conditions, J. Nucl. Mater. 282 (2000) 1-31.

[3] K. Iwasaki, T. Matsui, K. Yanai, R. Yuda, Y. Arita, T. Nagasaki, N. Yokoyama, I. Tokura, K. Une, K. Harada, Effect of Gd_2O_3 Dispersion on the Thermal Conductivity of UO_2, J. Nucl. Sci. Technol. 46 (2009) 673-676.

[4] J.-G. Kim, Y.-K. Ha, S.-D. Park, K.-Y. Jee, W.-H. Kim, Effect of a Trivalent Dopant, Gd^{3+}, on the Oxidation of Uranium Dioxide, J. Nucl. Mater. (2001) 327-331.

[5] T. Ohmichi, S. Fukushima, A. Maeda, H. Watanabe, On the Relation between Lattice Parameter and O/M Ratio for Uradium Dioxide-Trivalent Rare Earth Oxide Solid Solution, J.

Nucl. Mater. 102 (1981) 40-46.

[6] A. Baena, T. Cardinaels, K. Govers, J. Pakarinen, K. Binnemans, M. Verwerft, Lattice Contraction and Lattice Deformation of UO_2 and ThO_2 Doped with Gd_2O_3, J. Nucl. Mater. 467 (2015) 135-143.

[7] H. He, P.G. Keech, M.E. Broczkowski, J.J. Noël, D.W. Shoesmith, Characterization of the Influence of Fission Product Doping on the Anodic Reactivity of Uranium Dioxide, Can. J. Chem. 85 (2007) 702-713.

[8] H. He, D.W. Shoesmith, Raman Spectroscopic Studies of Defect Structures and Phase Transition in Hyper-stoichiometric UO_{2+x}, Phys. Chem. Chem. Phy. 12 (2010) 8108-8117.

[9] M. Razdan, D.W. Shoesmith, Influence of Trivalent-Dopants on the Structural and Electrochemical Properties of Uranium Dioxide (UO_2), J. Electrochem. Soc. 161 (2014) H105-H113.

[10] L. Desgranges, G. Baldinozzi, P. Simon, G. Guimbretière, A. Canizares, Raman Spectrum of U_4O_9: a New Interpretation of Damage Lines in UO_2, J. Raman Spectrosc. 43 (2012) 455-458.

[11] Z. Talip, T. Wiss, P.E. Raison, J. Paillier, D. Manara, J. Somers, R.J.M. Konings, Raman and X-ray Studies of Uranium-Lanthanum-Mixed Oxides Before and After Air Oxidation, J. Am. Ceram. Soc. 98 (2015) 2278-2285.

[12] D. Manara, B. Renker, Raman Spectra of Stoichiometric and Hyperstoichiometric Uranium Dioxide, J. Nucl. Mater. 321 (2003) 233-237.

[13] G. Guimbretière, A. Canizarès, L. Desgranges, R. Caraballo, F. Duval, C. Jegou, M. Magnin, P. Simon, In situ Raman Estimation of Irradiation-induced Heating of UO_2, J. Nucl. Mater. 478 (2016) 172-175.

[14] L. Li, F. Chen, J.-Q. Lu, M.-F. Luo, Study of Defect Sites in $Ce_{1-x}M_xO_{2-\delta}$(x= 0.2) Solid Solutions Using Raman Spectroscopy, J. Phys. Chem. A 115 (2011) 7972-7977.

[15] K. Park, D.R. Olander, Defect Models for the Oxygen Potentials of Gadolinium and Europium-doped Urania, J. Nucl. Mater. 187 (1992) 89-96.

[16] L. Desgranges, Y. Pontillon, P. Matheron, M. Marcet, P. Simon, G. Guimbretière, F. Porcher, Miscibility Gap in the U–Nd–O Phase Diagram: a New Approach of Nuclear Oxides in the Environment?, Inorg. Chem. 51 (2012) 9147-9149.

[17] D.W. Shoesmith, S. Sunder, W.H. Hocking, Electrochemistry of UO_2 Nuclear Fuel, in "Electrochemistry of Novel Materials", edited by J. Lipkowski, and P.N. Ross, VCH publishers, New York, 1994.

[18] B.G. Santos, J.J. Noël, D.W. Shoesmith, The Effect of pH on the Anodic Dissolution of SIMFUEL (UO_2), J. Electroanal. Chem. 586 (2006) 1-11.

[19] M. Razdan, D.W. Shoesmith, The Electrochemical Reactivity of 6.0 wt% Gd-Doped UO_2 in Aqueous Carbonate/Bicarbonate Solutions, J. Electrochem. Soc. 161 (2014) H225-H234.

Chapter 7

7 An Attempt to Simulate the Influence of Radiolytic H_2 on UO_2 by Producing H Radicals Electrochemically

7.1 Introduction

Hydrogen has been shown to suppress the corrosion of spent fuels, α-emitter doped UO_2, SIMFUELs and γ and α irradiated UO_2 [1-9]. A number of mechanisms have been either demonstrated or proposed to explain these effects all of which involve the activation of H_2, known to be unreactive in the molecular form at room temperature, to produce the strongly reducing H radical which scavenges radiolytic oxidants and suppresses UO_2 oxidation and dissolution (i.e., corrosion) [10]. These processes have been clearly demonstrated to occur on SIMFUELs containing noble metal (ε) particles, when the oxidation of H_2 to H^+, via adsorbed $H^\bullet$, on the particles supports the reduction of oxidized U^V/U^{VI} surface species on the galvanically-coupled UO_2 matrix. This is facilitated on SIMFUELs by the rare earth (RE^{III}) doping of the UO_2 matrix which increases the conductivity enabling coupling to occur widely across the surface. This mechanism would also be expected on spent fuels which contain such particles.

In the absence of noble metal particles (e.g., for α-emitter doped UO_2 and γ and α irradiated un-doped UO_2) a similar H_2 activation mechanism has been proposed but has not been demonstrated [7-9, 11]. In this chapter, an attempt is made to simulate the influence of a combination of radiation and dissolved H_2 using electrochemical methods to produce H radicals.

7.2 Experimental

7.2.1 Electrode Materials and Preparation

The materials used in this study are 12.9 wt% Dy_2O_3 doped UO_2 (Dy-UO_2) and non-stoichiometric UO_{2+x} (x = 0.002, 0.10). Details of the nature and characterization of these materials were discussed in Chapter 2.

7.2.2 Electrochemical Cell and Equipment.

The details of the cell are given in Chapter 2. All electrochemical measurements were carried out using a Solartron model 1287 potentiostat to control applied potentials and record current responses. All potentials are quoted against a saturated calomel reference electrode (SCE (0.241V vs SHE)).

7.2.3 Solution Preparation

Solutions were prepared using deionized water with a resistance of 18.2 MΩ cm purified by a Millipore Milli-Q Plus unit which removes organic and inorganic impurities. All experiments were Ar-purged (ultra-high purity, Praxair) and conducted at room temperature. The base electrolyte was 0.1 mol L^{-1} NaCl, and the solution pH was adjusted to 10.0 with NaOH (Caledon). For solutions containing 0.001 mol L^{-1} $NaHCO_3$ (Caledon), the pH was 8.0.

7.2.4 Electrochemical Procedure

Before electrochemical measurements, the working electrode was polished on wet 1200 grit SiC paper, sonicated for 1 minute and then rinsed with deionized water. A cathodic potential (E_{PRE}) was then applied to the working electrode for 5 minutes. Subsequently, a number of different treatments were applied: (i) a potential of –0.6 V was applied and the current measured as a function of time for 5 minutes; (ii) the potential was scanned to 0 V and back at a scan rate of 10 mV s^{-1}; (iii) the electrode was switched to open circuit and the corrosion potential (E_{CORR}) recorded for 1 hour.

7.3 Results and Discussion

7.3.1 The Influence of Surface Pre-treatment on the Potentiostatic Polarization Curve

Fig. 7.1 shows the potentiostatic current-time curves recorded on the Dy-UO_2 and $UO_{2.002}$ electrodes at −0.6 V following different pretreatments. If the electrodes are only polished prior to application of −0.6 V the current is initially cathodic and decreases rapidly over the first ~20 s to a very low value. However, if the electrode is first pretreated at a negative potential (E_{PRE} = −1.2 V) at which a cathodic current is measured, the current immediately becomes anodic when the potential is increased to −0.6 V and then decreases until a steady-state, slightly positive current is established. The value and duration of this anodic current depends on the time the electrode is held at E_{PRE}, as shown in Figure 7.1B for the $UO_{2.002}$ electrode. Although not shown, a substantial cathodic current is measured at E_{PRE}, the great majority of which can be attributed to the reduction of H_2O to H_2. However, these results indicate that the electrode itself is reduced at E_{PRE} and then reoxidized when the applied potential is increased to −0.6 V.

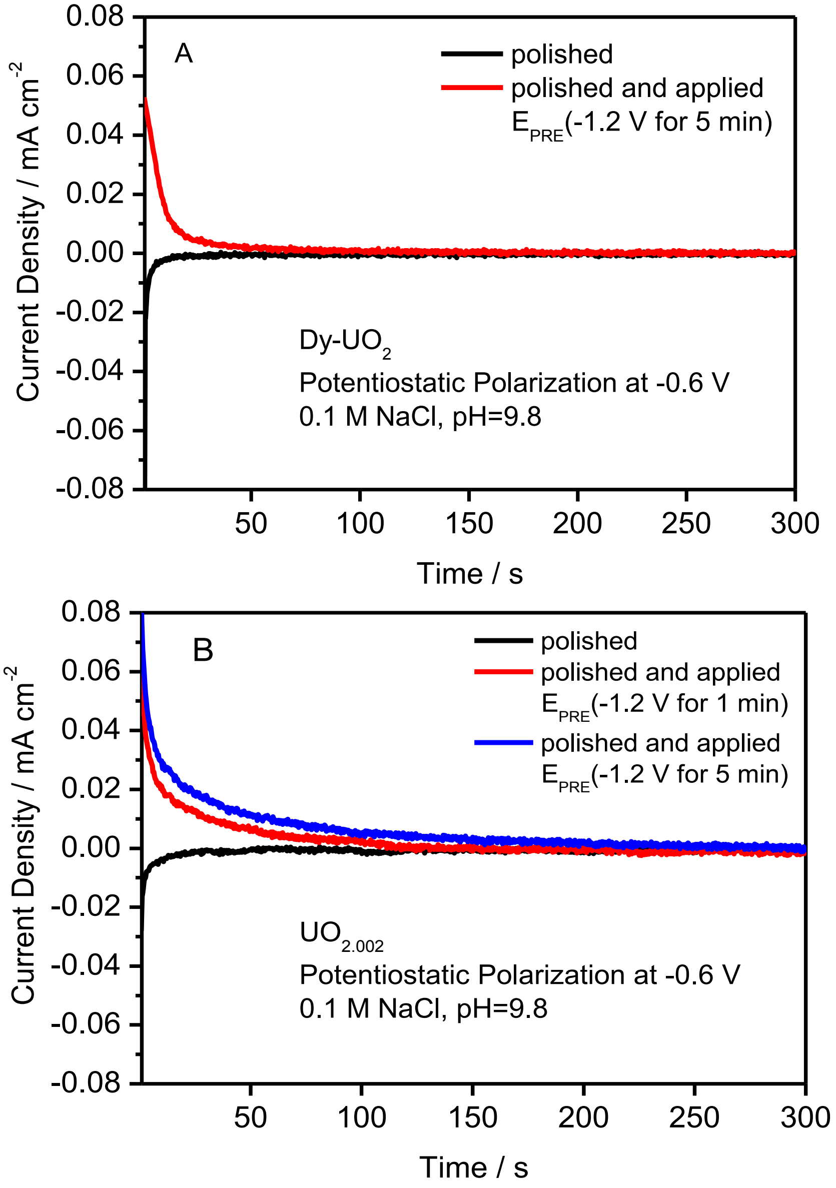

Figure 7.1: Potentiostatic current-time curves recorded on the Dy-UO_2 (A) and $UO_{2.002}$ (B) electrodes at −0.6 V in Ar-purged 0.1 mol L^{-1} NaCl, pH = 9.8.

7.3.2 The Influence of Surface Pre-treatment on Cyclic Voltammetric Measurements

Figure 7.2 shows the influence of various values of E_{PRE} on the voltammetric scans subsequently recorded on the Dy-UO_2, $UO_{2.002}$ and $UO_{2.10}$ electrodes. For the Dy-UO_2 the anodic current recorded in the anodic scan increases as E_{PRE} is made more negative when a larger current for

H_2O reduction would be sustained. After reduction at −1.2 V, a small, but measurable, anodic current is observed over the potential range −0.9 V to −0.2 V, beyond which the current increases due to the onset of anodic dissolution. On the reverse scan the reduction peaks at ~–0.7 V and ~–0.85 V indicate that anodic oxidation of the electrode surface occurred during the forward scan. As discussed in chapter 5 these peaks can be attributed to the reduction of a UO_{2+x} layer (–0.7 V) and a deposited $UO_3.yH_2O$ layer (–0.85 V). The current in the region –0.9 V to –0.4 V can be attributed to oxidation of surface states with anodic oxidation of the UO_2 matrix to UO_{2+x} beginning at ~–0.4 V and anodic dissolution as UO_2^{2+} and its deposition as $UO_3.yH_2O$ commencing for $E \geq –0.2$ V.

When E_{PRE} is made more negative the observed anodic current in the potential range –0.9 V to –0.4 V is substantially increased. Despite this increase in anodic current the cathodic currents observed on the reverse scan decrease indicating that the enhanced anodic processes observed on the forward scan does not lead to a more oxidized surface. This suggests the anodic current is consumed reoxidizing the surface reduced at E_{PRE}, and the resulting reoxidized surface is either subsequently irreversibly oxidized or less susceptible to oxidation than the original matrix. Figure 7.2B shows this effect of E_{PRE} is minor on the $UO_{2.002}$ electrode, the individual stages of matrix oxidation and reduction being only marginally affected by the cathodic pretreatment.

For RE^{III} doped UO_2, replacement of a fraction of the U^{IV} ions with RE^{III} ions requires either the creation of an equivalent number of U^V atoms or oxygen vacancies (O_v) to maintain overall charge balance. For 12.9 wt% Dy_2O_3 doped UO_2, these charge balance mechanisms lead to a chemical composition for Dy-UO_2 of either $(U^{IV}_{0.648}U^{V}_{0.176}Dy^{III}_{0.176})O_2$ or $(U^{IV}_{0.824}Dy^{III}_{0.176})O_{1.912}$, respectively, with previous studies yielding evidence for both mechanisms for Gd^{III} doped UO_2

(chapter 6) and SIMFUELs [12]. Thus, the fractional U^{V} content of the Dy-UO_2 will be between 0 and 0.176. XPS analysis shows the fraction of U^{V} in the surface of freshly polished Dy-UO_2 is 0.12 [13]. By comparison the U^{V} content of the slightly hyper-stoichiometric $UO_{2.002}$ is considerably lower ($(U^{IV}_{0.996}U^{V}_{0.004})O_{2.002}$). This difference suggests the very marked reduction and reoxidation of Dy-UO_2 can be attributed to the reduction of U^{V} atoms in the doped matrix at sufficiently negative values of E_{PRE}.

The observation that H_2O and U^{V} reduction occur simultaneously suggests that the H radicals produced by H_2O reduction could be responsible for the reduction of U^{V}. As illustrated in Figure 7.3, H radicals, created electrochemically on the surface, would be expected to be mobile within the matrix. Since they are also highly reducing they could reduce the U^{V} states with the H^{+} produced maintain charge balance without the need to eject O^{II} ions from the matrix. On the subsequent anodic scan the reoxidation of these reduced U atoms would then account for the observed anodic currents. This reduction/reoxidation process would be expected to become more extensive as the value of E_{PRE} is reduced from −1.2 V to −1.5 V, as observed in Figure 7.2A, since the rate of production of H radicals by H_2O reduction would be increased. By contrast, reduction-reoxidation would be only a minor effect on $UO_{2.002}$ for which the U^{V} content is very low, as observed in Figure 7.2B. This mechanism is further supported by the more marked influence of E_{PRE} on the reduction-reoxidation process on $UO_{2.1}$, Figure 7.2C, which has a considerably higher U^{V} content $((U^{IV}_{0.80}U^{V}_{0.20})O_{2.10})$, although on this electrode the process is partially obscured by the much higher overall reactivity of $UO_{2.1}$ [14] indicated by the much larger currents observed.

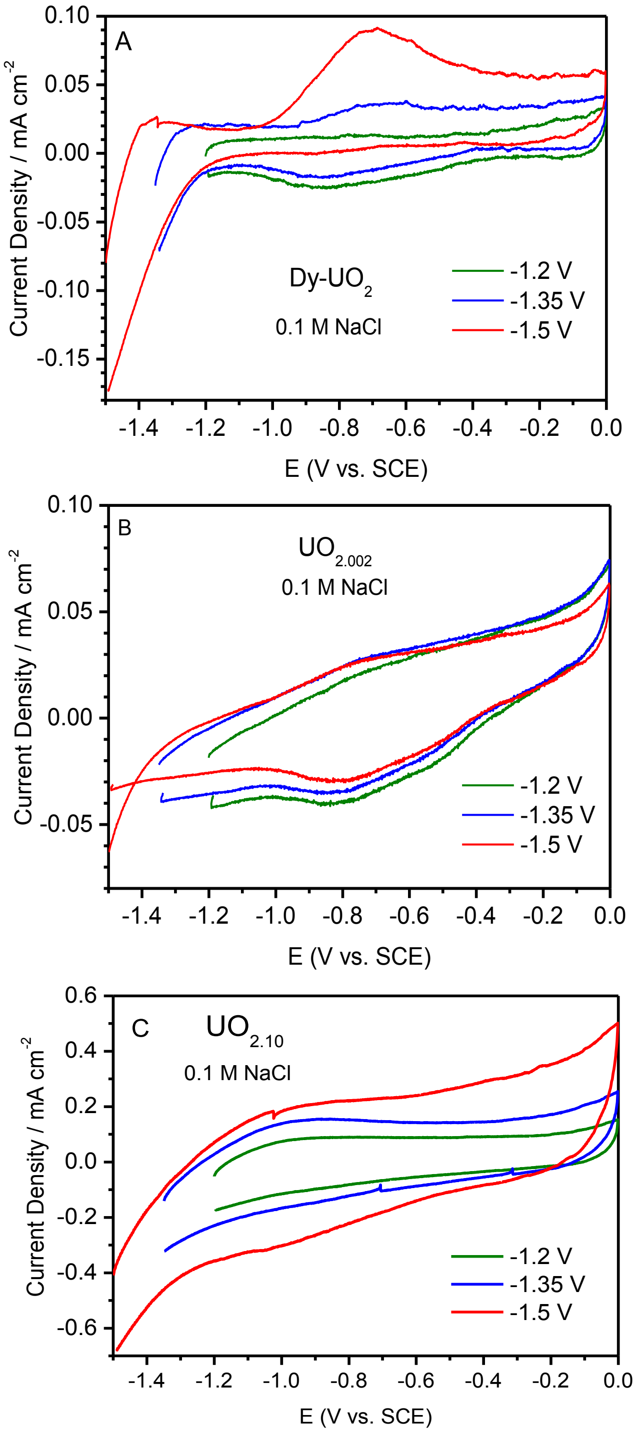

Figure 7.2: CVs recorded on the Dy-UO$_2$ (A), UO$_{2.002}$ (B) and UO$_{2.10}$ (C) electrodes in an Ar-purged 0.1 mol L^{-1} NaCl, pH = 10.0. The scan rate = 10 mV s^{-1}. Before each measurement,

the electrode was polished and cathodically treated at E_{PRE} (−1.2 V, −1.35 V or −1.5 V) for 5 minutes.

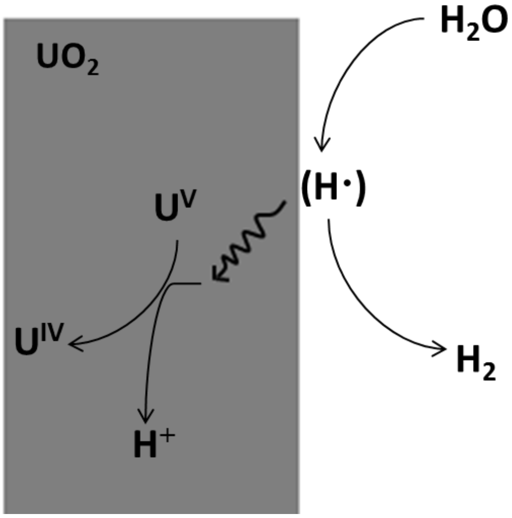

Figure 7.3: Schematic showing the formation of H radicals during H_2O reduction on the UO_2 surface and their diffusion into the UO_2 matrix leading to the reduction of U^V states in the matrix.

7.3.3 The Influence of Surface Pre-treatment on the Corrosion Potential (E_{CORR})

Fig. 7.4 shows the influence of E_{PRE} on the corrosion potential, E_{CORR}, for the Dy-UO_2 and $UO_{2.002}$ electrodes. For the polished, but cathodically untreated electrodes, the values of E_{CORR} are around ~−0.2 V. The minor changes with time may reflect the response of these electrodes to the combination of HCO_3^-/CO_3^{2-} and traces of dissolved O_2 in the solutions. In both cases the air-formed oxide present on the unreduced surface would dissolve slowly in the solution. Previously, it has been shown that the value of E_{CORR} is an indicator of the degree of surface oxidation [15] over the potential range −0.4 V to ~0.05 V, Figure 7.5. This would then suggest that the slow decrease in E_{CORR} observed on the Dy-UO_2 electrode reflects a decrease in the U^V/U^{VI} content of the surface due to the dissolution of the air-formed oxide to reveal a surface which is stabilized against further oxidation by traces of O_2 present in the solution. This would be consistent with the observations presented in Chapter 5 which showed the Dy-doped lattice was stabilized against oxidation. By contrast, the slow increase in E_{CORR} on the $UO_{2.002}$ electrode would indicate a slow oxidation of this surface. The results in Chapter 5 show the composition of the surface of this electrode is non-uniform and enhanced oxidation of the more hyper-stoichiometric surface locations would be anticipated [14].

Application of a cathodic potential to the Dy-UO_2 electrode leads to a very negative initial E_{CORR} which becomes increasingly more negative as E_{PRE} is made more negative. With time E_{CORR} increases with the rate of increase decreasing as E_{PRE} is made more negative. For the $UO_{2.002}$ electrode the E_{CORR} on initially switching to open circuit is less negative. The subsequent increase in E_{CORR} is almost independent of E_{PRE}, with E_{CORR} approaching a value between –0.3 V and –0.4 V, with the latter value representing the potential at which matrix oxidation of RE^{III}-doped UO_2 is first detectable (Chapter 5, [13]). These results indicate that the electrochemically reduced surface produced on both electrodes is unstable as indicated by the eventual relaxation of E_{CORR} to the oxidation threshold potential. This relaxation takes considerably longer on the Dy-UO_2 electrode confirming that the cathodic treatment of this electrode leads to more substantial changes than occur for the $UO_{2.002}$ electrode, consistent with the voltammetric observations, Figure 7.2, and expected as a consequence of the higher U^V content.

This relaxation suggests that U^V is reformed within the oxide matrix on open circuit. This would require that the reaction sequence illustrated in Figure 7.3 be reversible once the formation of H radicals at E_{PRE} is stopped. Whether or not the reduction process is fully reversible with the electrode regaining its original U^V content would require that E_{CORR} be followed for longer periods of time than employed in this study. The exact mechanism of this relaxation remains to be elucidated but preliminary electrochemical impedance spectroscopy measurements suggest the transport of H radicals in the reduced matrix to the oxide surface prior to the formation and release of H_2 may be rate-determining.

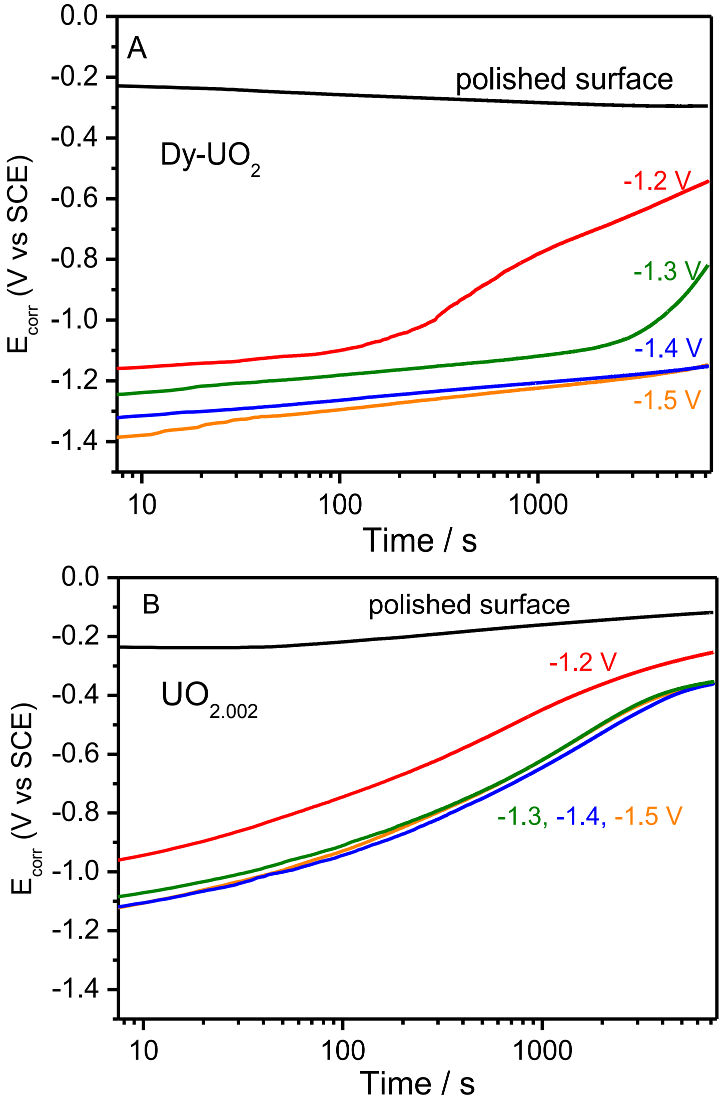

Figure 7.4: Corrosion potential (E_{CORR}) measured on the Dy-UO_2 (A) and $UO_{2.002}$ (B) electrodes in Ar-purged 0.1 mol L^{-1} NaCl with 0.001 mol L^{-1} $NaHCO_3$, pH = 8.0. The electrodes were pretreated by polishing or at different values of E_{PRE} for 5 minutes.

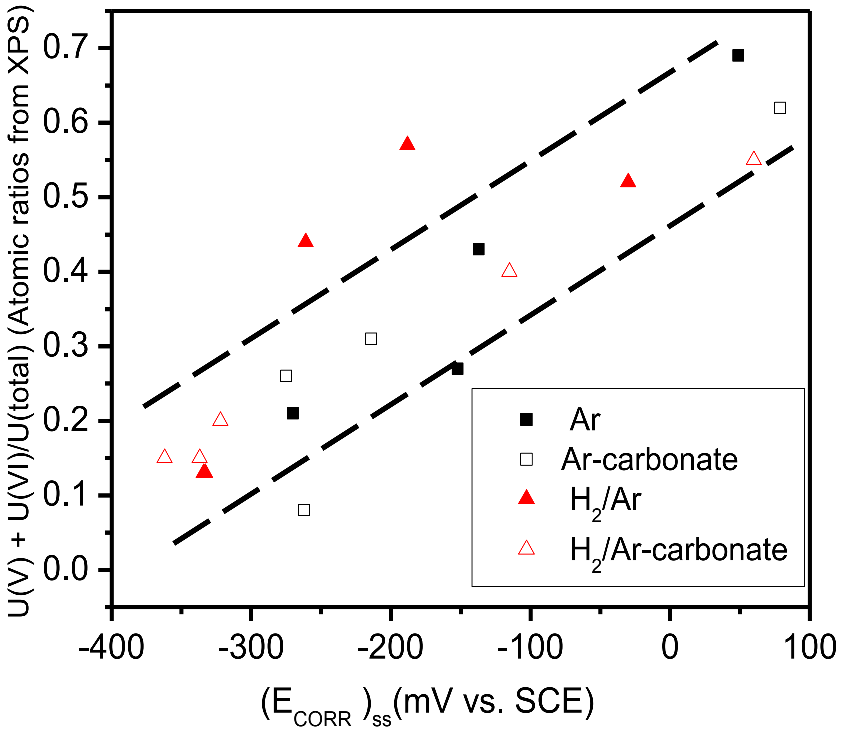

Figure 7.5: Comparison of $(U^V + U^{VI})/U_{total}$ ratio as a function of steady-state E_{CORR} values measured on a 1.5 at% SIMFUEL electrode in 0.1 mol L^{-1} NaCl with and without HCO_3^- /CO_3^{2-} purged with Ar and/or H_2 demonstrating the linear relationship between composition and E_{CORR} [15].

7.3.4 Comparison to the Influence of γ Radiation in the Presence of Dissolved H_2

This influence of electrochemical treatment can be compared to the observations of King et al [8, 11], who observed that γ-irradiation of a solution containing dissolved H_2 also lead to a very negative value of E_{CORR} in the range –0.6 V to –0.8 V and still decreasing after ~20 h. In the absence of dissolved H_2, E_{CORR} values were in the range –0.25 V to –0.35 V as observed here for the untreated electrodes. In experiments in which the radiation source was subsequently removed a similar relaxation in E_{CORR} towards a value representing the oxidation threshold was similarly observed. The UO_2 specimens used in the experiments of King et al. were undoped and not well characterized but likely to be closer in properties to $UO_{2.002}$ than to Dy-UO_2.

This similarity in the response of E_{CORR} suggests a similar reduction of the UO_2 matrix is induced by the combination of γ radiation and H_2 to that caused electrochemically by the application of a potential sufficiently negative to reduce H_2O. As illustrated schematically in Figure 7.5 in the presence of a potentiostatically applied potential reduction of U^V states to U^{IV} can occur both directly by electrochemical reduction and by reaction with absorbed H radicals. In the γ-radiation case a radiation-induced surface activation of H_2 could produce the reactive H radicals leading to the reduction of U^V states.

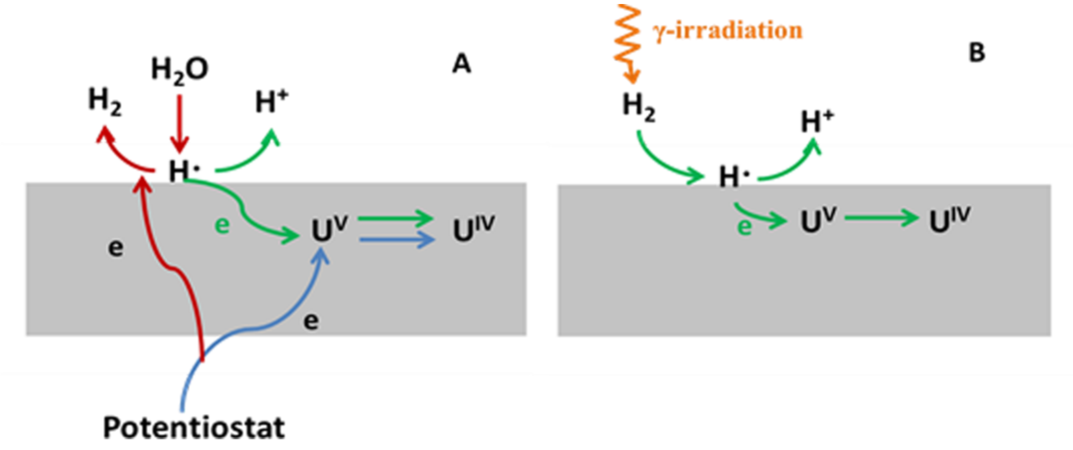

Figure 7.6: Schematic illustration comparing the proposed mechanisms for the electrochemical (A) and radiolytic (B) reduction of U^V states within a doped or non-stoichiometric UO_2 matrix.

7.4 Summary and Conclusions

The influence of the electrochemical reduction of Dy-doped and non-stoichiometric UO_2 has been compared. When the applied potential is sufficiently negative that H_2O reduction occurs leading to the formation of reactive H radicals, the radicals are mobile within the matrix and lead to the reduction of U^V states within the oxide which are present due either to the Dy^{III} doping or the non-stoichiometry. The extent of reduction is determined by the U^V content of the oxide and the rate of production of H radicals. On subsequently switching to open circuit a relaxation of the corrosion potential suggests the reduction of U^V is, at least partially, reversible. Comparison of the corrosion potential behavior observed in experiments in which H_2-containing solutions are γ-irradiated suggests a similar mechanism is operative involving the radiolytic production of surface H radicals leading to matrix reduction.

7.5 References

[1] P. Carbol, J. Cobos-Sabate, J. Glatz, C. Ronchi, V. Rondinella, D.H. Wegen, T. Wiss, A. Loida, V. Metz, B. Kienzler, K. Spahiu, B. Grambow, J. Quinones, A. Martinez Esparza Valiente, The Effect of Dissolved Hydrogen on the Dissolution of ^{233}U Doped UO_2(s), High Burn-up Spent Fuel and MOX Fuel, Report TR-05-09, Swedish Nuclear Fuel and Waste Management Co (SKB), Stockholm, 2005.

[2] S. Rollin, K. Spahiu, U.-B. Eklund, Determination of Dissolution Rates of Spent Fuel in Carbonate Solutions under Different Redox Conditions with a Flow-through Experiment, J. Nucl. Mater. 297 (2001) 231-243.

[3] D.W. Shoesmith, The Role of Dissolved Hydrogen on the Corrosion/dissolution of Spent Nuclear Fuel, Report NWMO TR-2008-19, Nuclear Waste Management Organization, Toronto, ON, 2008.

[4] M.E. Broczkowski, P.G. Keech, J.J. Noël, D.W. Shoesmith, Corrosion of Uranium Dioxide Containing Simulated Fission Products in Dilute Hydrogen Peroxide and Dissolved Hydrogen, J. Electrochem. Soc. 157 (2010) C275-C281.

[5] M.E. Broczkowski, J.J. Noël, D.W. Shoesmith, The Inhibiting Effects of Hydrogen on the Corrosion of Uranium Dioxide under Nuclear Waste Disposal Conditions, J. Nucl. Mater. 346 (2005) 16-23.

[6] M.E. Broczkowski, J.J. Noël, D.W. Shoesmith, The Influence of Dissolved Hydrogen on the Surface Composition of Doped Uranium Dioxide under Aqueous Corrosion Conditions, J. Electroanal. Chem. 602 (2007) 8-16.

[7] J.C. Wren, D.W. Shoesmith, S. Sunder, Corrosion Behavior of Uranium Dioxide in Alpha Radiolytically Decomposed Water, J. Electrochem. Soc. 152 (2005) B470.

[8] F. King, M.J. Quinn, N.H. Miller, The Effect of Hydrogen and Gamma Radiation on the Oxidation of UO_2 in 0.1 M NaCl solution, Report TR-99-27, Swedish Nuclear Fuel and Waste Management Co (SKB), Stockholm, 1999.

[9] A. Traboulsi, J. Vandenborre, G. Blain, B. Humbert, J. Barbet, M. Fattahi, Radiolytic Corrosion of Uranium Dioxide: Role of Molecular Species, J. Phys. Chem. C 118 (2014) 1071-1080.

[10] M.E. Broczkowski, D. Zagidulin, D.W. Shoesmith, The Role of Dissolved Hydrogen on the Corrosion of Spent Nuclear Fuel, In "Nuclear Energy and the Environment", American Chemical Society Symposium Proceedings, Vol 1046, Chapter 26, 349-380.

[11] F. King, D.W. Shoesmith, Electrochemical Studies of the Effect of H_2 on UO_2 Dissolution, Report TR-04-20, Swedish Nuclear Fuel and Waste Management Co (SKB), Stockholm, 2004.

[12] H. He, P.G. Keech, M.E. Broczkowski, J.J. Noël, D.W. Shoesmith, Characterization of the Influence of Fission Product Doping on the Anodic Reactivity of Uranium Dioxide, Can. J. Chem. 85 (2007) 702-713.

[13] M. Razdan, D.W. Shoesmith, Influence of Trivalent-Dopants on the Structural and Electrochemical Properties of Uranium Dioxide (UO_2), J. Electrochem. Soc. 161 (2014) H105-H113.

[14] H. He, R. Zhu, Z. Qin, P.G. Keech, Z. Ding, D.W. Shoesmith, Determination of Local Corrosion Kinetics on Hyper-Stoichiometric UO_{2+x} by Scanning Electrochemical Microscopy, J. Electrochem. Soc. 156 (2009) C87-C94.

[15] M. Razdan, D.W Shoesmith, The Influence of Hydrogen Peroxide and Hydrogen on the Corrosion of Simulated Spent Nuclear Fuel, Faraday Discuss. 180 (2015) 283-299.

Chapter 8

8 Summary and Future Work

8.1 Summary

The overall research goal of this project is to investigate the corrosion process of spent nuclear fuel under permanent disposal conditions. Both modelling simulation and experimental approaches were presented in this thesis.

In chapter 3, a previously developed 2-D model for the corrosion of spent nuclear fuel inside a failed waste container has been adapted to consider the influence of the redox-controlling reactions occurring within fractures in the fuel. A number of reactions have been shown able to moderate the influence of H_2O_2 leading to a reduction in corrosion rate, including the surface-catalyzed decomposition of H_2O_2 and a number of reactions involving H_2. The catalytic decomposition of H_2O_2 on the fuel surface was shown to be a key reaction in moderating the corrosion of the fuel. For the remaining un-decomposed H_2O_2, the model suggested that, for CANDU fuel with moderate in-reactor burnup, only micromolar concentrations of external H_2 (produced by corrosion of the steel container) were required to completely suppress fuel corrosion and that, even within deep fractures in the fuel, the "demand" for external H_2 was only approximately 17 times that required on the outer planar surface of the fuel. By separating the influences on corrosion of radiolytic H_2 ($(H_2)_{int}$) and external H_2 from steel corrosion ($(H_2)_{ext}$), the model showed their relative influence was strongly affected by the dimensions of fractures, which acted as locations where radiolytically-produced H_2O_2 or H_2 could accumulate. This partially isolated these locations from the environment outside of the fracture. As the fractures became deeper and narrower, the influence of $(H_2)_{int}$ became more important in suppressing fuel corrosion, and the need for $(H_2)_{ext}$ became negligible.

In chapter 4, an attempt was made to validate the model developed for fuel corrosion inside a failed waste container by comparing the calculated corrosion rates with published data. The calculated steady-state corrosion rates are in good agreement with published dissolution rates measured on a range of α-emitter doped UO_2 and spent fuel specimens. The kinetics of the reaction of H_2O_2 with UO_2 was shown not to influence the calculated steady-state corrosion rate, only the time required to achieve the steady-state. This demonstrated that the corrosion rate was determined by the radiolytic production rate of H_2O_2 irrespective of the reactivity of the fuel surface. Calculations of corrosion rates for α-emitter doped UO_2 in a closed system demonstrated that the accumulation of O_2, primarily from H_2O_2 decomposition, lead to an increase in corrosion rate. This reflected the fact that, even though the rate constant for the reaction of O_2 with UO_2 was ~ 200 times less than that of for the reaction of H_2O_2, the effect of O_2 can be significant since the steady-state $[O_2]$ can be greater than that of H_2O_2 in a closed system. However, this calculation did not include the influence of radiolytic H_2 which could suppress the corrosion rate. When the influence of H_2 as a reductant reacting on noble metal (ε) particles was included, the model can be used to predict the corrosion rates of spent fuel. Due to the accumulation of radiolytic H_2 with time, and the corrosion rate was shown to decrease with time to a negligible level. The dose rate, H_2O_2 decomposition ratio, and the coverage of ε particles all influenced the time needed for the corrosion rate to decrease to a negligible level. These calculations indicated that corrosion of spent fuel in a closed system should be severely restricted by radiolytic H_2.

In chapter 5, a comparison of the anodic reactivity of close-to-stoichiometric $UO_{2.002}$, SIMFUEL and Gd-doped and Dy-doped UO_2 specimens was presented. The results showed that rare earth doping stabilized the matrix against oxidation to $U^{IV}{}_{1-2x}U^{V}{}_{2x}O_{2+x}$ and its further oxidation to soluble U^{VI}. Once dissolution became observable the order of reactivity was $UO_{2.002}$ > SIMFUEL > Gd-UO_2 > Dy-UO_2. For $UO_{2.002}$ the composition was found to be non-uniform with some surface locations being more non-stoichiometric and, hence, more reactive than others. For the RE^{III}-doped UO_2 the onset of matrix dissolution was accompanied by the enhanced oxidation of the matrix to $U^{IV}{}_{1-2x}U^{V}{}_{2x}O_{2+x}$. This can be attributed to the onset of tetragonal lattice distortions as surface oxidation of the matrix proceeded which lead to the clustering of defects, enhanced diffusion of O_I to deeper locations and destabilization of the fluorite lattice. HCO_3^-/CO_3^{2-} and HPO_4^{2-} were shown to have significantly different effects on the matrix oxidation and dissolution processes. At low potentials HPO_4^{2-} suppressed matrix oxidation compared to the behaviour in HCO_3^-/CO_3^{2-}. This may be related to the ability of HCO_3^-/CO_3^{2-} to stabilize the U^V state. At higher potentials, the oxidation to U^{VI} was promoted by HPO_4^{2-} but, compared to the behavior in HCO_3^-/CO_3^{2-}, dissolution was suppressed by the formation of an insoluble uranyl phosphate layer.

In Chapter 6, the influence of Gd^{III} doping on the structure of $(U_{1-y}Gd_y)O_2$ materials ($y = 0$, 0.01, 0.03, 0.05, 0.07 and 0.10) was characterized by XRD and Raman spectroscopy. XRD showed that the materials retained a fluorite lattice, which contracted as the Gd content increases up to 10%. Raman spectroscopy shows that Gd^{III} doping distorted the fluorite lattice leading to the formation of oxygen vacancies (O_v) and, possibly, MO_8-type complexes since both the oxidation state and ionic radius of Gd^{III} differ from those of U^{IV}. The reactivities of the $(U_{1-y}Gd_y)O_2$ specimens were compared electrochemically. Oxidation of $(U_{1-y}Gd_y)O_2$ proceeds in two stages: (1) the oxidation of a thin surface layer to a mixed U^{IV}/U^{V} oxide ($U^{IV}_{1-2x}U^{V}_{2x}O_{2+x}$); (2) the oxidation of this $U^{IV}_{1-2x}U^{V}_{2x}O_{2+x}$ layer to U^{VI}, which dissolves as $U^{VI}O_2(CO_3)_2^{2-}$ in the carbonate-containing solution. No influence of Gd content was observed on the first stage of oxidation. For the second stage, the anodic reactivity appeared to increase very slightly up to $y = 0.05$ possibly due to the formation of (O_v)s. At higher doping levels a clear decrease in reactivity was observed which could reflect the lattice contraction which became marked at these doping levels. Overall the increase in doping did not exert a major effect on reactivity possibly due to this competition between an increase in the number of O_v and a contraction in the lattice parameter.

In chapter 7, an attempt is made to understand the mechanism of the suppression of UO_2 corrosion in the presence of γ-irradiation and H_2 by simulating the process electrochemically. Heavily-doped Dy-UO_2 (Dy_2O_3, 12.9 wt%) and $UO_{2.002}$ specimens were pretreated at a cathodic potential (in the range of −1.2 V to −1.5 V) for a period of time. The surface of Dy-UO_2 was shown to be more extensively reduced than that of $UO_{2.002}$. This was attributed to the reduction of U^{V} states in the matrix which are present at much higher levels in Dy-UO_2 than in $UO_{2.002}$. Since reduction only occurred at potentials at which H_2O reduction to H_2 occurs, it was proposed that reduction of U^{V} was caused by reaction with H radicals produced as surface intermediates in H_2O reduction. Since these radicals are mobile within the UO_2 matrix, U^{V} reduction occurs in significant depths into the matrix. That reduction of the surface was demonstrated by the extent of the surface reoxidation required in subsequent voltammetric experiments and by the adoption of very negative corrosion potentials after cathodic pretreatment. The subsequent relaxation of the corrosion potential to more positive values showed the reduction process ($U^{V} + H^{\bullet} \rightarrow U^{IV} + H^{+}$) was reversible. Although not as marked a similar negative corrosion potential has been observed by others in irradiated H_2-containing solutions. As observed when the electrochemical potential was removed, the corrosion potential relaxed when the radiation filed was removed. This similarity in behavior suggests a similar matrix reduction process is caused by surface H radicals produced by γ irradiation.

8.2 Future Work

The primary goal of the model is to simulate the corrosion process inside a failed waste container, and a number of features need to be considered in the future.

- A number of mechanistic details and kinetic deficiencies remain unresolved. The kinetics of reactions involving H_2, H_2O_2 and the decomposition of H_2O_2 are not known within the concentration ranges important for spent nuclear fuel. While these deficiencies may be covered by conservative assumptions in the calculations, they preclude any attempts to validate the model. An experimental program is required to generate the necessary kinetic database.

- In the current model it was assumed that the concentrations of steel corrosion products (Fe^{2+} and H_2) are constant. In reality, the supply of Fe^{2+} and H_2 will be determined by the corrosion performance of the steel container vessel. Consequently, a more detailed analysis of the corrosion of the steel vessel is required to improve the model.

- Presently, it is assumed in the model that the ε-particles are evenly distributed on the fuel surface and within fractures. However, these particles are distributed inhomogeneously in a pattern reflecting the burn-up characteristics of the fuel. Their ability to control redox conditions will therefore vary with location within the fuel. The sensitivity to this distribution needs to be simulated in the model.

- Presently the α-radiolysis model accounts only for the radiolysis of H_2O. Further model development is required to account for the influence of groundwater species such as chloride and carbonate on aqueous radiolysis and UO_2 corrosion.

- While the influence of RE^{III} doping on the anodic reactivity has been shown to be minor, whether or not it influences the cathodic kinetics (e.g., the reduction of H_2O_2) remains to be investigated.

- The presently developed 2-dimensional model needs to be expanded to a 3-dimnesional model able to predict fuel corrosion behavior within a failed CANDU fuel bundle.

Curriculum Vitae

Name:
Nazhen Liu

Post-secondary Education and Degrees:
Ph.D. Physical & Analytical Chemistry (Sep. 2012- Dec.2016), University of Western Ontario

Ph.D. Organometallic Chemistry (Sep. 2006- Oct.2010), Shandong University

B.Sc. Chemistry (Sep. 2002- Jun. 2006), Qufu Normal University

Honours and Awards:
NACE corrosion 2015 student travel award, 2015

Western graduate research scholarship, 2012-2016

Christian Sivertz Scholarship, 2012

CSC Scholarship, 2010

Outstanding Graduate, 2006

Related Work Experience:
Teaching Assistant, The University of Western Ontario, 2012-2016.

Publications:

1. **Nazhen Liu**, Linda Wu, Zack Qin, David W. Shoesmith*, Roles of Radiolytic and Externally Generated H_2 in the Corrosion of Fractured Spent Nuclear Fuel, Environmental Science & Technology, 2016, 50, 12348.

2. **Nazhen Liu**, Zack Qin, James J. Noël, David W. Shoesmith*, Modelling the Radiolytic Corrosion of α-doped UO_2 and Spent Nuclear Fuel, submitted to Environmental Science & Technology.

3. **Nazhen Liu**, Heming He, James J. Noël, David W. Shoesmith*, The Electrochemical Study of Dy_2O_3 Doped UO_2 in Slightly Alkaline Sodium Carbonate/bicarbonate and Phosphate Solutions, submitted to Electrochimica Acta.

4. **Nazhen Liu**, Jandee Kim, Jeongmook Lee, Young-Sang Youn, Jong-Goo Kim, Jong-Yun Kim, James J. Noël, David W. Shoesmith*, Influence of Gd Doping on the Structure and Electrochemical Behavior of UO_2, submitted to Electrochimica Acta.

5. Jeongmook Lee, Jandee Kim, Young-Sang Youn, **Nazhen Liu**, Jong-Goo Kim, Yeong-Keong Ha, David W. Shoesmith, Jong-Yun Kim*, Raman Study on Structure of $U_{1-y}Gd_yO_{2-x}$ (y=0.005, 0.01, 0.03, 0.05 and 0.1) Solid Solutions, Journal of Nuclear Materials, 2016, accepted.

6. Shannon Hill, **Nazhen Liu**, Zack Qin, Dmitrij Zagidulin, David Shoesmith*, Interactions between Carbon Steel and UO_2 Corrosion Fronts inside a Failed Nuclear Waste Container, 17th International Conference on Environmental Degradation of Materials in Nuclear Power Systems – Water Reactors, Ottawa, Ontario, Canada, 2015.

7. Linda Wu, **Nazhen Liu**, Zack Qin, David W. Shoesmith*, Modelling the Radiolytic Corrosion of Fractured Nuclear Fuel under Permanent Disposal Conditions, Journal of the Electrochemical Society, 2014, 161 (8), 3259.

8. **Nazhen Liu**, Gengyu Zhu, Hongjian Sun, Xiaoyan Li*, Simple Synthesis and Structure Characterization of a Phosphoniomethylidyne Tantalum (V) Complex, Inorganic Chemistry Communications, 2013, 27, 36.

9. **Nazhen Liu**, Xiaoyan Li, Xiaofeng Xu, Zhiping Wang, Hongjian Sun*, Synthesis, Structure and DFT Study of Dinuclear Iron, Cobalt and Nickel Complexes with Cyclopentadienyl-Metal Moieties, Dalton Transactions, 2011, 40, 6886.

10. **Nazhen Liu**, Xiaoyan Li, Hongjian Sun*, Synthesis and Properties of Novel Ortho-Metallated Cobalt (I) and Iron (II) Complexes through C-H Bond Activation of Dibenzylphenylphosphine, Journal of Organometallic Chemistry, 2011, 696, 2537.

11. Jiong Jia, Chenggen Wang, **Nazhen Liu**, Xiaoyan Li*, {2-[(Benzylphenylphosphanyl-κP) methyl]-phenyl-κC^1}iodidobis(trimethylphosphane)cobalt(II), Acta Crystallographica Section E, 2011, E67, m991.

12. **Nazhen Liu**, Aichen Wang, Hongjian Sun, Xiaoyan Li*, Simple Synthesis of (Triphenylphosphoniomethylidene)(pentamethylcyclopentadienyl) titanium(IV) Dichloride and Its Reaction with Carbon Monoxide, Organometallics, 2009, 29, 1996.

Conferences presentations:

1. **Nazhen Liu**, Linda Wu, Zack Qin, David Shoesmith, The influence of H_2 from water radiolysis and steel corrosion on the corrosion of nuclear fuel inside a failed waste container, Spent Fuel Workshop 2016, Stockholm, Sweden, May 3-4, 2016. (Talk)

2. **Nazhen Liu**, David Shoesmith, Electrochemical study of lattice-doped UO_2 in slightly alkaline sodium carbonate/bicarbonate solutions, Spent Fuel Workshop 2016, Stockholm, Sweden, May 3-4, 2016. (Talk)

3. **Nazhen Liu**, Zack Qin, David Shoesmith, Modelling the Radiolytic Corrosion of α-doped UO_2, Gordon Research Conference: Corrosion-Aqueous, New London, NH. July 10-15, 2016, & Gordon Research Seminar, July 9-10, 2016. (Poster)

4. **Nazhen Liu**, Linda Wu, Zack Qin, David Shoesmith, The influence of H_2 from water radiolysis and steel corrosion on the corrosion of nuclear fuel inside a failed waste container, NACE Corrosion 2015, Dallas, TX, March 15-19, 2015. (Talk)

5. **Nazhen Liu**, David Shoesmith, Electrochemical study of lattice-doped UO_2 in slightly alkaline sodium carbonate/bicarbonate solutions, 7th International Symposium on

Applicationof Chemical and Analytical Technologies in Nuclear Industries, Daejeon, Korea, September 11, 2015. (Poster)

6. **Nazhen Liu**, David Shoesmith, Electrochemical study of lattice-doped UO_2 in slightly alkaline sodium carbonate/bicarbonate solutions, University Network of Excellence in Nuclear Engineering (UNENE), Toronto, ON, December, 2015. (Poster)
7. **Nazhen Liu**, Linda Wu, Zack Qin, David Shoesmith, The influence of H_2 from water radiolysis and steel corrosion on the corrosion of nuclear fuel inside a failed waste container, University Network of Excellence in Nuclear Engineering (UNENE), Toronto, ON, December, 2014. (Poster)
8. **Nazhen Liu**, David Shoesmith, Electrochemical study of lattice-doped UO_2 in slightly alkaline sodium carbonate/bicarbonate solutions, Gordon Research Conference: Corrosion-Aqueous, New London, NH. July 13-18, 2014, & Gordon Research Seminar, July 12-13, 2014. (Poster)